Universidad del País Vasco Euskal Herriko Unibertsitatea

UPV EHU CSIC | INSTITUTO BIOFISIKA INSTITUTUA

Doctoral Thesis

Lipid regulation of Atg8 family protein recruitment and membrane modulation of mitophagy and autophagic cell death

Zuriñe Antón Helas

2017

Supervisor: Prof. Alicia Alonso Izquierdo

Biofisika Institutua (CSIC, UPV/EHU)

Department of Biochemistry and Molecular Biology

Doctoral Thesis

Lipid regulation of Atg8 family protein recruitment and membrane modulation of mitophagy and autophagic cell death

Zuriñe Antón Helas

2017

Supervisor: Prof. Alicia Alonso Izquierdo

Contents

Abbreviations

2-AG	2-arachidonoylglycerol
2D/3D	two- or three-dimensional
4H	four-helix bundle
a.u.	arbitrary units
$A_{260}/_{280}$	absorbance at 260 or 280 nm
A488	Alexa Fluor 488
AC	alternating current
AGO2	argonaute 2
AIM	Atg8-family interacting motif
AKT	RAC-alpha serine/threonine-protein kinase
ALPS	amphipathic lipid packing sensor
Ambra1	autophagy and beclin 1 regulator 1
Amp	ampicillin
AMPK	AMP-dependent protein kinase
Ams1p	α-mannosidase
ANTS	8-aminonapthalene-1,3,6-trisulfonic acid
AP	autophagosome
Ape1p	aminopeptidase 1
A-SMase	acid sphingomyelinase
ATG	autophagy-related
ATP	adenosine triphosphate
ATPB	ATP synthase subunit beta
AVd	degradative autophagic vacuole
AVi	initial autophagic vacuole
BafA1	bafilomycin A1
BAK	BCL-2 associated killer protein

BAR	bin–amphiphysin–rvs domain
BAX	BCL-2 associated X protein
BCA	bis-cinchoninic acid
BCL-2	B-cell CLL/lymphoma 2
BCL-x	B-cell lymphoma-extra
BDMA	N-benzyldimethylamine
Beclin 1	coiled-coil myosin-like BCL-2-interacting protein
BH	BCL-2 homology domain
BID	BH3 interacting domain death agonist
BNIP3	BCL-2 interacting protein 3
BSA	bovine serum albumin
CALCOCO2/NDP52	calcium-binding and coiled-coil domain-containing protein 2
CAPK	ceramide-activated protein kinase
CCCP	carbonyl cyanide m-chlorophenyl hydrazine
CD	circular dichroism
CD-95	cluster of differentiation 95
CDase	ceramidase
cDNA	complementary DNA
CDP-DAG	cytidine diphosphate diacylglycerol
Cer	ceramide
CERS	ceramide synthase
CFP	cyan fluorescent protein
Chol/Ch	cholesterol
CL	cardiolipin
CL*	*E.coli* cardiolipin
CLEM	correlative light and electron microscopy
CMA	chaperone-mediated autophagy
CMV	cytomegalovirus
CNR/CB	cannabinoid receptor
COL4A3BP/CERT	collagen type IV α-3-binding protein

c_p	heat capacity
CTSB/L	cathepsin B or L
Cvt	cytoplasm-to-vacuole targeting
CYCS	cytochrome c somatic
Cyt c	cytochrome c
DABCO	1,4-diazabicyclo[2.2.2]octane
DAG	diacylglycerol
DAPI	4',6-diamidino-2-phenylindole
ddH_2O	double distilled water
DDSA	dodecenyl succinic anhydride
DEGS1/2	delta(4)-desaturase, sphingolipid 1 or 2
Deptor	DEP-domain-containing mTOR-interacting protein
DFCP-1	double FYVE domain-containing protein 1
dhCer	dihydroceramide
dhSM	dihydrosphingomielin
DLCL	dilysocardiolipin
DLS	dynamic light scattering
DMEM	Dulbecco's modified Eagle's medium
DMSO	dimethylsulfoxide
DNase	deoxyribonuclease
DNM1L/DRP1	dynamin-1-like protein
Dodec/EtOH	dodecane/etanol
DOPE	1,2-dioleoyl-*sn*-glycero-3-phosphatidylethanolamine
DPX	*p*-xylene-bis-pyridinium bromide
DSC	differential scanning calorimetry
dsDNA	double-stranded DNA
DsRed	discosoma red fluorescent protein
DTT	DL-dithiothreitol
E2F1	E2F transcription factor 1
EBSS	Earle's balanced salt solution

EC50	half maximal effective concentration
ECD	evolutionarily conserved domain
eCer	egg ceramide
EDTA	ethylenediaminetetraacetic acid
EEA1	early endosome antigen 1
EM	electron microscopy
EPR	electron paramagnetic resonance
ER	endoplasmic reticulum
ERGIC	ER-Golgi intermediate compartment
ESCRT	endosomal sorting complex required for transport
FA	fatty acid
FBS	fetal bovine serum
FCCP	carbonyl cyanide p-trifluoromethoxyphenylhydrazone
FIP200	focal adhesion kinase family interacting protein 200 kDa
Fis1	mitochondrial fission 1 protein
FLM	fluorescence light microscopy
FM	fluorescence microscopy
FoxO1/3	forkhead box O1 or 3
FT	flow-through
FT-IR	Fourier-transform infrared spectroscopy
FUNDC1	FUN14 domain containing 1
FYCO1	FYVE and coiled-coil domain-containing protein 1
GABA(A)	GABA type A
GABARAP	GABA type A receptor-associated protein
GABARAPL1/2/3	GABA type A receptor-associated protein like 1, 2 or 3
GATE-16	Golgi-associated ATPase enhancer of 16 kDa
GCS	glucosylceramide synthase
GFP	green fluorescent protein
GlcCer	glucosylceramide
GOS28	Golgi SNAP receptor complex member 1

gp78	glycoprotein 78
GPI	glycosylphosphatidylinositol
GSLs	glycosphingolipids
GSSG	glutathione disulfide
GST	glutathione S-transferase
GT11	N-[(1R,2S)-2-hydroxy-1-hydroxymethyl-2-(2-tridecyl-1-cyclopropenyl)ethyl]octanamide
GTP	guanosine triphosphate
GUV	giant unilamellar vesicle
GβL	G-protein β-subunit-like protein
HEK293T	human embryonic kidney 293T
HEPES	2-[4-(2-hydroxyethyl)piperazin-1-yl]ethanesulfonic acid
H_{II}	inverted-hexagonal lipid phase
hIPS	human induced-pluripotent stem cells
HIV/GIB	human immunodeficiency virus
HOPS	homotypic fusion and protein sorting
HPF	high-pressure freezing
HRP	horseradish peroxidase
HSP60	heat shock protein 60 kDa
IANBD	*N*,*N*'-dimethyl-*N*-(iodoacetyl)-*N*'-(7-nitrobenz-2-oxa-1,3-diazol-4-yl)ethylenediamine
IMM	inner mitochondrial membrane
iPSC	induced pluripotent stem-cell
IPTG	isopropyl-β-D-1-thiogalactopiranoside
IRGM	immunity related GTPaseM
ISP-1	myriocin
ITC	isothermal titration calorimetry
KAP1	KRAB associated protein 1
k_B	Boltzmann constant
KDSR	3-ketodihydrosphingosine reductase
LAMP2	lysosomal-associated membrane protein 2

LB	Luria-Bertani
LC3A/B/B2/C	MAP1LC3; microtubule-associated protein 1 light chain 3 A, B, B2 or C
LDL	low-density lipoprotein
LIR	LC3-interacting region
LM	light microscopy
LMP	lysosomal membrane permeabilization
L_o	liquid-ordered lamellar lipid phase
LPC	lysophosphatidylcholine
LUV	large unilamellar vesicle
L_α	fluid, liquid-disordered or liquid-crystalline lamellar lipid phase
L_β	gel or solid-ordered lamellar lipid phase
$L_{\beta'}$	oblique lamellar lipid phase
$L_{\beta I}$	interdigitated lamellar lipid phase
MAPK	mitogen-activated protein kinase
mAU	milli absorbance units
MEF	mouse embryonic fibroblast
Mff	mitochondrial fission factor
Mfn	mitofusin
Miro	mitochondrial Rho GTPase
MLCL	monolysocardiolipin
MLV	multilamellar vesicle
MNA	methyl nadic anhydride
MtCK	mitochondrial creatine kinase
mtDNA	mitochondrial DNA
mTORC1	mammalian target of rapamycin complex 1
MTS	mitochondrial targeting sequence
Mul1	mitochondrial ubiquitin ligase activator of NFKB 1
NBD	7-nitrobenz-2-oxa-1,3-diazol-4-yl
NBR1	neighbor of BRCA1 (breast cancer early-onset 1) gene 1
NIX	NIP3-like protein X

NMR	nuclear magnetic resonance
Norm.	normalized
Nox	NADPH oxidase
NSF	N-ethylmaleimide sensitive factor
nSMase	neutral sphingomyelinase
NUPR1/p8	nuclear protein 1
OATL1	ornithine aminotransferase-like 1
OD_{600}	optical density at 600 nm
OMM	outer mitochondrial membrane
OPA1	optic atrophy 1 protein
OPTN	optineurin
PA	phosphatidic acid
PARK2/Parkin	E3 ubiquitin-protein ligase parkin
PARL	presenilin-associated rhomboid-like protein
PAS	phagophore assembly site
PBS	phosphate buffered saline
PC/PtdCho	phosphatidylcholine
PCR	polymerase chain reaction
PD	Parkinson disease
PDI	polydispersity index
PDI (protein)	protein disulfide isomerase
PE/PtdEtn	phosphatidylethanolamine
PFA	paraformaldehyde
PG	phosphatidylglycerol
PH	pleckstrin homology
PI3KC1/3	class I or III phosphatidylinositol-3-kinase
PINK1	PTEN-induced putative kinase 1
PIPES	piperazine-N,N′-bis(2-ethanesulfonic acid)
PIs	phosphoinositides
PKA	cAMP-dependent protein kinase

PKCα	protein kinase C alpha
PLA2/C/D	phospholipase A2, C or D
PLO	protein-lipid overlay
PLS3	phospholipid scramblase-3
PP1/2A	protein phosphatase 1 or 2A
PRAS40	proline-rich AKT substrate 40 kDa
PROPPINs	β-propellers that bind polyphosphoinositides
PS	phosphatidylserine
pSM	palmitoylsphingomyelin
Pt	platinum
PtdIns	phosphatidylinositol
PtdIns[3,4,5]P_3	phosphatidylinositol-3,4,5-trisphophate
PtdIns[3,4]P_2	phosphatidylinositol-3,4-bisphosphate
PtdIns[4,5]P_2	phosphatidylinositol-4,5-bisphosphate
PtdIns3P/PI3P	phosphatidylinositol-3-phosphate
PtdIns4P	phosphatidylinositol-4-phosphate
PTFE	polytetrafluoroethylene
$P_{\beta'}$	rippled lamellar gel phase
QELS	quasi-elastic light scattering
Rab	Ras-related GTP-binding protein
Raptor	regulatory associated protein of mTOR
R_h	hydrodynamic radius
Rho-PE	Rhodamine-PE
RING	really interesting new gene
ROI	region of interest
ROS	reactive oxygen species
Rot	rotenone
RPE1	hTERT-immortalized human retinal pigment epithelial 1
rRNA	ribosomal RNA
S1P	sphingosine 1-phosphate

SASA	solvent-accessible surface area
SDM	site-directed mutagenesis
SDS-PAGE	sodium dodecyl sulfate polyacrylamide gel electrophoresis
SEC	size exclusion chromatography
SH2	src homology 2
shRNA	small hairpin RNA
SIN	self-inactivating
siRNA	small interfering RNA
SLRs	sequestosome 1-like receptors
SM	sphingomyelin
SMase	sphingomyelinase
SMPD1	sphingomyelinase phosphodiesterase 1
SMS	sphingomyelin synthase
SNARE	SNAP soluble NSF attachment protein receptor
SphK	sphingosine kinase
SPR	surface plasmon resonance
SPT	serine palmitoyltransferase
SQSTM1/p62	sequestosome-1
SR	serine-arginine
Stbd1	starch-binding-domain-containing protein 1
SUV	small unilamellar vesicle
TAX1BP1	Tax1 binding protein 1
TBC1D2B	TBC1 domain family member 2B
tBID	truncated-BH3 interacting domain death agonist
TCEP	tris(2-carboxyethyl) phosphine
TEM	transmission electron microscopy
THC	Δ9-tetrahydrocannabinol
TIM	translocase of the inner membrane
TLCL	tetralinoleoylcardiolipin
Tm	lipid phase transition temperature

TMCL	tetramyristoylcardiolipin
TNF	tumor necrosis factor
TOCL	tetraoleoylcardiolipin
TOM	translocase of the outer membrane
TOMM20	mitochondrial import receptor subunit TOM20 homolog
TR-FRET	time-resolved fluorescence resonance energy transfer
TRIB3	tribbles pseudokinase 3
tRNA	transfer RNA
Ub	ubiquitin
UBL	ubiquitin-like
ULK1/2	uncoordinated-51 (unc-51)-like kinase 1 or 2
UPR	unfolded protein response
Uth1p	probable secreted beta-glucosidase UTH1
UVRAG	UV-radiation resistance associated gene
V-ATPase	vacuolar H^+-ATPase
VCP/p97	type II AAA+ ATPase valosin-containing protein
VDAC	voltage dependent anion channel
Veh	vehicle
VHL	von Hippel-Lindau
VPS15/34	vacuolar protein sorting mutant 15 or 34
WIPI1/2	WD repeat domain phosphoinositide-interacting protein 1 or 2
WPRE	Woodchuck hepatitis virus posttranscriptional regulatory element
WT	wild-type
ΔH	lipid phase transition enthalpy
$\Delta T_{1/2}$	width at half-height lipid phase transition
Δπ	surface pressure increase
Δψ	membrane potential
ε	molar extinction coefficient
θ	ellipticity
$\lambda_{em(max)}$	wavelength at maximum fluorescence emission

$\lambda_{ex/em}$	fluorescence excitation or emission wavelength
π	surface pressure
π_0/π_i	initial surface pressure
π_c	critical surface pressure

Index of Experimental Protocols

Chapter 1

Introduction and Aims

CHAPTER 1:

Introduction and Aims

1.1 Cell Membranes

1.1.1 Common Properties and Functions

Living cells need to be connected with and protected from the outer environment. Membranes confer the main protection against the different environmental conditions for survival. Plasma membrane surrounds and delimits the cells, creating a selective permeability barrier to the most soluble molecules. Unlike prokaryotes, eukaryotic cells have not only a plasma membrane but also intracellular membranes surrounding various organelles. All of these membranes are part of an extensive endomembrane system and constitute a selective barrier that regulates the exchange of molecules between defined compartments.

The plasma membrane is composed of a thin layer of lipid molecules with large amounts of embedded proteins (Singer & Nicolson, 1972; Goñi, 2014). Both lipids and proteins participate in anchoring the membrane to the cytoskeleton thus providing a shape to the cell, and interact with the extracellular matrix to maintain tissue organization. Furthermore, many other processes such as cell signaling, cell adhesion, ion conductivity, nutrient uptake or disposal of unwanted material are regulated by membrane components and take place either within or in the membrane vicinity.

The cell membrane is selectively permeable and facilitates the transport of materials needed for survival. Due to this selective transport property membranes can maintain the cell potential. The movement of solutes across the membrane is controlled by some mechanisms that often involve proteins. Small molecules such as carbon dioxide and oxygen can move across the membrane by simple diffusion. In contrast, charged particles (ions) or larger nutrients (amino acids, sugars) need a more complex

mechanism of transport which entails the participation of proteins and an energy expense.

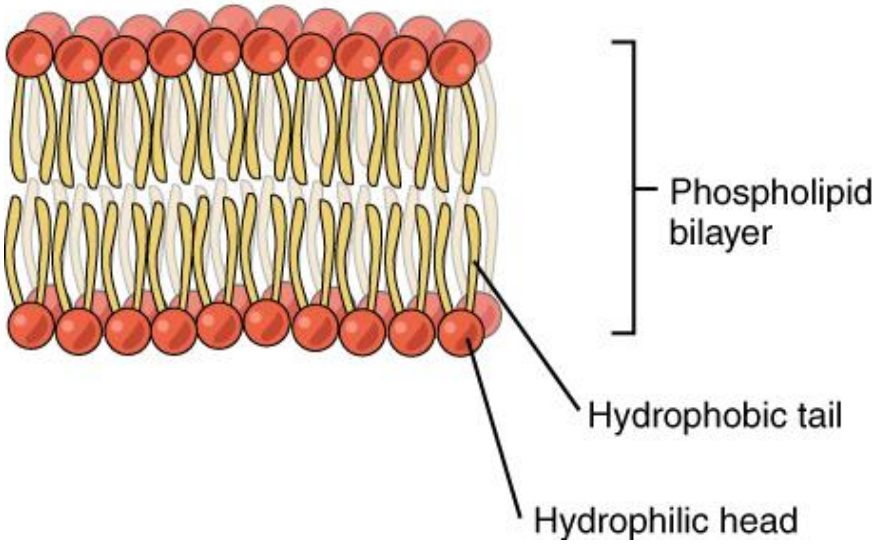

Figure 1.1. Schematic diagram of a lipid bilayer. (Adapted from https://www.boundless.com/biology/textbooks/boundless-biology-textbook/biological-macromolecules-3/lipids-55/phospholipids-300-11433/).

Membrane lipids are amphipatic molecules containing a hydrophobic tail and a polar head group, and can often self-assembly into lipid bilayers (**Figure 1.1**). When exposed to a water solvent, these lipids can be spontaneously arranged so that the hydrophilic head groups interact with the water molecules isolating the hydrophobic tails from the water environment (Israelachvili *et al.*, 1980). Thus, lipids in cell membranes characteristically adopt a bilayer structure with the hydrophobic tails facing each other and the polar heads interacting with the cytoplasm or extracellular medium. Proteins, the other main component, accommodate along the membrane extension usually up to 50% of the plasma membrane mass.

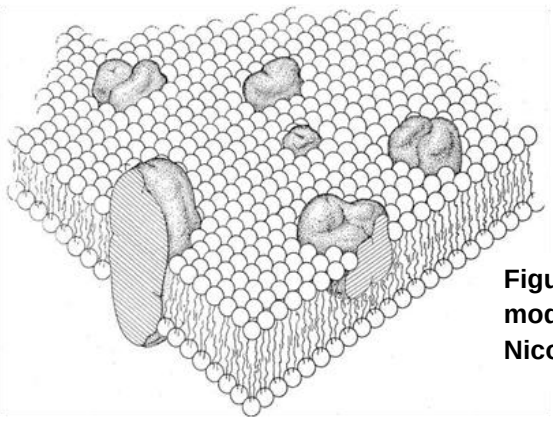

Figure 1.2. Lipid and protein "fluid mosaic" model of biomembrane structure by Singer-Nicolson. (Taken from Singer & Nicolson, 1972).

In this context, Singer and Nicholson proposed the current view of cell membranes as a fluid mosaic model, in which lipids and proteins can rotate and diffuse easily along the plane of the membrane (**Figure 1.2**). Thus the membrane would be asymmetric as a consequence of the restricted transbilayer movement. Membrane proteins are usually classified as peripheral or integral proteins. Integral (also called intrinsic) proteins have one or more segments embedded in the phospholipid bilayer. Most integral proteins contain hydrophobic residues that interact with the fatty acyl chains of phospholipids in order to anchor the protein to the membrane. However, the polypeptide chain does not always enter the phospholipid bilayer, as it is the case of proteins anchored by covalent binding to fatty acids. Moreover peripheral (also called extrinsic) proteins usually interact with the lipid polar head groups or polar moieties of intrinsic proteins.

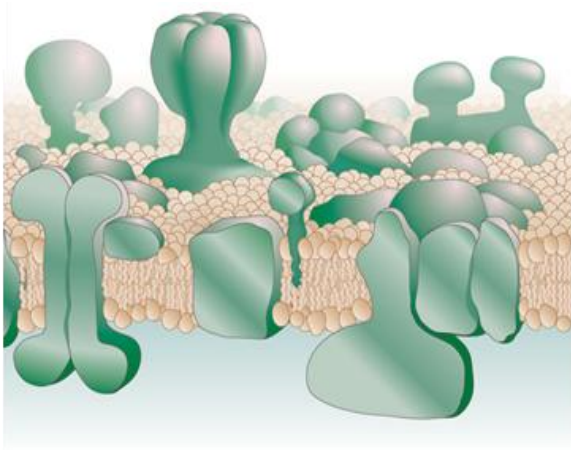

Figure 1.3. An amended and updated version of the Singer-Nicolson model. (Adapted from Engelman, 2005).

Subsequent adjustments and evolutions of this model have emerged in the following decades (Jacobson *et al.*, 1995; Engelman, 2005; Goñi, 2014). Nowadays the intrinsic membrane proteins are considered to be very abundant, and distributed homogeneously along the membrane (**Figure 1.3**). Some proteins are not always in contact with the membrane, existing part-time in the cytosol and part-time docked to a membrane. Moreover, biological membranes present lateral heterogeneity. They can be divided into domains composed of specific proteins or lipids, allowing spatial segregation of biological processes associated with membranes such as ion and metabolite transport, signaling, cell adhesion, and migration. Additionally, in practice the membrane bilayer is not flat. Local curvature of the membrane can be caused by the asymmetry and non-lamellar organization of lipids. Some non-bilayer lipid structures can transiently occur, with important biological functions, as is the case of membrane fusion events or cell division. Lipid asymmetry in the membrane has been discovered to be controlled by flippase or scramblase proteins. Lipid flip-flop motion is

of great importance for instance during an autophagic cell response, in which the externalization of CL, a phospholipid present mostly in the inner mitochondrial membrane, is promoted to potentiate mitochondria recognition and mitophagy (Chu *et al.*, 2013; Maguire *et al.*, 2016). This issue has been examined in this thesis and will be addressed more thoroughly later.

1.1.2 Membrane Lipids

About 50% of most animal cell membranes consists of lipids (mainly phospholipids, glycolipids and sterols). Lipids include a heterogeneous group of molecules, with important biological functions. In the cell, they are involved in the formation of cellular membranes. But largest amounts of lipids are used for energy storage, principally as triacylglycerols and sterol esters, in lipid droplets. Also, lipids can act as first and second messengers in signal transduction and molecular recognition processes (Bartke & Hannun, 2009; van Meer, 2005; van Meer *et al.*, 2008).

Cellular membranes are formed by polar lipids, which consist of a hydrophobic and a hydrophilic area. The propensity of the hydrophobic moieties to self-associate, and the tendency of the hydrophilic moieties to interact with the aqueous environment are the physical basis of the spontaneous formation of membranes. Regarding the head group charge, all these lipids can be either neutral (zwitterionic) or electrically (usually negatively) charged. From the head group, generally 1 or 2 fatty acyl hydrophobic tails emerge. These can contain from 2 to 28 carbon atoms and also can be saturated or unsaturated with one or more *cis* or *trans* double bounds (Berg *et al.*, 2002) (**Figure 1.4**).

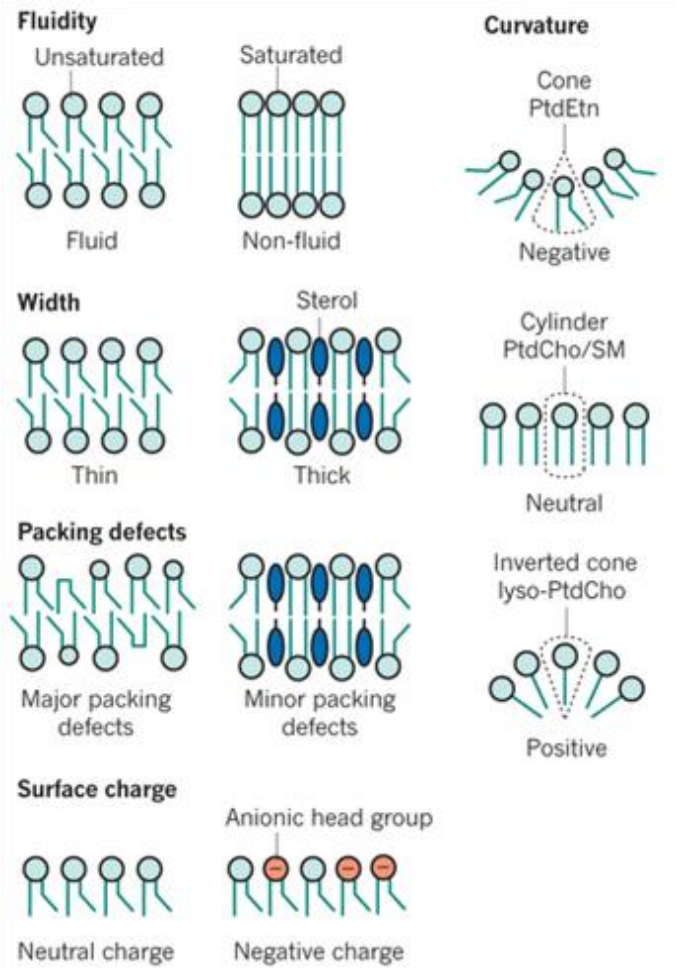

Figure 1.4. Physical membrane properties are influenced by lipid composition. Fluidity is promoted by lipids with short, unsaturated fatty acids. The double bonds introduce kinks that lower the packing density of the acyl chains and inhibit transition of the membrane from a fluid to a solid gel phase. Thickness is promoted by acyl-chain length and sterols, which order and stretch the acyl chains. High levels of packing defects are found in lipids with unsaturated acyl chains and small head groups. Surface charge is determined by the presence of anionic lipids such as PS and PIs. Curvature is determined by lipid shape. Lipids with a small area ratio of polar head to acyl chain (creating a cone shape) induce negative curvature, lipids with an equal head to chain ratio (creating a cylinder shape) are neutral, and those with a much larger head compared with the acyl chain area (creating an inverted cone shape) induce a positive curvature. (Adapted from Holthuis & Menon, 2014).

1.1.2.1 Classification of Membrane Lipids

The predominant lipids in cell membranes are glycerolipids, sphingolipids and sterols.

A) Glycerolipids

Glycerolipids are the major structural lipids in eukaryotic membranes. There are 2 classes of glycerolipids, glycerophospholipids (e.g. CL) and glyceroglycolipids. Glycerophospholipid structure is based on a glycerol molecule to which 2 fatty acids are bound, mostly via ester linkages to the carbons in *sn*-1 and *sn*-2 positions of glycerol. A phosphate group is attached to the carbon in the glycerol *sn*-3 position, and a polar residue is esterified to the phosphate group (**Figure 1.5**). Depending on the length and saturation of the acyl chains attached to the glycerol, and on the polar group bound to the phosphate, a large variety of glycerophospholipid species arises.

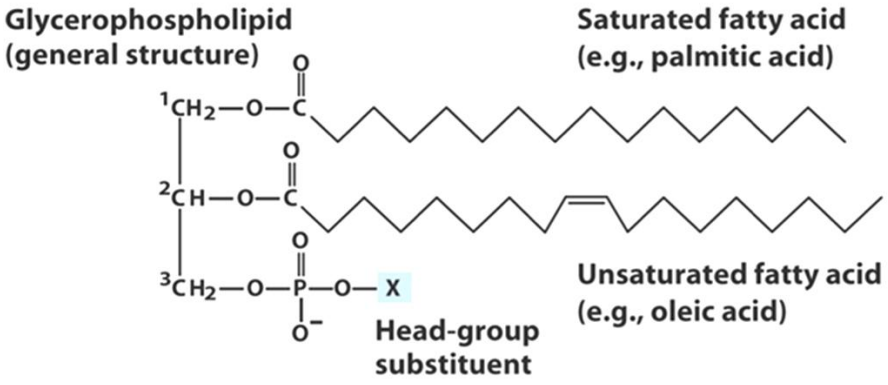

Figure 1.5. General structure of glycerophospholipids. (Taken from https://www.studyblue.com/notes/note/n/lipids/deck/1546284).

The other class of glycerolipids, glyceroglycolipids, is less abundant in animal cell membranes but is present in huge quantities in plant and some bacterial membranes. They lack a phosphate group, but contain a mono- or oligo-saccharide group linked through a glycosyl linkage to carbon *sn*-3 of glycerol.

B) Sphingolipids

Sphingolipids can be sorted into phosphosphingolipids and glycosphingolipids. Their hydrophobic backbone is sphingosine, a long chain unsaturated amino octadecyl alcohol. N-hexadecanoyl-D-*erythro*-sphingosine, or ceramide, an important sphingolipid in cell signaling, is originated by a fatty acyl chain attached through an amide linkage to

sphingosine (**Figure 1.6**). Binding of a phosphorylcholine polar residue to ceramide originates sphingomyelin, an abundant phosphosphingolipid in the external leaflet of cell plasma membrane.

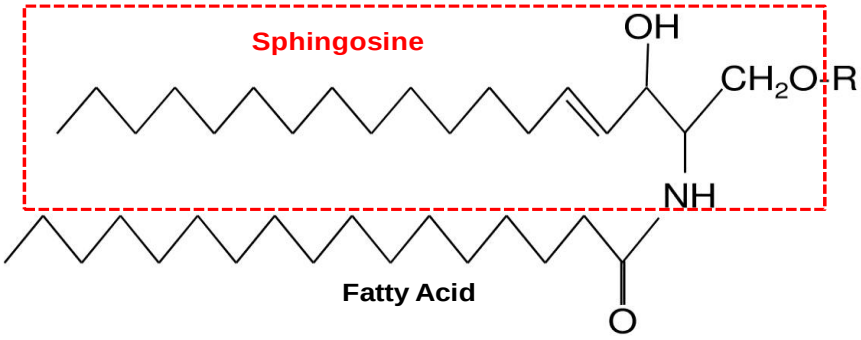

Figure 1.6. General structure of sphingolipids. Sphingosine in a red square, fatty acid in black, and R corresponds to the variable head group. (Taken from Fuller, 2010).

The binding of complex sugar structures gives rise to a class of sphingolipids named glycosphingolipids, which can be classified into cerebrosides and gangliosides, depending on the number of sugar residues and the presence of sialic acids.

C) Sterols

Sterols are the third class of lipids that integrate cell membranes. These lipids are the major non-polar lipids in cell membranes. Sterols have a hydrophobic four-membered fused ring rigid structure, and a small polar head group. In general, sterols are synthesized via the mevalonate pathway of isoprenoid metabolism. The most abundant sterol in mammals is cholesterol (**Figure 1.7**), whereas ergosterol predominates in yeast.

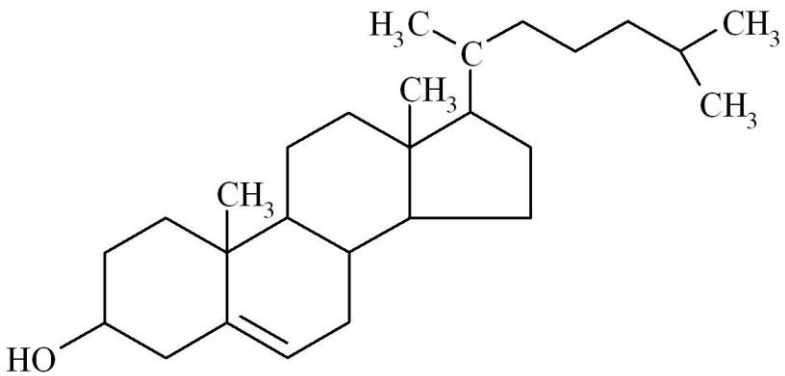

Figure 1.7. Structure of cholesterol. (Taken from http://chemed.chem.purdue.edu/genchem/topicreview/bp/1organic/hydro.html).

1.1.2.2 Lipid Distribution and Asymmetry

Eukaryotic cells contain well over 1000 different lipid species in the membranes. Variation in headgroups and aliphatic chains of each kind of lipid generates this enormous lipid diversity. Interestingly phospholipids, sphingolipids and sterols are not distributed homogeneously throughout the main organelles of mammals, conferring special characteristics to them (**Figure 1.8**). This segregation reflects the different physiological role, local lipid metabolism of each lipid in the cell, and specific physicochemical membrane properties generated by differences in lipid composition (**Figure 1.4**). For example, sphingomyelin and cholesterol are mainly found in the plasma membrane, while cardiolipin can be found almost exclusively in mitochondrial membranes.

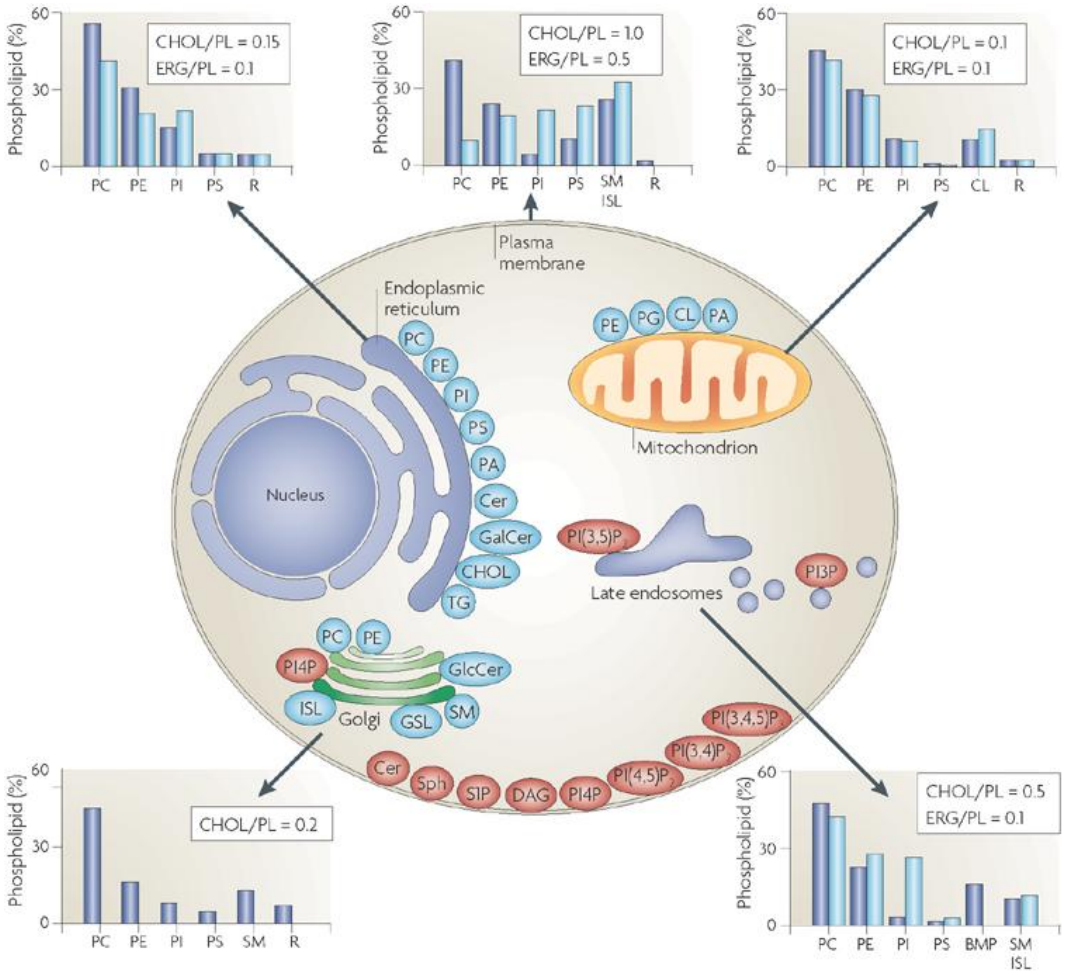

Figure 1.8. **Lipid compositions of different membranes within the cell.** (Taken from van Meer *et al.*, 2008).

Furthermore, lipid heterogeneity is not only present between different membranes in the cell, but also within single membranes. Lipids can be asymmetrically distributed between the two monolayers of a lipid bilayer. This characteristic is named lipid transversal asymmetry and is a necessary feature of all cell membranes in order to be functional. In human erythrocytes, for example, almost all lipids containing choline in their polar head (PC and SM) are predominantly located in the outer monolayer, whereas lipids containing the amino group (PE and PS) are mostly located in the inner monolayer (**Figure 1.9**). Therefore, not only the composition but also the charge of the two hemimembranes is very different, the inner one being negatively charged, while the outer one is electrically neutral. The main reason for lipid composition differences between both monolayers is the asymmetric synthesis of certain lipids or the presence of transporters that allow unidirectional lipid translocation.

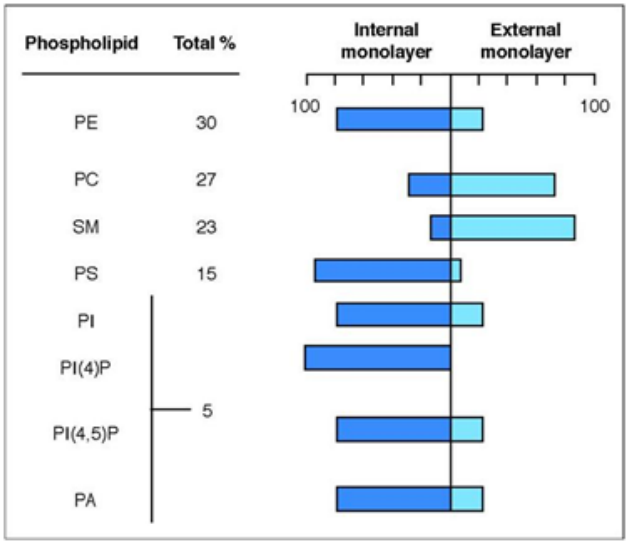

Figure 1.9. Asymmetric phospholipid distribution in erythrocyte plasma membrane.

In model membranes the rate of spontaneous polar lipid movement between bilayer leaflets is slow (hours to days for PC) and is governed by the size, charge and polarity of the headgroup. The half time for translocation is days for complex GSLs but seconds for Cer, DAG and sterols. Hence, in cell membranes some proteins (flippases, floppases, scramblases), facilitate this movement, sometimes with energy cost under specific circumstances (Contreras *et al.*, 2010).

In addition, lipids are not homogeneously located even along one leaflet of the membrane. Lipids display certain lateral asymmetry. Membrane fluidity is connected to the lipid motion, and regulates the capacity of free lateral movement. In this context, lipid domains are related to this lateral heterogeneity.

1.1.2.3 Lipid Polymorphism

Morphological plasticity of biological membranes is critical for cellular life, as cells need to quickly reorganize their membranes for a proper response to a given stimulus. Cell membranes are basically organized in a one-dimensional lamellar structure. However, some crucial events are characterized by the formation of more complex non-lamellar structures, such as the inverted hexagonal or cubic phases. From macromolecule transversal motion across the membrane to cell division, many processes require the generation of these unstable structures (Epand, 1998). Membrane fusion and fission processes, that include virus infection, vesicular transport from the ER to the Golgi or endocytic and exocytic transport, are good examples of energetically unfavorable events that require the transient formation of non-lamellar structures (Gilbert, 2016; Kozlov & Chernomordik, 2015). However lipid polymorphism is not only associated to two-dimensional structural changes. For instance, the formation of laterally segregated structures within a membrane, where protein complexes can adopt a more stable conformation is dependent on one-dimensional alterations of lipid order or fluidity. Fluidity of the membrane depends mainly on the lipid composition (**Figure 1.4**) and temperature, and it must be properly regulated so that processes such as transport or enzymatic activities occur correctly.

A lipid phase is a thermodynamic concept corresponding to different structural patterns that a lipid or a lipid mixture adopts in aqueous solution. Biological membranes under equilibrium conditions are composed of a lipid bilayer in a lamellar configuration, where the most significant phases are: L_α, L_β and a phase with intermediate properties between fluid and gel denoted as L_o. In a L_α phase, lipids are free to diffuse laterally and rotationally, and display their acyl chains in a disordered state with high flexibility. At least one of the acyl chains is normally unsaturated. Lipids in the L_β phase have highly ordered acyl chains and display high proportions of trans C-C conformers, being almost immobile and not allowing lateral or rotational motion (Marsh, 1980). The L_β to L_α phase transition is usually know as the main phase transition (**Figure 1.10**).

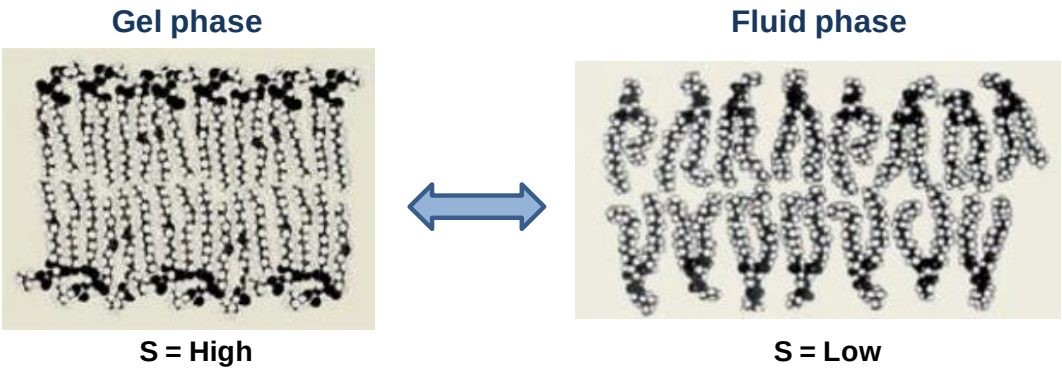

Figure 1.10. Lamellar gel-fluid phase transition and its associated height and chain order transformation. S represents the acyl chain order parameter. (Adapted from van Meer *et al.*, 2008).

Other lamellar phases include $L_{\beta'}$, in which acyl chains are tilted with respect to the plane of the membrane, the interdigitated $L_{\beta I}$ where acyl chains from the two membrane layers are interdigitated (typical from lipids with a short and a large acyl chain), and the rippled $P_{\beta'}$ phase, which can be adopted by a few saturated phosphatidylcholines and phosphatidylglycerols, and characterized by the ripples seen by electron microscopy in freeze-fractured surfaces of lipid samples in this phase.

The formation of some non-lamellar structures is strongly influenced by the lipid molecular geometry. About 30% of membrane lipids can adopt or induce non-lamellar structures in model systems. Differences in the cross-sectional areas between the polar head group and the hydrophobic tail could determine the overall structure of the lipid aggregates (Israelachvili *et al.*, 1980). From this point of view, lipids are mainly classified into 3 groups: lipids with conical, cylindrical or inverted-conical shapes (**Figure 1.11**). These shapes could be summarized by the morphological parameter S:

$$S = V/A_oL_c$$

Equation 1. Morphological parameter S.

where:

V = is the volume of the lipid molecule,

A_o = is the area of the molecule in the lipid-water interface and

L_c = the length of the extended acyl chain.

Taking into account these parameters and the lipid cross-sectional area in the hydrophobic tail "A_H", which would reflect a volume of $V = A_H L_c$ for a lipid displaying cylindrical shape, the different morphological geometries can be reviewed as:

- $A_0 = A_H$ (S = 1): The molecule presents a cylindrical shape.
- $A_0 < A_H$ (S > 1): The molecule presents a conical shape.
- $A_0 > A_H$ (S < 1): The molecule presents an inverted-conical shape.

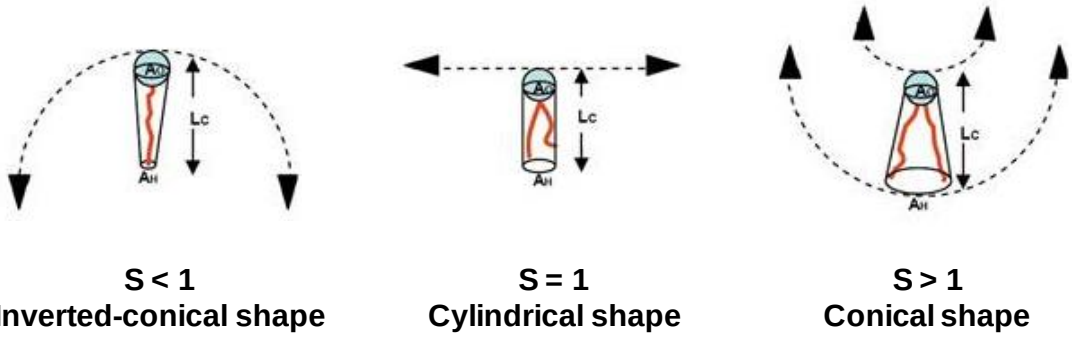

Figure 1.11. Molecular shape of physiological lipids.

However, it is difficult to quantitatively calculate the shape and curvature of the phases adopted by lipids, since the area and volume of the molecules also depend on factors such as the amount of water present, ionic strength, pH, temperature, divalent cations and proteins. Pure lipids in aqueous solutions will self-aggregate into different structures depending on their molecular geometry. Cylindrical shapes displaying lipids as PC or SM will become organized in the form of lamellar bilayers. Cone shaped lipids as PE, DAG or sterols will tend to form "hexagonal" (tubular) arrangements, while inverted-cone-shaped lipids as is the case of lysophospholipids (LPC) will aggregate into micelles (**Figure 1.4**). However, these non-cylindrical lipids could be part of a lipid bilayer structure whenever lipids such as PC, SM or PS are present. For instance, a 20 to 50 mol % of cylindrical lipids are necessary when mixed with conical lipids in order to have an overall lamellar structure (Cullis *et al.*, 1986).

Thus, it could be summarized that lipid polymorphism reflects the lipid behavior under specific physical conditions in which long-range ordered structures are generated by the lipids in a given phase. Lipid polymorphism may be directly associated with many cellular functions, including membrane fusion, vesicle formation during cell division, protein trafficking, endocytosis, stabilization of protein complexes in

the membrane or movement of molecules in the membrane and through it. All these processes involve the transient appearance of non-lamellar organization zones in the membrane.

1.1.3 Protein-Lipid Interactions

Membrane proteins are associated in different ways with membranes and enable them to carry out their distinctive activities. Each particular bilayer contains a specific pool of proteins that confers to it some particular properties.

As discussed in Section 1.1.1, membrane proteins are commonly classified as peripheral or integral proteins. Integral (also called intrinsic) proteins contain one or more segments embedded in the phospholipid bilayer. Most integral proteins contain hydrophobic residues that interact with the fatty acyl chains of phospholipids in order to anchor the protein to the membrane. However, the polypeptide chain does not always enter the phospholipid bilayer, as is the case of proteins anchored by covalent binding to fatty acids. On the other hand, peripheral (also called extrinsic) proteins usually interact with the lipid polar head groups or intrinsic proteins.

Moreover, a large amount of membrane proteins do not spend their whole life attached to the membrane. Some of them contact the lipid bilayer only under certain conditions, thereby remaining membrane bound (either as integral or as peripheral proteins) or returning promptly to the aqueous medium (non-permanent membrane proteins). In this regard, these non-permanent proteins can be classified according to the reversibility of the membrane contact or to the nature of the interaction. The first criterion assumes that there are some proteins that interact reversibly with the membrane and others with very long-lived (irreversible) contacts. The second one sorts the proteins into groups depending of the strength of the interaction, considering weak or strong associations, either in a transient or a permanent way, with the membrane (Goñi, 2002).

Protein-membrane association can also rely on specific protein domains that recognize some peculiarities of the membrane (Hurley, 2006; Lemmon, 2008; Moravcevic *et al.*, 2010). At least 10 different types of protein domains bind phospholipids at the membrane surface. These interactions can fall into 2 classes: highly specific, involving the recognition of a particular phospholipid in the membrane, or non-specific, implying a physical property of the membrane surface (Lemmon,

2008). For instance, C1, C2, PH, PX, FYVE or PROPPINs domains belong to the first type. In contrast, BAR domains, ALPS motifs or N-terminal amphiphatic α-helices recognize physical properties such as membrane curvature (Antonny, 2011).

In the autophagy network, the main object of study in this thesis, there are several proteins that associate with different cell membranes. Those proteins may associate through a lipid moiety, a fatty acid or prenyl group, a GPI anchor, an amphipathic alpha helix, a domain such as FYVE (that binds PtdIns3P), or a PH domain (that binds PtdIns[3,4]P_2). Usually, Atg8 and mammalian Atg8 protein family associate with autophagosomal membranes through PE that is covalently attached to the C-terminal glycine residue. This type of modification is so far unique to the Atg8 family. Peripheral membrane proteins known to be involved in autophagosome formation include for example ULK1 and ULK2, known to be present in a salt- and detergent-resistant membrane fraction, and DFCP-1, that contains a FYVE domain (Tooze, 2010). Moreover, the initiation of the autophagic signaling under starvation conditions starts in the plasma membrane where phosphoinositides are recognized by proteins (phosphatidylinositol-3-kinase or phosphoinositide phosphatases). In addition, from the beginning to the end of autophagosome formation a huge amount of membrane material is constantly moving through different cell localizations with many proteins transiently associated, such as ATG9, ATG5-12-16 complex, ATG3, ATG14 or WIPI proteins (reviewed in Ktistakis & Tooze, 2016). In the context of this work, cardiolipin and ceramide have recently been proposed as novel cargo receptors for the Atg8 ortholog LC3 that interacts with them in the outer mitochondrial membrane and mediates selective removal of mitochondria (Chu *et al.*, 2013; Maguire *et al.*, 2016; Sentelle *et al.*, 2012).

1.1.4 Membrane Domains

Membranes, and in particular the cell plasma membrane, are not homogeneous, but rather contain lateral heterogeneities, usually called domains, of sizes from the hundreds of nanometers to perhaps a micron, enriched in certain lipids and proteins that provide them with characteristic functional properties (Engelman, 2005; Goñi, 2014). It is not clear at present whether distinct domains are a minor part of an otherwise continuous membrane, or else the plasma membrane consists essentially of apposed heterogeneous regions.

The poor miscibility of certain lipids in the bilayer may be an important factor in the origin of cell membrane domains. Triangular phase diagrams of mixtures of phospholipids and cholesterol, constructed using a variety of techniques (de Almeida *et al.*, 2003; Goñi *et al.*, 2008; Heberle & Feigenson, 2011; Veatch & Keller, 2005) suggest the presence of multiple coexisting phases, e.g. $L_d + L_o$, $L_d + L_o + L_\beta$, $L_o + L_\beta$, at a given temperature. In $L_\alpha + L_\beta$ coexisting domains formed by mixtures of cholesterol, a saturated and two unsaturated phosphatidylcholines, the liquid domain size increases with the mismatch in bilayer thickness between the L_o and L_d bilayers (Heberle *et al.*, 2013). No less important than lipid immiscibility is probably a number of membrane properties that concur in restricting the mobility (translational diffusion) of proteins (Tomishige *et al.*, 1998). Of special significance in this context is the anchoring of membrane integral proteins to cytoskeletal proteins, so that the translational (but not rotational) diffusion of the former is prevented. Considering that one of these anchored proteins can interact with several others, plus the general hindering of diffusion caused by membrane crowding, and the occasional preferential binding of a given lipid to a certain protein, as well as the above-discussed lipid immiscibility, it is understandable that membrane domain formation may be the rule rather than the exception.

The larger, micron-sized domains, are often referred to as “platforms”. Examples of the latter are the large ceramide-containing domains formed upon degradation of sphingomyelin by acid sphingomyelinase in response to a stress signal that initiates in turn a cascade of signaling events leading to apoptosis (Stancevic & Kolesnick, 2010; Zhang *et al.*, 2009). Of course the situation may vary with the cell, tissue or organelle type of membrane.

Simons and Ikonen (1997) proposed the “membrane raft hypothesis” (Simons & Ikonen, 1997). Rafts would be small (10–200 nm), heterogeneous, highly dynamic, sterol- and sphingolipid-enriched domains that compartmentalize cellular processes (Pike, 2006; Shaikh & Edidin, 2006). Rafts would be related to intracellular sphingolipid traffic, as well as playing several signaling functions. Because of their predicted small size and short life there is no solid experimental evidence of their existence.

In summary lateral heterogeneity is the consequence of non-ideal lipid miscibility, different lipid-packing parameters, protein–protein contacts (including interactions between integral and peripheral proteins), protein–lipid interactions, and integral protein crowding collisions between protein ectodomains (Goñi, 2014). Membrane domains assist in the organization of proteins (for their transport into small vesicles or to perform their functions in complexes), being very important in signaling

processes, intracellular lipid transport, signal transduction, cell morphogenesis, traffic through cell membranes and entry of toxins and viruses (Carquin *et al.*, 2016).

1.2 Autophagy

Autophagy (from the Greek auto-, "self" and phagein, "to eat") is a general biological process conserved among eukaryotes that allows the regulated degradation of unnecessary or dysfunctional cellular materials. This event occurs under physiological conditions of cell development, differentiation or immunity, but it can be highly active in the context of disease to promote survival, or in some cases cell death, or under starvation conditions when it provides nutrients to maintain vital cellular functions. Not surprisingly, impaired autophagy underlies a wide range of pathological conditions.

1.2.1 Origin and Types of Autophagy

The process of autophagy was observed by Keith R. Porter and his postdoctoral student Thomas Ashford at the Rockefeller Institute, New York. In January 1962 they reported an increased number of lysosomes in the liver cells of rat after addition of glucagon, and that some displaced lysosomes towards the centre of the cell contained other cell organelles such as mitochondria. This was the first reported evidence in the English literature of intracellular digestion of cell organelles. In early 1963, the American Journal of Pathology published a detailed ultrastructural description of focal cytoplasmic degradation, which referenced a 1955 German study of injury-induced sequestration. Z. Hruban and colleagues recognized 3 continuous stages of maturation of the sequestered cytoplasm to lysosomes, and noted that the process was not limited to injury states, but also functioned under physiological conditions for reutilization of cellular materials (Hruban *et al.*, 1963). Inspired by this discovery, the term "autophagy" was invented by Christian de Duve (de Duve, 1963), the Nobel Laureate discoverer of lysosomes and peroxisomes. Unlike Porter and Ashford, de Duve conceived the term as a part of lysosomal function while describing the role of glucagon as a major inducer of cell degradation in the liver (Klionsky, 2008). With his postdoctoral student Russell L. Peter, he subsequently established that lysosomes are indeed responsible for glucagon-induced autophagy. This was the first time that lysosomes were established as the sites of intracellular autophagy.

Three different types of autophagy have been described in mammalian cells (**Figure 1.12**) (Okamoto, 2014):

a) Macroautophagy is the main autophagic pathway, occurring mainly to eradicate damaged cell organelles or unused proteins. This involves the formation of a double membrane around cytoplasmic substrates resulting in the organelle known as autophagosome. The autophagosome travels through the cytoplasm to a lysosome, and the two organelles fuse; intersection with endosomal pathways also occurs. Within the lysosome, the contents of the autophagosome are degraded via acidic lysosomal hydrolases. This pathway is conserved from yeast to humans.

b) Microautophagy, in turn, involves the direct engulfment of cytoplasmic material by the lysosome. This occurs by invagination, meaning the inward folding of the lysosomal membrane, or cellular protrusion. It is also conserved from yeast to humans.

c) CMA refers to the chaperone-dependent selection of soluble cytosolic proteins that are then targeted to lysosomes and directly translocated across the lysosome membrane for degradation. It is found only in mammals and contributes to the regulation of cellular metabolism (Bejarano & Cuervo, 2010; Tasset & Cuervo, 2016).

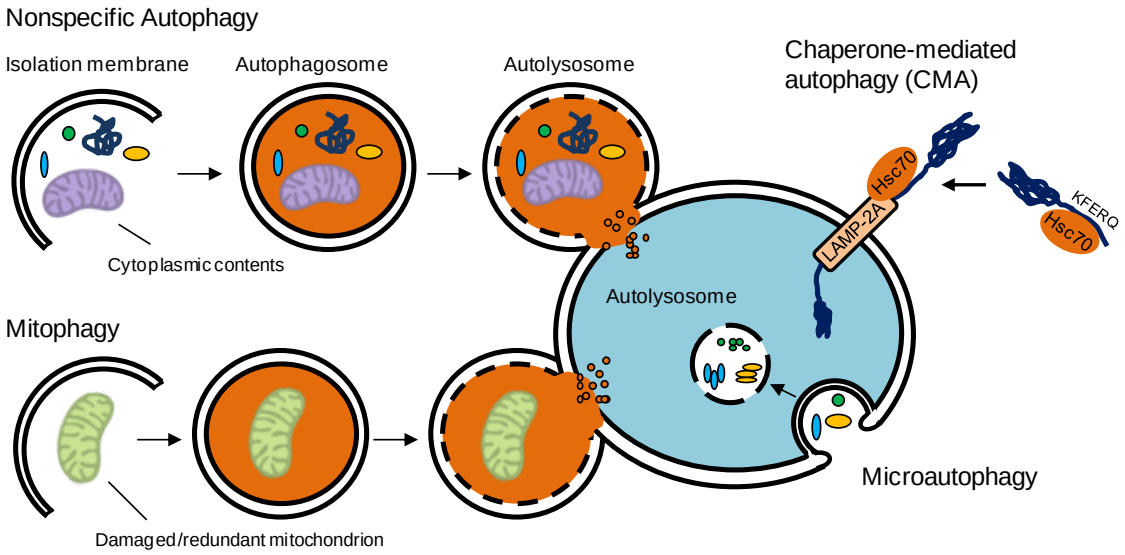

Figure 1.12. Mammalian autophagy pathways. Nonspecific macroautophagy, specific macroautophagy (e.g. mitophagy), CMA and microautophagy.

Autophagy can also be classified into selective or non-selective autophagy, depending on whether there are signals to degrade a specific cellular component or else it is a bulk process. This is particularly important for the cell when only some specific organelles are damaged (Sica *et al.*, 2015). In this context, the word organellophagy arises. Different organelles could be specifically selected to be degraded using the macroautophagy or microautophagy pathways. In the last years almost every cell organelle has been suggested to be a candidate for this selective mode of autophagy. For instance, mitochondria (mitophagy), peroxisome (pexophagy), lipid droplets (lipophagy), nucleus (nucleophagy), lysosome (lysophagy), ER (reticulophagy) or ribosomes (ribophagy) (Okamoto, 2014; Choi *et al.*, 2016; Khaminets *et al.*, 2015; Mochida *et al.*, 2015).

In this thesis, mitophagy (specific removal of mitochondria) and non-selective autophagy have been studied, thus in the context of this work autophagy is to be understood as macroautophagy, the most widely studied and potentially the most powerful form of autophagy.

1.2.2 Roles of Autophagy

1.2.2.1 Autophagy Promotes Cell Survival

The recycling of cellular components by autophagy is crucial for cells to survive many environmental challenges like amino-acid or nitrogen starvation (Kuma *et al.*, 2004; Takeshige *et al.*, 1992), hypoxia (Decker & Wildenthal, 1980) or cellular detachment (Debnath, 2009). Autophagy also helps to maintain cell survival by responding to and reducing various intracellular challenges like oxidative stress [e.g. selective mitophagy of damaged ROS-producing mitochondria (Twig *et al.*, 2008; Narendra *et al.*, 2008; Nowikovsky *et al.*, 2007; Scherz-Shouval & Elazar, 2007)] or ER stress [by supporting the unfolded protein response (Ding *et al.*, 2007; Ogata *et al.*, 2006)]. Autophagy also plays a role in cellular preservation by clearing toxic protein aggregates [e.g. aggregation-prone proteins associated with protein conformational disorders like Huntington disease (Bjørkøy *et al.*, 2005; Ravikumar *et al.*, 2002)] and invading intracellular pathogens (xenophagy) (Gutierrez *et al.*, 2004; Miao *et al.*, 2015). Finally, autophagy participates in cellular remodeling during major processes including cell growth (Mathew & White, 2011) and development (Cecconi & Levine, 2008). Therefore, autophagy is essential for cellular maintenance and survival, and this is supported by the association of autophagy with life span extension in yeast and

Caenorhabditis elegans (Bergamini *et al.*, 2003; Meléndez *et al.*, 2003; Tang *et al.*, 2008). A negative aspect is that transformed cells from established tumors are also thought to utilize autophagy to support their own survival (Mathew & White, 2011).

Conversely, defective or insufficient autophagy has been associated with many pathologies including late onset neurodegenerative conditions such as Huntington disease, Alzheimer disease and Parkinson disease, that are linked to an accumulation of toxic misfolded protein aggregates in the brain (Vidal *et al.*, 2014; Rubinsztein, 2006). Autophagy has also often been found decreased during malignant transformation and this may contribute to oncogenesis and cancer progression (Galluzzi *et al.*, 2015; Mizushima *et al.*, 2008; Mowers *et al.*, 2016). For instance, Beclin 1 – an important activator of the autophagy pathway – has been identified as a tumor suppressor gene (Liang *et al.*, 1999), and deletion of several proteins involved in autophagy (e.g. ATG5, ATG4C, UVRAG) has been associated with cancer susceptibility in specific tissues (Levine & Kroemer, 2008). Finally, the numerous pathogens (bacteria, viruses and parasites) known to be delivered for lysosomal degradation by xenophagy, and the participation of autophagy in the activation of innate and adaptive immunity suggest that autophagy is also a *bona fide* immunological process with important functions against a range of disease states (Deretic, 2011; Levine & Kroemer, 2008; Münz, 2015).

1.2.2.2 Autophagy and Cell Death

While autophagy is generally considered to be a cytoprotective process, the occurrence of increased numbers of autophagosomes in dying cells has led to the concept of autophagic cell death. The association of autophagy with a specific, apoptosis-independent, cell death program (autophagic cell death, also formerly named type 2 programmed cell death) (Baehrecke, 2003; Pyo *et al.*, 2005; Shimizu *et al.*, 2004), was first characterized morphologically, but the widespread use of this term to describe death “with” autophagy has become controversial. A recent re-definition of autophagic cell death, has limited it to death caused “by” autophagy (i.e. increased autophagic flux, when cells can be rescued by inhibition of autophagy), and showed that the autophagic cell death described in many systems is not supported by sufficient evidence to insure that autophagy is responsible for death (Shen & Codogno, 2011; Shen *et al.*, 2012). Instead, induction of autophagy as a survival mechanism prior to cell death may explain the association of large numbers of autophagosomes with dying cells in many of these studies (González-Polo *et al.*, 2005; Ravikumar *et al.*, 2006). For

instance, a recent study attempted to address the long lasting dilemma of autophagic cell death in cancer cells by treating U2OS osteosarcoma cells with a large cohort of cytotoxic agents tested in anti-cancer therapies (Shen *et al.*, 2011). The data confirmed the activation of autophagy with 80 of these reagents - accumulation of GFP-LC3 puncta due to increased autophagic flux or decreased degradation of autophagosomes - but revealed that cell death caused by these compounds could not be prevented by inhibition of autophagy with ATG5 or ATG7 shRNA (Shen *et al.*, 2011; Shen *et al.*, 2012). Moreover several findings from Velasco and coworkers (Salazar *et al.*, 2009) revealed that cannabinoids induce autophagy-mediated cell death in different types of tumor cells, including glioma/astrocytoma and pancreatic cancer cells. In this case, induction of autophagy would be an essential part of the mechanism, as discussed in greater detail below.

Many other studies highlighted the contribution of autophagy to the regulation of cell death. This is mainly supported by the association of cell death with prolonged autophagy activation [e.g. by hypoxia (Azad *et al.*, 2008) or oxidative stress (Chen *et al.*, 2008; Chen *et al.*, 2007)]. Moreover, a non-apoptotic cell death mediated by Beclin 1 and ATG5 has been described in apoptosis-resistant BAX/BAK double-knockout MEFs upon treatment with apoptosis-inducing reagents (e.g. etoposide, staurosporine) (Shimizu *et al.*, 2004). However, as mentioned above, in other cases the cross-talk between autophagy and apoptosis is essential (Salazar *et al.*, 2009; Shen *et al.*, 2012; Yu *et al.*, 2004). Therefore autophagy may contribute to cell death in many ways. These selected examples reflect the intricate and not fully understood relationship of autophagy with apoptotic and non-apoptotic cell death, which probably varies depending on the nature of stimuli and targeted tissues.

1.2.2.3 Autophagy in Development and Differentiation

Accumulating evidence suggests functions for autophagy when degradation of cell constituents is necessary for cellular remodeling during development and cellular differentiation. In mice, deletion of the autophagy regulator Beclin 1 causes widespread cell death and early embryonic lethality (Qu *et al.*, 2003; Yue *et al.*, 2003). However deletion of essential factors of the early autophagosome assembly machinery (ATG5 or ATG7) cause a suckling defect without dramatically altering other aspects of development until the animals die of metabolic stress during the neonatal starvation period (Komatsu *et al.*, 2005; Kuma *et al.*, 2004). However, the recent description of ATG5/ATG7-independent alternative autophagy taking place in these animals may

explain the mild effect of these deletions on development (Nishida *et al.*, 2009). Interestingly, tissue-specific deletions of ATG5 or ATG7, using various experimental strategies, confirmed important roles for autophagy in cell survival and in brain development (e.g. motor functions, neurodegeneration) (Aufschnaiter *et al.*, 2016; Cecconi & Levine, 2008; Hara *et al.*, 2006; Read *et al.*, 2011; Komatsu *et al.*, 2007). Impairment of autophagy with knockout mice has also been associated with specific developmental defects - e.g. of the inner ear for ATG4B (Mariño *et al.*, 2010) or of the immune system for ATG5 - and a predisposition to develop tumors (Cecconi & Levine, 2008; Levine & Kroemer, 2008; Mariño *et al.*, 2007).

Autophagy has also been associated with cellular remodeling during differentiation of several cell types. For instance, autophagosome formation is specifically upregulated during *in vitro* differentiation of podocytes (Asanuma et al., 2003). Similarly, autophagy is induced and specifically regulated during *in vitro* differentiation of C2C12 cells into myotubes (Tanida *et al.*, 2006). Moreover, autophagosomes have been described in differentiating erythroid cells since the 1960s (Kent *et al.*, 1966) but how is this regulated during late stages of erythroid differentiation, and the potential contribution of autophagy during reticulocyte maturation, remain unclear (Griffiths *et al.*, 2012).

1.2.3 The Core Machinery in Macroautophagy

The landmark event in autophagy is the formation of a double-membrane structure called autophagosome (AP) (Noda & Inagaki, 2015). The first step for this process is the generation of an isolation membrane. The origin of the initial membrane is not yet known, but some evidences suggest as possible sources the ER, ERGIC, endosomes, the plasma membrane or even mitochondria (Ge *et al.*, 2013; Hamasaki *et al.*, 2013; Mari *et al.*, 2011; Mizushima *et al.*, 2011; and the recent review by Ktistakis & Tooze, 2016).

Hereafter, the adhesion and fusion of membrane structures is necessary for autophagosome elongation. While membrane material, in the form of vesicles, is reaching the preautophagosome, new selected or non-selected cellular contents start to come into this preformed structure. In a final step, the autophagosome closes and upon fusion with a lysosome, the inside contents are degraded by lysosomal hydrolases (**Figure 1.13**) (Tooze & Yoshimori, 2010; Hasegawa *et al.*, 2016).

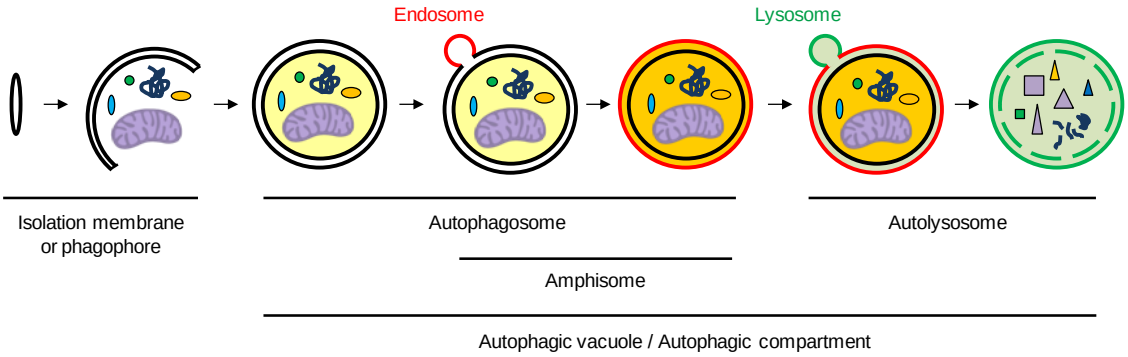

Figure 1.13. Outline of the general process of macroautophagy in mammals. Autophagosomes are double membrane vacuoles formed by elongation of an isolation membrane (or phagophore) around bulk or selected cytoplasmic material. Autophagosomes mature through multiple fusion events with early and late endosomes, and acquire a number of endosomal membrane proteins (in red) necessary for subsequent steps of maturation as well as the proton pump responsible for the acidification of their content (in orange). Autophagosomes can also be called amphisomes after fusion with multivesicular late endosomes. Finally, fusion of their outer membrane with lysosomes (in green) is responsible for the release of lysosomal enzymes between the inner and outer membranes and degradation of the inner membrane and its content. From fusion with lysosomes, autophagosomes become autolysosomes. (Adapted from Eskelinen, 2005 and Mizushima, 2007).

To date at least 35 ATG genes (**Table 1.1**), divided into several groups depending on the timing of their participation during AP biogenesis, have been identified and related to the process (Lamb *et al.*, 2013). Among them, the human Atg8 ubiquitin-like proteins, studied in this thesis, are late autophagosome-specific proteins that bind the AP and are involved in phagophore expansion (**Figure 1.14**) (for reviews see Mizushima *et al.*, 2011; Yang & Klionsky, 2010; and Ktistakis & Tooze, 2016).

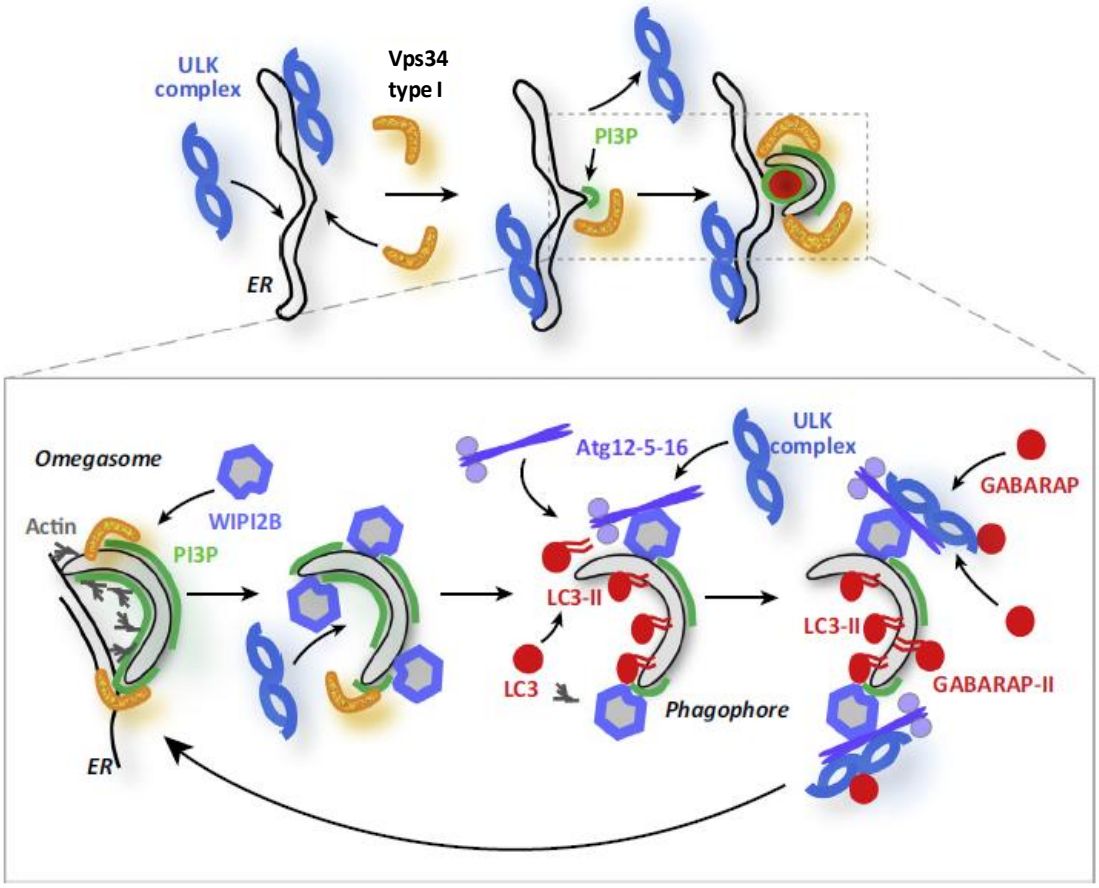

Figure 1.14. Molecular steps in the macroautophagy pathway. Recruitment of the ULK complex [ULK1/2, FIP200, ATG13, ATG101] and the Vps34 type I complex (BECLIN 1, VPS34, p150, ATG14) occurs on ER membranes, generating localized domains enriched in PI3P that form DFCP-1-enriched omegasomes (DFCP-1 is not shown). Actin is shown assembling into a network inside the phagophore, while on the outside it forms actin comet tails. Next, WIPI2B binds PI3P and recruits the ATG12–5-16L1 complex to mediate lipidation of LC3 family members. ATG16L1 also binds FIP200 in the ULK complex. The pool of ULK complex recruited by ATG12–5-16L1 could increase the active pool of ULK1, and reinforce the activity of the Vps34 complex and sustain PI3P production. Each ULK complex member also has LIR domains that bind LC3 family members. The binding of LC3/GABARAP family members via LIRs to the ULK–ATG12–5-16L1 assembly can also increase the active pool of ULK1 and sustain Vps34 activity. (Adapted from Ktistakis & Tooze, 2016).

Protein	Position in autophagic pathway	Alternative name and function
ULK1 and ULK2	ULK complex	Atg1 orthologs; Ser/Thr kinases that mediate mTOR signaling and ATG9 cycling
ATG13	ULK complex	ULK1 and ULK2 substrate that also modulates the activity of the ULK complex
FIP200	ULK complex	Atg17 ortholog; ULK1 and ULK2 substrate that also modulates the activity of the ULK complex
ATG101	ULK complex	Interacts with ULK1 and ATG13
Beclin 1	PI3K complex	Atg6 ortholog; part of the PI3K complex and also has a role in autophagy during initiation, formation and maturation
VPS34	PI3K complex	Catalytically active subunit of the PI3K complex
p150	PI3K complex	Vps15 ortholog; recruits the PI3K complex to membranes
ATG14L	PI3K complex	Atg14 ortholog; directs the PI3K complex to the omegasome; also known as Barkor
WIPI1 and WIPI2	PtdIns3P-binding protein	Atg18 orthologs; bind to PtdIns3P on the autophagosome
ATG3	LC3-PE conjugation	Similar to the E2 ubiquitin conjugating enzyme; conjugates LC3 to PE
ATG4	LC3-PE conjugation	Cys protease that cleaves C-terminal Gly residues from LC3 paralogs and is also required to recycle LC3 from the autophagosome outer membrane
ATG7	LC3-PE and ATG12 conjugation	Similar to E1 ubiquitin activating enzymes; activates ATG12 and LC3 paralogs
LC3A, LC3B and LC3C GABARAP, GABARAPL1 and GABARAPL2	LC3-PE conjugation	Atg8 orthologs; ubiquitin-like proteins that recruit cargo to autophagosomes and may aid in membrane fusion
ATG5	ATG5-ATG12 conjugation	Conjugated to ATG12
ATG10	ATG5-ATG12 conjugation	Similar to E2 ubiquitin conjugating enzyme; links ATG12 to an internal Lys residue in ATG5
ATG12	ATG5-ATG12 conjugation	Ubiquitin-like protein conjugated to ATG5 that functions in the activation of ATG3
ATG16L1	ATG5-ATG12 complex	Binds to the ATG5-ATG12 conjugate and directs LC3 conjugation at the isolation membrane
ATG9A and ATG9B	Integral membrane proteins	Atg9 orthologs; required for autophagosome formation
ATG2A and ATG2B	Localize to omegasome	Atg2 orthologs; required for closure of isolation membranes to form autophagosomes

Table 1.1. Essential ATG proteins for autophagosome formation. (Adapted from Lamb *et al.*, 2013).

1.2.4 Regulation and Induction of Autophagy

Autophagy induction is controlled by a complex regulatory mechanism involving different input signals that include nutrients, growth factors, hormones, ATP levels, and various others. Many signals converge at the level of the mammalian target of mTORC1. mTORC1 consists of mTOR, raptor, Deptor, PRAS40 and GβL (Wirawan *et al.*, 2012). When amino acids and growth factors are present, PI3KC1 activates mTORC1, which suppresses autophagic signaling. Active mTORC1 inhibits autophagy by binding and phosphorylating ULK1/ULK2 and ATG13 within the ULK complex (Joachim *et al.*, 2015). This complex is composed of ULK1/ULK2, ATG13, FIP200 and ATG101 (Noda & Inagaki, 2015). Consequently, repression of mTORC1 by nutrient deprivation or rapamycin treatment is commonly used to activate autophagy. Thus, when mTORC1 is inactivated, it dissociates from the ULK complex, allowing ULK activity (**Figure 1.15**) (Noda & Fujioka, 2015). In yeast, Atg17, Atg29 and Atg31 are also components of the Atg1 complex and participate in the recruitment of Atg9 vesicles to the PAS, through an Atg1-dependent interaction of Atg17 with Atg9 (Ragusa *et al.*, 2012; Stanley *et al.*, 2014; Rao *et al.*, 2016). This aspect represents an important difference between the yeast and mammalian pathway.

During starvation, ULK1 plays an important role in regulating ATG9 trafficking, the unique multispanning transmembrane protein, that cycles between the trans-Golgi network and the endosomal compartment in basal conditions. Upon autophagy induction, ATG9 is recruited to the growing autophagosome, where it might supply lipids needed for membrane elongation (Orsi *et al.*, 2012; Webber *et al.*, 2007; Joachim *et al.*, 2015; Karanasios *et al.*, 2016).

Recent data demonstrate that mitochondria have also a crucial role in the regulation of autophagy mediated by intracellular Ca^{2+} (Cárdenas *et al.*, 2010). Mitochondria take up Ca^{2+} that is released by the ER upon activation of inositol triphosphate receptors. In turn, Ca^{2+} uptake by mitochondria supports efficient oxidative phosphorylation, ATP generation and inhibition of autophagy through repression of AMPK activity. Interestingly, besides ATP mitochondria also regulate the initiation of autophagy through the production of ammonia generated by mitochondrial-dependent glutaminolysis (Eng *et al.*, 2010). Ammonia upregulates autophagy in a non-conventional manner, as it does not require either ULK1 or ULK2 (Cheong *et al.*, 2011). The ability of ammonia to upregulate autophagy might be important in cancer, as cancer cells typically display high levels of glutaminolysis, and autophagy appears to be crucial to tumorigenesis, at least in some settings (Galluzzi *et al.*, 2015; Guo *et al.*,

2011; Yang *et al.*, 2011). A recent study has found that, in yeast, mitochondria are also absolutely required to initiate autophagy by regulating the activity of PKA (Graef & Nunnari, 2011). In this case, it was observed that mitochondrial respiratory deficiency led to upregulation of PKA activity, which inhibited autophagy in 2 ways: by blocking Atg1-Atg13 complex activity (equivalent of the ULK1-ATG13-FIP200 complex) and by inhibiting the expression of Atg8.

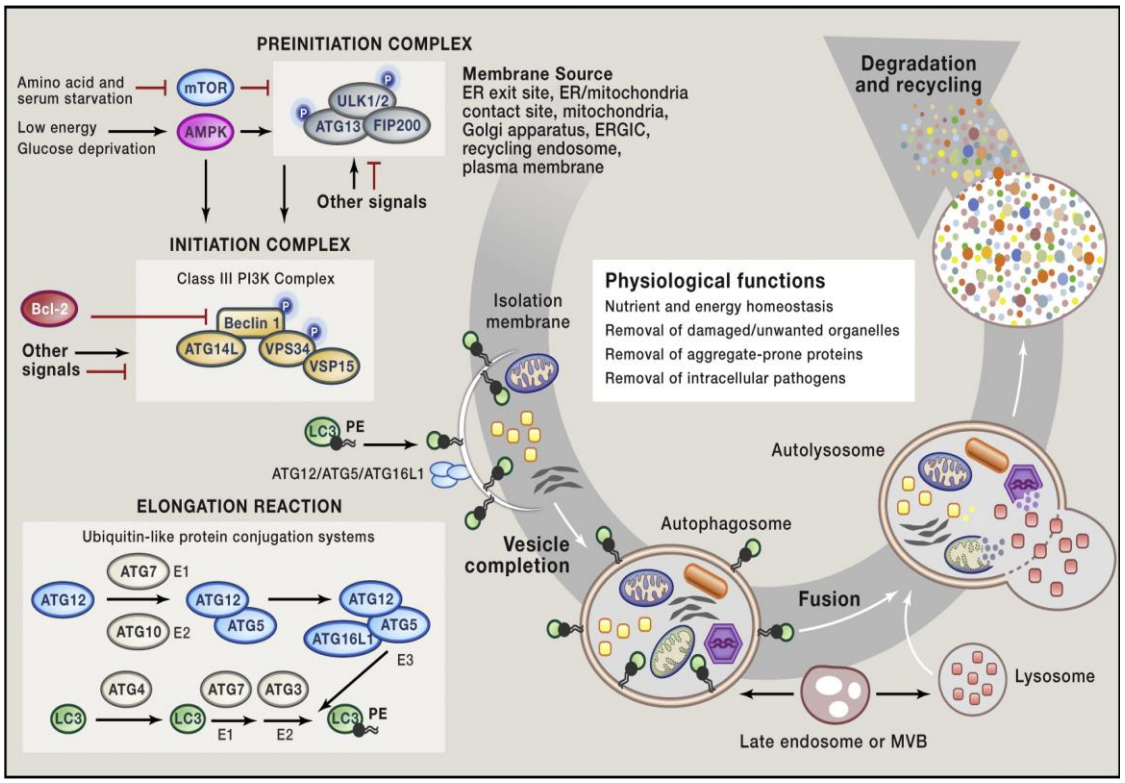

Figure 1.15. Macroautophagy signaling pathway. From top to bottom, different signals act as upstream mTOR inhibitors. ULK and PI3KC3 complex participate and recruit more proteins for membrane nucleation. Both, Atg8 and Atg5 UBL systems work in collaboration in autophagosome elongation and closure. (Taken from Green & Levine, 2014).

After autophagy induction, several protein complexes participate in the isolation membrane elongation to build the mature autophagosome. This process can be divided into 3 stages: vesicle nucleation, elongation and maturation. In order to develop these actions, proteins take part each one in a specific step (reviewed in Ktistakis & Tooze, 2016). In the first step, a huge number of different proteins are recruited to the site of autophagosome formation, in a process called autophagosome nucleation. PI3KC3, p150, Ambra1 and Beclin 1 form the core of the PI3KC3 complex, which can also bind the product of UVRAG or ATG14L. Within the complex, Beclin 1 is the target to which some protein regulators of PI3KC3 bind in order to modulate the generation of PtdIns3P. This phospholipid plays the role of recruiting more ATG proteins to the

nucleation site (Horenkamp *et al.*, 2015; Juris *et al.*, 2015). Among the PtdIns3P interacting proteins, WIPI1 and WIPI2 (Dooley *et al.*, 2014; Polson *et al.*, 2010), ATG2 and DFCP-1 are the most well known even if their exact role needs to be further studied.

Afterwards two UBL conjugation systems participate in autophagosome membrane elongation, shaping and closure. These two systems are interconnected and need to act together for a proper autophagosome growing *in vivo*. The first UBL system is composed of ATG5, ATG12, ATG10 and ATG16L1. Initially, ATG12 is activated by ATG7 (E1-like enzyme), transferred to ATG10 (E2-like enzyme) and finally covalently bound to ATG5. ATG12-ATG5 interacts also with ATG16L1 to create a complex that homodimerizes forming a multimeric complex (**Figure 1.15**). The final action of this complex is to interact with the outer autophagosomal membrane and to act as the E3 ligase enzyme of the second UBL conjugation system (Romanov et al., 2012; Walczak & Martens, 2013). This second UBL system is constituted by ATG4, ATG7, ATG3 and LC3 (**Figure 1.15**). First of all LC3 is cleaved in its C-terminal end by ATG4, exposing a glycine. Next LC3 is associated with ATG7 and then transferred to ATG3 in an ATP-dependent trans-thioesterification process. Once bound to ATG3, the latter directs LC3 to the autophagosomal membrane, and in collaboration with the E3-ligase complex catalyzes the conjugation of LC3 to PE to produce LC3-PE (Nakatogawa *et al.*, 2007; Noda *et al.*, 2011; Tanida *et al.*, 2004b; Hsu & Shi, 2016).

The final product, LC3-PE, is considered as the main autophagy-specific marker in cells, and is also the best known effector in autophagosome elongation (Hsu & Shi, 2016). Moreover LC3 in the preautophagosomal membrane recruits partner proteins, through its LIR motif, involved in autophagy regulation and autophagosome growth (Hurley & Schulman, 2014; Noda *et al.*, 2010; Stolz *et al.*, 2014). Once the autophagosome is formed and closed with the corresponding material to degrade, ATG4 participates again removing LC3-PE from the outer autophagosomal membrane in the recycling of LC3. Nevertheless, LC3 associated to the inner autophagosomal membrane will be degraded by the lysosomal enzymes. More about the Atg8 UBL system will be discussed in Section 1.2.5.

In the last step of autophagy and regarding the enclosed material degradation, autophagosome travels along the cytoplasm through microtubules and fuses with the lysosomes (Shen & Mizushima, 2014). The outer autophagosomal membrane fuses with the lysosomes so that the inner autophagosomal membrane and their contents come into contact with the lysosomal hydrolases and lipases. Many proteins take part

in the autophagosome-lysosome fusion event, such as LAMP2, Rab, HOPS, SNAREs, LC3, ESCRT, FYCO1 and UVRAG-C-Vps tethering complex (Wirawan *et al.*, 2012). The result of the autophagy process is the generation of recycled amino acids, fatty acids and nucleosides that will come back to the cytosol for new anabolic reactions.

1.2.5 Atg8 Conjugation System

As mentioned before, the autophagosome elongation and sealing process involves two UBL systems, Atg8 and Atg5. Both of them work together *in vivo*, although *in vitro* the presence of the second one is not strictly necessary for their main goal, Atg8 lipidation. Since the main work in this thesis is focused on the human Atg8 orthologs, a detailed description of the Atg8 UBL system is shown below (for reviews see Yang & Klionsky, 2010 and Mizushima *et al.*, 2011).

Atg8, a crucial protein in the autophagic process of autophagosome elongation in yeast, is the central player and also the final effector of the UBL system. At least 8 Atg8 orthologs have been identified in mammals, divided into two subfamilies, LC3 and GABARAP. LC3A, LC3B, LC3B2 and LC3C constitute the LC3 subfamily, whereas GABARAP, GABARAPL1/GEC1, GABARAPL2/GATE-16 and GABARAPL3 comprise the GABARAP one (Weidberg *et al.*, 2010). It is noteworthy that the expression of GABARAPL3 has been demonstrated at the transcriptional level only (Xin *et al.*, 2001); the corresponding open reading frame might therefore represent a pseudogene. In the context of this thesis, LC3B, GABARAP, GABARAPL1 and GABARAPL2 will be studied.

Atg8 UBL system contains 3 other proteins, ATG4, ATG7 (E1-like enzyme) and ATG3 (E2-like enzyme). ATG4 is a cysteine protease responsible for the post-translational cleavage of human Atg8 orthologs last amino acids to expose a conserved C-terminal glycine [Gly120 for LC3B and Gly116 for all GABARAP subfamily members (Kabeya *et al.*, 2004; Tanida *et al.*, 2003; Tanida *et al.*, 2004a; Tanida *et al.*, 2006)]. This glycine is essential for the final conjugation to PE and localization to autophagosomal membranes depending on their lipidated status (Kabeya *et al.*, 2000, 2004; Tanida *et al.*, 2004a). After that cleavage, LC3 (and other Atg8 orthologs) interact with the E1-like enzyme of the system, ATG7 (**Figure 1.16**). ATG7 is a symmetric homodimer with two catalytic cysteine residues that allow activation of two different UBL proteins, LC3 and ATG12 (Hong et al., 2011; Kaiser et al., 2013). ATG3, the E2-like enzyme of this system, receives LC3 from ATG7 and is thought to be

engaged in bringing LC3 to the membrane for its final lipidation. This final reaction is stimulated by the other UBL system participating in autophagy, the ATG5-ATG12-ATG16 complex. This complex acts as the E3-ligase enzyme of this sophisticated reaction.

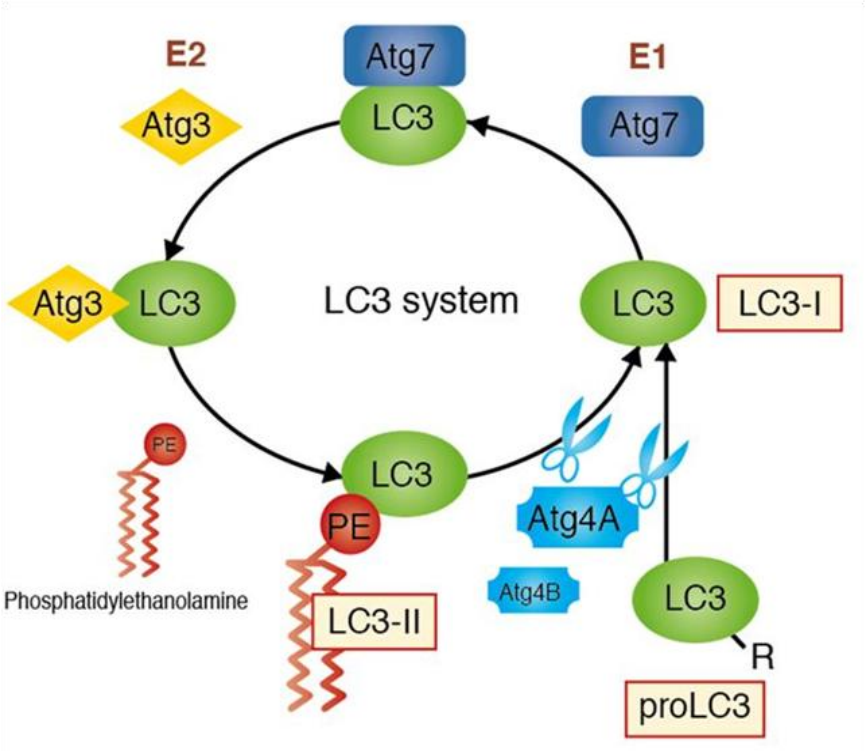

Figure 1.16. Schematic representation of Atg8 UBL system. (Taken from http://ruo.mbl.co.jp/g/product/protein/autophagy/autophagy.html).

1.2.5.1 Human Atg8 Orthologs

As mentioned above, Atg8 orthologs in mammals are divided into 2 subfamilies: LC3 (LC3A, LC3B, LC3B2 and LC3C) and GABARAP (GABARAP, GABARAPL1, GABARAPL2 and GABARAPL3) (Weidberg *et al.*, 2010). LC3B is the most extensively studied ortholog in mammals and it participates in autophagosome biogenesis as does Atg8 in yeast. GABARAPL2 and GABARAP were identified as an intra-Golgi vesicular transport factor and a protein that facilitates clustering of GABA(A) receptors in combination with microtubules, respectively (Tanida *et al.*, 2004b). Both of them are the most recently but less characterized orthologs in terms of their role in autophagosome formation.

A) Characteristic Sequence and Structural Features

Each Atg8 subfamily is very well conserved across its entire length (apart from the few N-terminal residues in LC3) and proteins are also very similar to each other in most of their positions (Schaaf *et al.*, 2016; Shpilka *et al.*, 2011). The few positions that are only conserved in each family and differ between the subfamilies may account for some of the functional differences between them (**Figure 1.17**). However at present it is unclear what functions, if any, are associated to the particular sequence features.

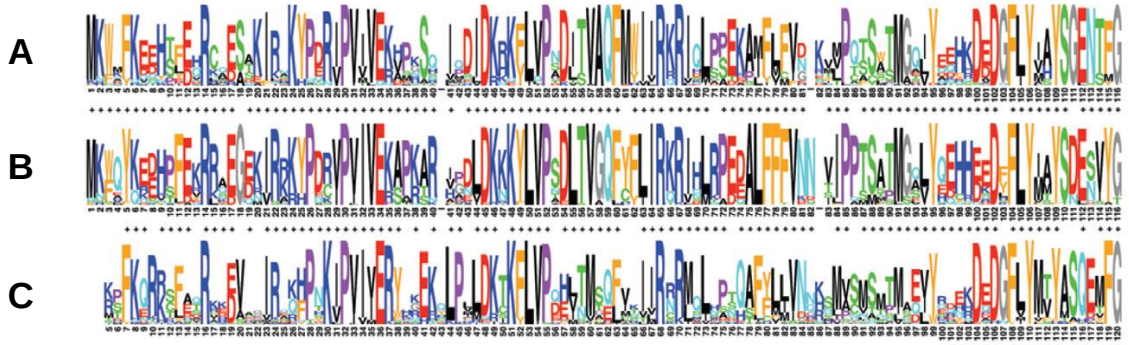

Figure 1.17. Human Atg8 orthologs sequence features. (**A**) GABARAPL2, (**B**) GABARAP and (**C**) LC3. Sequence logos show the conservation (overall height) and residue prevalence of multiple alignment positions (Schneider & Stephens, 1990). The alignment includes the core conserved sequence regions, only excluding short non-conserved distal regions of some sequences. Plus signs indicate similar positions between alignments of the GABARAPL2 and GABARAP and between the GABARAP and LC3 subfamilies. (Adapted from Shpilka *et al.*, 2011).

LC3B, GABARAP and GABARAPL2/GATE-16, as well as the other Atg8 orthologs from mammalian, protozoan, and fungal cells, share a strong structural similarity with ubiquitin, despite the lack of similarity in amino acid sequence (Shpilka *et al.*, 2011; Schaaf *et al.*, 2016). The C-terminal ubiquitin core (also called β-grasp motif) is mainly conserved and usually comprises a four-stranded β-sheet of the mixed type (i.e. the two inner strands are arranged in parallel and are flanked by antiparallel outer segments) and one or two helices shielding the concave face of the sheet (Coyle *et al.*, 2002; Kumeta *et al.*, 2010; Paz *et al.*, 2000; Schwarten *et al.*, 2010; Sugawara *et al.*, 2004) (**Figure 1.18**). This domain contains a basic feature that is conserved among family members and is suggested to have a role in protein-protein interactions.

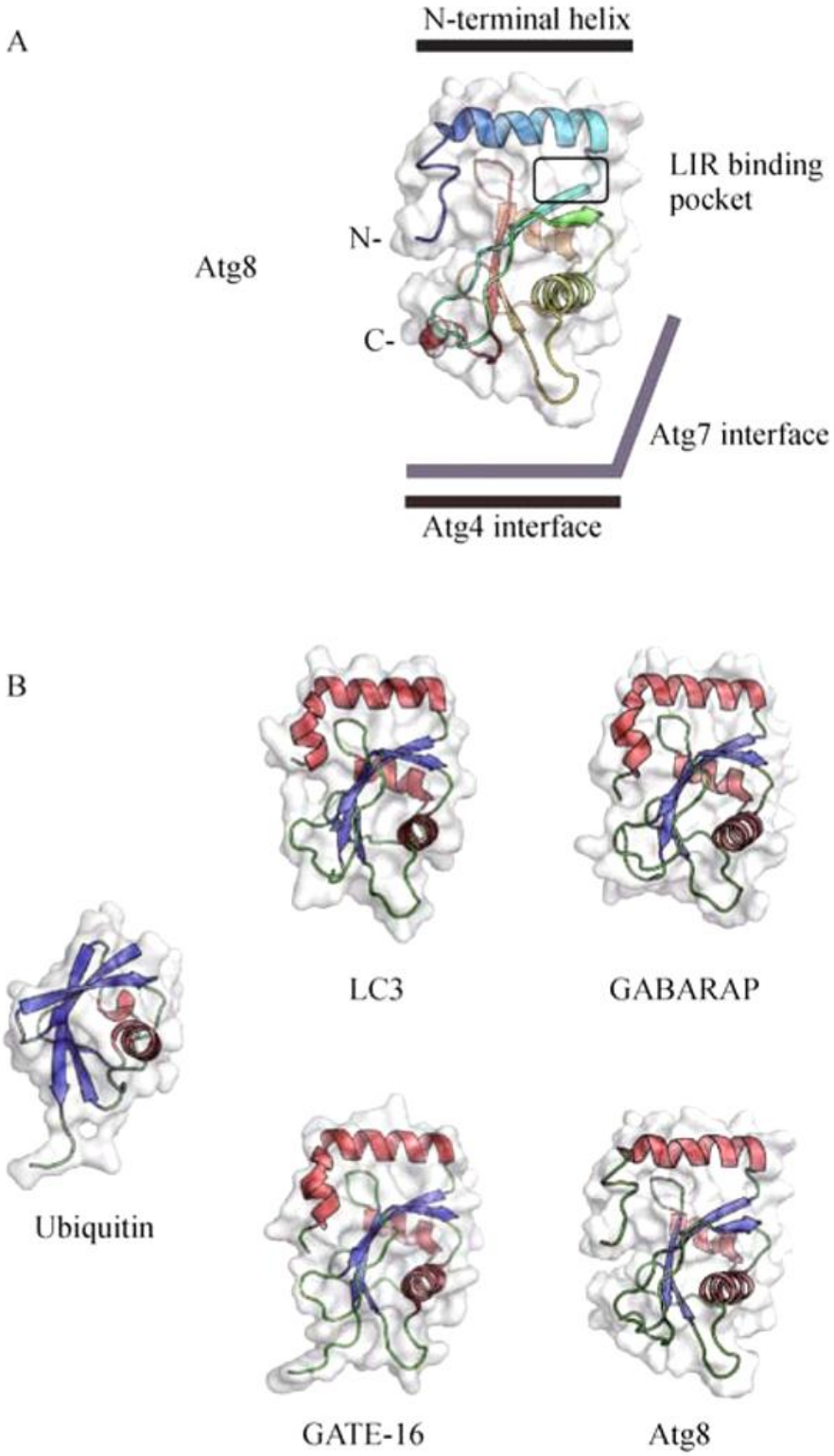

Figure 1.18. Crystal structures of Atg8, mammalian Atg8 orthologs and ubiquitin. (**A**) NMR structure of yeast Atg8. Several interaction interfaces are labeled. Atg8 functions to recruit specific cargo and core autophagy machinery through interaction with a conserved motif, the LIR or the AIM, which associates with Atg8 in a specific hydrophobic pocket. (**B**) Comparison of Atg8-family protein structures exhibiting the ubiquitin-like fold. PDB: 2KQ7 (Atg8), 1UGM (LC3), 1GNU (GABARAP), 1EO6 (GABARAPL2/GATE-16), 1UBI (ubiquitin). (Taken from Chew & Yip, 2014).

In addition to the ubiquitin core, human Atg8 orthologs contain an N-terminal extension with two additional helices, attached to the convex face of the β-sheet. This stretch is a hallmark of all Atg8-like proteins distinguishing them from other members of the ubiquitin superfamily, and the larger differences are located in these regions surrounding the C-terminal core (**Figures 1.18 and 1.19**). For example, the N-terminal sequence is relatively basic in LC3 but acidic in GABARAP and GABARAPL2. The crystal structure of GABARAP showed that Atg8-family proteins may have the ability to adopt two distinct conformations, with the N-terminal helix mediating an intermolecular interaction with another Atg8 molecule: a closed conformation, in which the α helices project down towards the surface of the ubiquitin core, and an open conformation, in which the 10 N-terminal amino acids are directed away from the ubiquitin core (Coyle *et al.*, 2002). The latter conformation is stabilized by the oligomeric state of the protein and points to flexibility in the Atg8 N-terminal region. In support of this hypothesis, NMR has demonstrated the structural flexibility of the N-terminal region of yeast Atg8 (Schwarten *et al.*, 2010; Kumeta *et al.*, 2010). The potential of Atg8 to form higher order homo-oligomers via the dynamic N-terminal tail may be the mechanism that underlies the putative membrane tethering function of membrane-anchored Atg8-PE.

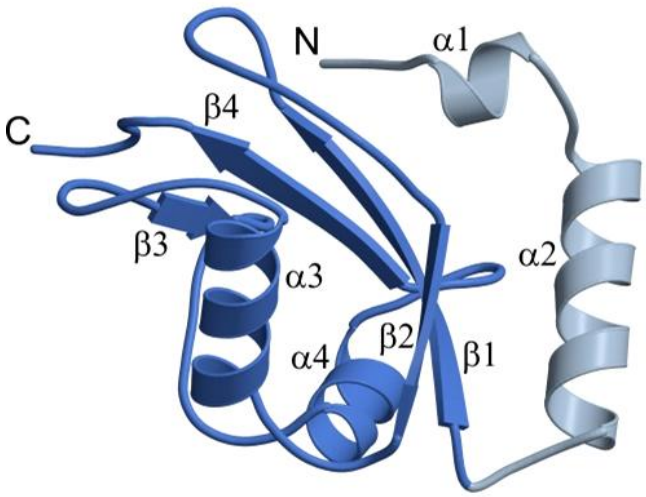

Figure 1.19. The characteristic fold of Atg8 family proteins, as exemplified by the GABARAPL2 crystal structure. The β-grasp motif (dark blue) is a hallmark of the ubiquitin superfamily. While all Atg8 orthologs contain a unique N-terminal extension (light blue), different arrangements are found in other ubiquitlin-like proteins. PDB: 1EO6. (Adapted from Weiergräber *et al.*, 2013).

Apart from GABARAPL2 and GABARAP, the three-dimensional structures of other members of the Atg8 family have been determined, including GABARAPL1, which is closely related to GABARAP, LC3A, LC3B (Kouno *et al.*, 2005), and yeast Atg8 itself (Schwarten *et al.*, 2010; Kumeta *et al.*, 2010). The latest addition to this list

is LC3C, the crystal structure of which has been determined in complex with an autophagy receptor (von Muhlinen *et al.*, 2012). While all these structures displayed the expected overall fold, they did also add to the controversy regarding the flexibility of the N-terminal subdomains. For instance, the NMR structure of LC3B did not show any indication of fluctuations around the α1-α2 hinge (Kouno *et al.*, 2005), which is at variance with the previous findings for GABARAP showing that the N-terminal portion exhibits an equilibrium of two or more conformations (Stangler *et al.*, 2002). Current evidence suggests that conformational polymorphism may be an intrinsic property of the N-terminal subdomain, at least in a subset of Atg8-like proteins. Note however that the functional significance of these observations still needs to be established.

Taken together, these findings suggest that the Atg8 N-terminal region plays a crucial role in the functions of these proteins (Nakatogawa *et al.*, 2007; Shvets *et al.*, 2011; Weidberg *et al.*, 2011; Schaaf *et al.*, 2016). Therefore, differences between the various Atg8 proteins in this region might reflect different functions.

B) Divergent Roles of Atg8 Orthologs

For about 15 years Atg8 has been known to be essential for efficient autophagosome formation in yeast (Lang *et al.*, 1998). In higher metazoans such as mammals, gene deletion experiments have not shown a marked phenotype (O'Sullivan *et al.*, 2005) due to the presence of several paralogs, indicating that significant functional redundancy might exist among Atg8 family members. These proteins are ubiquitous, despite differences in their levels of expression depending on tissue and stress conditions (Shpilka et al., 2011; Schaaf et al., 2016). To mention but a few examples, GABARAPL1 is highly expressed in the central nervous system (Nemos *et al.*, 2003), GABARAPL2 is strongly expressed in the brain, and LC3C, which is transcribed at lower levels than other members of the LC3 subfamily is expressed predominantly in the lung (He *et al.*, 2003; Xin *et al.*, 2001).

Upregulation of Atg8 proteins is observed under various stress conditions (Egami *et al.*, 2005; Kirisako *et al.*, 1999; van Zutphen *et al.*, 2010; Zois *et al.*, 2011). Although the signaling pathways and transcription factors regulating Atg8 gene expression are only partially characterized, several reports have shown that the transcription factors FoxO1, FoxO3 and E2F1 regulate Atg8 proteins in this process in mammalian cells (Mammucari *et al.*, 2007; Polager *et al.*, 2008; Sengupta *et al.*, 2009; Zhao *et al.*, 2007). Deciphering the expression patterns of specific Atg8 genes at

transcriptional and translational levels may shed new light on their different physiological roles.

Some Atg8 orthologs have been described in autophagy-independent cellular processes. LC3 was first isolated through its interaction with microtubules (Mann & Hammarback, 1994). At least LC3B and GABARAP are able to bind tubulin and microtubules via their N-terminal subdomain by electrostatic interactions (Coyle *et al.*, 2002; Kouno *et al.*, 2005; Wang *et al.*, 1999). LC3B has been proposed to act as an adaptor protein between microtubules and autophagosomes but no autophagy-independent role has been described for this ortholog (Kouno *et al.*, 2005), whereas the GABARAP family members have been identified through their roles in membrane trafficking (**Figure 1.20**). GABARAPL2 is a modulator of intra-Golgi transport through its coupling activity between NSF and the Golgi SNARE, GOS28 (Sagiv *et al.*, 2000). Interestingly, GABARAP and GABARAPL1 are also able to interact with NSF (Chen *et al.*, 2006; Kittler *et al.*, 2001). GABARAP has been shown to promote tubulin polymerization with its N-terminal tubulin-binding subdomain and interact with GABA(A) receptors with its C-terminal Ubl domain, possibly through interactions with one of its β sheets (Coyle *et al.*, 2002). Both GABARAP and GABARAPL1 associate with the ER, Golgi network and transport vesicles for the trafficking of GABA(A) receptors to the plasma membrane, perhaps explaining their strong expression in brain tissues (Chen *et al.*, 2006; Leil *et al.*, 2004). GABARAPL1 is also involved in the transport of the G-coupled κ-opioid receptor (Chen *et al.*, 2006) while GABARAP has been shown to interact with the transferrin receptor (Green *et al.*, 2002) and possibly the angiotensin II type I receptor (Cook et al., 2008), these orthologs could therefore be involved in trafficking other plasma membrane proteins. Interestingly, the trafficking of both the GABA(A) and opioid receptors requires the C-terminal processing of GABARAP and GABARAPL1 at their conserved Gly116, but the necessity for ubiquitin-like conjugation to lipids has not been investigated in the context of trafficking (Chen *et al.*, 2011; Chen *et al.*, 2007).

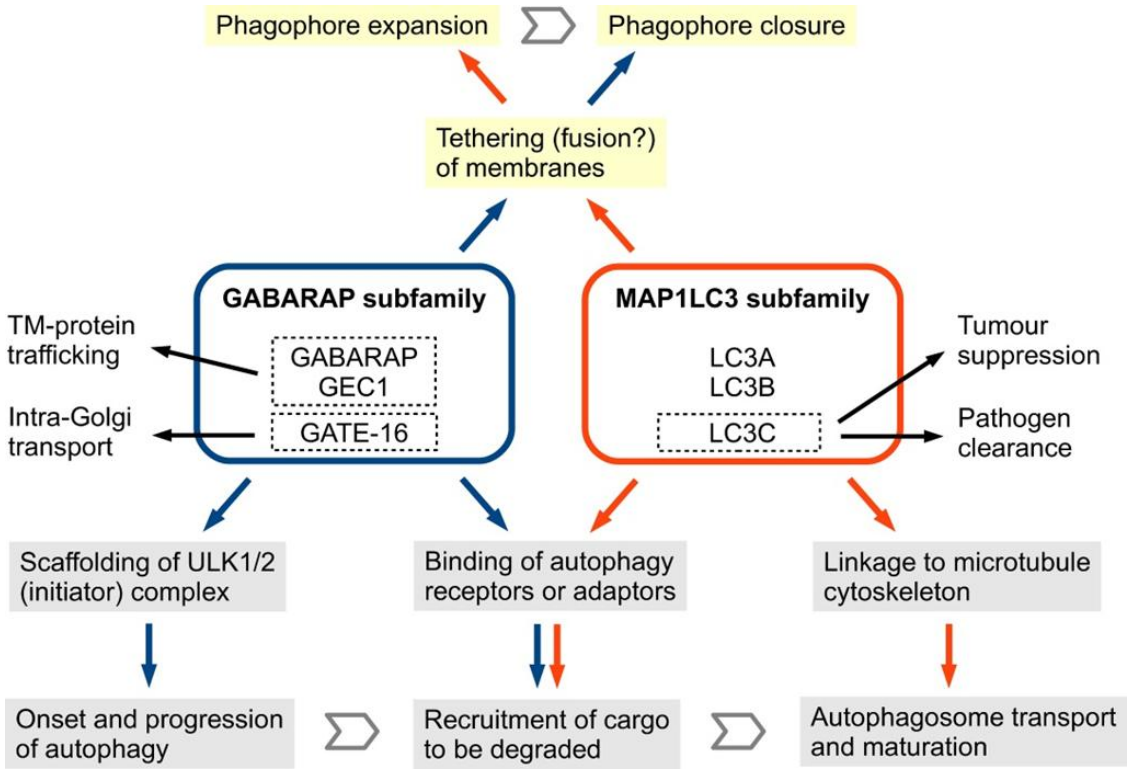

Figure 1.20. Schematic overview of the functions of GABARAP and LC3 subfamily proteins in mammalian cells. Activities which are essential for the autophagy pathway are highlighted by grey and yellow shading, signifying the involvement of protein-protein and protein-lipid interactions, respectively. Additional functions relevant for certain aspects of autophagy (in case of LC3C) or implicated in unrelated pathways (for GABARAP subfamily members) are indicated as well. (Taken from Weiergräber *et al.*, 2013).

In the context of autophagy, these molecules are well-established as binding partners of core autophagy components and adaptor proteins; as a result, they have been implicated not only in the recruitment of specific cargo destined for degradation (Stolz *et al.*, 2014), but also in the organization of functional multi-protein complexes. By virtue of their reversible membrane association, they are perfectly suited for this type of regulated scaffolding function. The binding specificities may differ markedly between members of the two subfamilies, depending on the interaction partner (reviewed in Schaaf *et al.*, 2016). The components of the ULK1/2 complex, for instance, clearly prefer GABARAP-like over LC3-like proteins (Alemu *et al.*, 2012) (**Figure 1.20**), and current evidence suggests that Atg1/ULK is not only involved in the initiation stage, but also exerts important functions on the phagophore membrane (Kraft *et al.*, 2012; Nakatogawa *et al.*, 2012). Conversely, the adaptor protein FYCO1, which links autophagosomes to the microtubule cytoskeleton, displays a strong preference for LC3 (Pankiv *et al.*, 2010). Among all Atg8/LC3 binding proteins identified to date, the most restricted scope has been found for NDP52. While most ubiquitin-directed

autophagy receptors (p62, NBR1 and optineurin) interact with both GABARAP and LC3 subfamily proteins (Kirkin *et al.*, 2009a; Pankiv *et al.*, 2007; Wild *et al.*, 2011), NDP52 has been found to exclusively bind LC3C. LC3C appears to be unusual in more respects. Recent evidence indicates that it exerts functions which are non-redundant with or even contrary to conventional LC3 proteins (Stadel *et al.*, 2015). In addition to its role in microbial clearance, it has been ascribed a unique anti-carcinogenic activity. Specifically, experiments with kidney cancer cells revealed that the VHL protein regulates LC3B and LC3C expression in opposite ways, with LC3B promoting tumor growth and LC3C suppressing it (Mikhaylova *et al.*, 2012) and while it is tempting to speculate that this striking observation is related to differential recruitment of critical autophagy targets, the identity of these cargoes is still elusive. Moreover, LC3 isoforms (LC3A, B and C) are shown to have different subcellular expression patterns in several human cancer cell lines and also in normal MRC5 fibroblasts (Koukourakis *et al.*, 2015). LC3A has a perinuclear and nuclear localization, LC3B is equally distributed throughout the cytoplasm and localizes in the nucleolar regions, and LC3C is located in the cytoplasm and strongly in the nuclei, where it co-localizes with LC3A and Beclin 1 (Koukourakis *et al.*, 2015). Therefore the distribution of these molecules is not identical; however whether these three LC3 proteins have a distinct biological role in autophagy remains obscure.

Regarding autophagosome formation, yeast Atg8 can mediate membrane fusion events *in vitro* (Nakatogawa *et al.*, 2007), and has been shown to regulate the elongation of the isolation membrane and consequently the size of autophagosomes (Xie *et al.*, 2008). In mammals, LC3B, GABARAP and GABARAPL2 are also able to mediate membrane fusion *in vitro*, and deletion of different residues of their N-terminal sequence alters autophagosome biogenesis and causes an accumulation of ATG16-labelled phagophores (Landajuela *et al.*, 2016; Weidberg *et al.*, 2011). LC3B is the most widely represented ortholog of Atg8 on autophagosomes, and, as mentioned before, has been used over the years as the principal marker of autophagy (e.g. used to measure autophagy induction or flux) (Klionsky *et al.*, 2008). Interestingly, both LC3 and GABARAP family members can be found on the same autophagosomes (Kabeya *et al.*, 2004; Weidberg *et al.*, 2010), and recent work has suggested that they are both necessary for autophagosome formation but probably act consecutively (Weidberg *et al.*, 2010). Silencing all the members of either Atg8 subfamilies causes an accumulation of incomplete phagophores, but differences in the size and number of these structures as well as the cumulative or attenuating effect of overexpressing other members (LC3B or GABARAPL2), suggested that LC3 subfamily proteins are

important during the elongation step of the phagophore membrane whereas GABARAP subfamily proteins act downstream, possibly during the membrane closure step (Weidberg *et al.*, 2010).

The diversity of human Atg8 orthologs may also play a role in cargo recognition (Stolz *et al.*, 2014). While NBR1 and p62 interact widely with the main six human Atg8 orthologs (Behrends *et al.*, 2010; Kirkin *et al.*, 2009a; Shvets *et al.*, 2008), Nix binds preferentially to GABARAP subfamily proteins (Novak *et al.*, 2010). Interestingly, a systematic proteomics study of the autophagy network highlighted 67 interactors for the six main human Atg8 orthologs, including 31 proteins binding only one specific Atg8 ortholog (Behrends *et al.*, 2010). These interactions are likely to uncover more functions and possibly more specificity in the role of individual human Atg8 orthologs. For instance, TBC1D2B was reported as an Atg8-binding protein (Behrends *et al.*, 2010), and a recent study suggested a role for Atg8 as a scaffold protein for signal transduction through OATL1 and TBC1D2B to regulate autophagosome maturation, with a stronger affinity of OATL1 for GABARAP out of the three Atg8 orthologs tested (Itoh *et al.*, 2011).

The function of various Atg8 orthologs may also be regulated differently (reviewed in Schaaf *et al.*, 2016). For instance, phosphorylation of the Ser 12 residue of LC3A was reported to inhibit autophagosome formation (Cherra *et al.*, 2010), and this residue is conserved in GABARAPL2 but in none of the other main Atg8 orthologs.

To conclude, Atg8 proteins act in diverse intracellular trafficking and autophagy processes. Atg8 is essential during autophagosome assembly through both its functions in lipid fusion events - for the elongation and closure of the isolation membranes - and participation in cargo selection. Although the mammalian Atg8 subfamilies seem to act differently during the formation of autophagosomes, the need for up to four members from each subfamily has yet to be explained. In particular, it is crucial to determine whether different members of one subfamily occupy the same autophagosomes or whether each member acts on a distinct autophagosome. This may help in deciphering whether autophagy, induced by different stress conditions, results in the formation of ‘specialized’ autophagosomes containing distinct Atg8 members.

Another major question is how these factors orchestrate their dual role in membrane fusion and cargo recruitment into autophagosomes. Increasing evidence shows that the numerous Atg8 orthologs described in mammals have both common and specific functions and interactors, therefore variations in their expression in

different tissues are likely to participate in the regulation of autophagy for different purposes. Moreover, although it is feasible that different members of the Atg8 family are crucial for selective autophagy, substantial proteomic data are needed to establish the cargo specificity of each Atg8 member. In the context of this work, the possible specific roles among human Atg8 orthologs have been examined in both selective and nonselective autophagic processes.

1.2.6 Non-selective versus Selective Autophagy

While autophagy has been initially described as a mechanism of bulk degradation, serving to replenish nutrient and energy resources under stress conditions, accumulating evidence suggests that specific targeting for autophagic proteolysis plays a crucial role in cellular homeostasis. Indeed, it is now clear that the turnover of damaged organelles such as mitochondria (mitophagy), peroxisomes (pexophagy), ribosomes (ribophagy) or endoplasmic reticulum (reticulophagy); removal of protein aggregates (aggrephagy), and elimination of intracellular pathogens (xenophagy), are highly selective and tightly regulated autophagic processes (Khaminets *et al.*, 2015; Mochida *et al.*, 2015; Sica *et al.*, 2015).

Selective autophagy may occur either via positive selection for incorporation into autophagosomes [e.g., by posttranslational modifications like ubiquitination or acetylation (Jeong *et al.*, 2009; Kirkin *et al.*, 2009b)] and/or by negative selection (e.g., due to decreased accessibility of certain proteins or organelles for autophagic engulfment). Specificity is accomplished by a number of autophagy receptor (or adaptor) proteins which associate with Atg8-like proteins on the phagophore surface and selectively mediate the autophagosomal degradation of the different cargoes (**Figure 1.21**). Our knowledge about the network of autophagy regulators has increased dramatically, bringing a new understanding of this highly selective and precisely regulated membrane-dependent process.

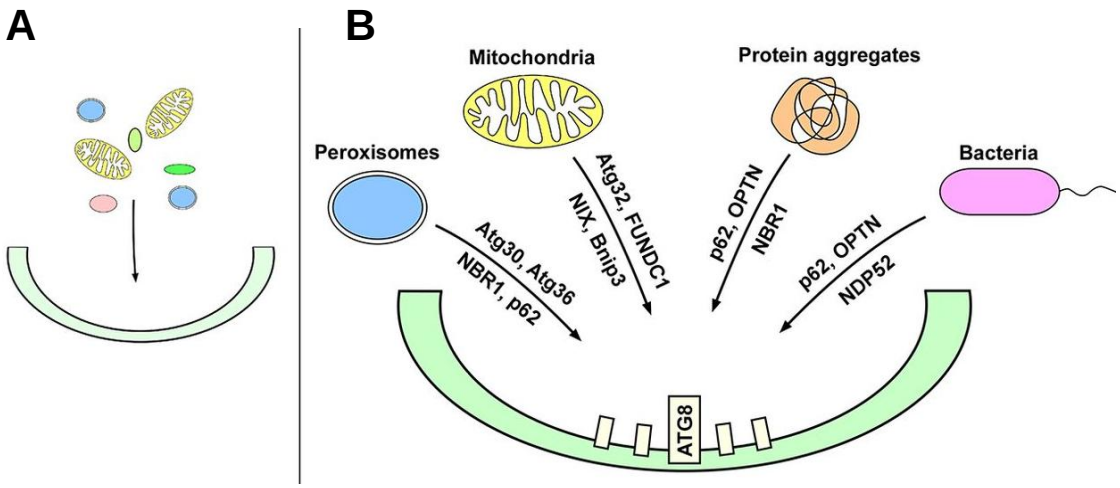

Figure 1.21. Nonselective versus selective autophagy. (**A**) During nonselective bulk autophagy, cytosolic cargoes are indiscriminately sequestered to the forming autophagosome, the phagophore. (**B**) Selective autophagy enriches the phagophore for specific cargoes in a process dependent on receptor proteins. Several different cargoes have been identified and indicated here along with some of the autophagy receptors commonly associated with selective turnover of these structures including OPTN, NBR1, NDP52, NIX and FUNDC1. (Adapted from Svenning & Johansen, 2013).

1.2.6.1 General Mechanisms for Cargo Selection in Mammals

Identification of novel autophagy receptors orchestrating the process of recognition and delivery occurs concomitantly with an improved knowledge about cargoes (Stolz *et al.*, 2014). Their function can be described by four common criteria:

(i) Autophagy receptors bind Atg8/LC3 through a conserved binding site, the LIR motif or AIM – W/YxxL/I.

(ii) Autophagy receptors are degraded with the cargo.

(iii) Deletion of autophagy receptors should not interfere with the function of the basic autophagy machinery.

(iv) Protein-protein binding domains or membrane-binding domains mediate interaction with the cargo.

On the basis of structural features and on how they interact with the respective cargoes, autophagy receptors can be divided into the following four different groups (**Figure 1.22**):

(i) SLRs share several structural and functional similarities with p62/SQSTM1 (Deretic, 2012). All SLRs contain dimerization or polymerization domains, bind ubiquitin and interact with members of the human Atg8 family proteins. These autophagy receptors recognize ubiquitinated cargoes via C-terminal ubiquitin-binding domains with defined affinities for different ubiquitin moieties. However, in some cases they can also bind directly the unmodified cargo (Johansen & Lamark, 2011; Shaid *et al.*, 2013).

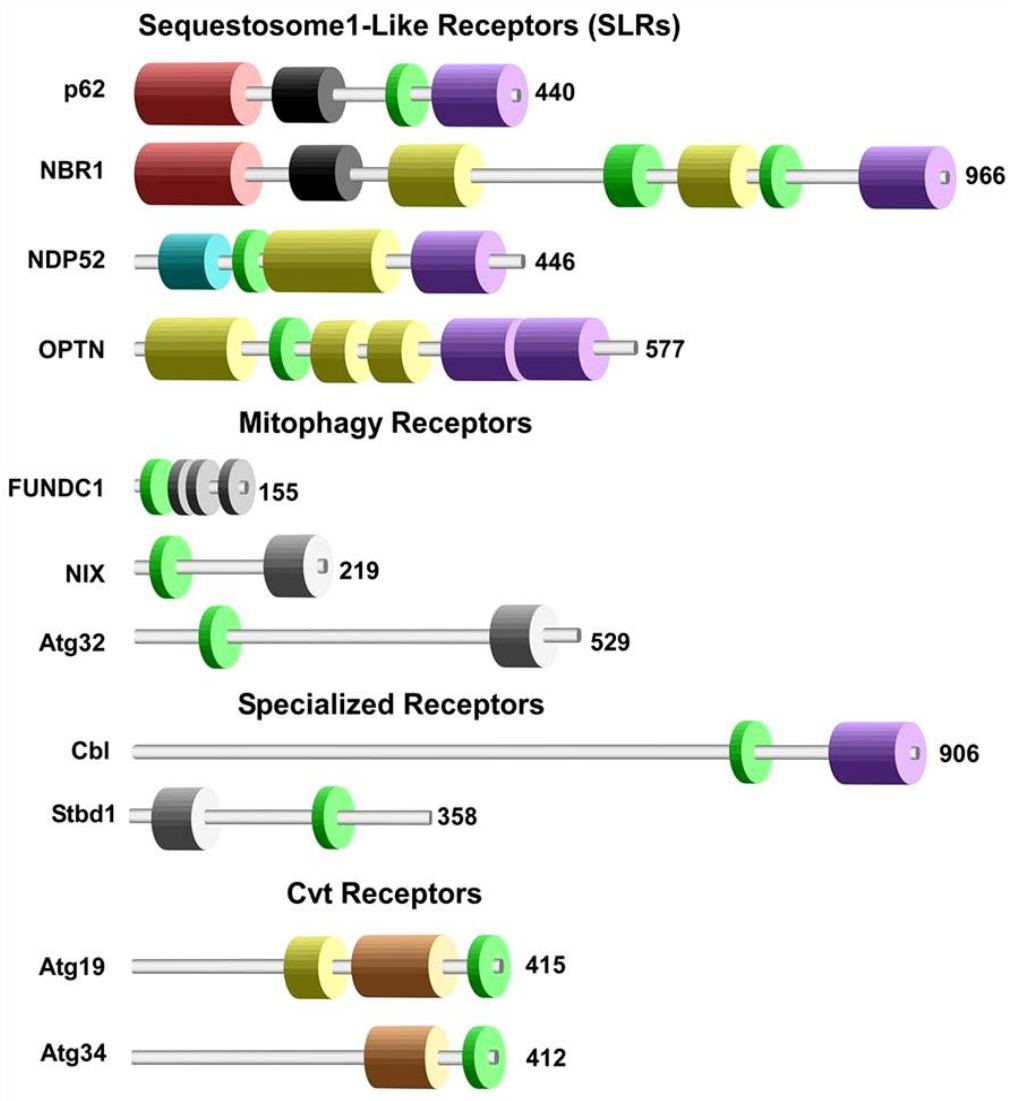

Figure 1.22. Schematic illustration of protein domain architectures of different autophagy receptors. The Cbl protein contains additional domains (from the N terminus: 4H, EF, SH2 and RING) not shown here for clarity. (Adapted from Svenning & Johansen, 2013).

(ii) Autophagic removal of damaged mitochondria (mitophagy) represents the best-studied example of selective autophagy mediated by membrane-associated receptors (Sica *et al.*, 2015). Mammalian NIX, BNIP3, FUNDC1 and yeast Atg32 localize to the mitochondrial outer membrane, where they are anchored by

transmembrane domains and mediate selective clearance of mitochondria through LIR-dependent interaction with Atg8 family proteins (Hanna *et al.*, 2012; Kanki *et al.*, 2009; Liu *et al.*, 2012; Novak *et al.*, 2010; Okamoto *et al.*, 2009; Sakakibara *et al.*, 2015)

(iii) Recently, some specialized autophagy receptors have emerged as exemplified by the Stbd1 and the E3-ubiquitin ligase Cbl. Stbd1 is suggested to act as a selective autophagy receptor for glycogen in a process named glycophagy (Jiang *et al.*, 2011).

(iv) In the yeast Cvt pathway, the vacuolar hydrolases Ape1p and Ams1p are selectively imported to the yeast vacuole through direct binding to the autophagy receptor Atg19. Binding initiates the formation of a multimeric, or aggregated, Cvt complex. Atg19 then interacts with the adaptor Atg11, which mediates translocation to the forming autophagosome where Atg19 binds to Atg8 to facilitate delivery of the hydrolases (Liu *et al.*, 2016; Lynch-Day & Klionsky, 2010). Although Atg19 acts under nutrient-rich conditions, the homologous protein Atg34 acts under nutrient starvation-induced autophagy to transport Ape1p and Ams1p to the vacuole (Suzuki *et al.*, 2010).

So far, four human ubiquitin-binding autophagy receptors have been described; p62/SQSTM1, NBR1 (Kirkin *et al.*, 2009a), NDP52 (Thurston *et al.*, 2009) and optineurin (Wild *et al.*, 2011). In mammals, the best described selective substrates of autophagy are p62/SQMTM1 and NBR1 (**Figure 1.22**). They both interact directly with the human Atg8 ortholog LC3B through a LIR motif and p62 can bind at least the five main human Atg8 orthologs, suggesting that this interaction may be conserved for all mammalian Atg8 orthologs (Bjørkøy *et al.*, 2005; Noda *et al.*, 2010; Pankiv *et al.*, 2007). Although p62 and NBR1 can interact and form oligomers, they work independently in cells (Kirkin *et al.*, 2009a). Both the N- and C-terminal sequences of Atg8/LC3B are important to interact with the AIM motifs of p62 (Ichimura *et al.*, 2008; Shvets *et al.*, 2008) and NRB1 (Kirkin *et al.*, 2009a). The presence of Atg8/LC3B on the isolation membrane, including the area that will become the inside of the inner membrane upon autophagosome completion, suggested that this interaction might be the main driver for p62 and NBR1 targeting to isolation membranes and engulfment in autophagosomes (Kirkin *et al.*, 2009a). This is supported by the requirement for the AIM motif to efficiently carry out turnover of p62 and NBR1 by autophagy (Ichimura *et al.*, 2008; Kirkin *et al.*, 2009a). However oligomerized p62 can also localize to the site of autophagosome formation prior to recruitment of LC3B and independently of its AIM motif, suggesting that the AIM motif interaction with LC3B/Atg8s is not sufficient to target p62 for degradation or that p62 may be able to initiate and determine the site of

autophagosome formation (Itakura & Mizushima, 2011). Although the order and site of recruitment are unclear, the AIM dependent interaction of autophagy adaptor proteins with Atg8 orthologs probably contributes to cargo selection through binding of these cargoes to autophagic membranes (reviewed in Noda *et al.*, 2010).

p62 and NBR1 are also called adaptor cargo receptors as they bind ubiquitinated proteins and target them for autophagic degradation (Kirkin *et al.*, 2009a; Pankiv *et al.*, 2007). For instance, p62 is involved in the degradation of protein aggregates, but also peroxisomes, mitochondria and intracellular bacteria through ubiquitination signals (Bjørkøy *et al.*, 2005; Geisler *et al.*, 2010; Kim *et al.*, 2008; Zheng *et al.*, 2009). Both p62 and NRB1 are largely involved in the autophagy-dependent clearance of toxic protein aggregates associated with Parkinson disease, Huntington disease, and neurodegeneration in general (Bjørkøy *et al.*, 2005; Pankiv *et al.*, 2007; Ravikumar *et al.*, 2002; Rubinsztein, 2006).

The two other SLRs, optineurin and NDP52 (**Figure 1.22**), have both been linked to the selective autophagy of bacteria (xenophagy) (Thurston *et al.*, 2009; Wild *et al.*, 2011). Optineurin has additionally been implicated in ubiquitinin dependent selective autophagy of various protein aggregates (Korac *et al.*, 2013). The domain architecture of both proteins comprises coiled-coil domains, functional LIR motifs and C-terminal ubiquitin-binding domains. Optineurin has been identified in protein aggregates of several neurodegenerative diseases, and given its ability to self-interact and oligomerize through coiled-coil domains it is likely to function as an aggregating cargo receptor like p62. Optineurin is also involved in ubiquitin-independent aggrephagy of huntingtin aggregates (Korac *et al.*, 2013). Less is known about the aggrephagy properties of NDP52, but it has been implicated recently in selective autophagy of the microRNA processing DICER and the AGO2 effector (Gibbings *et al.*, 2012).

1.3 Mitophagy: a Selective Macroautophagy Pathway

Thought to have once existed as autonomous oxygen-utilizing bacteria, mitochondria now function as the powerhouses of eukaryotic cells. Visible by light microscopy as rod-shaped structures, mitochondria are formed of two membranes, the innermost of which is folded and houses the respiratory chain complexes and enzymes essential for ATP synthesis via oxidative phosphorylation (Rich & Maréchal, 2010). The steady transfer of genetic material from mtDNA to the host nucleus has permitted the

cell to exercise precise control over mitochondrial activity. Along with 22 tRNAs and 2 rRNAs, only 13 mitochondrial respiratory chain polypeptides remain encoded by the circular mtDNA (Taanman, 1999). Importantly, we can now appreciate that mitochondria are employed by cells in a variety of other cellular processes besides ATP production, including Ca^{2+} signaling and apoptosis. As a reflection of the diverse roles played by mitochondria, cells have been forced to implement strict control mechanisms over mitochondrial function and health. Indeed, disturbances in mitochondrial quality control result in an increasingly damaged and dysfunctional mitochondrial population leading to a range of human pathologies including ischaemia, diabetes and neurodegeneration (Aufschnaiter *et al.*, 2016; Chan, 2006; Madrigal-Matute & Cuervo, 2016). Defective mitochondria produce ATP less efficiently and harbor the potential to generate vast quantities of ROS that, if unchecked, can cause hazardous peroxidation of proteins and lipids along with long-lasting mtDNA damage (Murphy *et al.*, 2011; Yakes & Van Houten, 1997). Deleterious mtDNA mutations are also likely to manifest within a defective mitochondrial population and further compromise mitochondrial activity (Youle & Narendra, 2011). Extensive mitochondrial damage can even cause the organelle to become “leaky”; releasing pro-apoptotic proteins into the cytoplasm, often with catastrophic consequences (Tatsuta & Langer, 2008).

Much debate exists over precisely how mitochondria contribute to disease pathogenesis. In some cases, it is uncertain whether an accumulation of unhealthy mitochondria is a cause or a consequence of disease. However, the susceptibility of high-energy demanding cells such as neurons to mitochondrial disorders along with the identification of specific disease causing mutations in mitochondrial quality control genes has driven a great deal of research into the regulation of mitochondrial homeostasis (Aufschnaiter *et al.*, 2016).

In yeast and mammals, cells turn over mitochondria through autophagy for quality control and to adapt to changing cellular needs (Ashrafi & Schwarz, 2013; Kiššová *et al.*, 2004; Tal *et al.*, 2007). This process is especially important for the selective removal of damaged mitochondria that are associated with the increased production of ROS and membrane permeabilization (Youle and Narendra, 2011) mentioned above. This cellular process is thought to delay aging (García-Prat *et al.*, 2016) and its dysregulation is linked to multiple human pathological states including neurodegeneration, myopathies and cancer (Aufschnaiter *et al.*, 2016; Kubli & Gustafsson, 2012; Lu *et al.*, 2013; Nixon, 2013).

In mammalian cells, mitophagy appears to occur predominantly via the macroautophagy pathway (Tolkovsky, 2009). When mitophagy was first described, the distinction between it and the nonselective autophagy pathway was hazy. Upon the discovery of proteins that function solely in the autophagic degradation of mitochondria (Kiššova *et al.*, 2004), it soon became clear that mitophagy has evolved as a unique quality control mechanism. By sequestering dysfunctional (or sometimes redundant) mitochondria into double membrane autophagosomes and trafficking them to lysosomes, cells are able to neutralize any threat posed by the faulty powerhouses (**Figure 1.23**). Over the last 10 years, developments in techniques such as live-cell imaging have allowed us to make exciting progress in the study of mitophagy dynamics and regulation.

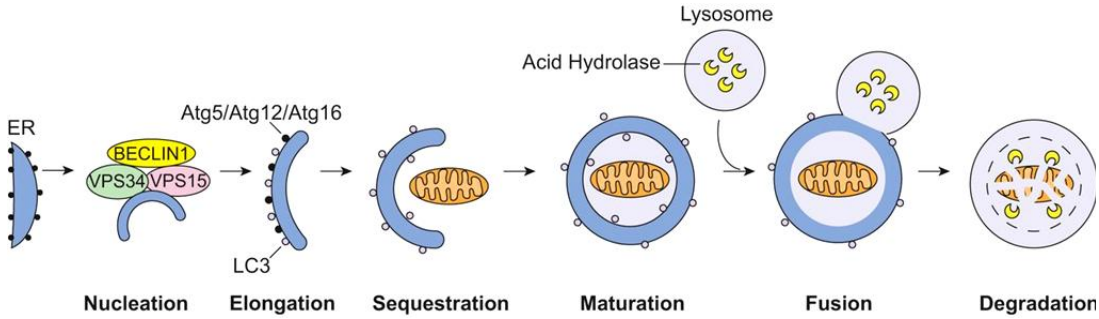

Figure 1.23. Overview of selective mitochondrial autophagy. Mitophagy begins with a nucleation step by the BECLIN 1/VPS34/VPS15 complex, which initiates formation of the autophagosome. Next, ATG5/ATG12/ATG16 and LC3 are involved in elongating the membrane. The autophagosome then fuses around a mitochondrion, sequestering it inside the mature double membrane vesicle. Finally, the autophagosome fuses with a lysosome and the mitochondrion is degraded by lysosomal hydrolases. (Taken from Moyzis *et al.*, 2015).

Mitophagy has been studied in a number of different systems both *in vitro* and *in vivo* and it has emerged that mitochondrial degradation can be initiated by different environmental and developmental cues. It is now clear that mitophagy is not solely a defence mechanism triggered by mitochondrial damage but also an essential feature of both cellular quality control and adaptation.

1.3.1 Mitophagy Mechanisms

1.3.1.1 Mitophagy in Yeast

Mitophagy in yeast depends on the delivery of mitochondria to the acidic lysosome-like vacuole for degradation. Yeast initiate mitophagy in response to a number of conditions including nitrogen starvation and rapamycin treatment (Bhatia-Kiššova & Camougrand, 2010). They have proven key in demonstrating that mitophagy can proceed via tightly regulated mechanisms distinct from the common autophagy pathway. Proteins such as the OMM protein Uth1p were first demonstrated to directly regulate mitophagy under certain conditions (Kiššova *et al.*, 2004).

Subsequent genetic screens identified another OMM protein, Atg32, as being essential for mitophagy (Kanki *et al.*, 2009; Okamoto *et al.*, 2009; Sakakibara *et al.*, 2015). In order to guide ill-fated mitochondria to the autophagosome, Atg32 binds directly with the resident autophagosome protein Atg8 and also interacts with the previously identified selective autophagy adaptor protein Atg11 (Kanki & Klionsky, 2008). Interestingly, expression of the cytosolic domain of Atg32 in peroxisomes induces the degradation of these organelles by pexophagy (Kondo-Okamoto et al., 2012), suggesting that Atg32 can inherently initiate organelle autophagy. The important scaffolding protein and Atg32 interactor Atg11 has recently been shown to recruit mitochondrial fission machinery to the mitochondria, thus facilitating mitophagy (Mao *et al.*, 2013)

1.3.1.2 Mitophagy during Erythropoiesis

A striking example of mitophagy being employed to remove healthy yet redundant mitochondria occurs during mammalian red blood cell development (erythropoiesis). Mature red blood cells are devoid of mitochondria following the selective elimination of their entire mitochondrial population by a distinct mitophagy pathway (Kundu *et al.*, 2008). During normal erythroid terminal differentiation, expression of the OMM NIP3-like protein NIX is augmented (Aerbajinai *et al.*, 2003) and this is necessary for complete mitochondrial depletion (Sandoval *et al.*, 2008; Schweers *et al.*, 2007). Importantly, the absence of NIX causes defective erythroid maturation and anaemia in mice (Sandoval *et al.*, 2008). Barde and colleagues discovered that NIX expression, along with other mitophagy genes such as ULK1 and Beclin 1, is dictated during differentiation by the combination of protein- and RNA-

mediated transcriptional control (Barde *et al.*, 2013). They found that increased Nix expression first requires transcriptional cofactor KAP1-mediated repression of Nix-targeting microRNA. Thus, overexpression of specific microRNAs or knockout of KAP1 resulted in mitophagy inhibition and severe anemia in mice (Barde *et al.*, 2013).

Similar to Atg32 in yeast, NIX confers selectivity for mitochondrial engulfment by the autophagosome. NIX directly interacts with autophagosomal marker proteins LC3 and GABARAP via its LIR motif (Novak *et al.*, 2010; Yoshii & Mizushima, 2015) allowing the recruitment and formation of autophagosomes around the mitochondria. Besides interacting directly with autophagosome components, NIX can also regulate mitophagy by facilitating mitochondrial membrane depolarization and ROS generation (Ding *et al.*, 2010). A NIX-regulated increase in ROS production may provide a key step in mitophagy by enhancing autophagosome biogenesis via mTOR inhibition (Ding *et al.*, 2010).

1.3.1.3 PARK2-mediated Mitophagy

Mutations in the E3-ubiquitin ligase PARK2 (Kitada *et al.*, 1998) and PINK1 (Valente *et al.*, 2004) cause autosomal recessive forms of Parkinson disease. Mutations in the genes encoding both proteins have been identified as genetic risk factors in familiar cases of the neurodegenerative disease. However it was not initially clear how these two proteins contributed to the severe pathogenesis. The spotlight was cast on a possible role in mitochondrial quality control when *in vivo* studies demonstrated that these mutations manifest as mitochondrial dysfunction (Gautier et al., 2008; Hoepken et al., 2007). Following initial studies that genetically linked PINK1 with PARK2 (Clark *et al.*, 2006; Exner *et al.*, 2007; Park *et al.*, 2006), the question remained of how mutations in these proteins might result in the accumulation of dysfunctional mitochondria. One answer was provided when Narendra and co-workers discovered that PARK2 normally functions to target damaged mitochondria for degradation by mitophagy (Lazarou *et al.*, 2015; Narendra *et al.*, 2008; Rüb *et al.*, 2016). Live-cell imaging of cultured cells expressing fluorescently-tagged PARK2 revealed the remarkably dynamic recruitment of cytosolic PARK2 to damaged mitochondria. These PARK2-decorated mitochondria are then sequestered into autophagosomes and delivered to lysosomes for degradation. Interestingly many PARK2 over-expressing cells can clear their entire mitochondrial population after the induction of global mitochondrial damage by treatment with mitochondrial depolarizing drugs.

In a healthy mitochondrion PINK1 is imported and rapidly turned over at the IMM via constitutive proteolytic processing by the protease PARL (Deas *et al.*, 2011; Greene *et al.*, 2012; Jin *et al.*, 2010). Upon dissipation of the inner Δψ, which is required to drive ATP production and mitochondrial protein import, PINK1 becomes stabilized on the OMM permitting it to recruit its binding partner PARK2 (Lazarou *et al.*, 2015; Matsuda *et al.*, 2010; Narendra *et al.*, 2010a) (**Figure 1.24**). Although the mitochondrial membrane potential seems to affect the localization, processing, and arguably stability of PINK1 (Jin *et al.*, 2010), the dependence of the PINK1 import reaction on the membrane potential is not as absolute as other preproteins following the canonical pathway to the IMM or matrix (Becker *et al.*, 2012). The results of the latter and other studies suggest that, in the presence of an inner membrane potential, the PINK1 polypeptide is partially inserted into the IMM through the TOM and TIM23 complexes (reviewed in Rüb *et al.*, 2016). PINK1 interaction with PARK2 is necessary for its phosphorylation and self-association which appears important for activation of its ubiquitin ligase activity (Kane *et al.*, 2014; Kondapalli *et al.*, 2012; Lazarou *et al.*, 2012; Shiba-Fukushima *et al.*, 2012). Most remarkably, PINK1 phosphorylates not only PARK2, but also ubiquitin in the context of PARK2 activation (Kane *et al.*, 2014; Kazlauskaite *et al.*, 2014; Koyano *et al.*, 2014).

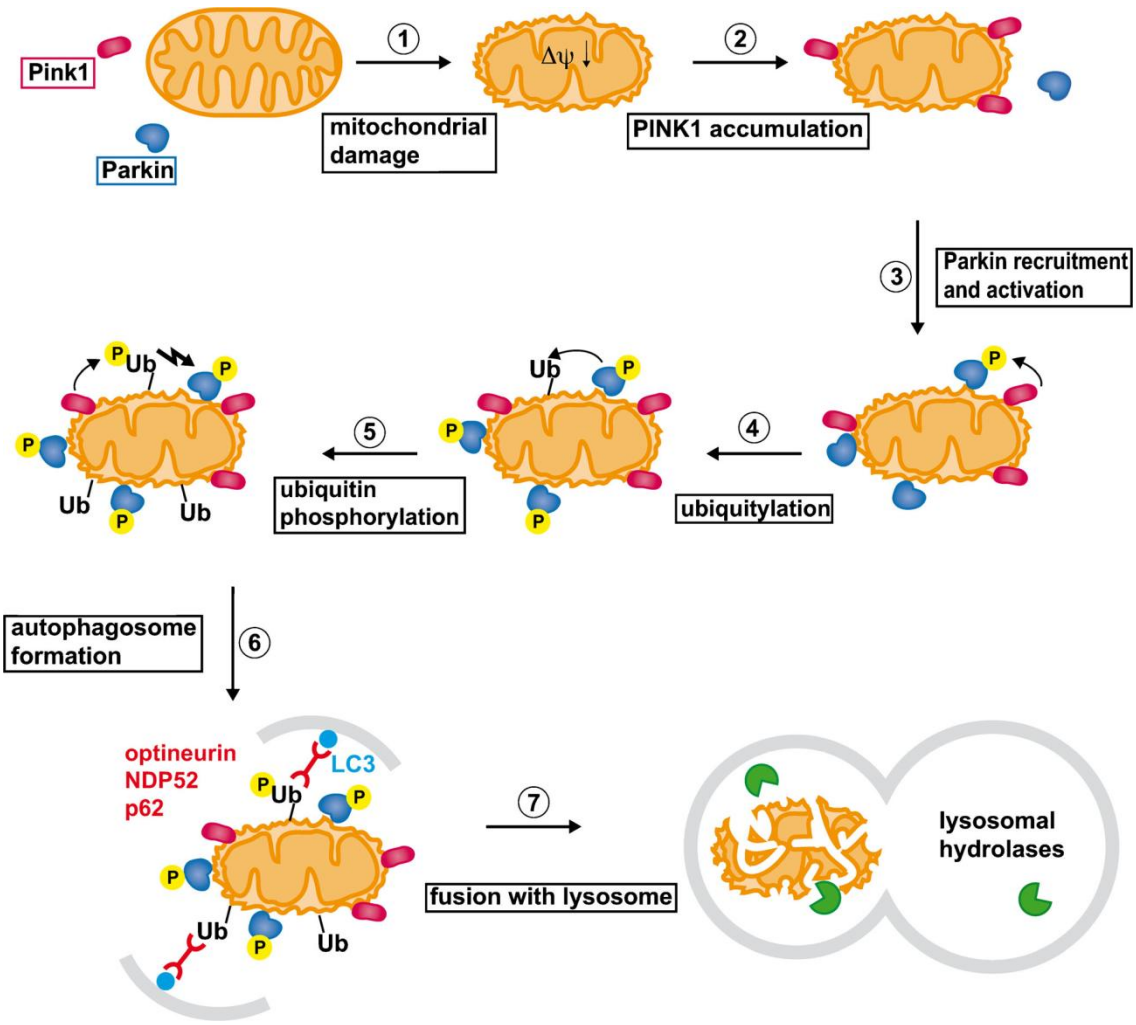

Figure 1.24. Current model of PINK1/PARK2-mediated mitophagy. Under steady-state conditions, PINK1 levels are very low. Mitochondrial stress conditions may lead to mitochondrial damage, accompanied by a decrease or loss of the mitochondrial Δψ (**1**). In the absence of Δψ, PINK1 accumulates at the OMM (**2**). PINK1 recruits and activates the usually cytosolic E3 ubiquitin ligase PARK2 in a process involving PINK1-mediated phosphorylation of PARK2 at Ser65 (**3**). PARK2 conjugates Ub to various OMM proteins (**4**). PINK1 phosphorylates Ub attached to OMM proteins. The resulting phospho-Ub further activates PARK2 (**5**). Adaptor proteins (red) that bind both Ub and the autophagic protein LC3 (light blue) mediate sequestration of the organelle in an autophagosomal membrane (gray lines) (**6**). The autophagosome then fuses with a lysosome, delivering its complete content to degradation by lysosomal hydrolases (green; **7**). (Taken from Rüb *et al.*, 2016).

The cytosolic protein PARK2, encoded by the PARK2 gene, is an E3 ubiquitin-protein ligase (Winklhofer, 2014). High-resolution crystal structures of PARK2 have revealed that, under steady-state conditions, the enzyme is maintained in an self-inhibited state (Riley *et al.*, 2013; Trempe & Fon, 2013; Wauer & Komander, 2013). Following its mitochondrial recruitment and activation, PARK2 is thought to non-specifically ubiquitinate multiple targets on the OMM including VDAC (Geisler *et al.*, 2010), Mfn1/2 (GTPases that mediate mitochondrial fusion) (Gegg *et al.*, 2010; Tanaka *et al.*, 2010), and the mitochondrial transport adaptor protein, Miro, which anchors kinesin motor proteins to the mitochondrial surface (Glater *et al.*, 2006; Wang *et al.*, 2011b). The ubiquitination and proteasomal degradation of some of these targets initiate further mitophagy reactions by marking the entire organelle for elimination via autophagy. The formation of the isolation membrane around damaged mitochondria is mediated by autophagy receptors that are able to bind to ubiquitinated proteins through their ubiquitin-binding domain and to LC3 on autophagosomal membranes through a LIR (Pankiv *et al.* 2007). So far, several receptors playing a role in PINK1/PARK2-mediated mitophagy have been identified (Pickrell & Youle, 2015; Yoshii & Mizushima, 2015), including SQSTM1/p62 (Geisler *et al.,* 2010), NBR1 (Kirkin *et al.,* 2009a), NDP52 (Lazarou *et al.,* 2015), and optineurin (Wong & Holzbaur, 2014).

The main hallmark of dysfunctional mitochondria is represented by a loss of the electric inner Δψ generated by the respiratory chain. Indeed, treatment of cells with the protonophore CCCP, which leads to an uncoupling of the respiratory chain, is generally used to simulate mitochondrial dysfunction. After the addition of CCCP to cells, it has been observed that endogenous PINK1 levels become barely detectable after 3 h incubation and reach a maximum level after 12–16 h. Under these conditions, only the full-length polypeptide is observed, and all PINK1 molecules co-purify with mitochondria. After removal of the uncoupler, PINK1 amounts return relatively quickly to very low levels (Matsuda *et al.*, 2010; Narendra *et al.,* 2010a). This observation that PINK1 significantly accumulates at potential-deficient mitochondria also led to the conclusion that PINK1 is a prominent sensor for mitochondrial damage (reviewed in Rüb *et al.*, 2016). In human cells exposed to CCCP, PARK2 was also shown to translocate from the cytosol to damaged mitochondria upon loss of Δψ and to mediate the autophagic removal of the organelle (Narendra *et al.*, 2008).

The mitochondrial accumulation of PINK1 has also been associated with other types of mitochondrial defects, such as elevated levels of ROS (Priyadarshini *et al.*, 2013) or an accumulation of misfolded proteins in the mitochondrial matrix (Jin & Youle, 2013). However, it is likely that ROS treatment, proteotoxic stress, or any other

type of mitochondrial damage may indirectly result in a Δψ depletion similar to the activity of the uncoupler CCCP.

A study has proposed that NIX is important for early depolarization of mitochondria and has a dual role during mitophagy in response to CCCP treatment in cells overexpressing PARK2 (Ding *et al.*, 2010). NIX-associated depolarization causes the recruitment of PARK2 to mitochondria, allowing p62-mediated mitophagy (Ding *et al.*, 2010). Moreover, NIX has been shown to participate in autophagy induction through enhanced superoxide release and partial inhibition of mTOR activity (Ding *et al.*, 2010). These results suggest that the function of NIX in mitophagy is not restricted to erythroid cells, and that NIX can participate to mitophagy upstream of the PARK2 selective mitophagy pathway.

PARK2 is not the only ubiquitin ligase shown to direct mitophagy. Increased activity of the ubiquitin ligase Mul1 enhances mitophagy during skeletal muscle wasting. Suppression of Mul1 maintains mitochondrial number and partially prevents muscle wasting in mice exposed to muscle-wasting stimuli (Lokireddy *et al.*, 2012). Finally, gp78 is another E3 ubiquitin ligase recently identified to drive depolarization-induced mitophagy in a PARK2 independent manner (Fu *et al.*, 2013). Interestingly, gp78 is ER associated and, upon mitochondrial depolarization, its ubiquitination activity recruits LC3 to engulf mitochondria in close proximity to the ER (Fu *et al.*, 2013).

1.3.2 Origin and Targeting of Mitophagosomes

One of the key steps in the mitophagy process is the recognition of the mitochondria that needs to be removed by the autophagosome. Exactly how autophagosomes are recruited to damaged mitochondria remains an intriguing question (Randow & Youle, 2014). The adaptor protein p62 can bind both ubiquitin and LC3 and is seen to accumulate on mitochondria that have been poly-ubiquitinated by PARK2 (Geisler *et al.*, 2010; Narendra *et al.*, 2010b). Despite this, whilst a role for p62 in mitochondrial clustering looks likely (Narendra *et al.*, 2010b), conflicting reports exist as to whether p62 is actually essential for the recruitment of autophagosomes to mitochondria (or *vice versa*) (Geisler *et al.*, 2010; Narendra *et al.*, 2010b). Besides p62, two other potential autophagy adapter proteins have been identified as substrates for PARK2 following mitochondrial depolarization: TAX1BP1 (Newman *et al.*, 2012) and CALCOCO2/NDP52 (von Muhlinen *et al.*, 2012). Interestingly, CALCOCO2/NDP52 has already been shown to target invasive bacteria for autophagy by interacting specifically

with LC3C via a non-canonical LIR motif (von Muhlinen *et al.*, 2012; Randow & Youle, 2014).

As has been seen with Atg32 in yeast and NIX in mammalian erythrocytes, mitophagy does not always depend on cytosolic adapter proteins for recruitment by the autophagosome. Indeed, as mentioned above, FUNDC1 binds LC3 via its LIR motif and this interaction is enhanced upon FUNDC1 dephosporylation during hypoxic conditions (Liu *et al.*, 2012). Overall, hypoxia-induced mitophagy offers another mechanism whereby mitochondria are targeted for mitophagy by regulated and direct interaction between OMM and autophagosome proteins.

There are not only protein receptors for cargo recognition but also some lipids act as receptors for mitochondrial targeting of the human autophagic machinery. Cer18 has been reported as being a receptor for anchoring lipidated and autophagosome-associated LC3 (LC3-II) to mitochondrial membranes, through direct interaction of Cer18 with LC3-II (Sentelle *et al.*, 2012). Cardiolipin externalization to the outer mitochondrial membrane has also been proposed to act as a signal for the human Atg8 ortholog LC3 (Chu *et al.*, 2013; Maguire *et al.*, 2016). The latter would mediate both mitochondrial recognition and autophagosome formation, ultimately leading to removal of damaged mitochondria. This issue will be addressed more extensively in Section 1.4.

Much of the research on autophagosome biogenesis has focused on non-selective forms of autophagy and not on mitophagy *per se*. A recent report suggests that the autophagic isolation membrane can form *de novo* on depolarized mitochondria as opposed to being recruited from elsewhere in the cytoplasm (Itakura *et al.*, 2012). Prior to LC3 recruitment, they have found that the initial stages of PARK2-mediated mitophagy feature the recruitment of autophagy protein ATG9A, and autophagy inducing kinase complex, ULK1, to damaged mitochondria (Itakura *et al.*, 2012). Further work is required to fully answer the intriguing question of whether an autophagosome produced for mitochondrial removal differs from an autophagosome produced in response to starvation.

1.3.3 Mitophagy Regulation by Mitochondrial Dynamics

Mitochondria are highly dynamic organelles that continuously change their shape through frequent fusion, fission and movement throughout the cell. These

dynamics are crucial for the life and death of the cells and they have been linked to many of the classical mitochondria-associated cellular pathways including calcium signaling, apoptosis and the cell cycle, and ultimately to neurologic disorders and metabolic diseases. Moreover, obstructing mitochondrial fusion and promoting fission appears to be a common step in mitophagy initiation (Hsu & Shi, 2016; Ni *et al.*, 2015).

1.3.3.1 Role of Mitochondrial Fission during Mitophagy

Mitochondrial fission is driven by Drp1 (Smirnova *et al.*, 2001) and regulated by OMM proteins Fis1 (James *et al.*, 2003) and Mff (Otera *et al.*, 2010) (**Figure 1.25**). Unlike Fis1 and Mff, the GTPase Drp1 is a cytoplasmic protein that localizes to sites of mitochondrial fission in a rigorously regulated manner. Drp1 activity may depend on its self-oligomerization at Mff-marked sites of division before GTP-hydrolysis occurs to drive fission (Otera *et al.*, 2013). Prior to Drp1 recruitment, future sites of mitochondrial division can also be identified by ER-tubule mediated constriction (Friedman *et al.*, 2011). Besides the role of Drp1-mediated fission in mitophagy, Drp1 plays important roles in apoptosis and cell division by regulating mitochondrial fragmentation (Otera *et al.*, 2013).

It is generally accepted that mitochondrial fission is a prerequisite for mitophagy in many mammalian cell types. As others have pointed out, it is logical for an elongated mitochondrion of over 5 μm in length to be chopped up prior to engulfment by 0.5 μm diameter autophagosomes (Gomes & Scorrano, 2011). Twig and coworkers first demonstrated that fission can generate fragmented mitochondria with a low membrane potential and reduced levels of OPA1 (Twig *et al.*, 2008) (**Figure 1.25**). These mitochondria therefore have an inherent inability to re-fuse with the healthy mitochondrial network (Youle & van der Bliek, 2012). Following their expulsion from the mitochondrial network, the mitochondria are finally removed by mitophagy. Inhibition of Drp1 mediated fission by expression of dominant negative Drp1 (K38A) was found to inhibit mitophagy (Twig *et al.*, 2008) and this agrees with more recent data demonstrating the failure of PARK2-mediated mitophagy in Drp1-/- MEFs (Tanaka *et al.*, 2010). Very recently, PINK1 has been shown to be able to signal an increased fission reaction by affecting mitochondria-associated PKA, which normally inhibits Drp1 (Pryde *et al.*, 2016).

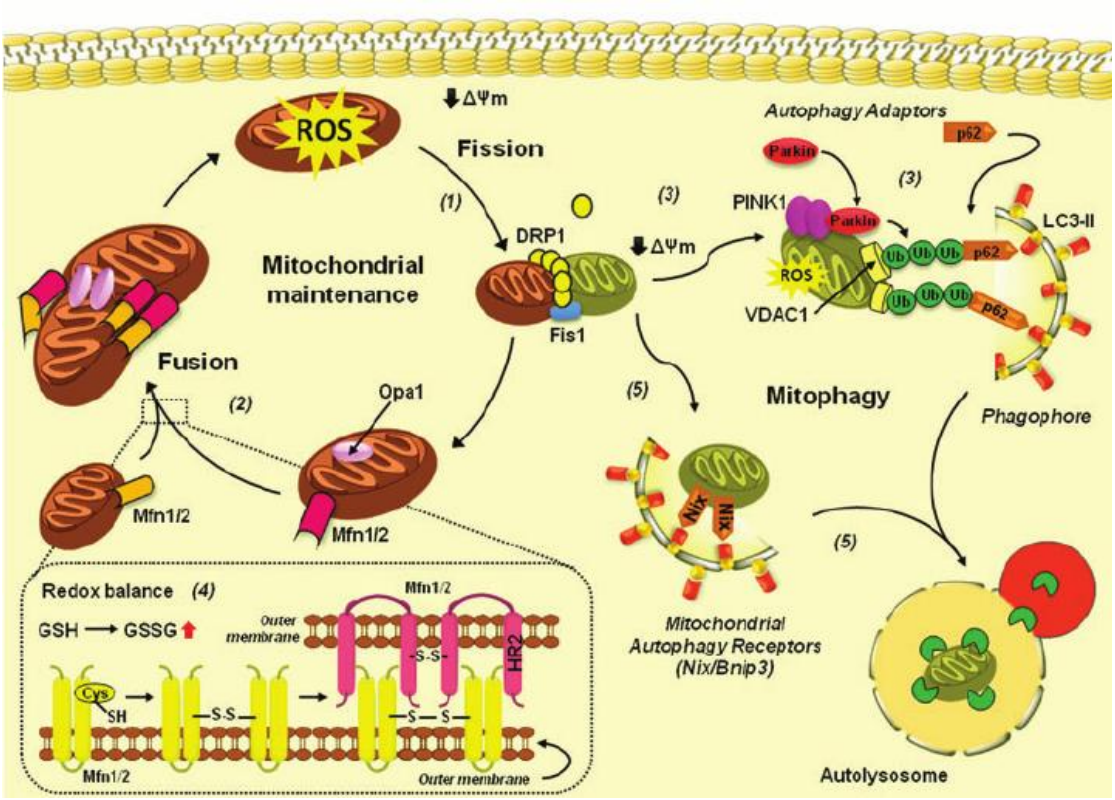

Figure 1.25. Mitochondrial fusion, fission and mitophagy. (**1**) Fission requires local organization of Fis1 and recruitment of the GTPase DRP1 for assembly of the fission machinery that subsequently leads to membrane scission. (**2**) Fusion is mediated by the dynamin GTPases Mfn1/2 at the outer membrane and OPA1 at the inner membrane that tether adjacent mitochondria together. (**3**) After fission, reduced mitochondrial membrane potential leads to the translocation of PINK1and PARK2 to the mitochondria, where it promotes the ubiquitination of proteins in the mitochondrial membrane such as VDAC1, which recruit the autophagy receptor p62 that targets mitochondria for removal. (**4**) GSSG accumulation has been demonstrated to mediate the oxidation of cysteines within Mfn1/2 causing the tethering of Mfn1/2 to enhance membrane fusion. (**5**) Nix-dependent autophagy is involved in the removal of ‘‘healthy’’ mitochondria during development. (Taken from Navarro-Yepes *et al.*, 2014).

Of course, mitochondrial fission can also be facilitated by reduced fusion capability, thus providing further opportunity for dynamic control of mitochondrial turnover. In PARK2-mediated mitophagy, PARK2 translocation to depolarized mitochondria triggers the ubiquitination of Mfns in *Drosophila* and mammalian cells (Gegg *et al.*, 2010; Rana *et al.*, 2013; Ziviani *et al.*, 2010). PARK2-mediated ubiquitination of Mfns leads to their degradation in a proteasome-dependent manner (Tanaka *et al.*, 2010), further isolating dysfunctional mitochondria from the rest of the network. Proteasomal degradation of Mfns requires assistance by VCP/p97 (Tanaka *et al.*, 2010). PARK2 ubiquitination of OMM proteins has recently been shown to promote

the recruitment of VCP to mitochondria (Kim *et al.*, 2013). Mutations in VCP cause a severe “multisystem degenerative disease” that can manifest in the form of several disorders including amyotrophic lateral sclerosis, Parkinson disease and Paget disease of bone (Abramzon *et al.*, 2012; Spina *et al.*, 2013; Watts *et al.*, 2004). Overexpression of disease-associated mutated forms of VCP prevents PARK2-mediated mitophagy in MEFs, suggesting that a blockade of the PINK1/PARK2 pathway due to VCP mutation and persistence of Mfns may contribute to the pathogenesis of the multisystem degenerative disease (Kim *et al.*, 2013).

1.3.3.2 Fusion Protects Mitochondria from Mitophagy

The mitochondrial fusion machinery consists of 3 key proteins: the OMM GTPases Mfn1 and Mfn2 (Santel & Fuller, 2001) and the IMM protein OPA1 (Misaka *et al.*, 2002) (**Figure 1.25**).

Fusion has been demonstrated via genetic studies to be required for mtDNA maintenance (Chen *et al.*, 2010) and to at least occur in conjunction with increased mitochondrial ATP production (Tondera *et al.*, 2009). Recent reports have described how during starvation mitochondria undergo fusion and are spared from mitophagy in order to maintain ATP production. Cells can therefore protect their mitochondria during starvation-induced macroautophagy by maintaining an elongated mitochondrial network (Gomes *et al.*, 2011a; Rambold *et al.*, 2011). It appears that mitochondria are protected from mitophagy during starvation by both the inhibition of fission and maintenance of fusion. Indeed mitophagy could be encouraged during starvation if fusion factors such as OPA1 or Mfn2 were depleted (Gomes *et al.*, 2011a; Rambold *et al.*, 2011) and conversely the absence of Drp1 further prevented mitochondrial turnover (Gomes *et al.*, 2011a).

Despite recent advances, there is a long way to go in order to truly understand the crosstalk between mitochondrial dynamics and mitophagy and how this impacts on disease pathology. Starvation-induced mitochondrial elongation depends on the type of nutrient starvation, indicating that tight control of mitochondrial dynamics depends on intricate signaling pathways yet to be properly defined (Gomes *et al.*, 2011b). It is also important to bear in mind that mitochondrial networks differ from cell type to cell type.

1.4 The Role of Specific Lipids in Autophagy and Mitophagy

Increasing evidence indicates that during autophagy some lipids, far from being inert structural elements of the autophagosome, autolysosome or OMM, can affect the function of specific autophagic proteins, either through specific binding interactions or via changes in the physical properties of the lipid bilayers (Chu *et al.*, 2013; Chu *et al.*, 2014; Dany & Ogretmen, 2015; Li *et al.*, 2015; Morad & Cabot, 2013; Salazar *et al.*, 2009; Sentelle *et al.*, 2012; Shatz *et al.*, 2016).

1.4.1 Cardiolipin

CL belong to a class of ancient phospholipids found in membranes of both prokaryotes and eukaryotes though at different locations: they comprise an abundant component of the bacterial plasma membrane, but are confined almost exclusively to mitochondria in eukaryotes (Daum & Vance, 1997; Schlame, 2008; Hoch, 1992). CL biosynthetic pathways are also different: they are biosynthesized from 2 molecules of PG in bacteria, but from one PG and one CDP-DAG in eukaryotes (Tian *et al.*, 2012). Molecular species of bacterial and mitochondrial CL are also different: while shorter carbon chain and saturated or monounsaturated CL species are typical of the former, longer chain polyunsaturated CL are predominant in mitochondria (Schlame, 2008).

In eukaryotes, CL is the signature glycerophospholipid of mitochondria and it is implicated in many mitochondrial functions in healthy cells, including maintenance of normal organelle ultrastructure, energy metabolism, protein import processes, and mitochondrial dynamics (Hsu & Shi, 2016; Maguire *et al.*, 2016). In addition, CL has also been implicated in the autophagic pathway of mitophagy, an issue that has been examined in this study (see Chapters 3 and 4).

The structure of CL is characterized by a glycerol backbone connected to two phosphatidyl lipids thus including four acyl chains and two negative charges of phosphate groups. This structure is more flexible than regular phospholipids because CL possesses two chiral carbons and four fatty acyl chains that are usually polyunsaturated, at least in mammals (Ardail *et al.*, 1990). If all four FA-residues are identical, CL molecules are symmetric; however, integration of at least one different FA-residue in the CL disturbs the symmetric organization of the molecule. In several tissues, such as heart, muscles or liver, symmetric CL molecules with all four FA represented by C18:2 are most common (Schlame *et al.*, 2005) (**Figure 1.26**). The

dimeric structure and polyunsaturated fatty acyl chains of CL on the mitochondrial membranes may be responsible for its ability to switch between lamellar and negative curvature profiles, and this makes CL a perfect brick with which to build the inner folded cristae (Acehan *et al.*, 2009; Schlame, 2013; Xu *et al.*, 2006).

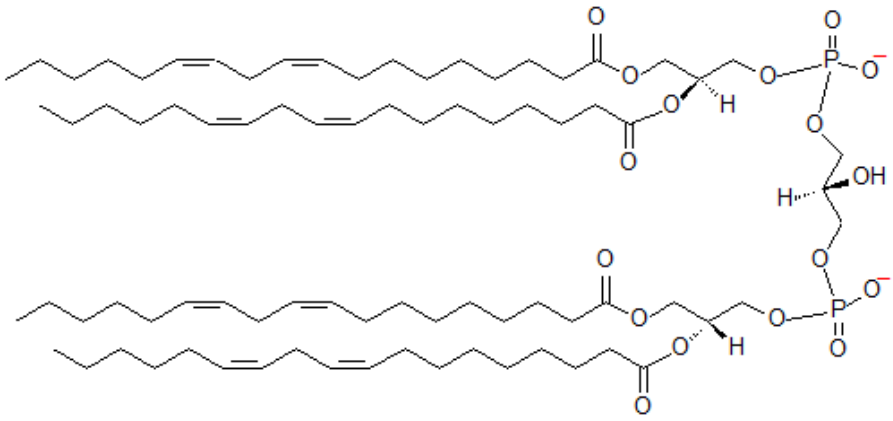

Figure 1.26. Structure of TLCL (CL 18:2). (Adapted from http://www.lipidhome.co.uk/lipids/complex/dpg/index.htm).

Mitochondrial membranes are characterized by a high content of glycerophospholipids, whereas sterols and sphingolipids are only present in low amounts (Daum & Vance, 1997). The lipid compositions of the OMM and the IMM differ significantly (de Kroon *et al.*, 1997; Zinser & Daum, 1995). Regarding the relative abundance of glycerophospholipids at the OMM and the IMM, a consensus exists for PC, PE, and PtdIns. However, the CL content on each mitochondrial membrane has been the subject of some debate. The majority of CL is synthesized from ER-derived PA along an enzymatic cascade at the matrix side of the IMM. Accumulation of CL depends on PA transfer from the ER to the inner leaflet of the IMM and the subsequent redistribution of newly synthesized CL between both membranes (Claypool & Koehler, 2012; Osman *et al.*, 2011; Tamura *et al.*, 2013). Moreover, the topography of cardiolipin synthase – the catalyst of the final stage in CL biosynthesis – is one of the major defining factors for CL asymmetry in the IMM.

Originally, CL was thought to be present almost exclusively within the IMM representing on average approximately ≈ 5% of the total lipid content of the OMM. However, it has been demonstrated that CL distribution across mitochondrial membranes is highly asymmetric and it changes dramatically upon mitochondrial injury and depolarization: a significant portion of CL are translocated to the OMM (Baile *et al.*,

2013; Gonzalvez & Gottlieb, 2007). For instance, Charleen T. Chu and colleagues found by mass spectrometry that in primary rat cortical neurons and SH-SY5Y cells treated with the electron transport chain complex I inhibitor rotenone and other promitophagy stimuli both the content and species of CL in the OMM were increased. Notably, under sublethal treatments with rotenone, that were sufficient to trigger autophagy, CL peroxidation products were not detected (Chu *et al.*, 2013; reviewed in Chu *et al.*, 2014). Moreover, autophagic machinery recognized CL more effectively than its metabolites, including mono- and dilyso-CL as well as CL oxidation products (Chu *et al.*, 2013). This implies that CL oxidation is not a requirement for removal of injured mitochondria via mitophagy (**Figure 1.27**). This seems to be at odds with the accepted opinion that oxidative stress and lipid peroxidation are inherent to mitochondrial injury and mitophagy (Kirkland *et al.*, 2002). Indeed, in pro-apoptotic mechanisms, the major specific feature of CL engagement requires not only the appearance of CL in the OMM but also its oxidative modification (Kagan *et al.*, 2005).

The preferential localization of CL in mitochondrial membranes includes not only a highly selective distribution of CL into IMM compared to OMM but also a possible enrichment of the inner versus outer leaflets of IMM with CL (Gallet *et al.*, 1997; Harb *et al.*, 1981). While some of the reactions of CL remodeling (Cao *et al.*, 2004) may be occurring in ER, thus physiologically requiring CL trans-membrane translocations (Esposti *et al.*, 2001), it is believed that in normally functioning mitochondria CL are found only in IMM whereby the inner leaflet may contain higher amounts of CL than the outer leaflet (Hovius *et al.*, 1990; Krebs *et al.*, 1979).

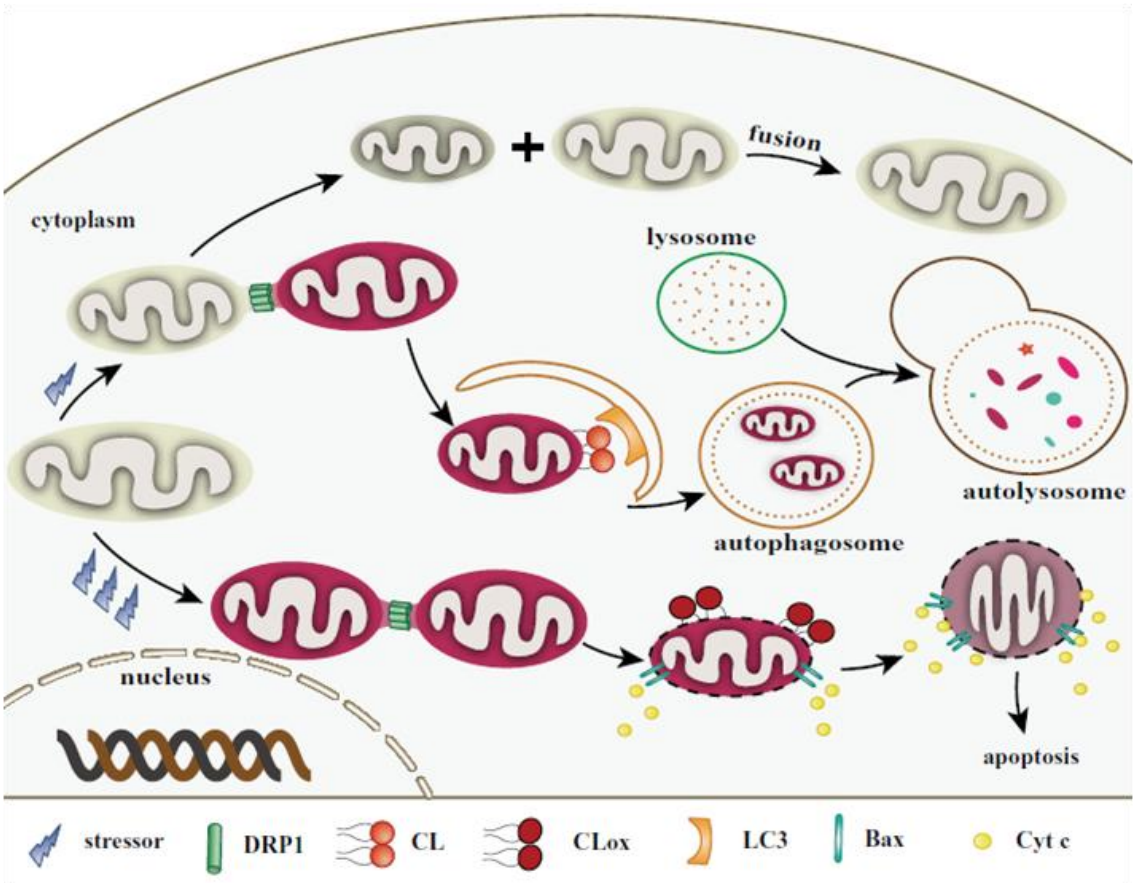

Figure 1.27. Roles of cardiolipin in mitophagy and apoptosis. (**1**) **Under low and mild stress:** DRP1 localizes to mitochondria by binding to CL. Mitochondria are divided into 2 daughter units. The one with lower membrane potential is probably degraded via mitophagy. LC3 may target damaged mitochondria by combining with CL on the OMM. The one with higher membrane potential may be repaired by fusing with a healthy mitochondrion. (**2**) **During apoptotic/high stress:** abundant ROS are produced. CL is oxidized by cytochrome c under the help of hydrogen peroxide and transfers to the OMM. Mitochondria are also divided by DRP1 and other fission-related proteins. The mitochondrial membrane pore is built via Bax oligomerization in the presence of tBID. Cyt c and other apoptotic factors then escape into the cytosol triggering a subsequent caspase cascade. (Adapted from Li *et al.*, 2015).

Externalization of CL from the inner leaflet of IMM to the surface of OMM requires at least three translocations:

(i) from the inner to the outer leaflet of IMM,

(ii) from the outer leaflet of IMM to the inner leaflet of OMM, and finally

(iii) from the inner to the outer leaflet of OMM.

PLS3, Nm23-H4, MtCK, and tBid help to reshape mitochondrial membranes by transferring CL (Kagan *et al.*, 2006; 2014). PLS3 is a mitochondrial enzyme responsible for the translocation of CL from the inner to the outer leaflet of the OMM during mitophagy and apoptosis (Chu *et al.*, 2013; Liu *et al.*, 2003; Van *et al.*, 2007). tBid, a member of the BH3-only subgroup of the pro-death proteins, targets mitochondria by combining with CL on the OMM (Kim *et al.*, 2004; Lutter *et al.*, 2000; Sorice *et al.*, 2004). PLA2 is activated by tBid, yielding MLCL and DLCL (Kagan *et al.*, 2006). It also serves as a transmembrane transporter carrying lyso-CL and CL outwards. Moreover, tBid further activates PLS3 and forms a positive feedback loop that increases the amount of CL on the OMM (He *et al.*, 2007; Kagan *et al.*, 2006; Liu *et al.*, 2008). MtCK and Nm23-H4 are both basic peripheral membrane proteins. Octameric MtCK binds to CL on the IMM and VDAC protein on the OMM, appearing as a bridge across the mitochondrial membranes (Epand *et al.*, 2007b). In addition, Nm23-H4, a mitochondrial nucleoside diphosphate kinase, can also act as a bridge, attaching simultaneously to the IMM and OMM and allowing the transfer of CL (Epand *et al.*, 2007a; Schlattner *et al.*, 2013). The main transacylase, tafazzin, may also be involved in the migration of CL. Tafazzin exists in the outer leaflet of the IMM and the inner leaflet of the OMM; thus, it can be regarded as existing in the intermembrane space. It may only replace the acyl chains of certain nonbilayer CL *in vitro* (Hsu *et al.*, 2015; Schlame *et al.*, 2012; Schlame, 2013).

As mentioned before, Chu and coworkers proposed that the OMM-localized CL acts as a mitochondrial receptor for LC3 triggering mitophagy (**Figure 1.27**). Indeed, preventing this interaction inhibited rotenone-induced mitochondrial delivery to autophagosomes and lysosomes (Chu *et al.*, 2013). This LC3-CL pathway may be different from the PINK1/PARK2 pathway upstream of the damage mechanisms, since the LC3-CL pathway shows no depolarization in mitochondria. Although it has been proposed by molecular docking that LC3 contains cardiolipin-binding sites important for the engulfment of mitochondria by the autophagic system (Chu *et al.*, 2013) the molecular basis of the LC3-CL interaction remains to be fully elucidated. In this work

quantitative biophysical and cellular techniques have been applied to examine the molecular mechanisms underlying this interaction and the possibility of CL promoting LC3B mitochondrial association by changing the physical properties of the OMM lipid bilayer has been studied, and not only via a direct and specific protein-lipid interaction. Moreover, in order to determine whether mechanisms underlying LC3B-CL interaction are protein-specific or they are the same for all Atg8 human orthologs, CL interaction with GABARAP, GABARAPL1 and GABARAPL2 has also been analyzed.

CL also interacts with other autophagy-related proteins such as DRP1 which as mentioned before plays a role in mitochondrial fission (Frank *et al.*, 2001; Smirnova *et al.*, 2001) or IRGM which affects mitochondrial depolarization and fission as well as subsequent mitophagy.

Finally, CL may also contribute to the formation of autophagosomes by associating with Beclin 1 and LC3. Interestingly, Beclin 1 preferentially interacts with membranes that are enriched in CL through an ECD (Huang *et al.*, 2012). Three aromatic amino acids on the tip of the ECD present a hydrophobic finger that may be the binding site. The ER and mitochondria provide membrane sources for the formation of the phagophore (reviewed in Ktistakis & Tooze, 2016). Since Beclin 1 has a close relationship with mitochondria, it may be the linker that uses the mitochondrial membrane to build the pre-autophagosomal structure. Mitochondrial membranes may also be available for pre-autophagosomal structure elongation, since CL shows a close connection with LC3, which itself has a role in the growth of phagophores (Füllgrabe *et al.*, 2014).

1.4.2 Ceramides

An additional class of molecules that regulate autophagy is constituted by sphingolipids, present in numerous biological membranes. Some of them play an important role in cell signaling as second messengers. A large number of sphingolipid subspecies in cells influence membrane structure, interactions with the extracellular matrix and neighboring cells, vesicular trafficking, and the formation of specialized structures such as phagosomes and autophagosomes (Grassmé *et al.*, 2007; Schenck *et al.*, 2007). Thus sphingolipids are emerging as major players in several aspects of cell physiology and in the pathology of many diseases including cancer and Alzheimer disease (Grassmé *et al.*, 2007; Schenck *et al.*, 2007). Many categories of sphingolipids have been shown to be abnormal in cancer and these can coordinate signals from the

external environment with cell division and survival pathways (Ogretmen & Hannun, 2004).

The sphingolipid metabolism is a highly dynamic process generating second messengers, including ceramide, sphingosine, and S1P (Ogretmen & Hannun, 2004; Spiegel & Milstien, 2003). Resting cells typically have very low levels of sphingolipid metabolites. Ceramide is the central molecule in sphingolipid metabolism, with roles in cell growth, cell death, proliferation, and stress response (Spiegel & Milstien, 2003).

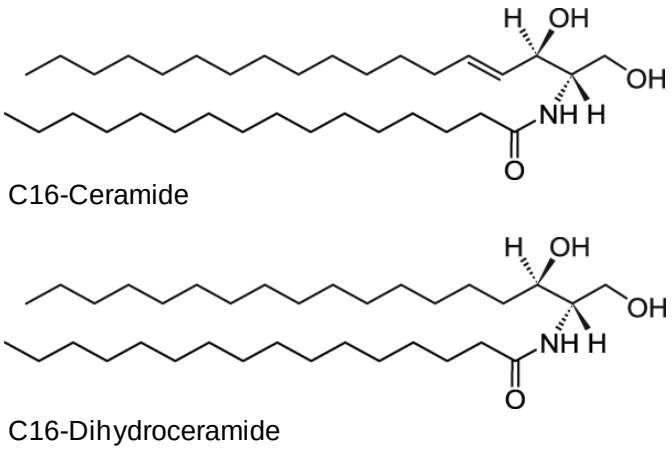

Figure 1.28. Structures of C16-ceramide and C16-dihydroceramide. (Taken from https://avantilipids.com/).

Ceramides (N-acyl sphingosines) are molecules formed by D-*erythro*-sphingosine to whose C2 amino group a fatty acid is linked through an amide bond. Most physiological ceramides have an acyl chain whose length varies between 16 and 26 carbons, and may be monounsaturated or saturated (**Figure 1.28**). Ceramides are synthesized predominantly in the endoplasmic reticulum while sphingomyelin biosynthesis occurs in the Golgi apparatus, and to a lesser extent also in the plasma membrane. These two sphingomyelin formation sites are connected by vesicular transport. They can be synthesized in 2 different ways:

(i) *de novo* synthesis, by condensation of serine and palmitoyl-CoA forming 3-oxosphinganine, finally leading to the production of dihydroceramide. Dihydroceramide as a final step is oxidized forming ceramide by the introduction of a *trans* double bond in position 4-5;

(ii) produced by the action of enzymes involved in the hydrolysis of sphingomyeline, called acid sphingomyelinases (localized in acidic compartments) and neutral sphingomyelinases (localized in the plasma membrane and mitochondria) (Goñi *et al.*, 2012).

A) Ceramides as a Second Messenger

Ceramides or their metabolic products appear to mediate effects induced by the extracellular stimuli, leading to different effects including cell proliferation, differentiation, autophagy and apoptosis.

It is now clear that agents that block cell growth induce ceramide formation, either by sphingomyelinase, activating *de novo* synthesis pathways or regulating other ceramide metabolism enzymes such as ceramidases. These inductors include TNFα, Fas ligand, interferon-γ, interleukine-1, nitric oxide, daunorubicin, radiation and HIV infection. Moreover, clear evidence suggests that ceramide plays an important role in mediating or modulating the apoptotic response and cell cycle suppression caused by those agents: (i) molecules capable of accumulating ceramide include, and probably are limited to, the majority of agents capable of inducing growth suppression or apoptosis, (ii) endogenous ceramide changes occur before the apoptosis execution phase begins (for example, before caspase activation), (iii) addition of permeable ceramide analogues induces apoptosis in several cell lines (Gangoiti *et al.*, 2010).

Identification of target molecules which appear to be controlled by ceramides reinforces the hypothesis that ceramides play an important role in signal transduction (**Figure 1.29**). It is well known that ceramides activate PP1 and PP2A, the protein phosphatases that dephosphorylate and inactivate PKCα, and dephosphorylate BCL-2 (Ruvolo *et al.*, 1999). Moreover, ceramides activate a CAPK which in turn triggers the MAPK kinases cascade (Zhang *et al.*, 1997) and regulates the cell cycle. At the same time, it is known that both ceramides and their target molecules play an important role in mitochondria and apoptosis. For example, when isolated mitochondria are treated with ceramides, inhibition of complex III of the mitochondrial respiratory chain has been observed (Gudz *et al.*, 1997). Also ceramides favor the formation of ROS both in intact mitochondria and cells (García-Ruiz *et al.*, 1997). Moreover, a mitochondrial ceramidase has been identified (El Bawab *et al.*, 2000) which strongly suggests the existence of a mitochondrial signaling pathway for ceramide metabolism which would have a significant role in the functioning of mitochondria and especially in the regulation of apoptosis.

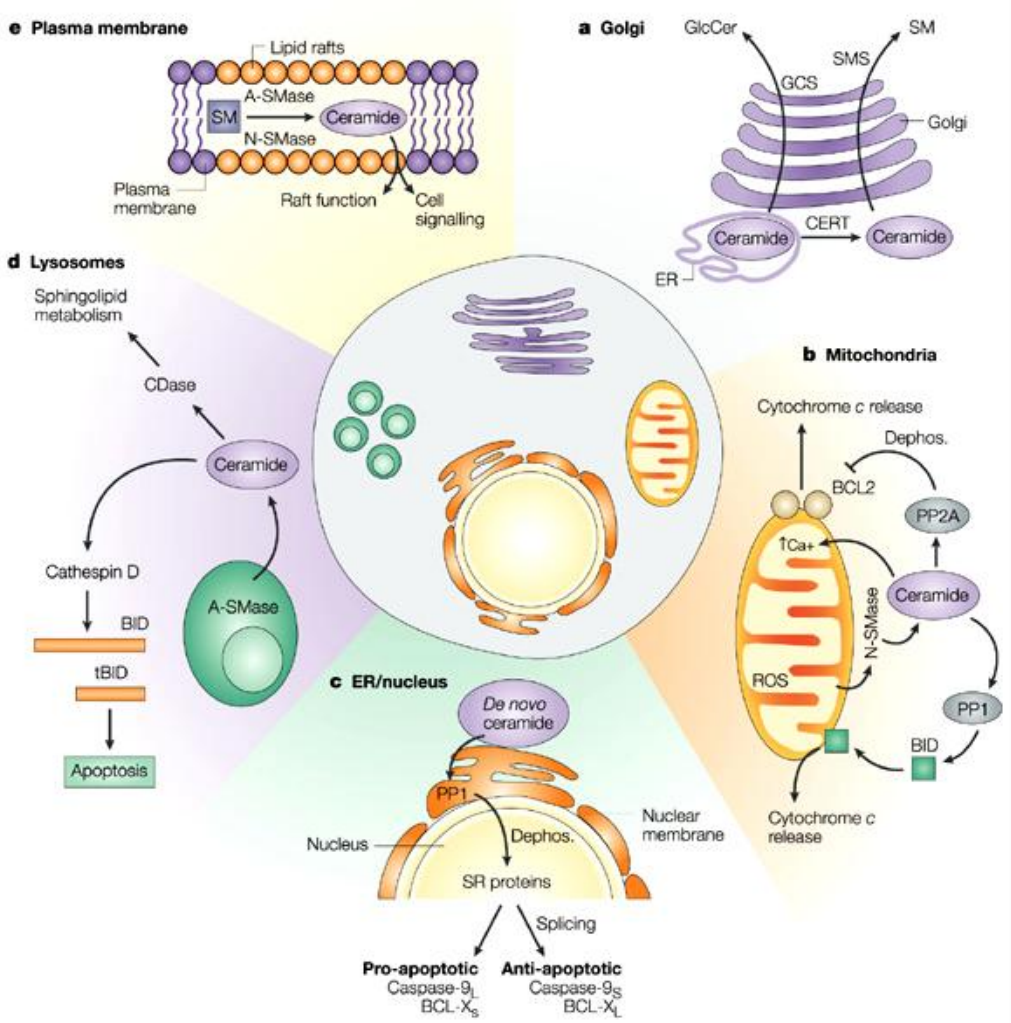

Figure 1.29. Compartmentalized pathways of ceramide signaling. *De novo*-generated ceramide in the ER is transported by CERT to the Golgi membranes (**a**) for the synthesis of SM. Ceramide can also be converted to GlcCer by the action of GCS in the Golgi, but this is not CERT-dependent. In mitochondria (**b**), ceramide is generated by N-SMase, which can be activated by ROS. Ceramide generated here can activate PP1 and PP2A. PP2A can then dephosphorylate and inactivate anti-apoptotic proteins such as BCL-2 and AKT, leading to apoptosis. PP1 also acts on the pro-apoptotic protein BID. In the ER/nucleus (**c**), *de novo*-generated ceramide can activate PP1, which leads to dephosphorylation of SR proteins that mediate the alternative splicing of BCL-X. In lysosomes (**d**), ceramide is generated by the action of A-SMase. Here, ceramide can activate cathepsin D and mediate activation of the pro-apoptotic protein BID, cleaving it to tBID and leading to activation of caspase-9 and 3, resulting in apoptosis. The generation of ceramide in the plasma membrane (**e**) can occur within specific subcompartments of the membrane known as lipid rafts. Ceramide produced here can affect specific signaling pathways generated by receptors aggregated in the rafts, such as Fas. (Taken from Ogretmen & Hannun, 2004).

Ceramide can give rise to ceramide 1-phosphate, sphingosine, and S1P. Ceramide is deacylated to yield sphingosine, which is phosphorylated by SphK to produce S1P (Spiegel & Milstien, 2003). Cells maintain a dynamic equilibrium in the levels of ceramide, sphingosine, and S1P. It is now accepted that ceramide, sphingosine, and S1P have opposing effects in cellular stress responses (Spiegel &

Milstien, 2003; Ogretmen & Hannun, 2004). As mentioned above, many cytokines, growth factors, drugs and stress result in increases in endogenous ceramide levels through *de novo* synthesis and/or the hydrolysis of sphingomyelin (Goñi *et al.*, 2012; Salazar *et al.*, 2009) and these increased ceramide levels may lead to cell growth arrest and apoptosis (Hannun & Luberto, 2000). For instance, certain anticancer drugs induce apoptosis via increasing *de novo* synthesis of ceramide (Garzotto *et al.*, 1998, 1999). Moreover many other external stimuli, particularly growth and survival factors, activate SphK, leading to an increase in S1P levels and a concomitant decrease in ceramide levels. Thus the dynamic balance between ceramide, sphingosine, and S1P is important in determining whether cells survive or die (Spiegel & Milstien, 2003). This led to the proposal of a "sphingolipid rheostat," according to which the relative amount of these antagonistic metabolites is critical in determining cell fate (Cuvillier *et al.*, 1996).

Ceramide plays not only a role in apoptosis but also participates in the autophagic cell response. In most cancer cell lines, autophagy is associated with increased levels of intracellular long-chain dihydroceramides and ceramides, although it is becoming increasingly clear that dihydroceramides are the predominant inducers of autophagy (Morad *et al.*, 2013). Moreover Corcelle-Termeau and colleagues have recently shown that sphingomyelin accumulation associated with Niemann-Pick diseases type A and B disturbs ATG9A trafficking and the maturation and closure of early autophagic membranes (Corcelle-Termeau *et al.*, 2016).

Ceramides can inhibit AKT, and this leads to the downregulation of mTOR activity and the promotion of autophagy (**Figure 1.30**). In various cancer models, dihydroceramide and ceramide trigger autophagy by eliciting cellular starvation through the downregulation of nutrient transporter proteins, which is also associated with the downregulation of mTOR activity (Pattingre *et al.*, 2009). Moreover ceramide and dihydroceramide can block mTOR activity by inhibiting PLD (Venable *et al.*, 1996), an upstream regulator of mTOR activity.

Moreover, BNIP3, an inducer of mitophagy, is a member of the BH3-only family of proteins, and ceramide-induced autophagy in malignant glioma is accompanied by the activation of BNIP3 transcription (Daido *et al.*, 2004). This in turn increases LC3 expression and disrupts Beclin 1–BCL-2 complexes (**Figure 1.30**), events that may be managed through the activation of FoXO3-mediated signaling. AMPK, another upstream regulator of mTOR, is a key energy sensor that is implicated in the induction of ceramide-moderated autophagy through phosphorylation of ATG1 (also known as

ULK1) (Peralta & Edinger, 2009). Ceramide can also promote autophagic responses by targeting VPS34 (also known as PI3KC3) complex, which leads to dissociation and hence to the activation of VPS34, the class III PI3K that mediates vesicle-trafficking processes such as endocytosis and autophagy; its activation is required for autophagy initiation (Pozuelo-Rubio, 2011).

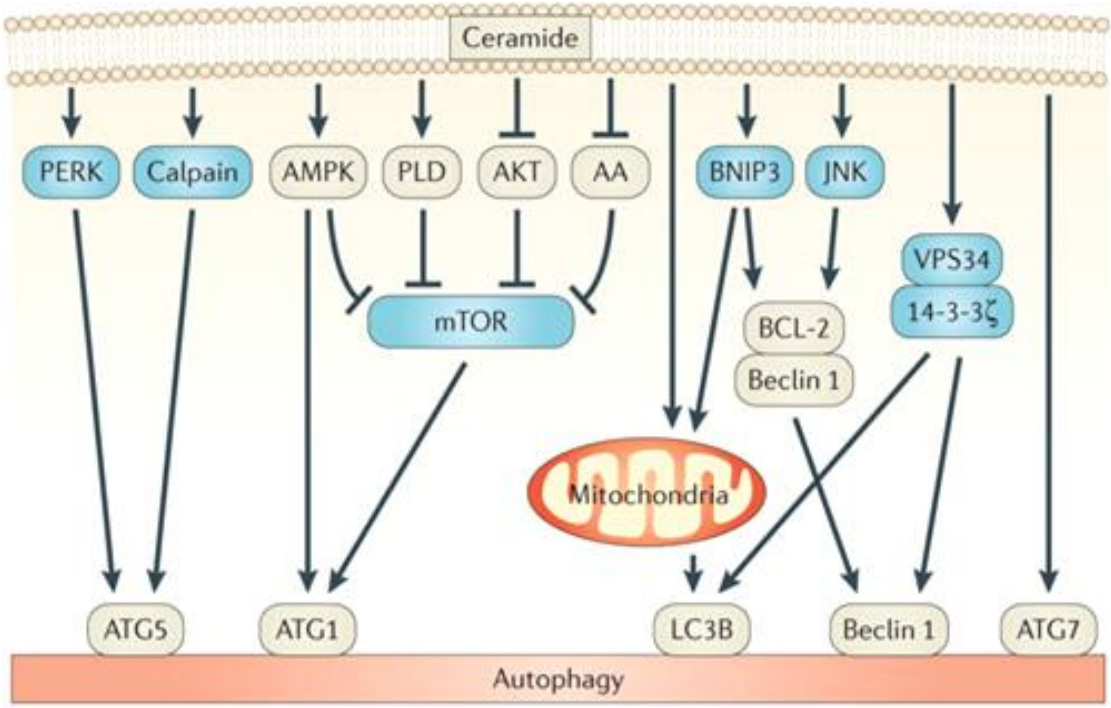

Figure 1.30. Pathways of ceramide-driven autophagic response. The major intracellular elements that are involved in ceramide-induced autophagic responses are shown. (Taken from Morad & Cabot, 2013).

Velasco's group has shown that cannabinoid administration curbs the growth of several models of tumor xenografts in rats and mice and therefore these compounds are considered a novel family of potential anticancer agents. The mechanism of cannabinoid anti-cancer action relies, at least in part, on its ability to stimulate cancer cell death (Salazar *et al.*, 2009; Patsos *et al.*, 2010). In the model proposed for the activation of autophagy-mediated cancer cell death, THC, the primary psychoactive compound of cannabis and an analogue of the natural cannabinoid anandamide, leads to the stimulation of sphingolipid synthesis *de novo* in the ER and subsequent activation of an ER stress-related signaling route. The stimulation of this pathway promotes autophagy and is indispensable for the pro-apoptotic and anti-tumoral action of THC. In order to gain understanding of those THC treatment effects, in this work the effects of the increased ceramide and dihydroceramide levels on membrane properties

have been explored. The next section will focus on the existing data regarding the behavior of ceramide in membranes.

In parallel, C18-ceramide has been recently shown to directly interact with the autophagosome-bound form of LC3 leading to lethal mitophagy (Sentelle *et al.*, 2012; Dany & Ogretmen, 2015). In this case, ceramide-induced autophagic cell-death in human cancer cells occurs via a selective autophagy process and is independent of apoptosis. LC3B ceramide binding-sites predicted by molecular modeling have been shown to be essential for this ceramide sintase1-mediated mitochondrial targeting (Sentelle *et al.*, 2012). In the context of this thesis, the novel receptor functions of both ceramide and cardiolipin anchoring LC3 to mitochondrial membranes and the specific mechanisms for this cargo recognition have been studied.

B) Ceramide Behavior in the Membrane

The presence of ceramide in the bilayer causes changes in the membrane properties (charge, fluidity, permeability). A significant effect of sphingomyelinase activity is the generation of ceramide-rich domains, which are formed due to the lateral segregation of generated ceramides. The causes of domain formation can be very diverse, although the most important one is probably the ability of ceramides (and sphingolipids in general) to form an extensive hydrogen bond network at the polar headgroup level. While glycerophospholipids can only act as hydrogen acceptors, sphingolipids (such as sphingomyelin and ceramides) may act as acceptors and also as donors through their hydroxyl and amide groups (Goñi & Alonso, 2009). The ability of ceramides to segregate laterally into ordered domains is crucial in biophysical processes and can have important physiological implications. It has been suggested that when an extracellular signal (for example Fas attached to a ligand) activates SMase at the plasma membrane, the appearance of ceramide as an enzyme end-product results in the reorganization of rafts into larger macrodomains where Fas is grouped. Receptor clustering is believed to activate downstream effectors within the cell (Goñi & Alonso, 2009).

Ceramide has also the ability to alter the permeability barrier of both model and cellular membranes. Ruiz-Argüello and coworkers were the first to observe that the generation of ceramides in the bilayer produces release of contents from both liposomes and resealed erythrocyte ghosts (Ruiz-Argüello *et al.*, 1996). Later studies found that ceramides were able to disrupt the mitochondrial membrane causing release

of cytochrome c. Two ceramide properties may be important in the membrane restructuring process that causes the release. One is the ability of ceramides to induce a negative curvature in the bilayer, that is, a curvature with a sign opposite to that normally found in cell membranes. The other is their tendency to segregate into ceramide-rich domains. The interface between ceramide-rich and -poor domains is probably the region through which the release occurs.

As mentioned above, this study focuses on the possible changes in membrane properties caused by an increase in ceramide levels that would lead to autophagic cell death. With this purpose, experiments in which ceramides and dihydroceramides are added in different proportions have been performed and their ability to destabilize the membrane has been studied.

To summarize, different mechanisms have been proposed to explain the role of ceramides in the control of autophagy: (i) autophagic cell death associated with increased levels of ceramides, (ii) ceramide-induced autophagy via activation or inhibition of different signaling molecules, and (iii) lethal mitophagy triggered by direct interaction of ceramide with LC3. However, further investigations on the interplay between sphingolipids and autophagy are required, since a better understanding of these interrelationships could lead to new strategies for controlling autophagy in neurodegeneration, infection, cancer, and other diseases.

1.5 Aims

The present work intends to obtain a better understanding of how damaged mitochondria are recognized by the autophagosomes and the molecular mechanisms involved in the process. Cardiolipin externalization to the outer mitochondrial membrane is proposed to act as a signal for LC3 during mitophagy. Ceramide is also proposed to function as a cargo receptor for LC3 during this process and to play a role during nonselective autophagic cell death. The molecular mechanisms and specific roles of these protein-lipid interactions and the effect of these lipids in membrane properties constitute the basis of our interest in both mitophagy and nonselective autophagy pathways. Quantitative biophysical approaches applying model membrane techniques, well established in our laboratory, together with cell biology techniques have been used to advance in our knowledge of these aspects.

The specific aims of this thesis are the following:

- To perform *in vitro* physical studies of the interaction of various human Atg8 orthologs with cardiolipin, and to determine the structural and functional consequences of such interactions at the membrane level.

- To investigate the role of the above interaction in mitochondrial targeting during mitophagy in different human cell lines.

- To explore membrane behavior in THC-mediated autophagic cancer cell death and to investigate the molecular mechanisms underlying the LC3B-ceramide interaction during lethal mitophagy and subsequent tumor suppression.

Chapter 2

Experimental Techniques

CHAPTER 2:

Experimental Techniques

2.1 Molecular Biology Methods

Molecular biology techniques allow us to isolate, purify and modify DNA sequences (Sambrook & MacCallum, 2001). In this work standard recombinant DNA techniques have been applied in order to clone cDNAs of several human Atg proteins into bacterial expression vectors as well as to perform mutations in their sequences for analyzing the implication of selected residues in the overall protein function.

2.1.1 DNA Amplification and Cloning

In order to clone the cDNA of interest, a DNA fragment is PCR-amplified and inserted into a self-replicating genetic element, generally a plasmid, usually called the vector. The process can be divided into: 1) PCR amplification, 2) Digestion, 3) DNA purification, 4) Ligation, 5) Transformation, 6) Extraction, and 7) Screening for positive clones (**Figure 2.1**).

1. *PCR Amplification and Purification*

cDNA of interest was PCR-amplified using a MastercyclerPro Thermocycler (Eppendorf AG, Hamburg, Germany) with PfuTurbo DNA Polymerase (Agilent Technologies, Santa Clara, CA, USA) using the indicated general PCR conditions. Forward and reverse primers, carrying the appropriate restriction sites allowing ligation in the target vectors, were synthesized by Sigma-Aldrich (St. Louis, Missouri, USA). The PCR product was subjected to purification using QIAquick Gel Extraction Kit (Qiagen, Valencia, CA, USA).

2. *Digestion*

Both PCR product and target vector were digested with the same restriction enzymes (New England Biolabs, Mississauga, Ontario, Canada or Roche, Basel, Switzerland) for 1 h at 37ºC in a 20 µL reaction. To avoid self-ligation, the vector was subjected to dephosphorylation using shrimp alkaline phosphatase (USB Corp, Cleveland, OH, USA) for 1 h at 37ºC in the reaction mix previously used for restriction enzyme digestion.

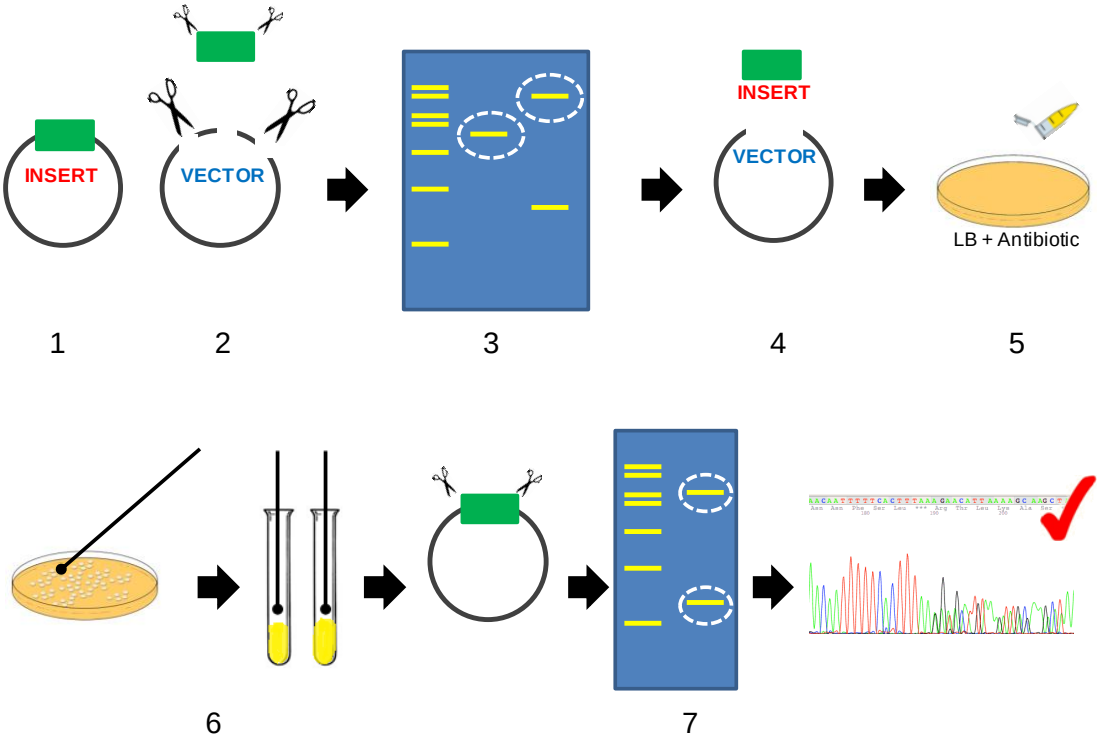

Figure 2.1. General cloning steps. (**1**) PCR amplification, (**2**) Digestion, (**3**) Purification, (**4**) Ligation, (**5**) Transformation, (**6**) DNA isolation and (**7**) Screening for positive clones.

3. *Purification of Digestion Products*

Agarose gel electrophoresis was used to isolate or purify DNA fragments produced by PCR or digestion. Gel was prepared by melting 1% agarose (w/v, Bioline, London, UK) in 1x TAE buffer (usually 1.5 g agarose in 150 mL of 1x TAE). The mixture was heated to boiling point until homogenous. This gel was left to cool down to approximately 60°C and 2.5 µL of a 10 mg/mL solution of ethidium bromide (Bio-Rad, Hercules, CA, USA) were added per 100 mL of gel, before pouring the gel in a casting tray with removable well-forming combs. The gel was left to set for 30 min at room temperature. Combs were removed and the

gel was covered with TAE buffer in a MiniPlus (HU10) horizontal electrophoresis tank (Anachem, Luton, UK).

DNA samples were diluted 4:1 (v/v) in 5x Loading Dye Solution (Thermo Fisher Scientific, Waltham, MA, USA) or 9:1 (v/v) in 10x DNA loading buffer and loaded on agarose gels in parallel with 5 µL GeneRuler 1 kb DNA ladder (Fermentas, Waltham, MA, USA) to determine the size of DNA fragments. Electrophoresis was performed at 100 volts with an EC105 power pack (Thermo Fisher Scientific) for a minimum of 25 min. DNA bands were visualized under UV light with a UV transilluminator and images were acquired with an Olympus Camedia C-5060 digital camera. For cloning, DNA bands of interest were excised to be purified. Known amounts of DNA ladders and samples were also used to visually estimate the amount of DNA in samples on gels, prior to ligation. DNA products were gel purified using the QIAquick Gel Extraction Kit (Qiagen) according to the manufacturer's instructions. This kit allows purification of DNA by taking advantage of its affinity for silica-gel-membrane columns in the presence of high concentrations of salt.

4. *Ligation*

Ligation reaction was used to insert DNA fragments of choice into linearized and dephosphorylated vectors previously cut with restriction enzymes producing compatible 5' overhanging sequences. Ligations were performed in 20 µL reactions at 16ºC overnight in the presence of 1 unit of T4 DNA ligase in 1x Ligase Buffer (Roche).

5. *Transformation of E.coli Competent Cells*

For cell transformation with ligation products, *E. coli* competent bacteria were thawed on ice and 20 µL of ligation mixture (0.5 to 1 µL of intact plasmid DNA) was added to 50 µL or 100 µL of *E. coli* DH5-α competent cells. Cells were first incubated on ice for 20 min, followed by a heat-shock reaction of 60 sec at 42ºC. The mixture was immediately transferred to an ice bucket and incubated for 5 min to allow cell recovery. Bacteria were left to recover with 1 mL LB medium in a shaking incubator at 37ºC for 45 min. Finally, cells were spun down in a benchtop centrifuge at 8,000 x g for 1 min and the pellet was resuspended in 50 µL LB, and plated on an agar plate containing the appropriate antibiotic. Only bacteria transformed with one or several copies of this vector will grow into colonies on these plates during an overnight incubation at 37ºC.

6. *Extraction of Plasmid DNA from E. coli*

Plasmid DNA (1 µg/mL) was most often extracted from *E. coli* using the small scale purification technique of the QIAprep Spin Miniprep kit (Qiagen). Bacteria from 5 mL of overnight culture were subjected to alkaline lysis followed by DNA purification according to the manufacturer's instructions. In the long term, plasmid DNA was stored at -20ºC.

7. *Screening for Positive Clones*

The plasmid vectors extracted using miniprep were screened for the presence of the insert of interest by digestion with appropriate restriction enzymes (as described in step 2) and subjected to electrophoresis. Any mutation introduced during PCR amplification was discarded by sequencing (Secugen S.L, Madrid). DNA concentration was determined by spectrophotometry measuring the A_{260} of the sample, and its purity was checked (with the A_{260}/A_{280} ratio, aiming for a ratio >1.8) in a Nanodrop^{TM} spectrophotometer (Thermo Fisher Scientific).

2.1.2 Site-directed Mutagenesis

In vitro site-directed mutagenesis is an invaluable technique for determining the contribution of individual amino acids to the structure and function of a given protein. Over the past 2 decades, highly effective simple methods for making site-directed mutations without subcloning have been developed (Fisher & Pei, 1997). In this work, Stratagene Quikchange Site-Directed Mutagenesis Kit (Agilent Technologies) has been used to perform point mutations in the proteins of interest.

The basic procedure utilizes an initial template dsDNA and 2 synthetic oligonucleotide primers containing the desired mutation (**Table 2.1**). The oligonucleotide primers, each complementary to opposite strands of the vector, are extended during temperature cycling by PCR using PfuTurbo DNA polymerase (Agilent Technologies). Incorporation of the oligonucleotide primers generates a mutated plasmid containing staggered nicks. Following temperature cycling, the product is treated with *DpnI*. The *DpnI* endonuclease (target sequence: 5´-Gm6ATC-3´) is specific for methylated and hemimethylated DNA and is used to digest the parental DNA template and to select for mutations containing synthesized DNA. The nicked vector containing the desired mutations is then used to transform DH5-α *E.coli* chemo-competent cells.

Primers		Sequence
LC3B^{R10,11A}	**Forward**	5´-GAAGGTGGCGGCCTGCTTGAA-3´
	Reverse	5´-TTCAAGCAGGCCGCCACCTTC-3´
LC3B^{Q15C}	**Forward**	5'-CGGACATCTTCTACTCTGCATTCGAAGGTGCGGCG CTGCT-3'
	Reverse	5'-CCATCTTCATCTTTCTCACACTCATACACCTCTG AGATT-3´
LC3B^{S101C}	**Forward**	5'- AGCAGCGCCGCACCTTCGAATGCAGAGTAGAAGAT GTCCG-3'
	Reverse	5'-AATCTCAGAGGTGTATGAGTGTGAGAAAGATGAA GATGG-3'
GABARAP^{R14,15A}	**Forward**	5´-CTTCTCGCCCTCAGAGGCGGCCTTCTCGAACG GATGC-3´
	Reverse	5´-GCATCCGTTCGAGAAGGCCGCCTCTGAGGGCG AGAAG-3´
GABARAP^{K47A}	**Forward**	5´-AGAAGGCACCAGGTATTTCGCTTTGTCCAGGTC-3´
	Reverse	5´-GACCTGGACAAAGCGAAATACCTGGTGCCTTCT-3´
GABARAP^{K46,47A}	**Forward**	5´-ATAGGAGACCTGGACGCAGCGAAATACCTGGT-3´
	Reverse	5´-ACCAGGTATTTCGCTGCGTCCAGGTCTCCTAT-3´
GABARAP^{K46,47,48A}	**Forward**	5´-GCACCAGGTATGCCGCTGCCTCCAG-3´
	Reverse	5´-CTGGAGGCAGCGGCATACCTGGTGC-3´
GABARAP^{S16C}	**Forward**	5´-CTCGCCCTCACAGCG GCGCTTCTC-3´
	Reverse	5´-GAGAAGCGCCGCTGTGAGGGCGAG-3´
GABARAP^{S88C}	**Forward**	5´-CCCATTGTGGCACAGGTGGGTGGAAT-3´
	Reverse	5´- ATTCCACCCACCTGTGCCACAATGGG-3´

Table 2.1. List of oligonucleotides used for site directed mutagenesis.

In the following protocol (**Protocol 1**), the general procedure used in this work to perform point mutations in LC3B and GABARAP is shown. However, for particular cases where the reaction failed, the protocol was modified by dropping the primer

concentration, increasing the template concentration, or decreasing the PCR annealing temperature.

Protocol 1. Site-directed Mutagenesis

1. Mutagenic primers are designed using Stratagene's web-based primer design program (http://www.stratagene.com/cprimerdesign.com) which designs primers with a melting temperature of at least 78ºC and centers the mutation in the middle of the sequence. All primers designed to introduce site-directed mutations were synthesized and purified by Sigma-Aldrich.
2. Mix:
    - 0.5 µL Forward primer (2.5 pmol/µL)
    - 0.5 µL Reverse primer (2.5 pmol/µL)
    - 0.5 µL Template DNA (10 ng/µL)
    - 0.5 µL 40 mM dNTP mix (10 mM each)
    - 0.5 µL Pfu Turbo Polymerase (2.5 U/µL)
    - 5 µL Polymerase buffer (5X)
    - 17.5 µL sterilized H_2O
3. PCR program:
    - 5 min 95ºC
    - Repeat 18 times
        - 30 sec 95ºC
        - 1 min 55ºC
        - 2 min 72ºC
    - 7 min 72ºC
4. *DpnI* digestion is performed by adding 0.25 µL of *DpnI* (20 U/µL) to the reaction mixture and incubating at 37ºC for 1 h.
5. After inactivation of *DpnI* (80°C for 20 min), the final reaction product is used to transform competent cells. Generally, 1 µL is added into 50 µL of DH5-α *E. coli* chemo-competent cells.
6. Finally a total of 5 colonies are selected, their DNA is amplified by miniprep (GeneJET Plasmid Miniprep Kit, Thermo Fisher Scientific) and sequenced to verify the presence of the mutation and to discard any PCR-introduced mutation (Secugen S.L.).

2.2 Recombinant Protein Expression and Purification

2.2.1 Protein Expression

LC3B, LC3B$^{G\Delta}$, GABARAPL2 and GABARAP cloned into the GST vector pGEX-6P1 (provided by Dr. I. Tanida, National Institute of Infectious Diseases, Tokyo, Japan), and their corresponding mutant forms were used to transform *E. coli* BL21 (DE3) cells. Proteins were expressed as GST-tagged fusion proteins. First, cells were picked from a *E.coli* BL21 (DE3) glycerol stock into a 100 mL flask containing LB-Amp medium, and were incubated in an orbital shaker at 37ºC overnight. The culture was escalated by adding 10 mL of the overnight saturated culture to 1 L LB-Amp medium, and the mixture was incubated at 37ºC to 0.7-0.8 OD_{600}, then 0.5 mM IPTG was added to start induction of the recombinant protein expression. Due to differences in protein expression levels and susceptibility to proteolysis, different induction and expression times were optimized for each protein (**Table 2.2**). After IPTG addition, samples were incubated in an orbital shaker for the indicated times and bacteria were collected by centrifugation (4,500 x g for 15 min, 4ºC) in a Beckman Coulter centrifuge using a JLA-9.100 rotor (Beckman Coulter, Brea, CA, USA). The supernatant was discarded and the pellet was stored at -80ºC for the purification steps.

Protein	Expression conditions
LC3B/GABARAPL2	3 h at 37ºC
GABARAP	4 h at 20ºC

Table 2.2. Conditions for expression of recombinant proteins.

2.2.2 Purification of GST-tagged Proteins

In order to start the purification procedure, cells were subjected to the disruption and lysate clearance steps. Bacterial pellets were resuspended in appropriate breaking buffer [10 mM PBS, 20 mM Tris-HCl, pH 7, 150 mM NaCl, supplemented with freshly prepared 1 mg/mL lysozyme (Sigma-Aldrich), 1 mM DTT (Sigma-Aldrich), bacterial protease inhibitors (Roche) and 2.5 µg/mL DNase (Sigma-Aldrich)]. The mixture was then incubated at 4ºC in an orbital shaker for 45 min to allow disruption of the bacterial cell wall by lysozyme. Samples were then subjected to sonication on ice (to avoid overheating) 10 sec on/10 sec off 40 cycles. After cell disruption, the resultant suspension was centrifuged at 30,000 x g for 30 min at 4ºC in a Beckman Coulter

centrifuge using JA-25-50 rotor (Beckman Coulter) to remove cellular debris. The pellet was discarded and the supernatant was filtered through 0.45 µm and 0.2 µm filters, and finally kept on ice for subsequent purification steps.

Buffer		Buffer composition
Washing buffer	**1**	PBS1x, pH 7.4 + 1 mM DTT
	2	PBS1x, 50 mM Tris-HCl, pH 8.7 + 1 mM DTT
	3	PBS1x, 50 mM Tris-HCl, pH 8.7, 500 mM NaCl + 1 mM DTT
PreScission buffer		50 mM Tris-HCl, pH 7.5, 150 mM NaCl, 1 mM EDTA + 1 mM DTT

Table 2.3. Buffer solutions used in GST-tagged protein purification.

GST-tagged LC3B, GABARAPL2 and GABARAP were purified by affinity chromatography using glutathione Sepharose 4B beads (GE Healthcare, Buckinghamshire, UK). For each 4 L bacterial culture, 1 mL beads was required. Beads were first washed 3 times with 10 bed volumes of distilled water and then 5 times with lysis buffer by centrifugation. The bacterial supernatant was mixed with washed beads and the mixture was incubated for 3 h in an orbital rotator at 4ºC to allow binding of GST to glutathione. The beads with bound proteins were packed in a gravity flow column (Bio-Rad), and the FT was removed. After that the column was washed with 10 bed volumes of each buffer described in **Table 2.3**. Then, 50 µL (stock: 2,000 units/mL) PreScission protease (GE Healthcare) were added in a 2-bed volume of PreScission buffer freshly prepared with 1 mM DTT. The mixture was transferred to a 15 mL Falcon tube and incubated for 4 h in an orbital rotator at 4ºC to allow efficient protease cleavage. The cleaved protein was eluted from the gravity flow column with PreScission buffer and 2 fractions of 4 mL were collected. After that another 4 mL PreScission buffer were added and the column containing the beads was stored overnight at 4ºC. Then, 2 more 4 mL fractions were eluted and subjected to SDS-PAGE analysis and Coomassie Blue-staining. Protein enriched fractions were concentrated as required and stored in 20% glycerol at -80°C. All proteins were purified from soluble fractions of bacterial extracts obtained in the absence of detergents, and were >90% pure.

2.3 Membrane Lipid Model Systems

The complexity of biological membranes, both from the structural and functional standpoint, presents numerous difficulties for their study. Therefore numerous model membrane systems have been developed for studying the properties of pure lipids, lipid mixtures, and reconstituted lipid-protein systems. A variety of model membrane systems is required as no single system is suitable for all the techniques used in their study. These model systems can be grouped as (1) monolayers, (2) planar bilayers, and (3) liposomes or vesicles (Gennis, 1989). In the present work two of them have been used: (i) lipid vesicles or liposomes, and (ii) lipid monolayers. A detailed explanation of their principal applications and their preparation procedures is given.

2.3.1 Lipid Vesicles (Liposomes)

A liposome is a lipid structure in a bilayer configuration enclosing an aqueous solution. Liposomes are spontaneously generated when dispersing cylindrically-shaped lipids in aqueous solutions, thus they constitute a convenient source of lipidic model membranes. Depending on the treatment, liposomes can be prepared to have a single or several bilayers or lamellae, unilamellar vesicles being the main system used in this work (**Figure 2.2**). Research with both kinds of vesicles and various biophysical techniques provides essential information for our understanding of most membrane processes.

Liposomes have been extensively used for measuring fusion, fission, solubilization, leakage, lipid flip-flop, lipid-protein binding, protein-protein binding and many more events. An interesting application is the use of liposomes for drug administration in medical treatments. By enclosing drug molecules within liposomes, side effects can be reduced and a more specific and gradual drug release within the target area can be achieved (Gregoriadis, 1978; Gregoriadis, 2008). Nowadays, liposomes as drug carriers are largely been tested in anticancer therapies (see Allen & Cullis, 2013; Noble *et al.*, 2014 and Yingchoncharoen *et al.*, 2016 for recent reviews on the methodology and liposome applications in cancer treatment).

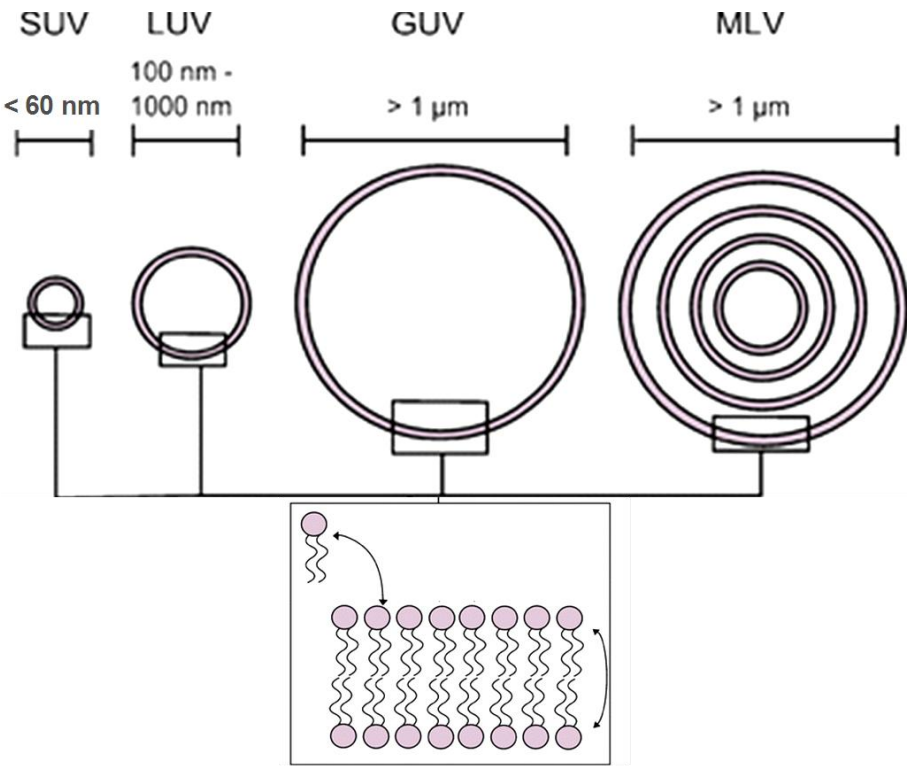

Figure 2.2. Outline of the phospholipid organization in vesicles of various sizes (SUV, LUV, GUV and MLV). Not drawn to scale.

2.3.2 Multilamellar Vesicles (MLVs)

In the early 60's, the British haematologist Alec Bangham and collaborators characterized the first known liposomes in Cambridge by looking at lecithin dispersions under electron microscopy (Bangham & Horne, 1964). As he pointed out, some "spherulites" containing concentric lamellae were formed. Vesicles were formed either by hand-shaking or by sonication, the latter inducing the formation of vesicles with fewer lamellae. These vesicles are nowadays commonly known as MLVs and mostly used in lipid biophysical studies for the characterization of lipid phases either by DSC, NMR or X-ray diffraction techniques. After lipid hydration and sample shaking, MLVs are spontaneously formed, containing usually 7-10 concentric bilayers, each of them separated by a thin water layer. Vesicles are heterogeneous in size, ranging from 100 to 5000 nm (**Figure 2.2**).

MLV generation is the simplest and fastest of all liposome formation methods. A detailed protocol for multilamellar vesicle preparation used in the present work is described (**Protocol 2**).

Protocol 2. MLVs

1. Pure lipid stocks are prepared by dissolving lipids in powder in chloroform/methanol (2:1 v/v) to the desired concentration.
2. The desired amount of lipid is pipetted from the stock in organic solution into a glass test tube.
3. The organic solvent is evaporated under a nitrogen gas flow.
4. To completely remove any traces of organic solvent, the sample is placed into a high vacuum desiccator for 2 h to obtain a solvent-free dried lipid film at the bottom of the test tube.
5. Finally the lipid is hydrated by pipetting the desired amount of an aqueous solution at a temperature above the lipid main phase transition temperature and the suspension is shaken by vigourous vortexing for lipid detachment from the bottom of the test tube. By increasing temperature, the lipid is hydrated faster and, when preparing vesicles with a mixture of lipids, a more homogeneous lipid composition through the vesicles can be expected by maintaining every lipid in the fluid phase state. This method is often enough for MLV preparation.

2.3.3 Large Unilamellar Vesicles (LUVs)

MLVs are easy and fast to prepare, but they have an important drawback. When treating vesicles with a solubilising agent, or when looking at a protein effect upon binding to the vesicle, only the effects of interaction with lipids on the external bilayer can be achieved, thus making difficult data analysis and interpretation. To overcome this issue, unilamellar vesicles are generally used (**Figure 2.2**). Unilamellar vesicles are classified according to their size, those with an average diameter of less than 60 nm being named SUVs, those with an average diameter between 100 and 500 nm are LUVs and those with larger, micrometer-ranged diameters, are GUVs. Apart from their size, they differ from each other in the method of preparation.

Large unilamellar vesicles present, in contrast to small vesicles, low curvature stress and so, when preparing LUVs containing a mixture of lipid species, a homogeneous lipid distribution through both monolayers in stable lipid vesicles is

generally obtained. In this way, LUVs represent a very good model system for most studies. LUVs are generally prepared by mechanical extrusion of MLV suspensions through polycarbonate porous filters of the desired pore size (Mayer *et al.*, 1986). A detailed protocol (**Protocol 3**) follows:

Protocol 3. LUVs

1. Steps 1-5 of MLV preparation protocol (**Protocol 2**).
2. The MLV solution is subjected to 10 freeze/thaw cycles in order to reduce the number of lamellae in the vesicles. This is obtained as a result of placing the vesicles in liquid nitrogen for 1 min, then placing these vesicles for 3 min in a water bath at a temperature above that of the lipid with the highest main transition temperature. Finally the suspension is vortexed before starting the next cycle.
3. Vesicles are extruded [LIPEX Liposome Extrusion System (Transferra Nanosciences, Burnaby, Canada)] 10 times through polycarbonate filters of the desired diameter (usually between 0.1 and 0.4 μm), using a high-pressure extruder (nitrogen gas flow). The extruder can be connected to a water bath in order to maintain the vesicles at a high temperature if necessary.
4. The concentration of the vesicle suspension is assayed using the Fiske-Subbarow method (**Protocol 6**), because some lipid can be lost in the process.
5. Finally vesicle size is checked using DLS (see Section 2.3.7).

2.3.4 Small Unilamellar Vesicles (SUVs)

Due to their small diameter (smaller than 60 nm) SUVs present a high curvature stress, which induces a lipid enrichment in the external monolayer as compared to the inner one (Szoka & Papahadjopoulos, 1980). Their curvature stress makes these vesicles good model membranes for the study of e.g. membrane fusion (Nieva *et al.*, 1989), because they may be subjected to such stress conditions *in vivo*. Small unilamellar vesicles are usually prepared by sonication of MLV suspensions. This is basically done either by bath sonication or probe tip sonication, in the latter case probes are immersed in the MLV suspension for sonication. In this way, large MLVs

are broken down into small unilamellar vesicles. In the present work, small unilamellar vesicles have been prepared by probe tip sonication (MSE Soniprep 150, MSE, Crawley, UK). Thus, the protocol for SUVs generation is that of the MLVs but with final sonication of the vesicles for 20 min (10 sec on/ 10 sec off) on ice. Finally, SUVs preparation is centrifuged at 14,500 rpm, 10 min to remove aggregates and traces of the sonicator tip. SUVs generation can be directly observed as the vesicle solution becomes transparent.

2.3.5 Giant Unilamellar Vesicles (GUVs)

Giant unilamellar vesicles are nowadays one of the most promising model systems in the study of membrane heterogeneity. Their size, in the order of 5 to 100 micrometers as prepared by electroformation, i.e. comparable to a cell, allows performing direct microscopy on individual vesicles. The generation of giant vesicles was first described in 1969 by John P. Reeves and Robert M. Dowben exposing dry lipid films to aqueous solutions at temperatures above those of the lipid main phase transition temperature for 24 hours (Reeves & Dowben, 1969). Giant vesicles were spontaneously generated but with very low total lipid yield and a very heterogeneous size distribution.

In 1986, Miglena I. Angelova and Dimiter S. Dimitrov developed a new method for the generation of giant vesicles based on the exposure of dry lipid films to an aqueous solution under electric fields, which is the most generally applied procedure in the present (Angelova & Dimitrov, 1986; Angelova *et al.*, 1992) (**Figure 2.3**). As in the initial procedure, the aqueous solution is kept at temperatures higher than that of the lipid with the highest main phase transition, but the method is much faster and a higher amount of homogeneous size vesicles can be obtained. Vesicle generation under electric fields is strongly dependent on the lipid composition, aqueous solution ionic strength and pH, and on the electric voltage and frequency conditions (Bagatolli, 2003). In particular, only very low ionic strengths can be used in the buffers to prepare GUVs under this procedure. However, the approach has considerably evolved and nowadays even the generation of giant vesicles from cell membranes in physiological salt solutions is possible (Montes *et al.*, 2007).

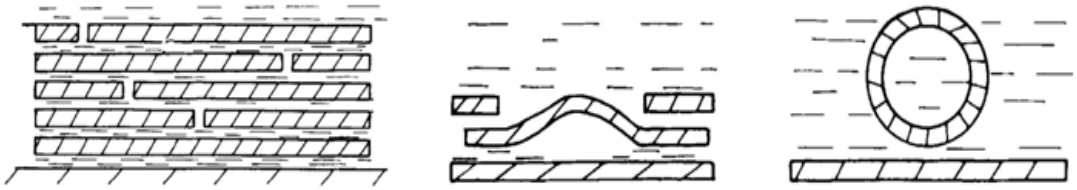

Figure 2.3 Outline of GUV electroformation. The electric field makes the lipid films (**A**) to grow/fuse (**B**) and detach (**C**) yielding GUV. (Adapted from Angelova & Dimitrov, 1986).

Regarding the present work, an important application for giant vesicles is the study of lipid lateral segregation by direct confocal microscopy of individual vesicles. With this aim 2 vesicle generation procedures have been applied to obtain: (i) giant vesicles in suspension, and (ii) giant vesicles attached to a platinum wire for direct microscopy measurements. A general overview for both procedures is given. For a detailed specification on buffer, electric field or microscopy conditions in a particular assay see Materials & Methods in the corresponding chapter.

2.3.5.1 GUVs in Suspension

GUVs in suspension are formed and subsequently translated to visualization chambers (**Protocol 4**). To enable their visualization, a high density sucrose solution is encapsulated in vesicles so that when transferred to chambers with an isosmotic solution, they sediment at the bottom of the chamber and can be imaged.

Protocol 4. GUVs in Suspension

1. Pure lipid stocks are prepared by diluting commercially available lipids in chloroform/methanol (2:1 v/v) to a 2 mM concentration. The desired percentage of a fluorescent dye (approximately 0.5%) is added to the lipid stock to allow the visualization of vesicles in a confocal fluorescence microscope.

(The protocol continues on the next page)

2. 4 µL of the appropriate stock solution are added onto the surface of different platinum electrodes in a specially designed chamber (Industrias Técnicas ITC, Bilbao) containing 4 holes with 2 platinum electrodes each.
3. The chamber is introduced into a high vacuum desiccator for 2 h to remove any remaining solvent traces and is then equilibrated for 15 min at the desired temperature by an incorporated water bath.
4. Next, the platinum wires are covered with a 300 mM sucrose solution previously equilibrated at the desired temperature.
5. The chamber holes are covered with a glass held in place with vacuum grease to avoid evaporation during electroformation.
6. The platinum electrodes are connected to a generator and the desired electric field (870 mV) is applied for approximately 2 h. Vesicles are then generated enclosing sucrose. Temperature during preparation is always higher than that of the lipid with the highest main phase transition temperature.
7. The applied frequency (10 Hz) is decreased for 1 h 30 min to induce vesicle detachment from the electrodes.
8. The electric field and water bath are disconnected and the vesicles left 30 min for equilibration.
9. The vesicle suspension is then transferred to microscopy chambers, which have been pre-treated with BSA (10 mg/mL) and contain an isosmotic aqueous solution or buffer without sucrose. In this way, vesicles sediment due to the higher density of the enclosed sucrose, and this allows direct fluorescent confocal microscopy measurements to be performed.

2.3.5.2 GUVs Attached to a Wire

GUVs for direct microscopy measurements are formed in home-made chambers and remain attached to a platinum wire where they are formed (**Figure 2.4**). The chamber is directly placed under the microscope.

The procedure for the generation of GUVs attached to a platinum wire is very

similar to that for giant vesicles in suspension but with 2 main variants: (i) a special chamber for direct microscopy supplied by Luis A. Bagatolli (Odense, Denmark) has been used for this purpose, and (ii) vesicles are prepared in the desired aqueous or buffer solution, and there is no need for sucrose to be encapsulated (**Protocol 5**).

Figure 2.4. Homemade chamber and PTFE circular wells for the formation of GUVs attached to a platinum wire.

Protocol 5. GUVs Attached to a Wire

1. Pure lipid stocks are prepared by diluting commercially available lipids in chloroform/methanol (2:1 v/v) to a 0.2 mM concentration. The desired percentage of a fluorescent dye (approximately 0.3%) is added to the lipid stock to allow the direct visualization of vesicles in a confocal fluorescence microscope.
2. 5 µL of the appropriate stock solution are added onto the surface of different platinum electrodes attached to specially designed PTFE circular wells.
3. The round units containing the wires are introduced into a high vacuum desiccator for 2 h to remove any remaining solvent traces.
4. Then, the units are fitted into specific holes within a specially designed home-made chamber (**Figure 2.4**) to which a glass cover slide has been previously attached with epoxy glue. Once fitted, the platinum wires stay in direct contact with the glass cover slide.

(The protocol continues on the next page)

5. The chamber is then equilibrated to the desired temperature for 15 min by an incorporated water bath.
6. Then the platinum wires are covered with the buffer solution, previously equilibrated at the desired temperature, and closed with tightly fitting caps to avoid evaporation during electroformation.
7. The chamber is connected to a generator (TG330 function generator, Thurlby Thandar instruments, Huntington, UK) through the platinum electrodes and the desired electric field is applied for 2 h following a detailed protocol of voltage and frequencies e.g: 6 min 0.08 V/ 20 min 1.0 V/ 90 min 3.0 V.
8. After this step, the electric field and water bath are disconnected and vesicles are left to equilibrate for 30 min.
9. The chamber is finally moved to the microscope and direct confocal fluorescence microscopy is performed on vesicles attached to the platinum wire.

2.3.6 Lipid Monolayers

Another model system for the study of lipid-lipid and/or lipid-protein interactions consists of monomolecular films at the air-water interface, the so-called lipid monolayers. An important advantage of this system compared to vesicles is that neither curvature nor heterogeneity effects are present, and furthermore there is a complete control of the surface pressure, lipid composition and molecular packing at any time. Its main detriment is the uncertainty of applying data from lipid monolayers to biological membrane bilayers. However, very precise information about lipid-lipid interaction behaviour can be obtained, a virtually impossible task using *in vivo* measurements in cell cultures.

A monolayer is generated by spreading a lipid solution, previously prepared by diluting lipids in highly volatile organic solutions such as pure chloroform or chloroform/methanol mixtures, on top of an aqueous solution. Due to their amphipathic nature, lipids self-organize with their hydrophilic headgroups in contact with the water environment and their acyl chains towards the air. Once generated, different

measurements within the monolayer are performed based on the accurate control of its surface pressure by the use of a Langmuir balance. This is commonly done by the Wilhelmy method, using a suspended probe located at the air-water interface that measures any deviation from water surface tension, e.g. those induced by the presence of the lipid monolayer (**Figure 2.5**).

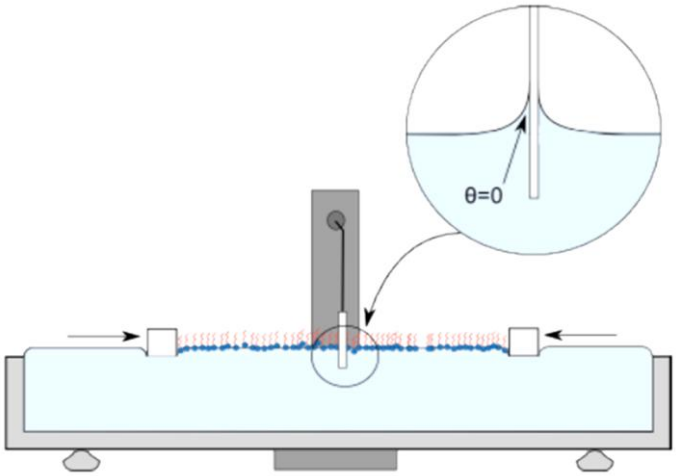

Figure 2.5. A lipid monolayer at the air-water interface of a Langmuir trough. Zoomed area: contact angle on the Wilhelmy plate at the interface. (Taken from NIMA Technology, Coventry, UK).

A special section in the current chapter (Section 2.7.2) has been introduced for a detailed overview of Langmuir balance-based approaches on lipid monolayers, applications and their methodological aspects.

2.3.7 Vesicle Size Measurement by Dynamic Light Scattering (DLS)

Vesicle size measurements were performed using the QELS technique, commonly known as DLS that is related to the Brownian motion of particles in solution. By the use of a laser beam focused within a small area in the solution, a measurement of the intensity fluctuations from the scattered light of sample particles crossing through the focused area is performed. The particles, vesicles in our case, scatter the light and this is recorded and related to the R_h of the vesicle by the Stokes-Einstein equation:

$$D = k_B T/6\pi\rho R_h$$

Equation 1. Stokes-Einstein equation.

where: D is the diffusion coefficient, k_B is the Boltzmann constant = 1.38 x 10^{-23} m^2 kg

s^{-2} K^{-1}, T is temperature, ρ is viscosity of the medium and R_h is the hydrodynamic radius of spherical particles.

The scattered light provides a correlation function from which, by the use of several algorithms, a vesicle size distribution in solution can be obtained (**Figure 2.6**). This value is accompanied by a PDI, which gives information on the size heterogeneity of the sample. The PDI varies between 0 and 1, where values close to zero indicate homogeneous monodisperse solutions.

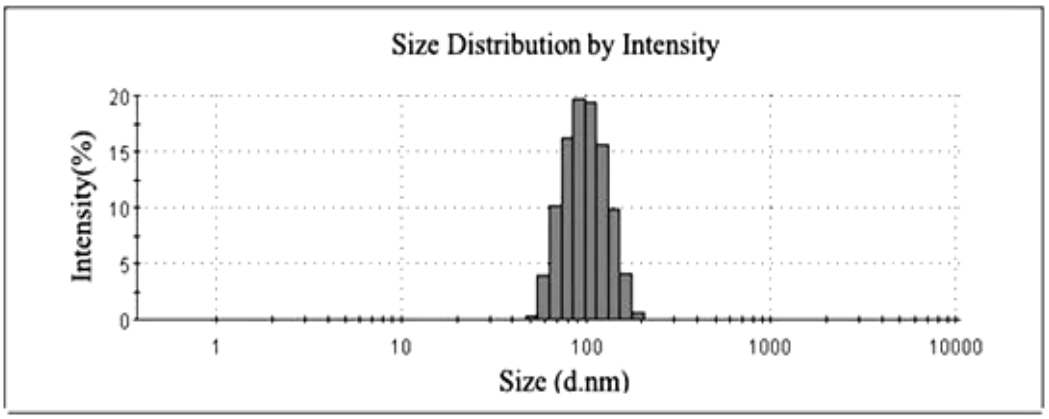

Figure 2.6. Size distribution plot of an egg PC vesicle population prepared using 100 nm polycarbonate filters.

Measurements in this thesis have been performed in a Malvern Zeta-Sizer Nano ZS (Malvern Instruments, Worcestershire, UK) with a detection range for sizes between 0.6 nm to 6 μm. 60 μL of the sample (around 0.4 mM in lipid) was placed in standard acryl cuvettes at room temperature with a He-Ne laser beam of 5 mW (λ = 633 nm) as the light source. The light scattered by the vesicles was detected with a photomultiplier placed at 173º to the beam and the results were analyzed by the commercial software of the instrument.

2.4 Phospholipid Assay (Fiske-Subbarow Method)

A well-established method has been applied for phospholipid assay based on the quantitation of inorganic phosphorus, an approach based on the initial procedure developed in 1925 by Cyrus H. Fiske and Yellapragada SubbaRow (Fiske & Subbarow, 1925) and later modified (Bartlett, 1959 and Böttcher *et al.*, 1961). Briefly, the approach consists of hydrolyzing the phospholipids until the lipid phosphate group is free to

interact with specific reagents that will color the solution in a concentration-dependent manner (**Protocol 6**).

Protocol 6. Phospholipid Assay (Fiske-Subbarow Method)

1. A phosphorus calibration curve must be set up from which the exact lipid sample concentration will be determined. 0, 25, 50, 75 and 100 nmol phosphorus are respectively pipetted into duplicate separate test tubes from a 1 mM NaH_2PO_4 standard solution.
2. The sample is pipetted into separate tubes (at least triplicate) to contain theoretically about 50 nmol lipid phosphorus, which will be in the centre of the calibration curve. When measuring volumes in organic solution, Hamilton syringes are used.
3. To each tube, 500 µL of 60% perchloric acid ($HClO_4$) are pipetted. The tubes are vigourously vortexed and introduced into a heating block at 205ºC for 45 min. In this way phospholipid hydrolysis is achieved yielding free inorganic phosphate.
4. Tubes are collected, cooled down to room temperature and the following solutions are pipetted:
   - 4 mL 1X ammonium heptamolybdate solution $[(NH_4)_6Mo_7O_{24}.4H_2O]$.
   - 500 µL 10% (v/v) ascorbic acid (added while vortexing).

   The inorganic phosphate reacts with molybdate, which subsequently reacts with the ascorbic acid giving a yellow-colored solution.
5. The tubes are introduced into a boiling water bath and left for 6 min. During that period, the solution color is blue-shifted depending on the amount of phosphorus.
6. Finally, tubes are cooled in water and absorbance at 812 nm measured for each of the samples. In the present work a Ultrospec 500 pro spectrophotometer from Amersham Biosciences (Piscataway, NJ, USA) was used for this purpose.
7. To obtain the sample phospholipid concentration, the standard absorbance is plotted against the phosphorus concentration and adjusted to a straight line. The slope of the curve and the sample absorbance are used to find out the sample concentration.

2.5 Differential Scanning Calorimetry (DSC)

DSC is a powerful technique for the measurement of lipid phase transitions. It is based on heat changes upon controlled temperature increase between 2 cells in an adiabatic chamber. In this way, the thermodynamic parameters for thermotropic phase transitions can be determined. DSC is often used for measuring lipid physical properties. In addition, protein denaturalization, protein-ligand binding and/or protein conformational changes can be studied as well. The present work will take advantage of this technique to assay lipid phase transitions that could give us important information on the generation of lipid domains.

In the 2 cells a reference (usually assay buffer solution) and lipids in the form of MLV are respectively introduced at the same volume (the solutions are always carefully degassed). The cells are then closed and driven to a high constant pressure to avoid liquid boiling and bubble generation. Both cells contain a Peltier system for heating and cooling the samples at controlled temperature rates, and are connected by a system that measures the temperature difference between both cells. Upon heating, cell temperature is equally increased until the sample undergoes a physical transformation releasing or absorbing energy, resulting in a change in the sample cell temperature with respect to that of the reference cell. At this point, and in order to maintain the same temperature in both cells, the system gives or removes heat from the sample cell, depending on the physical change being endothermic or exothermic respectively. This parameter is given by the calorimeter as heat capacity (c_p) in units of energy x temperature^{-1}. In this case, heat is the form of energy. In the context of this thesis, lipid phase transitions are endothermic and are usually normalized with the lipid molar concentration, resulting in c_p usually given in kcal/molºC or in kJ/molºC if thermal energy is expressed in joules.

The resulting scan of a sample is called thermogram, a plot of c_p vs. temperature. Lipid phase transitions typically display a peak on the thermogram, from which three main parameters can be obtained: Tm, $\Delta T_{1/2}$ and ΔH. Tm is usually given at the maximum of the transition, i.e. the centre for symmetric transitions. $\Delta T_{1/2}$ is the transition width in ºC at the middle of the transition height, and gives information on the transition cooperativity or molecular cooperativity between lipid molecules, phase transitions with high cooperativity showing lower $\Delta T_{1/2}$. ΔH measures the amount of heat required to complete the phase transition, and is obtained by integration of c_p along the temperatures of the phase transition. **Figure 2.7** represents a typical endotherm for sphingomyelin with the respective thermodynamic parameters.

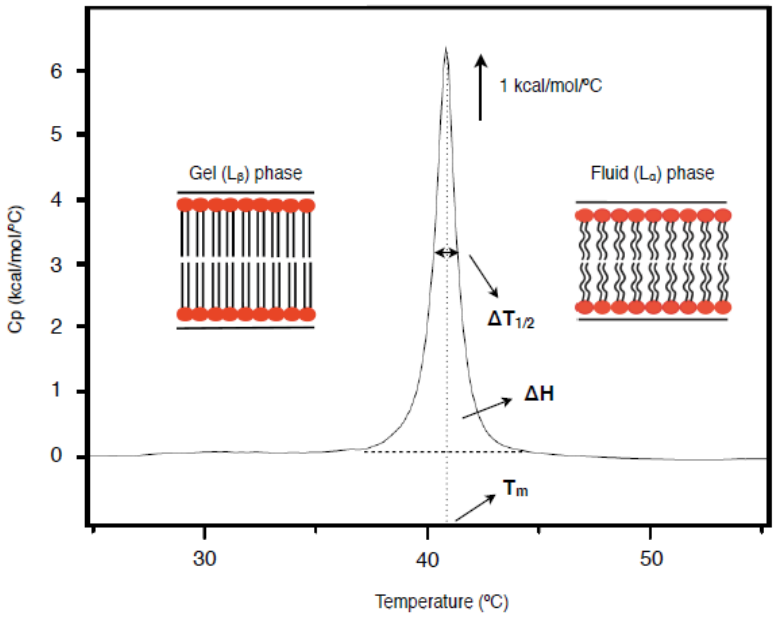

Figure 2.7. DSC thermogram of pure pSM. The endothermic main phase transition and its associated thermodynamic parameters are shown.

For lipid mixtures, commonly measured phase transitions under DSC are the L_β-L_α and the L_α-H_{II} phase transitions. A brief protocol for sample preparation, scan performance and data treatment is given (**Protocol 7**).

Protocol 7. Differential Scanning Calorimetry of MLVs

1. Previously degassed (at least 30 min) assay buffer solutions: 20 mM PIPES, 150 mM NaCl, 1 mM EDTA (pH 7.4) are introduced into both reference and sample cells of the calorimeter. In this work, a VP-DSC high-sensitivity scanning microcalorimeter (MicroCal, Northampton, MA, USA) was used.
2. A heating scan is performed, to obtain the buffer reference thermogram at the same conditions as for the sample.
3. Once the thermogram is finished, the buffer solution from the sample cell is replaced by the lipid sample in the form of MLV in the same buffer, carefully degassed.

(The protocol continues on the next page)

4. Then at least three heating scans are performed until a constant signal is obtained, in order to determine the specific thermodynamic parameters.
5. The sample is then collected and its concentration determined as lipid phosphorus.
6. For data treatment [performed under the software ORIGIN 7.0 (MicroCal) provided with the calorimeter], the reference buffer thermogram is subtracted from the sample third scan, and the resulting thermogram baseline is adjusted. Sample concentration is normalised and the specific parameters determined.

2.6 Protein Analysis

2.6.1 Protein Concentration Measurements

Protein concentration was quantified using either the BCA protein assay (Thermo Fisher Scientific) or absorbance measurements at 280 nm.

2.6.1.1 Bis-cinchoninic Acid (BCA) Assay

The reaction that leads to BCA color formation is strongly influenced by four amino acid residues (cysteine or cystine, tyrosine, and tryptophan) in the amino acid sequence of the protein. However, the universal peptide backbone also contributes to color formation, helping to minimize variability caused by protein compositional differences. In the first step, known as the biuret reaction, the chelation of copper with protein in an alkaline environment takes place to form a light blue complex. In the second step, BCA reacts with the reduced (cuprous) cation that was formed in step one.

The BCA-copper complex is water-soluble and exhibits a strong linear absorbance at 562 nm with increasing protein concentrations. The assay was performed using the standard test tube protocol and a set of prediluted BSA protein assay standards.

2.6.1.2 Absorbance at 280 nm

Proteins in solution absorb ultraviolet light with absorbance maxima at 280 nm, due to the presence of amino acids with aromatic rings. Secondary, tertiary, and

quaternary structure all affect absorbance, therefore factors such as pH or ionic strength can alter the absorbance spectrum. Following the Lambert-Beer equation with a theoretically calculated extinction coefficient, the protein concentration can be estimated.

$$A = \varepsilon c l$$

Equation 2. Lambert-Beer equation.

where A is absorbance, ε is the molar extinction coefficient, c is the concentration and l is the path length.

2.6.2 Protein Electrophoresis

Protein separation was achieved by SDS-PAGE in 12.5 or 15% (w/v) acrylamide gels. Samples were mixed with Laemmli loading buffer (6x) supplemented with β-mercapthoethanol and heated at 90ºC for 5 min. Broad-range and precision (unstained and prestained) standards (Bio-Rad) were used as molecular weight markers. Electrophoresis was performed at 150 V in running buffer (3.028 g Tris, 14.41 g glycine, 1 g SDS and H_2O to 1 L). For quick protein visualization, the gel was stained for at least 10 min in a solution containing 0.1% (v/v) Coomassie Brilliant Blue R-250, 40% (v/v) methanol and 10% (v/v) acetic acid. Background staining was eliminated by washing with 10% (v/v) acetic acid solution and images were taken on a Gel Doc™ EZ Imager (Bio-Rad).

2.6.3 Western Blotting

Transfer of proteins from an SDS-PAGE gel to nitrocellulose membranes (Bio-Rad) was performed with a Trans-Blot® (Bio-Rad) equipment. A gel sandwich with Trans-Blot filter papers and a nitrocellulose membrane was prepared and hydrated with transference buffer (2.25 g glycine, 5.81 g Tris, pH 8, 0.375 g SDS, 200 mL MetOH and H_2O to 1L). Protein transfer was performed at 22 V for 30 min at room temperature. After protein transfer, membranes were blocked with 5% skim milk in PBS and incubated with the specific primary (1:1000) and secondary (1:5000 to 1:10000) antibodies, the latter tagged with a HRP. Membrane washing was followed by protein detection in a Curix 60 processor with the SuperSignal™ West Pico Chemiluminescent Substrate (Thermo Fisher Scientific). The intensity of the sample signal was quantified in a GS-800 densitometer (Bio-Rad).

2.7 Protein-Lipid Interactions

In order to understand the molecular mechanisms by which a protein interacts with biological membranes, the affinity and specificity of the membrane-binding process and the protein topology or conformation in the lipid bilayer need to be studied.

Techniques such as X-ray cristallography or electron crystallization are the methods of choice to obtain high-resolution structures of membrane proteins. In the case of X-ray cristallography, lipids do not often survive the crystallization process and if copurified and crystallized, do not appear sufficiently ordered in the crystal to allow for their unambiguous characterization (Palsdottir & Hunte, 2004). Alternatively, electron crystallization is increasingly used to solve membrane protein structures with atomic resolution from 2D crystals in a lipid environment (Raunser & Walz, 2009). For structures in which crystals are not available, solid-state NMR spectroscopy (Aisenbrey *et al.*, 2013), FT-IR spectrosocopy (Subirade *et al.*, 1995), or EPR (Marsh, 2008) are techniques that can also provide invaluable information of protein-lipid interactions. Molecular dynamics simulations are also used to study membrane proteins (Lindahl & Sansom, 2008). Unlike NMR or X-ray based approaches, the motions and interactions of proteins and lipids can be monitored in atomistic detail with high temporal and spatial resolution. Such an *in silico* approach has been recently used to study the molecular recognition of a single sphingolipid species by a protein transmembrane domain (Contreras *et al.*, 2012).

In addition to the above-mentioned high-resolution techniques, a number of fluorometric, centrifugation, and microscopic assays are also available for studying the molecular mechanisms by which proteins interact with membranes (Contreras *et al.*, 2011; Zhao & Lappalainen, 2012). Each of these assays provides a distinct type of information and has specific technical limitations.

In the present work lipid dot-blot experiments, surface pressure measurements, and liposome sucrose gradient float-up centrifugation have been used to analyze the binding capacities of LC3B, GABARAPL2 and GABARAP to several autophagy-related lipids. Many factors need to be taken into account when designing an experiment for studying membrane interactions of a specific protein. These include: (i) vesicle lipid composition, (ii) protein:lipid ratio, (iii) membrane curvature, (iv) pH and (v) buffer salt concentration.

2.7.1 Protein-Lipid Overlay Assay (Lipid Dot-Blot)

The PLO assay enables the identification of the lipid ligands with which lipid binding proteins interact (Dowler *et al.*, 2002). The lipid binding specificities of numerous PH (Lemmon *et al.*, 1995), EEA1 (FYVE) (Stenmark *et al.*, 1996), and PX homology (Xu *et al.*, 2001) domain-containing proteins have been investigated using this assay. In many cases, the specificities of proteins for their lipid ligands determined with the PLO assays have been seen to correlate with the results obtained from more complex methodologies used to assess protein-lipid interactions.

As mentioned above, the results obtained from a PLO are qualitative. If quantitative association constants are required, then SPR or ITC (Swamy & Sankhala, 2013) are the recommended methods. However, these approaches are substantially more laborious and require relatively expensive equipment. The main advantage of the PLO assay over the other binding assays is that it allows the simultaneous analysis of the lipid binding specificities of many protein samples for a range of naturally occurring lipids. The results obtained from this type of assay provide a good qualitative indication of the relative affinity of different proteins for the lipid(s) with which they interact and moreover, the primary results obtained from the PLO assay are in the form of a standard immunoblot, which can be interpreted in a semiquantitative manner using image analysis software.

In the present thesis, lipid dot blot strips were prepared in the laboratory following the procedure described in **Protocol 8**, adapted from Dowler *et al.*, 2002.

Protocol 8. Protein-Lipid Overlay Assay

1. Stock solutions of different lipids are solubilized in 2:1:0.8 MeOH:$CHCl_3$:H_2O. If required, serial 1:3 dilutions are prepared from the stock.
2. Lipids (0.5 µL) are spotted onto Hybond C nitrocellulose (GE Healthcare) and allowed to dry for 1 h at room temperature.
3. To detect the protein by immunoblotting, the nitrocellulose is first blocked with 5% fat-free milk in PBS for 1 h at room temperature to avoid nonspecific interactions.

(The protocol continues on the next page)

4. The membrane is further incubated for 1 h with the protein in PreScission buffer at 37ºC.
5. The nitrocellulose is washed 4 times, 10 min each, with PBS, and soaked in 5% fat-free milk in PBS with the primary antibody at 1:1000 dilution overnight at 4ºC.
6. The nitrocellulose is washed 4 times with PBS and soaked in 5% fat free milk in PBS with HRP-conjugated antibody (Santa Cruz Biotechnology, Dallas, TX, USA) at a 1:5000 dilution for 1 h at room temperature.
7. After washing with PBS 4 times 10 min at room temperature, the protein is detected by chemiluminescence. Protein bands are digitalized and integrated densities are measured using Quantity One software (Bio-Rad).

2.7.2 Langmuir Balance

Due to their amphipathic character, lipids spread on top of a water surface orient their polar headgroups in close contact with the water surface while moving their hydrophobic acyl chains towards the air. In this simple way, a monomolecular lipid film at the air-water interface is generated, in other words, a lipid monolayer (see Section 2.3.6). The terms “Langmuir films” and “Langmuir balance” refer to the preparation and characterization of such structures, named after the intensive studies of the American chemist and physicist Irving Langmuir in this field (Langmuir, 1917). For his work in surface chemistry Langmuir was awarded the Nobel Prize in chemistry in 1932.

Langmuir balance measurements represent an important source for the characterization of lipid-lipid and lipid-protein interactions. In contrast with the use of vesicles or lipid bilayers, Langmuir balance approaches have the advantage of precisely controlling lateral pressure, molecular packing and lipid composition. There are no curvature or fluctuation effects in comparison to vesicles. Furthermore, the current development of the technique allows for instance direct microscopy measurements by incorporation of fluorescent probes within the monolayer, or transfer of lipid monolayer to solid supports for its analysis under atomic force microscopy, among others. In the present work, Langmuir balance-based approaches have been applied to the study of lipid-protein interactions.

2.7.2.1 Surface Pressure Measurements

Langmuir balance approaches are based on the measurement of the water surface tension by means of a suspended solid probe. The method is referred to as the "Wilhelmy plate" from Ludwig Wilhelmy, who first provided a way for measuring surface tension in 1863 (Wilhelmy, 1863). The Wilhelmy plate is very thin and usually made of platinum or cardboard, but other materials have been as well used: quartz, glass or mica. As explained, the Wilhelmy plate measures surface tension, which is the excess free cohesive energy present at a gas-liquid interface. Water molecules are exposed to forces from surrounding molecules, which are balanced in the bulk of a water solution due to the equal attraction in every direction. However, at a gas-liquid interface, water molecules in the interface are not subjected to attractive forces in every direction, and thus, an excess cohesive energy is generated which is called the surface free energy. This excess energy can be related to surface tension as force/length by means of the forces detected by the probe partly introduced into the gas-liquid interface as depicted in **Figure 2.8**, which can be further related with surface pressures. The overall forces detected by the solid probe are:

Total force = weight of the probe + probe buoyancy + surface tension

Equation 3. Overall forces detected by the Langmuir balance solid probe.

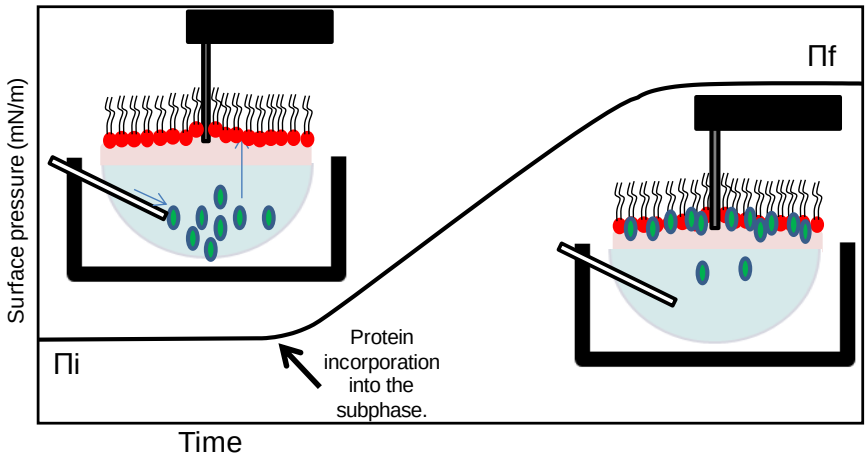

Figure 2.8. Schematic representation of the process of protein insertion into a lipid monolayer. Experimental set-up for a lipid monolayer experiment. Before adding the protein, the π_i of the monolayer is adjusted to the desired value. The protein inserts into the monolayer increasing the surface pressure until reaching equilibrium (π_f).

Before measurement, the pressure detected by the probe is adjusted to zero, thus discarding the weight force. The probe's buoyancy reflects the applied force of displaced water molecules upon probe immersion acting upwards, and is as well discarded as the probe is maintained at a constant depth during the measurement. Thus, the overall force can be reduced to surface tension, which is described on the following equation:

$$F = 2(w + t)(\gamma)(\cos \Theta)$$

Equation 3 bis. Reduced equation of the overall force.

where: w, t = width and thickness of the probe, γ = surface tension, Θ = contact angle.

When introducing the probe in the aqueous solution, a meniscus is formed, resulting in a contact angle of zero degrees as shown in **Figure 2.5**. In this way, the equation can be reduced to:

$$\gamma = \text{Force/Perimeter}$$

Equation 4. Surface tension.

or force/length which is given in units of dynes/cm = mN/m.

Water molecules give rise to one of the highest surface tensions due to their high intermolecular attractive forces, 72.8 mN/m at 22ºC and 1 atm. The presence of amphipathic molecules at the air-water interface disrupts the cohesive energy of water molecules, decreasing the water surface tension, this reduction being known as the surface pressure (π) with same units but opposite sign.

$$\pi = \gamma_o - \gamma$$

Equation 5. Surface pressure.

In conclusion, all the Langmuir balance measurements are performed following changes of surface pressure. Typically, a lipid solution in a highly volatile organic solvent [usually pure chloroform or chloroform/methanol (2:1 v/v)] is spread onto the surface of an aqueous solution (the air-liquid interface). As the solvent is evaporated, lipids organize themselves with the polar headgroup towards the aqueous solution and the hydrophobic chain towards the air. As the lipid spreads over the available surface area it decreases the water surface tension, i.e. increases the surface pressure. In this

way, for instance for lipid-protein interaction studies, a lipid monolayer is prepared by spreading the desired amount of lipid into an air-water interface at a controlled surface pressure. Protein is subsequently incorporated into the subphase and lipid-protein interaction followed in terms of surface pressure changes upon incorporation or adsorption of the protein into the monolayer (**Figure 2.8**). A particularly useful parameter to study the monolayer-penetrating capacity of a protein is to determine its π_c, this is, the value of π_i at which $\Delta\pi$ becomes zero. Note that cell membranes are proposed to have an average surface pressure around 30 mN/m (Janmey & Kinnunen, 2006; Marsh, 1996), although this value can vary largely.

A methodological overview on the preparation of Langmuir films can be found in Cruz & Pérez-Gil, (2007). Precise methodological conditions for each of the experiments carried out in the present work will be specifically found in the Materials & Methods section of the corresponding chapter.

2.7.3 Equilibrium Sucrose Gradient Centrifugation of Liposomes

Liposome flotation assays are widely applied for studying the affinity and lipid specificity of protein binding to membranes (Landeta *et al.*, 2011; Yethon *et al.*, 2003). In the liposome float-up experiment, the vesicles and bound proteins are enriched by density gradient centrifugation. In general, large unilamellar or multilamellar vesicles are the best model membrane systems for these studies. Another commonly used and more sensitive technique is vesicle sedimentation, but many membrane-interacting proteins have a tendency to aggregate or oligomerize, which results in their sedimentation in the absence of liposomes. In this situation, membrane binding of such proteins cannot be reliably examined by vesicle sedimentation assays and liposome flotation assays, which are not that sensitive to protein oligomerization or aggregation, can be used instead.

Liposome flotation assay starts by incubating proteins with liposomes [containing 0.05 mol percent Rho-PE for detection] at 37ºC. Then the sample is adjusted to 1.4 M sucrose using a sucrose stock solution prepared in PreScission buffer and loaded at the bottom of a discontinuous sucrose gradient (medium layer 0.8 M, upper layer 0.5 M sucrose). The sample was centrifuged at 4ºC for 3 h at 100,000 rpm in a Beckman Optima TLX benchtop ultracentrifuge, using a TLA-120.2 rotor (Beckman Coulter). During ultracentrifugation, due to their lower density, liposomes and liposome-bound proteins floated-up to the top fraction of the gradient whereas free

protein remained at the bottom (**Figure 2.9**). 250-µL aliquots were taken starting from the bottom (a total of 4 samples) and added to 50 µL 6X Loading Buffer. Then the top fraction (T), containing liposomes as indicated by the rhodamine fluorescence and the bottom fraction (B) containing the unbound protein (25 µL), were analyzed by Coomassie Blue-stained SDS-PAGE and western-blotting.

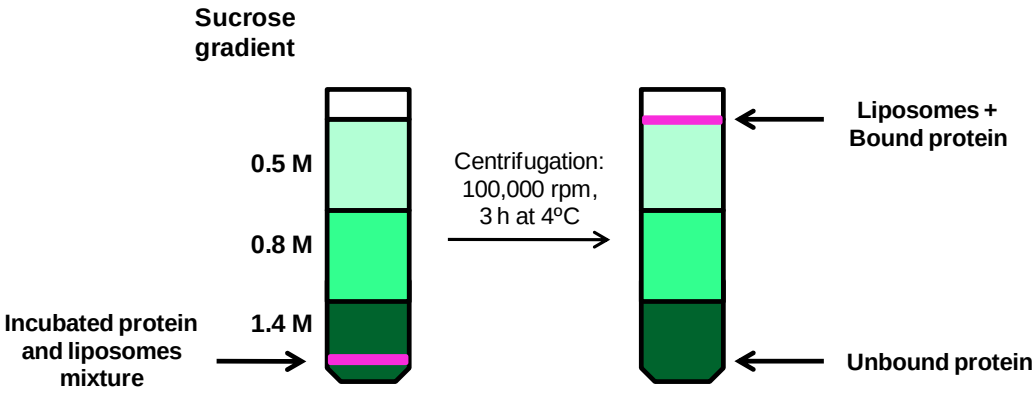

Figure 2.9. Schematic representation of an equilibrium sucrose gradient centrifugation assay. First, a sucrose gradient is generated with the sample in the test tube bottom. After centrifugation, liposomes and liposome-bound protein float-up while the unbound protein remains at the bottom.

2.8 Circular Dichroism (CD) Spectroscopy

CD allows the structural characterization of proteins at low-resolution, both in aqueous solutions and in model membrane systems. Although it does not provide the residue-specific information that can be obtained by X-ray crystallography or NMR, it is an excellent tool for rapid determination of the secondary structure and folding properties of peptides and proteins in physiological buffers.

This spectroscopic technique measures the differences in the absorption of the left- and right-handed components of circularly polarized light (Martin & Schilstra, 2008). Linearly polarized light can be described as a superposition of 2 circularly polarized light beams of equal phase and amplitude, but opposite directions. If after passage through the sample, the left and right components are not absorbed (or are absorbed to the same extent), combination of the components would regenerate plane-polarized radiation. However when this light passes through a sample containing optically active chiral molecules (such as amino acids) with different absorbance for each of the 2 circularly polarized components, the amplitude of the component

absorbed more strongly will be smaller than that of the other component and in consequence, the resultant radiation will be elliptically polarized (**Figure 2.10**).

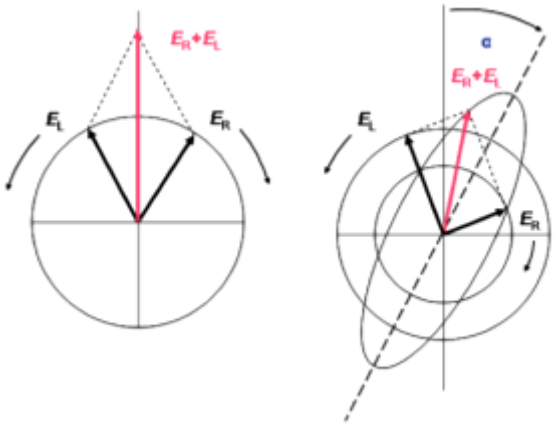

Figure 2.10. Origin of the CD effect. (**Left-hand side**) Linear polarized light can be viewed as a superposition of opposite circular polarized light of equal amplitude and phase. (**Right-hand side**) Different absorption of the left- and right-hand polarized components leads to ellipticity (CD). (Adapted from Kelly *et al.*, 2005).

As explained above, CD is measured as the difference in absorbance of left (AL) and right (AR) circularly polarized light:

$$\Delta A = AL - AR$$

Equation 6. Circular dichroism.

It can be also expressed as degrees of ellipticity (θ), defined as the tangent of the ratio of the minor to the major optical axes. It is very easy to inter-convert θ and ΔA using:

$$\theta = 32.982(\Delta A)$$

Equation 7. Ellipticity.

A CD spectrum of a determined protein is then obtained when plotting θ as a function of wavelength.

2.8.1 Determination of Protein Secondary Structure

The peptide bond is the primary chromophore contributing to the absorption of light in the far-UV spectra (from 170 to 250 nm). Moreover, the specific organization of the peptide bonds in the protein gives rise to isolated absorbing units that present unique spectral features. Thus, alpha-helix, beta-sheet and random-coiled structures produce each a characteristic shape and magnitude in the CD spectrum (**Figure. 2.11**).

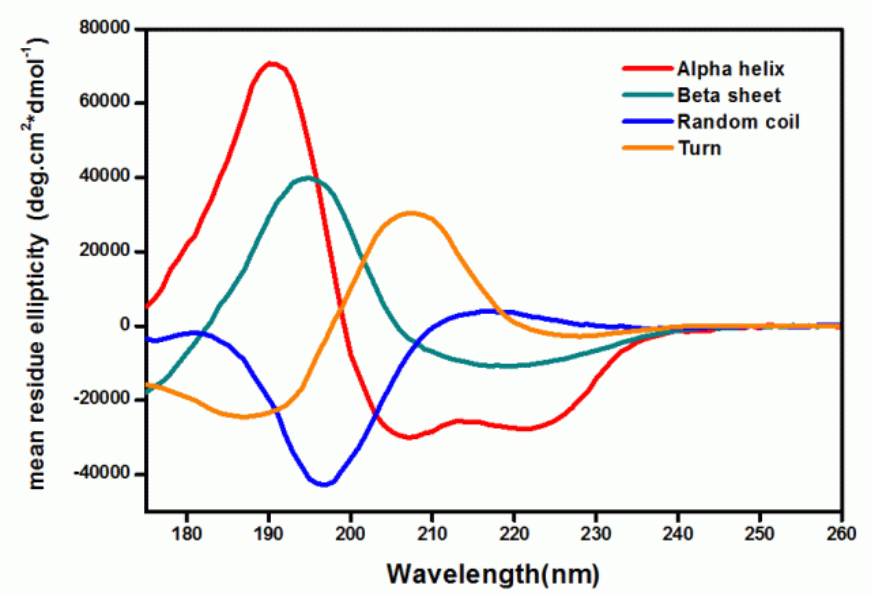

Figure 2.11. Far-UV spectra associated with various types of secondary structure. Different secondary structure elements display characteristic CD spectra: α-helical proteins have negative bands at 222 nm and 208 nm and a positive band at 193 nm. Proteins with well defined antiparallel β-pleated sheets have negative bands at 218 nm and positive bands at 195 nm. Finally, disordered proteins have very low ellipticity above 210 nm and negative bands near 195 nm.

In the present thesis, CD spectroscopy in the far-UV has been used to obtain a quantitative estimate of the average secondary structure of LC3B, GABARAPL2 and GABARAP as well as to assess the structural integrity of the mutant proteins. Measurements were performed in a thermally controlled Jasco J-810 spectropolarimeter (Jasco Spectroscopic Co. Ltd., Hachioji, Japan) at 37ºC using a 1 mm optical path quartz cuvette. Data were collected every 0.2 nm at 50 nm/min from 260 to 200 nm with a bandwidth of 2 nm, and results were averaged from 20 scans. Buffer contribution was subtracted, and data converted to mean residue molar ellipticity [θ] using the expression:

$$[\theta] = \theta/10cln \ (deg.cm^2.dmol^{-1})$$

Equation 8. Molar ellipticity.

where: θ is ellipticity (milidegrees), c is the protein concentration (M), l is the cuvette path length (cm), and n is the number of protein peptide bonds.

2.9 Fluorescence Spectroscopy Techniques

Fluorescence is one of the most sensitive spectroscopic techniques, that allows real time characterization of events occurring in membranes such as fusion, aggregation or permeation. It has been applied previously to study the fusogenic activity associated with hydrolytic enzymes (SMase and PLC) (Goñi *et al.*, 2003).

Approaches based on fluorescence spectroscopy are also useful for studying many aspects of lipid-protein interactions, due to their intrinsic sensitivity, suitable timescale, and minimal perturbation effects (Johnson, 2005). Steady-state fluorescence spectroscopy measurements (e.g., fluorescence intensity, spectrum shift, and quenching assays) provide information about molecular interactions within the system and can be applied to determine the interaction of a given protein with a membrane. Time-resolved fluorescence methods (e.g. TR-FRET) can additionally provide information about the dynamics of such interactions.

2.9.1 Intrinsic Tryptophan Fluorescence Spectroscopy

The intrinsic fluorescence of aromatic amino acids can be applied to the study of protein-lipid interactions. Tryptophan fluorescence is most commonly used. Changes in the intrinsic tryptophan fluorescence of proteins often occur upon conformational changes or ligand binding. In general, the quantum yield of tryptophan fluorescence increases in intensity (usually accompanied by a blue shift) when tryptophan is exposed to a more hydrophobic environment, and decreases when it is exposed to an aqueous medium (**Figure 2.12**). Thus, if the protein of interest harbors a tryptophan residue that is located at the membrane-binding interface or is sensitive to a possible conformational change, tryptophan fluorescence can be applied for determining changes caused by chaotropic agents, membrane-interaction or ligand-binding, among others (Bakás *et al.*, 1996; Kraft *et al.*, 2009; Lakowicz, 2007; Ostolaza & Goñi, 1995; Soloaga *et al.*, 1998; Zhao & Kinnunen, 2002).

For Trp measurements, sample components (protein or protein plus liposomes) were incubated for 1 h at 37ºC. After incubation, fluorescence spectra were recorded in a QuantaMaster spectrofluorometer (Photon Technology International, Birmingham, NJ, USA). Excitation wavelength was 295 nm, band pass was 5 nm, and emission spectra of Trp were measured from 310 nm to 450 nm at a rate of 1 nm/sec. Corrections were made for the appropriate blanks and for the wavelength-dependent bias of the optical and detection systems. These data were used to assess possible conformational changes of GABARAPL2 with CL-containing liposomes.

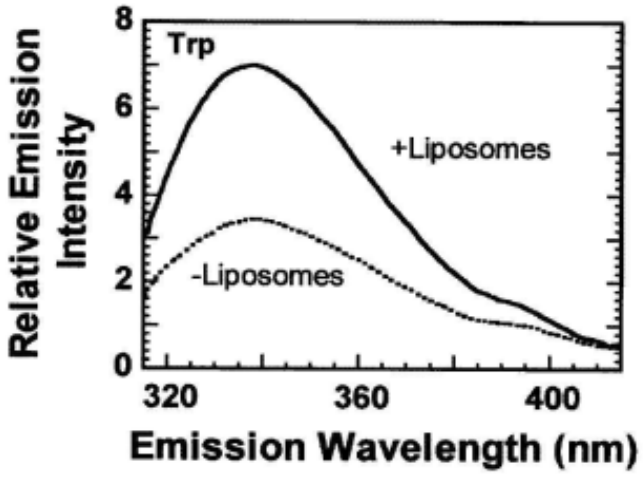

Figure 2.12. Intrinsic tryptophan fluorescence. Changes in the intrinsic tryptophan fluorescence of toxin perfringolysin O upon binding to cholesterol-containing liposomes (Taken from Heuck *et al.*, 2000).

2.9.2 NBD Fluorescence Spectroscopy

Alternatively to the intrinsic fluorescence of aromatic amino acids, extrinsic probes can be used for studying protein-lipid interactions, meaning that the lipid and/or protein are conjugated to a fluorescent dye. The number of commercially available dyes is enormous. Many of them, e.g. NBD, are very sensitive to the presence of water, while others, like fluorescein, are more sensitive to changes in the pH or the electrostatic environment. When choosing a fluorescent dye, several technical considerations must be recognized:

i. The dye should have a relatively small size, as very large probes are more likely to perturb protein structure or function.

ii. The dye should not be so hydrophobic that it buries itself in the bilayer irrespective of the conformation of the native unmodified polypeptide. For example, very hydrophobic dyes such as acrylodan or coumarin may alter the conformation of the polypeptide chain to which they are attached in order to bury themselves in the bilayer nonpolar core.

iii. After labeling, nonbound dye should be easily removable as such non-specific non-covalent bound dye will contribute to the observed signal interfering with the correct interpretation of spectral data.

Protocol 9. NBD Fluorescence Spectroscopy

1. Site-directed mutagenesis is used to remove all endogen cysteine residues present in the protein and to introduce a new Cys residue at the desired position in the generated Cys-free protein.
2. Labeling:
   - Cysteine-substituted proteins are concentrated to 2 to 3 mg/mL and incubated with 1 mM TCEP for 30 min at room temperature.
   - TCEP is removed by passing the sample through a PD-10 desalting column (GE Healthcare), previously equilibrated in the labelling buffer (10 mM HEPES, pH 7.3, 100 mM KCl, 1 mM EDTA).
   - IANBD (Molecular Probes, Eugene, OR, USA) dissolved in DMSO is then added in a small volume (15 to 25 µL) to the protein solution to give a final protein:probe molar ratio of 1:10 (NBD stock solution = 30 mM) and incubated overnight at 4ºC with gentle stirring protecting sample from the light.
   - The sample is centrifuged for 10 min at 14,000 x g and loaded onto a PD-10 column previously equilibrated with labeling buffer to separate the conjugate from unreacted labeling reagent.
   - For determining the degree of labeling the following equation is used:

$$\% \text{ Degree of labeling: } [(Abs_{NBD}/\varepsilon_{NBD})/(Abs_{prot}/\varepsilon_{prot})] \times 100$$

Equation 9. % Degree of labeling calculation.

where: Abs_{NBD} = NBD absorbance at 488 nm

Abs_{prot} = Protein absorbance at 280 nm

ε_{NBD} = NBD molar extinction coefficient (eM)

ε_{prot} = Protein molar extinction coefficient (eM).

(The protocol continues on the next page)

3. NBD-fluorescence measurements:

- Sample components (protein or protein plus liposomes) are incubated for 10 min at 37ºC prior to measurements.
- NBD spectra are recorded in a QuantaMaster spectrofluorometer (Photon Technology International) in a thermostatically controlled 1-cm path length cuvette with constant stirring under the following conditions:

λ_{ex} = 465 nm	Band-pass = 5 nm
λ_{em} = 520 - 650 nm	Cut-off filter at 515 nm
T^o = 37ºC	Rate = 1 nm/sec

In all cases, background intensities from samples lacking protein were substracted from the intensities measured in protein containing samples.

Given the considerations described above, IANBD, a thiol-specific iodoacetamide derivative of NBD, was chosen as one of the fluorescent probes in this study (see **Protocol 9**). When NBD moves from an aqueous milieu (i.e. the surface of a soluble protein) to a hydrophobic environment (i.e. the nonpolar interior of the membrane or a protein), its emission intensity increases while its wavelength of maximum emission shifts to the blue (**Figure 2.13**). In addition, since the protein is labeled with a unique NBD moiety at a single location in the protein, this approach also provides an opportunity to characterize the structural changes that occur at specific sites of the protein when it is associated to the membrane. Precise protein labeling methodological conditions will be specifically found in the Materials & Methods section of the corresponding chapter.

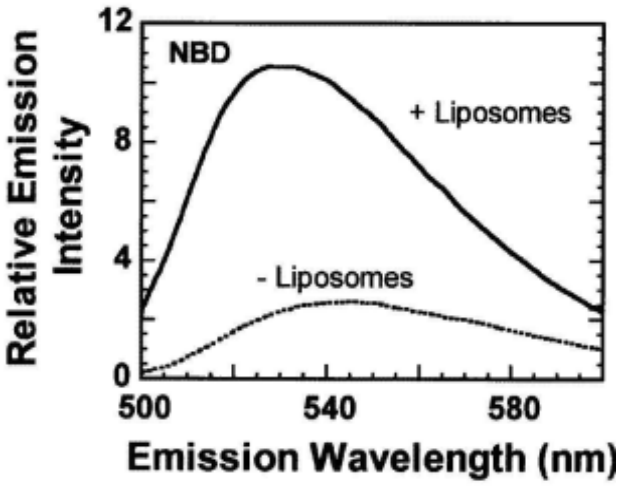

Figure 2.13. Site-specific NBD fluorescence. Changes in the fluorescence of the NBD moiety of NBD-labeled perfringolysin O upon binding to cholesterol-containing liposomes. (Taken from Heuck *et al.*, 2000).

2.9.3 Vesicle Contents Efflux Measurements (Leakage Assay)

This technique measures the ability of particular molecules to permeabilize the vesicle lipid bilayer. It is a simple approach in which vesicles are prepared enclosing fluorescent molecules. Upon specific molecule incubation, permeabilization is followed by changes in fluorescence. In the present study, the permeabilizing effects of ceramide and dihydroceramide have been tested by following the externalization of the well-known low-molecular weight ANTS fluorescent molecule and its quencher DPX.

The basis of this approach is depicted in **Figure 2.14**. By entrapping both ANTS and DPX inside the vesicles, their close proximity allows DPX to interact with ANTS quenching its fluorescence. Upon externalization, both molecules are diluted into the external medium and they hardly interact, inducing an increase of ANTS fluorescence. Thus by following ANTS fluorescence vesicle bilayer permeabilization or solubilization can be followed. This approach was initially developed in 1985 (Ellens *et al.*, 1985) to measure vesicle fusion, a situation in which both molecules were entrapped into separate vesicle populations and their fusion followed in terms of ANTS fluorescence quenching upon fusion and ANTS-DPX interaction (see Goñi *et al.*, 2003 and Nieva *et al.*, 1989). A full description of the assay conditions is given in **Protocol 10**.

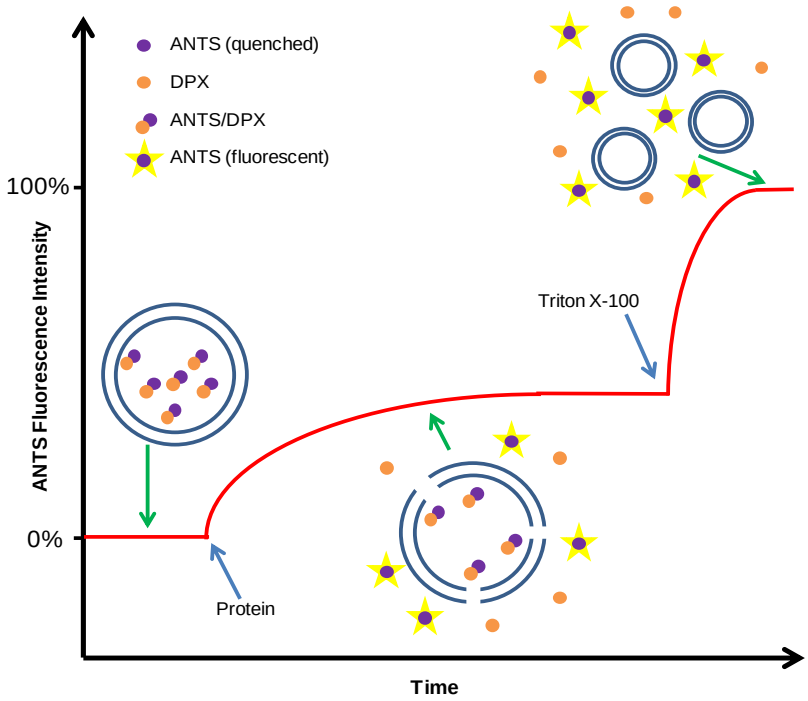

Figure 2.14. Schematic overview of the ANTS/DPX leakage assay. Upon incorporation of the permeabilizing agent (protein in this case) into the membrane, vesicle-enclosed ANTS and DPX are externalized through membrane defects. An increase in ANTS fluorescence is observed. Triton X-100 is generally added for complete vesicle solubilization into mixed vesicle lipid/surfactant/Triton X-100 micelles that gives the 100% leakage value (i.e. maximum ANTS fluorescence).

Protocol 10. Vesicle Contents Efflux Measurements

1. 100 nm LUVs are prepared as previously described (**Protocol 3**) in the following buffer containing both ANTS and DPX: 20 mM ANTS, 70 mM DPX, 40 mM NaCl, 10 mM HEPES, 10 mM $CaCl_2$, 2 mM $MgCl_2$ (pH 7).
2. A high DPX/ANTS ratio is used to ensure complete quenching inside vesicles. Samples are covered with aluminium foil to protect fluorescent molecules from bleaching.

(The protocol continues on the next page)

3. The vesicle suspension is passed through a Sephadex G-25 column to remove non-entrapped ANTS and DPX. A previously adjusted isosmotic buffer solution is used for this process: 150 mM NaCl, 10 mM HEPES, 10 mM $CaCl_2$, 2 mM $MgCl_2$ (pH 7).
4. Lipid concentration is determined as previously described (**Protocol 6**).
5. The permeabilizing agent is added to 0.3 mM vesicles in 1 mL glass tubes with continuous stirring and leakage is followed as ANTS fluorescence in a QuantaMaster spectrofluorometer (Photon Technology International) under the following conditions:

   λ_{ex} = 355 nm

   λ_{em} = 520 nm

   Interference filter at 450 nm

   T^o = 37ºC

   0% release = Initial fluorescence of intact vesicles.

   100% release = Fluorescence after complete vesicle solubilisation with 1 mM Triton X-100.

To calculate the amount of leakage the following equation is used:

$$\% \text{ Leakage} = [(F - F_0)/(F_{100} - F_0)] \times 100$$

Equation 10. % Leakage calculation.

where: F = Fluorescence at equilibrium

F_0 = Fluorescence at time zero

F_{100} = Maximum leakage (fluorescence after Triton X-100 addition)

2.10 Mammalian Cell Culture

2.10.1 Cell Culture Initiation and Maintenance

A list of the cell lines used in this thesis is presented in **Table 2.4**. Cell line stocks were routinely frozen gently at low passage numbers in their respective growth media supplemented with 10% DMSO and 40% FBS and stored at -80ºC and in liquid N_2. Recovery of cell lines required rapid thawing at 37ºC and dilution into 10 mL of regular growth media for overnight recovery. Media was changed the next day to remove remaining traces of DMSO. Unless stated, cortical neurons were cultured in 4-well plates and other cell lines in 10 cm-diameter tissue culture dishes at 37ºC in a humidified incubator with 5% CO_2.

Cell line	Source	Media used
U87MG	Human glioma cell line (ATCC®) (in collaboration with Dr. G. Velasco, Complutense University, Madrid)	DMEM (+ 10% FBS and 5 µg/mL penicillin/streptomycin)
mCherry-GFP-LC3B RPE1	Stable cell line	DMEM-High Glucose (+ 10% FBS)
mCherry-GFP-GABARAPL1 RPE1	Stable cell line	DMEM-High Glucose (+ 10% FBS)
GFP-ATG5 RPE1	Stable cell line	DMEM-High Glucose (+ 10% FBS)
iPSC-derived human cortical neurons	iPSC-derived cortical neurons (provided by Mr P. Stathakos and Dr. P. A. Nistor, Bristol, UK)	N2B27 containing 1:1 Neurobasal and DMEM/F-12 with glutamax (final glutamine concentration 1 mM) (+ 1:100 B27, 1:200 N2, 1:200 nonessential amino acids, 75 µM 2-mercaptoethanol, 100 units/mL penicillin, 100 µg/mL streptomycin)

Table 2.4. Cell lines used in this thesis. Stable cell lines were provided by Dr. J. Lane (University of Bristol, Bristol, UK). B27, N2, nonessential amino acids and 2-mercaptoethanol were obtained from LifeTechnologies (Carlsbad, CA, USA). Penicillin and streptomycin were obtained from Sigma-Aldrich. ATCC®, Rockville, MD, USA.

2.10.2 Transient Transfection

Cell transient transfection was performed using the Lipofectamine®2000 transfection reagent (Invitrogen, Carlsbad, CA, USA) according to the manufacturer's instructions. In short, DNA of interest was diluted in an appropriate volume of opti-MEM®, in a separate sterile 1.5 mL tube Lipofectamine®2000 was diluted in opti-MEM® and both were incubated for 5 min. The amount of Lipofectamine®2000/opti-MEM® was scaled up depending on the numbers of transfections. Meanwhile the appropriate number of cells to be transfected was prepared at the desired concentration in normal growth media minus antibiotics. Then the Lipofectamine®2000-DNA complexes were added dropwise to cells. Cells were cultured for 24 to 48 h at 37ºC and 5% CO_2 prior to processing.

The plasmids used for mammalian cell transient transfection and lentiviral transduction were kindly provided by Dr. J. Lane and Dr. A. Simonsen (Institute of Basic Medical Sciences, Oslo, Norway) (see **Table 2.5**).

2.10.3 Lentiviral Transduction

An alternative technique to transient transfection is to stably insert genes of interest in cell genomes using HIV-based lentiviral vectors. This HIV-1-based retrovirus allows the transduction of mammalian cell lines for sustained expression of any protein genetically encoded in the lentiviral expression vector. Two independent lentiviral systems have been used in this thesis (see **Table 2.5**):

2.10.3.1 Lentiviral pLVX-Puro Vector and Lenti-X™ HT Packaging System

The pLVX-Puro lentiviral expression vector combined with LentiX™ HT packaging system (Clontech Laboratories, Mountain View, CA, USA) form a commercially available system with high levels of safety and potential to transduce primary cells.

Lentiviruses were produced by co-transfecting 80-90% confluent HEK293T cells in 10 cm-diameter dishes with the pLVX-Puro constructs and LentiX™ HTX Packaging Mix (a mix of 5 plasmids encoding viral packaging proteins), according to the manufacturer's instructions. Lentiviruses were harvested by retrieving the complete cell media after 48 h and cleared using a 0.45 µm cellulose acetate filter. The cleared viral suspension was aliquoted into cryotubes and stored at -80ºC.

Due to poor expression levels with the pLVX-Puro vector the pxlg3-gfp system was chosen and used in the subsequent experiments.

Fusion Gene	Vector Backbone	Method
GABARAPL2-GFP	pDestEGFP	Transient transfection
GABARAP-GFP	pDestEGFP	Transient transfection
MTS-CFP	peCFP-N1	Transient transfection (sub-cloned in this project from the MTS-peGFP plasmid provided by Ms G. Mullally, Bristol, UK)
Mito-DsRed	pDsRed2	Transient transfection
Mito-CFP	peCFP-N1	Lentiviral transduction (lentiviral pLVX-Puro vector and Lenti-X^{TM} HT packaging system)
mCherry-GFP-LC3B	pmCherry-C1	Lentiviral transduction (lentiviral pLVX-Puro vector and Lenti-X^{TM} HT packaging system)
GFP-LC3B	peGFP-C1	Lentiviral transduction (pxlg3-gfp lentiviral system)
GFP-GABARAPL1	peGFP-C1	Lentiviral transduction (pxlg3-gfp lentiviral system)

Table 2.5. List of plasmids. Note: stable cell lines were generated indirectly using previously subcloned fusion genes into the lentiviral vector plasmid pxlg3-gfp or pLVX-Puro for lentiviral transduction.

2.10.3.2 Lentiviral pxlg3-gfp System

The pxlg3-gfp vector is a modified pHR'SIN-SEW vector (Demaison *et al.*, 2002) lacking the WPRE region (Danson *et al.*, 2007). The pHR'SIN-SEW vector is an HIV-based lentiviral vector developed from a SIN vector [in which the U3 region of the 3' LTR has been deleted (Zufferey *et al.*, 1998)] where the CMV promoter was replaced by the U3 part of the spleen focus forming virus strain P long terminal repeat sequence (SFFVU3LTR) (Demaison *et al.*, 2002). This vector was described among several plasmids specifically developed to transduce haematopoietic progenitor cells *in vitro* by

Demaison and colleagues (Demaison *et al.*, 2002). High levels of expression were observed with lentiviruses carrying GFP-LC3B or GFP-GABARAPL1 in a pxlg3-gfp vector (provided by Dr. J. Lane) in human cortical neurons.

When using either system for stable transduction of mammalian cells with lentiviruses of interest, target cells were plated in live imaging dishes to reach 50 to 70% confluence on the day of transduction. Thawed lentiviruses were added dropwise onto target cells in a viral suspension:media ratio of 1:4 (v/v). Transduced cells were incubated for 24 h and the contaminant media was replaced with fresh growth media. Cells were cultured for at least 72 h at 37ºC and 5% CO_2 prior to imaging.

2.11 Fluorescence Microscopy (FM)

Fluorescent proteins or lipids and antibody-bound fluorophores were used to label and image the localization of selected proteins (immunolabeled or tagged respectively) within cells, to characterize lipid domains in GUVs or to image protein binding to GUVs by illuminating the samples at the excitation wavelength of the selected fluorescent marker and visualizing the emission fluorescence signal using microscopy.

Both excitation and emission signals were selected by specific filter sets within the microscopes. Two types of microscopes have been used in this study: the wide-field microscope and the confocal microscope. The wide-field microscope allows rapid acquisition of images and good sensitivity but is better adapted to thin samples (e.g. adherent cells), and was used for time-lapse microscopy and imaging of fixed cells. However, confocal microscopy removes out-of-focus light and allows imaging of sections of cells, even in thick samples and was more adapted to image specific details of cells as well as GUVs, due to their circular shape.

2.11.1 Fixed-cell Imaging (Immunofluorescence)

2.11.1.1 Cell Fixation and Permeabilization

Depending on the nature of the antigen to be detected or organelle to be labeled and preserved as well as the antibodies to be used, cells can be fixed with organic solvents (e.g. methanol) or cross-linking reagents (e.g. paraformaldehyde).

Organic solvents extract lipids and dehydrate the cells while precipitating proteins. They may cause collapse of the architecture of the cells but preserve well antigenicity. Organic solvents are ideal for cytoskeletal and membrane-bound antigens. Cross-linking reagents form methylene bridges between a variety of amino-acid side groups. They preserve better the cellular architecture but can reduce antigenicity and unlike organic solvents, they only fix cells which still need to be permeabilized.

For immunofluorescence, cells need to be attached to a solid support. U87MG cells were grown on glass 12 mm-coverslips (Menzel-Gläser, Braunschweig, Germany). Coverslips were washed once in PBS and fixed with 4% PFA (Sigma-Aldrich) for 20 min at room temperature and washed. RPE1 cells were grown on glass 13 mm-coverslips (Menzel-Gläser). Coverslips were washed once in PBS and fixed with ice-cold methanol (Thermo Fisher Scientific) for 5 min (for HSP60 immunolabeling) or 2% PFA (Sigma-Aldrich) for 15 min at room temperature and washed. All washing steps consisted of 3 times 5 min washes in PBS.

PFA fixed cells were permeabilized for 5 min in 0.1 or 0.5% Triton X-100 (Sigma-Aldrich) in PBS and washed once more in the presence of a drop of 1 M glycine to block unreacted aldehyde groups and avoid unspecific binding of antibodies. As mentioned above, lipids were extracted during methanol fixation and therefore no permeabilization step was required.

2.11.1.2 Immunolabeling and Imaging

U87MG cells were incubated on coverslips with the appropriate primary antibodies (in case of LC3 the antibody recognizes the isoform B of the protein) diluted in PBS-0.1% BSA (Sigma-Aldrich) for 2 h. Coverslips were then washed 3 times in the same buffer for at least 5 min each. RPE1 cells were incubated on coverslips with the appropriate primary antibodies (in case of LC3 the antibody recognizes the isoform B of the protein) diluted in PBS (Sigma-Aldrich) for 20 min. Coverslips were then washed 3 times in PBS for at least 5 min each.

Secondary antibodies conjugated to fluorophores (for a detailed specification on antibody characteristics and conditions see Materials & Methods in the corresponding chapter) were incubated on the coverslips in the dark for 20 or 90 min at room temperature and washed a further 3 times with PBS. For DAPI nuclei staining, coverslips were placed in 0.1 µg/mL DAPI (nuclear stain with an emission wavelength of ~460 nm when bound to double stranded DNA) (Roche) for 5-10 min before 2 final PBS washes. After a brief rinse in ddH_2O, coverslips were mounted face down on glass

slides with Mowiol mounting medium (Calbiochem, Darmstadt, Germany) or Mowiol supplemented with DABCO (25 mg/mL; 4 µL per 13 mm-diameter coverslip).

Fixed-cell images were obtained using:

i. an Olympus IX-71 inverted wide-field microscope (Olympus UK Ltd., Essex, UK) with a 60x Uplan Flourite oil immersion objective lens (0.65–1.25 NA) fitted with a CoolSNAP HQ2 CCD camera (Photometrics, Tucson, AZ, USA) driven by MetaMorph software (Molecular Devices, Sunnyvale, CA, USA) and with two sources of light: a xenon lamp (LBLS-1256) for transmitted light and epifluorescence imaging, and a mercury lamp (Olympus U-RFL-T) when a brighter lamp was required.

ii. a Leica TCS SP2 confocal microscope (Leica Microsystems CMS GmbH, Wetzlar, Germany).

2.11.2 Live-cell Imaging

For live-cell imaging, cells were seeded in 35 mm glass-bottomed live-cell imaging dishes (MatTek Corp., Ashland, MA, USA) to allow for 60 to 70% confluency at the time of imaging.

For mitochondrial staining of RPE1 cells, adherent cells were transiently transfected with MTS-CFP or Mito-DsRed at least 24 h prior to processing. In case of cortical neurons, mitochondrial staining was performed incubating cells in pre-warmed media containing 50 nM MitoTracker®Red CMXRos (Molecular Probes, Life Technologies) for 15 min. Then staining media was aspirated and washed 3 times with PBS before replacement with fresh growth medium. MitoTracker®Red CMX-ROS stains active mitochondria and its accumulation in mitochondria depends on mitochondrial $\Delta\Psi$ but it is not completely lost upon depolarization and may be retained after fixation (Poot *et al.*, 1996). For LC3B and GABARAPL1 staining, neurons were transducted with the appropriate lentivirus at least 72 hours prior to the experiment.

Live-cell imaging was performed using an Olympus IX-71 inverted wide-field microscope with a xenon lamp for both transmitted light and epifluorescence (LBLS-1256). Images (phase contrast and fluorescence) were taken using a CoolSNAP HQ2 CCD camera (Photometrics) at fixed time intervals for several z positions under the control of MetaMorph software. All imaging was performed at 37ºC and 5% CO_2.

2.11.3 Fluorescence Confocal Microscopy

The development of confocal microscopy during the late 70's resulted in one of the major advances in optical microscopy. Specifically, fluorescence confocal microscopy allows analyzing the fluorescence coming from an individual thin in-focus plane of the sample, and this enables the construction of real 3D images. To discard fluorescence coming from out-of-focus planes, and in contrast to common epifluorescence microscopy, confocal imaging is achieved by introducing a pinhole next to the detector that allows only fluorescence coming from the in-focus plane to reach the detector. **Figure 2.15** shows a schematic picture of the central components of a fluorescence confocal microscope. Essentially, a laser beam is used as the excitation light, which is focused into a dichroic mirror that selects the light to be directed through an objective into a small spot within the sample. However, this is not enough to build a 3D image of the specimen being measured. For this purpose, special mirrors are introduced to scan the laser beam on the x-y plane, thus building a special confocal microscopy known as laser scanning confocal microscopy. In this way, by precisely controlling the z sample movement, three dimensional images can be constructed.

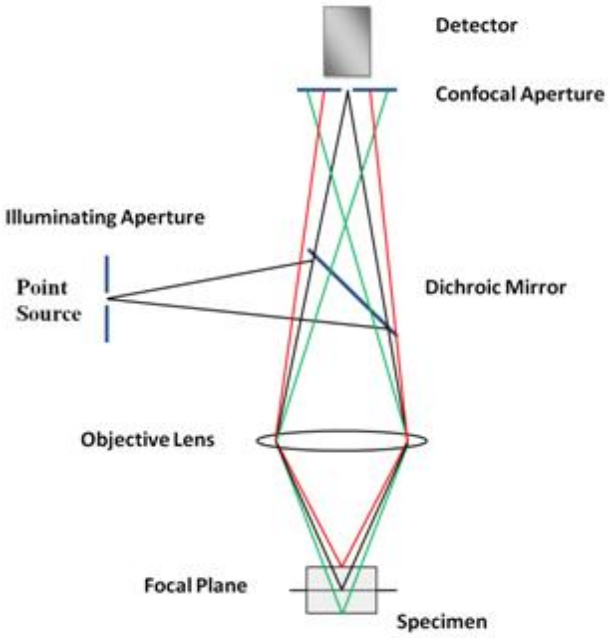

Figure 2.15. Central components of a fluorescence confocal microscope.

In the present work, laser scanning confocal microscopy has been applied to the characterization of lipid domains in GUVs or to observe protein binding to GUVs

using a Nikon D-ECLIPSE C1 confocal microscope (Nikon Inc., Melville, NY, USA), and for immunofluorescent localization of several proteins in fixed cells using a Leica TCS SP2 confocal microscope (Leica Microsystems CMS GmbH).

2.12 Correlative Light and Electron Microscopy (CLEM)

Bridging strengths of both microscopy techniques, interest in CLEM is increasing rapidly in recent years. This is reflected not only in an increasing number of scientific publications, but also in novel commercial products dedicated to CLEM investigation. In CLEM a specimen, preferably the same region, is first visualized by LM and next by EM (**Figure 2.16**). Typically FM is favored among other LM methods in CLEM studies as it can provide information about the localization of several proteins and cellular structures exploiting the widely available specific fluorescent labels and stains. Usually, FM inspection of the sample is done first, and then the sample is transferred to the electron microscope.

The FM can be employed to screen the sample for localization of a ROI or a rare occurrence in large and complex samples, based on the positions where particular fluorescently labeled proteins and/or structures are present. These selected ROIs are then scanned in TEM with high resolution and ultra-structural information. When CLEM is used to link live-cell imaging (FM) with EM (van Rijnsoever *et al.*, 2008; Spiegelhalter *et al.*, 2014), the dynamic live-imaging of samples provides the crucial information to understand complex cellular events in all its dimensions, including the temporal information (see Karreman *et al.*, 2016 for a recent review). Then the sample is fixed at a selected time point to combine these dynamic FM observations with the underlying cellular architectural information from EM imaging.

Despite its usefulness in targeting biologically relevant questions, wide-spread use of CLEM is hampered by the absence of optimized specimen preparation protocols, CLEM compatible labels, slow speed of data acquisition, the lack of FM-EM correlation accuracy, and the complexity of the experimental routines. There is a growing number of studies aimed at developing optimized protocols (Karreman *et al.*, 2014; Kolotuev *et al.*, 2010; Peddie & Collinson, 2014; Russell *et al.*, 2016), better labels (Grabenbauer *et al.*, 2005; Shu *et al.*, 2011), and improved technologies (Koning *et al.*, 2013; Verkade, 2008) to facilitate extensive CLEM studies.

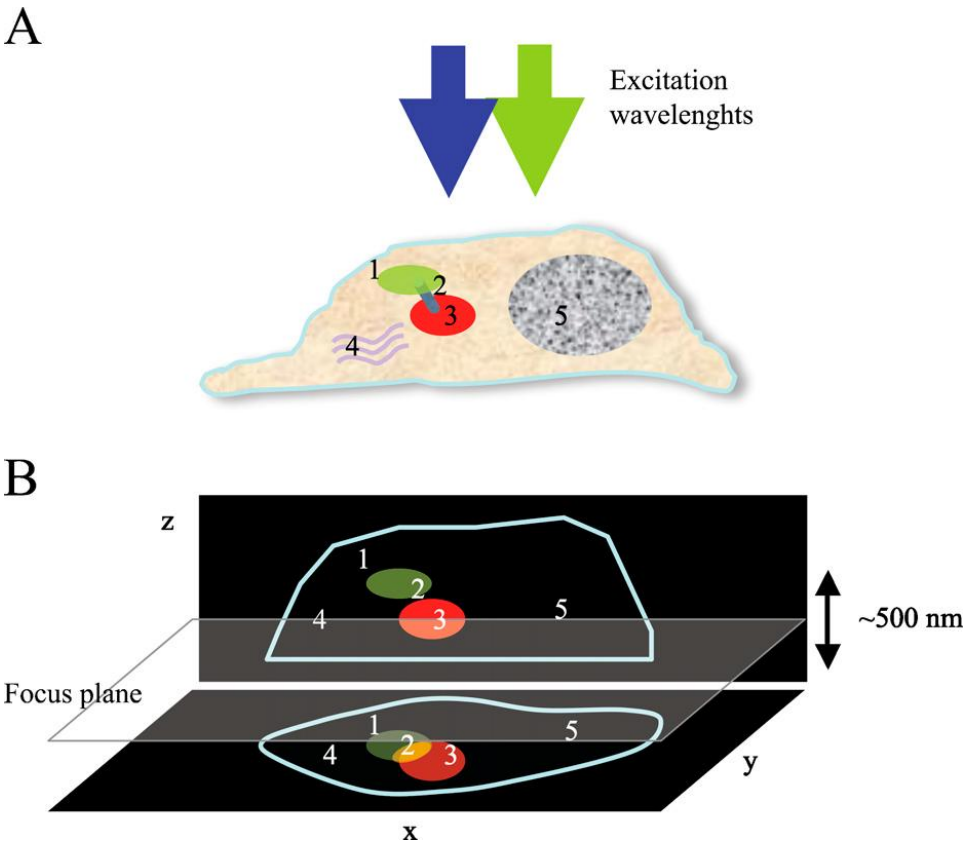

Figure 2.16. Advantages of CLEM. (**A**) Five features of a cell are highlighted (1–5). Blue and green arrows indicate different excitation wavelengths used for LM imaging. Whereas fluorescence imaging allows for the identification only of labeled items (2 and 3), EM provides the reference space where all objects are visible (1–5). Due to the limited axial resolution of FLM, objects that are closer than 200 nm are blurred into a single spot in the x-y projection (**B**). CLEM combines two techniques to obtain the highest resolution and information about structures or events occurring within cells. (Taken from Cortese *et al.*, 2009).

All CLEM experiments were performed using the reagents and instruments available in the Wolfson Bioimaging Facility (University of Bristol, Bristol, UK).

2.12.1 Cell Chemical Fixation and Embedding in Epon Resin

Cells grown in 35-mm glass-grid-bottomed dishes (MatTek Corp.) and previously imaged by FM (live-cell imaging) were processed using chemical fixation and embedding in Epon resin for TEM.

Chemical fixation is associated to a number of artefacts (reviewed in van Weering *et al.*, 2010), such as possible collapse of membranes due to dehydration and destabilization of cytoskeleton, which sometimes impaired the identification organelles.

A detailed protocol for cell fixation and embedding used in the present work is described (**Protocol 11**).

Protocol 11. Cell Chemical Fixation and Embedding in Epon Resin

1. Cells in suspension in growing media are fixed with an equal volume of 3% gluteraldehyde for 15 to 30 min.
2. Glutaraldehyde-fixed cells are washed twice with cacodylate buffer (0.1 M Na cacodylate).
3. The lipid stain OsO_4 (osmium tetroxide; Electron Microscopy Science, Hatfield, PA, USA) is then used to create contrast between membranes and cytoplasm. Samples are incubated for 1 h in the dark with 1.5% potassium ferricyanide, 1% OsO_4 and 0.1 M cacodylate.
4. Cells are then washed 3 times in 0.1 M cacodylate and a further 3 times in water.
5. For embedding into Epon resin, samples are first dehydrated on a rotator, for 3 times 5 min with 70% ethanol, 3 times 5 min with 90% ethanol and 2 times 5 min with 100% ethanol.
6. They are then incubated overnight on the rotator with 1:1 volume Epon resin (3 g Epon, 2 g DDSA, 1.25 g MNA, 0.1625 mL BDMA, all from TAAB Laboratories Equipment Ltd., Berks, UK) to ethanol.
7. Samples are transferred to pure Epon resin with 2 changes over the following 24 h. Epon resin is left to polymerize for 48 h at 60ºC.

2.12.2 Sectioning and Imaging of Embedded Samples

2.12.2.1 Block Preparation and Sectioning

To remove carriers from the resin blocks, each carrier was first cleared of excess resin with a blade. The blocks were immersed for 10 sec in liquid N_2 and a further 10 sec in hot water (80ºC) until ice crystals formed and the carriers were gently removed with a blade, leaving the cells of interest exposed at the top of the block.

Blocks were trimmed to form a pyramidal sectioning face using finder grid coordinates and the block face was then cut for thin serial sections of 70 nm using a diamond knife (3.0 mm and 45°C Diatome Ultra Diamond knife, Agar Scientific, Stansted, UK). Ribbons of sections were picked up on the dull side of 100 and/or 300 square mesh copper grids (3.05 mm, Agar Scientific) using tweezers.

2.12.2.2 Staining and Imaging by Electron Microscopy (EM)

Thin sections were counter-stained to increase contrast and improve visualization by TEM. Solutions were filtered through 0.22 µm filters before use. Grids were placed on drops of each solution, on Nescofilm, with the sections (dull side) in contact with the liquid.

Sections were first negatively stained for 10 min in 3% aqueous uranyl acetate in the dark and washed 3 times for 5 min in boiled cooled distilled water. Uranyl acetate is used as a negative stain; it increases electron density by deposition of heavy atom stains and consequently increases image contrast. Lead citrate was used to enhance the electron-scattering properties of biological specimens, resulting for instance in high intensity staining of cytoplasmic membranes, ribosomes and nuclear material in Epon resin sections (Reynolds, 1963). The lead citrate solution was prepared by mixing 1 mL of 189 mM lead nitrate with 1 mL of 282 mM sodium citrate stain, 0.38 mL of 1 M NaOH were then added and mixed. Grids were incubated 10 min in lead citrate stain in the dark, washed a further 3 times (5 min) in boiled cooled distilled water and allowed to dry during at least 45 min at room temperature.

Cells were observed by TEM using a Tecnai 12-FEI 120 kV BioTwin Spirit Transmission Electron Microscope (FEI Europe, Eindhoven, Netherlands) and images were obtained with a FEI Eagle 4 k x 4 k CCD camera. Each region of interest previously observed in live-imaging was captured at a magnification allowing the whole cell to be visible on the image and the magnification was recorded. Another 4 or 5 images covering the whole cell were taken at higher magnification to help identify organelle.

Chapter 3

Individual human Atg8 orthologs respond differently to cardiolipin in membranes: Specific properties of LC3B, GABARAPL2 and GABARAP

CHAPTER 3:

Individual human Atg8 orthologs respond differently to cardiolipin in membranes: Specific properties of LC3B, GABARAPL2 and GABARAP

3.1 Introduction

Macroautophagy, 'autophagy' in the context of this work, is an intracellular degradation pathway conserved in all eukaryotes (Mizushima & Komatsu, 2015; Yang & Klionsky, 2010). It involves the formation of a double-membrane structure, the phagophore, and its subsequent maturation to form an AP that fuses with lysosomes where the autophagosomal components are degraded (Shibutani & Yoshimori, 2014). This process does not only provide nutrients under amino-acid limiting conditions (nonselective autophagy) but works as well as a quality control system by selectively removing misfolded aggregate-prone proteins and damaged or superfluous organelles (selective autophagy) (Reggiori *et al.*, 2012). Thus far several cargo-specific autophagy processes have been reported, including the specific removal of mitochondria known as mitophagy (Ashrafi & Schwarz, 2013; Stolz *et al.*, 2014; Youle & Narendra, 2011). Beyond quality control, mitophagy is required for steady-state turnover of mitochondria (Tal *et al.*, 2007), for the adjustment of mitochondrion numbers to changing metabolic requirements (Kiššova et al., 2004) and during specialized developmental stages in mammalian cells (Schweers *et al.*, 2007). Several non-mutually exclusive mechanisms have been reported including changes in the nutrient conditions of yeast media (Kanki & Klionsky, 2008), damage- or drug-induced loss of mitochondrial membrane potential

(Wang *et al.*, 2012), decreased ATP production (Chistiakov *et al.*, 2014) or alteration of mitochondrial Ca^{2+} homeostasis (Cherra *et al.*, 2013). This cellular process is thought to delay aging (García-Prat *et al.*, 2016) and its dysregulation has been linked to multiple human pathological states including neurodegeneration (Nixon, 2013; Aufschnaiter *et al.*, 2016), myopathies (Kubli & Gustafsson, 2012) and cancer (Lu *et al.*, 2013).

Several molecular components involved in mitophagy have been identified both in yeast (Kanki *et al.*, 2015) and higher eukaryotes (Reggiori *et al.*, 2012; Youle & Narendra, 2011), including members of the Atg8 protein family (mammalian LC3 and GABARAP subfamilies). However one outstanding question is how damaged or superfluous mitochondria are primarily recognized by the autophagic machinery (Randow & Youle, 2014). Specific mitophagy receptors, by binding on one side to mitochondria and on the other end to the above autophagosome-specific proteins, physically link mitochondria to the growing phagophores. Lazarou and coworkers using knockout models of the 5 mitophagy receptors, namely TAX1BP1, OPTN, NBR1, p62, and NDP52, have found that LC3B is specifically recruited by OPTN and NDP52 during mitophagy and LC3C by TAX1BP1. Remarkably they have observed that GABARAP family proteins are not recruited to mitochondria, suggesting that they are not actively involved in mitophagy (Lazarou *et al.*, 2015). By contrast, other groups have found that GABARAPL1 colocalizes with depolarized mitochondria during basal, starvation, and apoptotic conditions (Novak *et al.*, 2010; Betin & Lane, 2009; Boyer-Guittaut *et al.*, 2014). In addition, CL externalization to the OMM has been shown to function as a signal for LC3 that mediates both mitochondrial recognition and AP formation, ultimately leading to targeted removal of damaged mitochondria (Chu *et al.*, 2013).

On the basis of these observations, we have attempted to gain further insight into the molecular basis of the interaction of LC3B with CL (Antón *et al.*, 2016). Here we show that LC3B interacts preferentially with CL over other di-anionic lipids such as PtdIns4P and that the LC3B-CL interaction relies on both electrostatic forces and CL-specific changes in membrane properties. We also provide evidence indicating that the LC3B C terminus remains exposed to the hydrophilic environment after protein binding to CL-enriched membranes. Finally, we extended our analysis to the LC3 paralogs GABARAPL2 and GABARAP, and we found that GABARAP, but not GABARAPL2, interacts with CL *in vitro*. Altogether, our study indicates that (i) LC3B-cardiolipin interaction is modulated by particular membrane properties that could allow the specific recognition of impaired mitochondria and (ii) the various human orthologs of yeast Atg8 may play specific roles in different autophagic processes.

3.2 Materials and Methods

3.2.1 Materials

PC from egg yolk was purchased from Lipid Products (Redhill, UK). Chol, bovine heart CL [90% TLCL (CL 18:2), 5% TOCL, 5% unknown], TOCL (CL 18:1), TMCL (CL 14:0), CL*, PtdIns4P, PtdIns[4,5]P_2, PtdIns[3,4,5]P_3, brain PS, liver PtdIns, egg PG, egg PA, Rho-PE, DOPE and eCer were purchased from Avanti Polar Lipids (Alabaster, AL, USA). Anti-LC3 monoclonal antibody, anti-GABARAP monoclonal antibody and anti-GABARAPL2 polyclonal antibody were from MBL International (Medical & Biological laboratories Co. Ltd., Nagoya, Japan).

3.2.2 DNA Constructs and Site-Directed Mutagenesis

Plasmids for expression of several Atg8 family proteins (LC3B, GABARAPL2 and GABARAP) and LC3B lacking the C-terminal Gly (LC3B$^{G\Delta}$) were kindly provided by Dr. I. Tanida. Note that each Atg8 ortholog is a truncated form ending in the reactive C-terminal Gly such that no ATG4-mediated preprocessing is necessary. These plasmids were used as templates for site-directed mutagenesis using QuikChange SDM kit (Stratagene, San Diego, CA, USA) according to the manufacturer's instructions. The following mutants were made using this SDM kit: a double mutant for Arg to Ala at positions 10 and 11 of LC3B (LC3B^{R10,11A}) and at positions 14 and 15 of GABARAP (GABARAP^{R14,15A}); a single mutant for Lys to Ala at position 47 of GABARAP (GABARAP^{K47A}); a double mutant for Lys to Ala at positions 46 and 47 of GABARAP (GABARAP^{K46,47A}); a triple mutant for Lys to Ala at positions 46, 47 and 48 of GABARAP (GABARAP^{K46,47,48A}); and single Cys point mutants of LC3B (LC3B^{Q15C} and LC3B^{S101C}) and GABARAP (GABARAP^{S16C} and GABARAP^{S88C}). All primers designed to introduce site-directed mutations were synthesized and purified by Sigma-Aldrich (See **Table 2.1**). The polymerase chain reaction-amplification products were evaluated by agarose gel electrophoresis and the parental methylated and hemimethylated DNA was digested by *DpnI* endonuclease (New England Biolabs). After inactivation of *DpnI* (80°C for 20 min), the digested polymerase chain reaction product was transformed into DH5-α *E. coli* chemo-competent cells and inoculated on LB (Sigma-Aldrich) plates containing 100 mg/mL ampicillin (Sigma-Aldrich). A total of 5 colonies were selected and their plasmids were isolated by mini-prep (GeneJET Plasmid Miniprep Kit, Thermo Fisher Scientific) and used for DNA sequencing (Secugen S.L.).

3.2.3 Recombinant Protein Expression and Purification

All proteins were purified from soluble fractions of bacterial extracts obtained in the absence of detergents, and were >90% pure as evaluated by Coomassie Blue-stained SDS-PAGE. *E.coli* BL21(DE3) cells were transformed with appropriate plasmids and cells were grown to OD_{600} of 0.8 and induced with 0.5 mM IPTG (Sigma-Aldrich) for 4 h at 20ºC in the case of GABARAP, GABARAP^{R14,15A}, GABARAP^{K47A}, GABARAP^{K46,47A}, GABARAP^{K46,47,48A}, GABARAP^{S16C}, GABARAP^{S88C} and 3 h at 37ºC for GABARAPL2 and LC3B, LC3B$^{G\Delta}$, LC3B^{R10,11A}, LC3B^{Q15C}, LC3B^{S101C}. Following centrifugation at 4,500 x g for 15 min, the pellet was resuspended and sonicated in breaking buffer [10 mM PBS, 20 mM Tris-HCl, pH 7, 150 mM NaCl, supplemented with freshly prepared 1 mg/mL lysozyme (Sigma-Aldrich), 1 mM DTT (Sigma-Aldrich), bacterial protease inhibitors (Roche) and 2.5 µg/mL DNase (Sigma-Aldrich)]. After removal of cellular debris by centrifugation at 30,000 x g for 30 min at 4ºC, the sample supernatant fraction was incubated with 1 mL glutathione Sepharose 4B (GE Healthcare) for 3 h at 4°C to bind GST-tagged proteins. Then PreScission Protease (GE Healthcare) was added at 100 units/mL in a 2-bed volume of PreScission Buffer (50 mM Tris-HCl pH 7.5, 150 mM NaCl, 1 mM EDTA) freshly prepared with 1 mM DTT and cleavage was performed for 4 h at 4°C. Cleaved protein was eluted and concentrated. Proteins were stored in 20% glycerol at -80°C.

3.2.4 Alexa Fluor 488 Protein Labeling

Purified proteins were first concentrated to 4-5 mg/mL (protein concentration should be at least 2 mg/mL for optimal results) and dialyzed against 0.1 M sodium bicarbonate (pH 8.2), 150 mM NaCl buffer to remove any amine-containing substances that would interfere with the conjugation reaction. Then 10 µL of the reactive dye solution [10 mg/mL of the Alexa Fluor® 488 dye (Molecular Probes) dissolved in DMSO (Sigma-Aldrich)] was slowly added to the protein solution. The reaction was incubated for 2 h at 37ºC with continuous stirring. A Sephadex G-25 chromatography column (GE Healthcare) was used to separate the conjugate from unreacted labeling reagent with PreScission buffer used as the eluent. The degree of labeling was determined measuring the absorbance of the protein-dye conjugate at 280 nm and at 488 nm for the dye. Labeled samples were subjected to SDS-PAGE and visualized using a VersaDoc MP 4000 Imaging System (Bio-Rad).

3.2.5 IANBD Cysteine-substituted Protein Labeling

In a typical labeling reaction, cysteine-substituted proteins were first

concentrated to 2-3 mg/mL and incubated with 1 mM TCEP (Sigma-Aldrich) for 30 min at room temperature. Then proteins were dialyzed against the labeling buffer [10 mM HEPES (Sigma-Aldrich), pH 7.3, 100 mM KCl, 1 mM EDTA] to remove TCEP. IANBD (Molecular Probes) dissolved in DMSO was then added in a small volume (15 to 25 µL) to the protein solution to give a final protein:probe molar ratio of 1:10 (NBD stock solution concentration was 30 mM). The mixture was incubated overnight at 4ºC with gentle stirring. Next the mixture was passed again through a PD-10 column (GE Healthcare) equilibrated with labeling buffer to separate the conjugate from unreacted labeling reagent. The stoichiometry of the NBD-protein conjugation reaction was calculated as the molar ratio of conjugated NBD and labeled proteins. The molar concentrations of the conjugated NBD and protein were determined from the absorbance at 488 nm (for NBD) and 280 nm (for proteins) using the molar extinction coefficients (eM) of 26500, 5960, 18450 and 11920 $M^{-1}cm^{-1}$ for NBD, LC3B, GABARAPL2 and GABARAP respectively.

3.2.6 Liposome Preparation

The appropriate lipids were mixed in organic solution [chloroform:methanol (2:1 v/v)] and the solvent was evaporated to dryness under a N_2 stream. Then the sample was kept under vacuum for 2 h to remove solvent traces and the lipids were swollen in PreScission buffer. Large unilamellar vesicles were prepared from swollen lipids, subjected to 10 freeze/thaw cycles, and then extruded [LIPEX Liposome Extrusion System (Transferra Nanosciences)] using 0.1 µm pore size Nuclepore filters (Whatman, Maidstone, UK) as described by Mayer and coworkers (Mayer *et al.*, 1986). SUVs were obtained by sonicating MLVs with a probe tip sonicator (MSE Soniprep 150, MSE) for 20 min (10 sec on, 10 sec off) on ice. Vesicle size was checked by quasi-elastic light scattering using a Malvern Zeta-Sizer 4 spectrometer (Malvern Instruments). LUVs had an average diameter of 100 nm and SUVs average diameter was 60 nm. Lipid concentration was determined by phosphate analysis.

3.2.7 Monolayer Surface Pressure Measurements

Surface pressure experiments were carried out in a multi-well Delta Pi-4 Langmuir balance (Kibron Inc., Helsinki, Finland) under constant stirring. Protein-induced changes in surface pressure at the air-water interface and protein-lipid monolayer interactions were studied at either 25ºC or 37ºC. Monolayers were formed by spreading a small amount of the lipid mixtures in chloroform:methanol (2:1 v/v) solution on top of assay buffer (20 mM HEPES pH 7.4, 150 mM NaCl, 1 mM $MgCl_2$, 0.2

mM DTT) until the desired initial surface pressure was reached. Proteins were injected with a micropipette through a hole connected to the subphase.

3.2.8 Protein-Lipid Overlay Assay

Stock solutions of different lipids were solubilized in 2:1:0.8 MeOH:$CHCl_3$:H_2O, spotted onto Hybond C nitrocellulose (GE Healthcare) and allowed to dry. To detect LC3B by immunoblotting, the nitrocellulose was first blocked with 5% fat-free milk in PBS for 1 h and further incubated for 1 h with LC3B in PreScission buffer at 37ºC. The nitrocellulose was washed 4 times, 10 min each, with PBS, and soaked in 5% fat-free milk in PBS with an anti-LC3 monoclonal antibody at 1:1000 dilution overnight at 4ºC. The nitrocellulose was washed 4 times with PBS and soaked in 5% fat free milk in PBS with HRP-conjugated anti-mouse antibody (Santa Cruz Biotechnology) at a 1:5000 dilution for 1 h at room temperature. After washing with PBS 4 x 10 min at room temperature, the protein was detected by chemiluminescence. Protein bands were digitalized and integrated densities were measured using Quantity One software (Bio-Rad).

3.2.9 Sucrose Gradient Centrifugation of Liposomes

Recombinant proteins as indicated (10 µM) were incubated with 3 mM liposomes (containing 0.05 mol percent Rho-PE for detection) for 1 h at 37ºC in 200 µL PreScission buffer. 125 µl protein/lipid mix was diluted to 300 µL in PreScission buffer containing 2.4 M sucrose (Sigma-Aldrich). Then the reaction mix was transferred to a centrifuge tube. The 1.4 M sucrose layer was overlaid with 400 µL PreScission buffer containing 0.8 M sucrose and 300 µL PreScission buffer containing 0.5 M sucrose. Sucrose step gradients were centrifuged in a TLA-120.2 rotor (Beckman Coulter) at 356,160 x g for 3 h at 4ºC. Four 250-µL fractions were pipetted, starting from the bottom. The top fraction (T), containing liposomes as indicated by the rhodamine fluorescence, and the bottom fraction (B) containing the unbound protein were analyzed by SDS-PAGE and western blotting.

3.2.10 Fluorescence Spectroscopy

Fluorescence measurements were performed in a QuantaMaster spectrofluorometer (Photon Technology International) in a thermostatically controlled 1-cm path length cuvette with constant stirring at 37°C. For Trp measurements, excitation wavelength was 295 nm, the band-pass was 5 nm, and emission spectra of Trp were measured between 310 nm and 450 nm at a rate of 1 nm/sec. For NBD fluorescence

measurements, the excitation wavelength was 465 nm, the band-pass was typically 5 nm, and emission spectra of NBD were measured between 520 nm and 650 nm at a rate of 1 nm/sec. A 515 nm cut-off filter was placed between the sample and the emission monochromator to avoid scattering interference. In all cases, background intensities from samples lacking protein were substracted from the intensities measured in protein containing samples.

3.2.11 Far-UV CD Measurements

Far-UV CD spectra were recorded on a Jasco J-810 spectropolarimeter (Jasco Spectroscopic Co. Ltd.) equipped with a JASCO PTC-423S temperature control unit using 1-mm path length cell. Data were collected every 0.2 nm at 50 nm/min from 260 to 200 nm with a bandwidth of 2 nm, and results were averaged from 20 scans. The contribution of buffer to the measured ellipticity was subtracted for each protein as the blank.

3.2.12 GUV Preparation

GUVs were prepared using the electroformation method developed by Angelova & Tsoneva, (1999). For direct visualization under the microscope a homemade chamber was used (Fidorra *et al.*, 2006). Transferred GUVs were formed in a PRETGUV 4 chamber supplied by Industrias Técnicas ITC. Stock solutions of lipids (2 mM total lipid containing 0.5 mol% Rho-PE) were prepared in chloroform:methanol (2:1, v/v), 4 µl of the lipid stocks were added onto the surface of Pt electrodes and solvent traces were removed by evacuating the chamber under high vacuum for at least 2 h. Next, the Pt electrodes were covered with 400 µl of a 300 mM sucrose solution. The Pt electrodes were connected to a generator (TG330 function generator, Thurlby Thandar Instruments) under AC field conditions (10 Hz, 1 VRMS for 2 h, followed by 2.5 Hz, 1 VRMS, 1 h 30 min).

3.2.13 Confocal Fluorescence Microscopy

After GUV formation, the vesicle suspension (in 300 mM sucrose) was transferred to microscopy chambers pretreated with BSA (2 mg/mL) and containing an equiosmolar buffer solution of 50 mM Tris-HCl, 150 mM NaCl, 1 mM EDTA and 1 mM DTT, pH 7.5. Due to the different density of the two solutions, the vesicles sedimented at the bottom of the chamber, and this facilitated observation under the microscope. Finally, LC3B- or GABARAP-Alexa 488 (10 µM) were added to study protein binding to GUVs after incubation at 37ºC. The chamber was placed on an inverted confocal

fluorescence microscope (Nikon D-ECLIPSE C1, Nikon). The excitation wavelengths were 488 nm for protein-Alexa488 and 561 nm for Rho-PE; and the emission was collected using 515 ± 15 nm and 593 ± 20 nm band-pass filters, respectively. Imaging was performed at room temperature. Image treatment was performed using the EZ-C1 3.20 software (Nikon).

3.2.14 Statistical Analyses

Statistical analyses were performed by ANOVA with a *post hoc* analysis by the Student-Neuman-Keuls test.

3.3 Results

3.3.1 Human Orthologs of Yeast Atg8

Atg8 family proteins are essential factors in the execution phase of autophagy (Mizushima *et al.*, 2011). Whereas the yeast *Saccharomyces cerevisiae* contains a single ATG8 gene, in humans the ATG8 family contains 4 LC3 subfamily genes (LC3A, LC3B, LC3B2 and LC3C) and 3 GABARAP subfamily paralog genes (GABARAP, GABARAPL1 and GABARAPL2); another human paralog of this subfamily, GABARAPL3, is currently considered to be a pseudogene, and no data at present link it with autophagy.

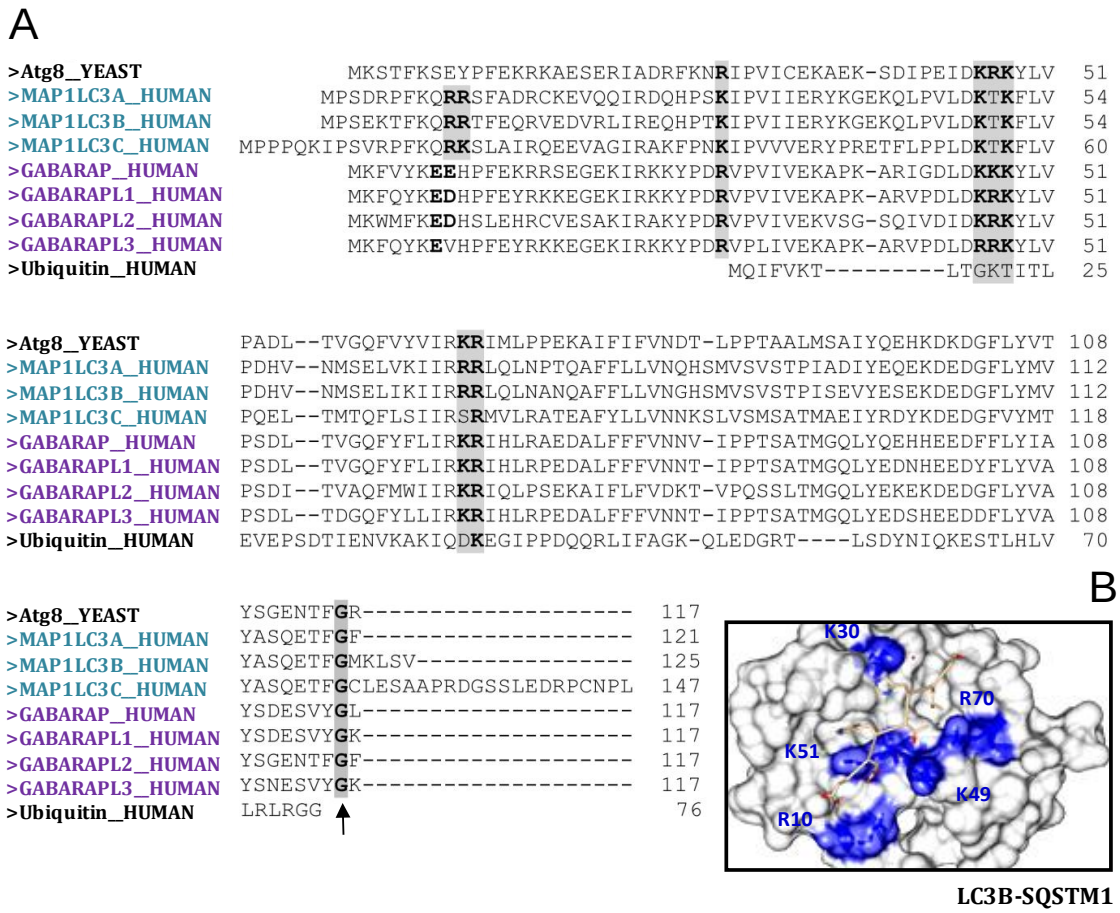

Figure 3.1. Human Atg8 family members. (**A**) Sequence alignment (Clustal Omega) of yeast Atg8, Atg8 human orthologs and ubiquitin. Highlighted in grey are the highly conserved basic amino acids, which have the potential to bind negatively charged amino acids located at the C- and N-terminal regions of the conserved LIR (consensus: W/Y/FxxL/I/V) present in the different cargo receptors during selective autophagy. (**B**) View of LC3B bound to the SQSTM1 LIR motif (PDB: 2ZJD). Highlighted in blue are the positively charged residues in LC3B that stabilize binding to SQSTM1 LIR motif. Picture was created by UCSF Chimera.

Originally implicated in intracellular trafficking processes all Atg8 orthologs are found within autophagosomes through binding to PE via a conserved C-terminal glycine (see **Figure 3.1A**, black arrow). Each of the 3 families is very well conserved across its entire length and all are very similar to each other in most of their positions (**Figure 3.1A**). However, the N-terminal region differs between the various mammalian Atg8 proteins (the N terminus of LC3 subfamily members is strongly basic, whereas in the GABARAP subfamilies this region is acidic) (see **Figure 3.10**). It has been proposed that differences between the various human Atg8 proteins in this N-terminal region might reflect their distinct functions. Moreover, in spite of being ubiquitously expressed some subfamily members are expressed at increased levels in certain tissues.

All Atg8 orthologs share a strong structural similarity containing 2 N-terminal α-helices (N-terminal arm) in addition to their C-terminal ubiquitin core (ubiquitin-like domain). The ubiquitin core contains a hydrophobic feature that is conserved among family members and is suggested to have a role in protein-protein interactions (**Figure 3.1B**), namely binding to the conjugation machinery proteins.

In this study, LC3B, GABARAPL2, GABARAP and their mutant forms were expressed in their GST-tagged form in *E. coli* BL21 (DE3) and purified using glutathione Sepharose beads. All Atg8 human orthologs were expressed and purified with the C-terminal Gly exposed (**Figure 3.2**).

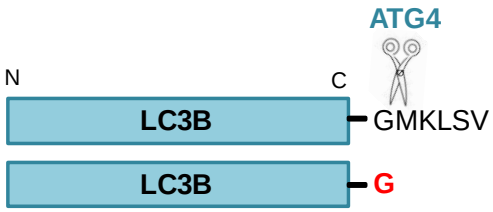

Figure 3.2. Schematic representation of the expressed Atg8 orthologs. LC3B wild type and LC3B with the C-terminal Gly exposed are shown. All human orthologs were expressed with the C-terminal Gly exposed such that no ATG4-mediated cleavage would be necessary.

Next, recombinant ATG protein purity was evaluated and the secondary structure and correct folding were assessed using CD. As expected from previously reported data of these proteins, LC3B, GABARAPL2 and GABARAP gave rise to CD spectra with minima near 205 nm compatible with a mix of α-helix and intrinsically disordered structures (**Figures 3.3 and 3.4**). Circular dichroism was also used to check for any conformational changes induced by protein mutagenesis or labeling.

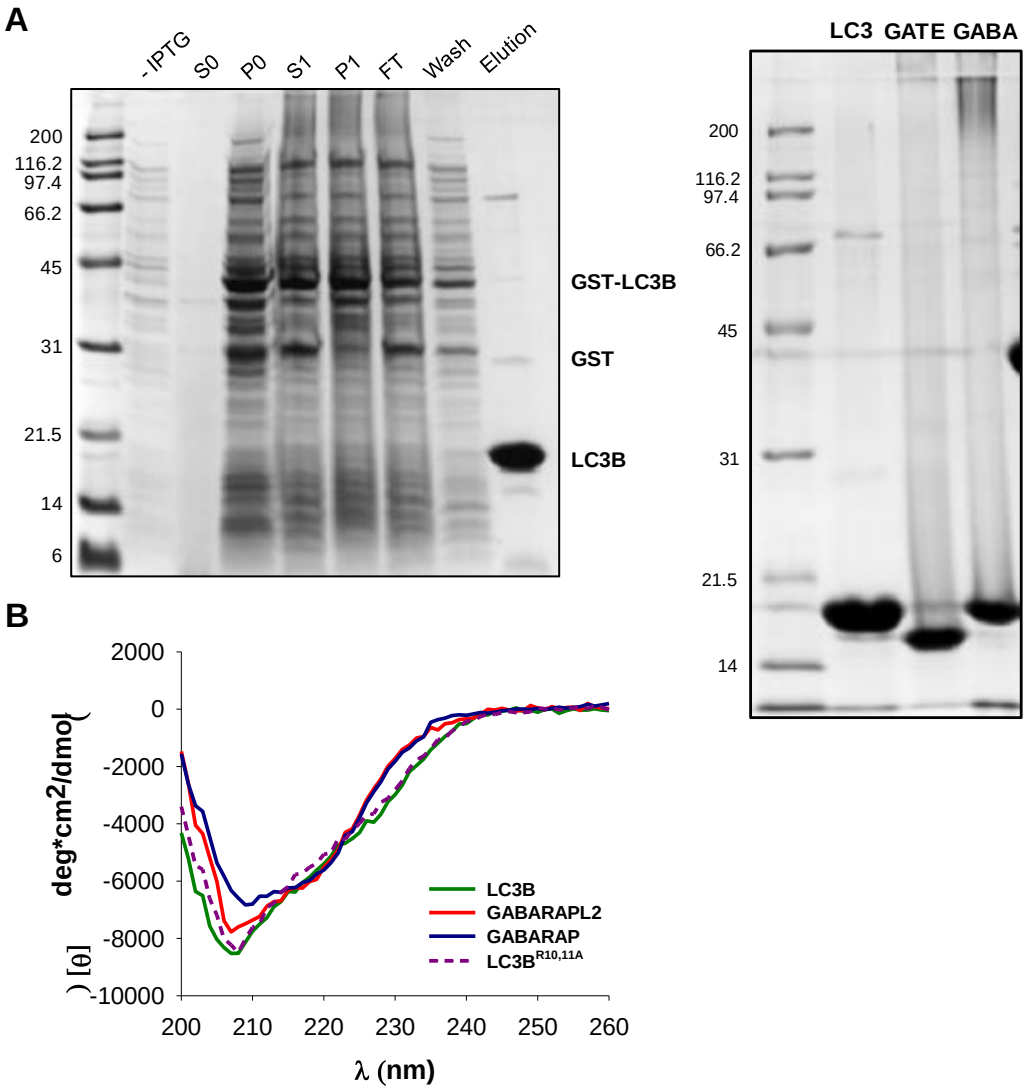

Figure 3.3. Expression and purification of recombinant LC3B, GABARAPL2/GATE-16 and GABARAP. (**A**) Coomassie Blue-stained gel showing purification steps. LC3B-expressing *E.coli* cells were lysed and soluble and insoluble fractions were separated by centrifugation. S0/P0 and S1/P1 correspond to the soluble and insoluble fractions before and after tip sonication, respectively. S1 was incubated with glutathione Sepharose beads for 3 h at 4ºC to allow binding of LC3B to the beads (left-hand panel). After SEC, all proteins were >90% pure as evaluated by Coomassie-stained SDS-PAGE (right-hand panel). Molecular masses are shown in kDa on the left-hand side. (**B**) CD analysis of Atg8 orthologs and LC3B^{R10,11A} mutant in 50 mM Na_2HPO_4, 20 mM KCl, pH 7.0.

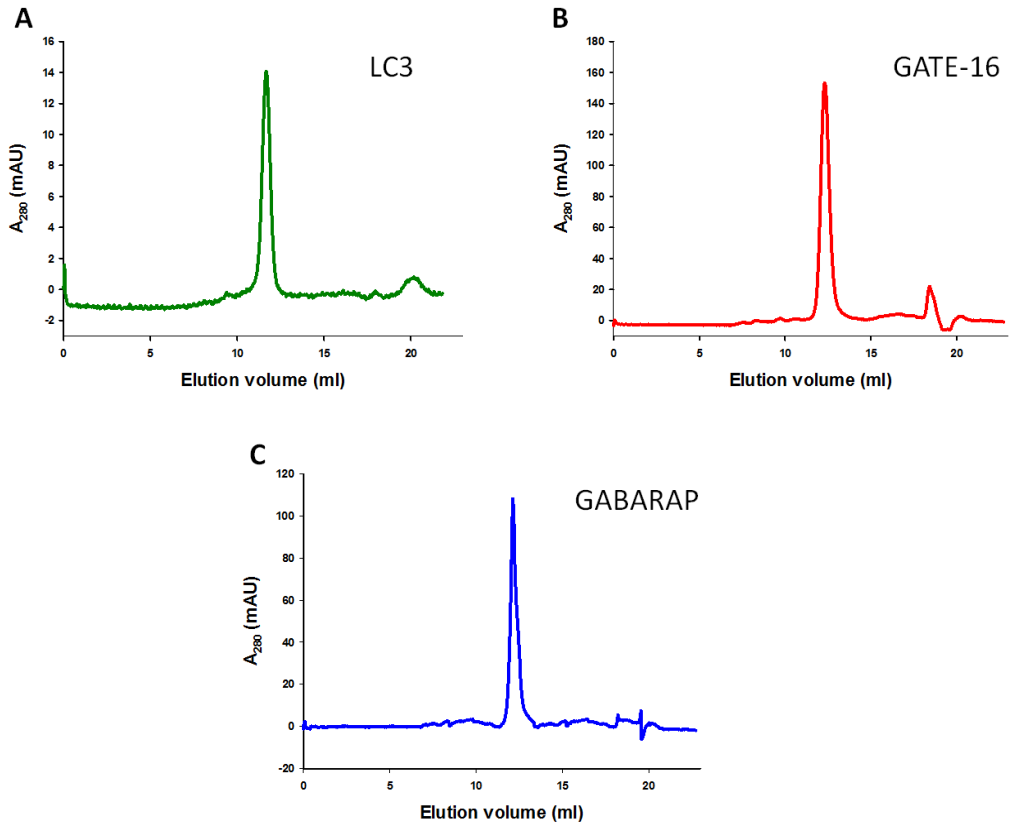

Figure 3.4. Elution profiles of human LC3B, GATE-16/GABARAPL2 and GABARAP (**A-C**). After elution from gluthatione beads, ATG proteins were subjected to size exclusion chromatography on a Superdex 75 10/300 GL column.

3.3.2 LC3B Interaction with CL-containing Membranes

CL, the signature lipid of mitochondria, is a unique glycerol-based phospholipid comprising two phosphate moieties and four acyl groups of which linoleic acid is predominant (Osman *et al.*, 2011). CL is essential not only for normal mitochondrial function (Maguire *et al.*, 2016; Ren *et al.*, 2014) but it also plays a prominent role in disease-related processes such as apoptosis (Gonzalvez & Gottlieb, 2007; Maguire *et al.*, 2016) or mitophagy (Chu *et al.*, 2013; Hsu & Shi *et al.*, 2016; Maguire *et al.*, 2016; Antón *et al.*, 2016). In fact, although CL is usually considered to be a specific component of the inner mitochondrial membrane, the intramitochondrial location of CL is highly dynamic and CL externalization to the outer mitochondrial membrane has recently been shown to act as a signal for LC3, resulting in LC3 translocation to the OMM and targeted removal of damaged mitochondria via autophagy (Chu *et al.*, 2013). Based on these observations, we decided to define in more detail the molecular mechanisms underlying LC3-CL interaction (Antón *et al.,* 2016).

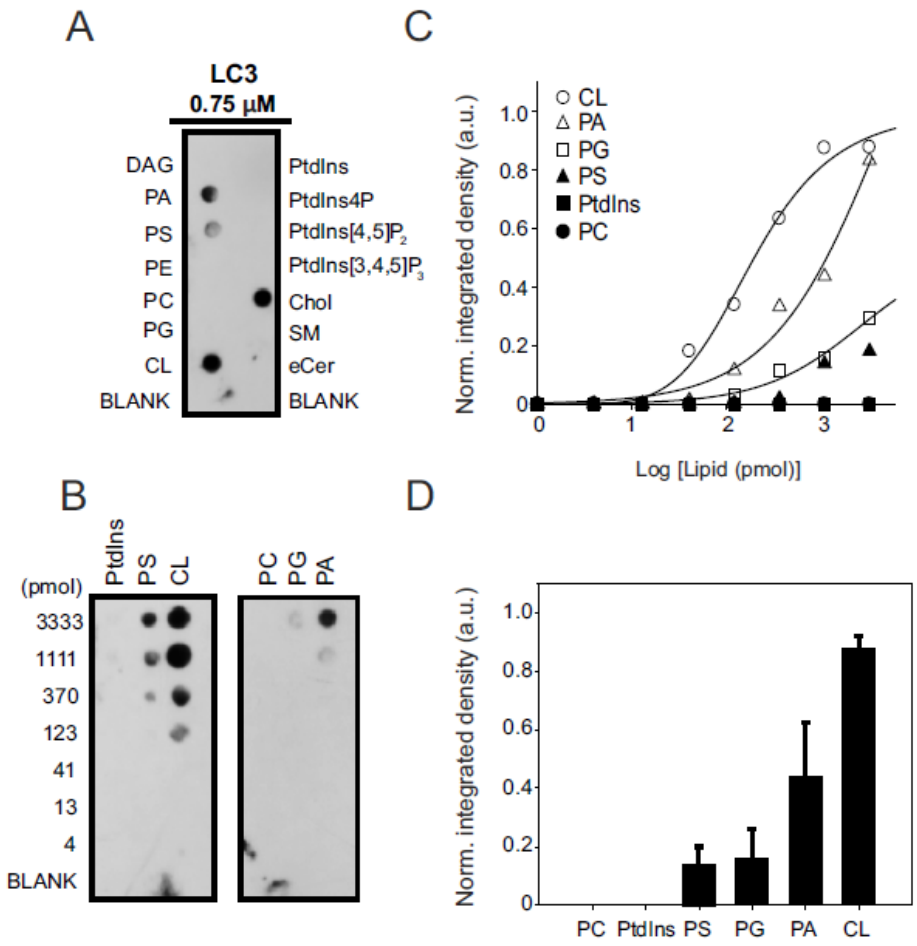

Figure 3.5. LC3B binds CL directly and preferentially over other anionic lipids. LC3B immunoreactivity is shown from a representative protein:lipid dot-blot experiment with some of the most common glycerolipids and sphingolipids present in mammalian cells (1 nmol of each lipid) (**A**) and with increasing amounts of some of those lipids (**B**). (**C**) Integrated LC3B immunoreactivity was measured at each spot and normalized for each lipid, and the data were fitted with a sigmoidal equation of the type f = (y0+a*xb)/(cb+xb), from which an apparent Hill coefficient (b) of 5.3 ± 1.2 for CL binding could be estimated (R^2 = 0.991). (**D**) Quantitative assessment of bound LC3B (0.75 µM) with 1.11 nmol of each lipid. LC3B immunoreactivity was measured at each spot by immunoblotting using anti-LC3 antibody and densitometry. Data shown as mean ± SEM (n = 3).

First we performed a PLO assay in which recombinant LC3B was incubated with a nitrocellulose membrane containing some of the most common glycerolipids and sphingolipids present in mammalian cells (**Figure 3.5A**). Among the lipid species examined, LC3B bound most strongly CL and Chol and less strongly the anionic lipids PS and PA. Interestingly, LC3B binding was not detectable for PtdIns4P, which has the same net negative charge as CL, nor with the polyanionic lipids PtdIns[4,5]P_2 or PtdIns[3,4,5]P_3, with even higher net negative charges. Dose-response experiments indicated that LC3B bound CL with 5-fold higher apparent affinity than PS or PG, and 2-fold higher affinity than PA (**Figure 3.5B,D**). These results indicate that LC3B

recognizes different anionic phospholipid species and displays a preference for CL. The dose-response data for LC3B-CL binding (**Figure 3.5C**) can be fitted to a sigmoidal curve, as detailed in the figure legend, showing a high positive cooperativity for the binding, apparent Hill coefficient n = 5.3. This might mean that binding of LC3B to one of the phosphate groups of CL would make easier the binding of the second phosphoryl moiety.

Next, we analyzed the interaction of LC3B with lipid monolayers using a Langmuir balance. Injection of LC3B into the aqueous phase led to a rapid, dose-dependent increase of lateral pressure (π) at the air-water interface (**Figure 3.6A, left-hand panel**). An increase in π is an indication that the protein is adsorbing onto the air-water interface, i.e. that it has surface-active properties. The increase in surface pressure appears to reach a plateau value of ~15 mN/m at 1.5 μM LC3B.

Lipid monolayers composed of either PC:DOPE (80:20 mol ratio), PC:DOPE:CL (55:20:25 mol ratio), PC:DOPE:PS (55:20:25 mol ratio), or PC:DOPE:PtdIns4P (55:20:25 mol ratio) were prepared with constant surface area at an initial pressure of 19 mN/m, i.e. above the surface pressure measured for the pure protein (~15 mN/m). Recombinant LC3B was added to the subphase, and the resulting increase in monolayer surface pressure was monitored in real-time (**Figure 3.6A, right-hand panel**). As shown in **Figure 3.6B**, the increase in surface pressure observed with PC:DOPE:CL monolayers under near-equilibrium conditions was higher than the value observed with electrically-neutral PC:DOPE monolayers, indicating that LC3B inserted more favorably into negatively charged monolayers.

For a quantitative measure of the LC3B ability to penetrate into lipid monolayers, critical surface pressure values were determined. In these experiments, the Δπ upon LC3B addition was measured as a function of the π_0. The data were fitted to a straight line, whose x-intercept corresponded to the monolayer π_c. The results in **Figure 3.6B** show that LC3B insertion was highest (or easiest) when anionic lipids were present in the monolayer. The $LC3B^{G\Delta}$ mutant was also examined, lacking the C-terminal Gly of LC3B, to test whether differences observed in LC3B also appeared in its inactive mutant form. $LC3B^{G\Delta}$ was found to be surface-active and it also exhibited a higher insertion into PC:DOPE:CL monolayers.

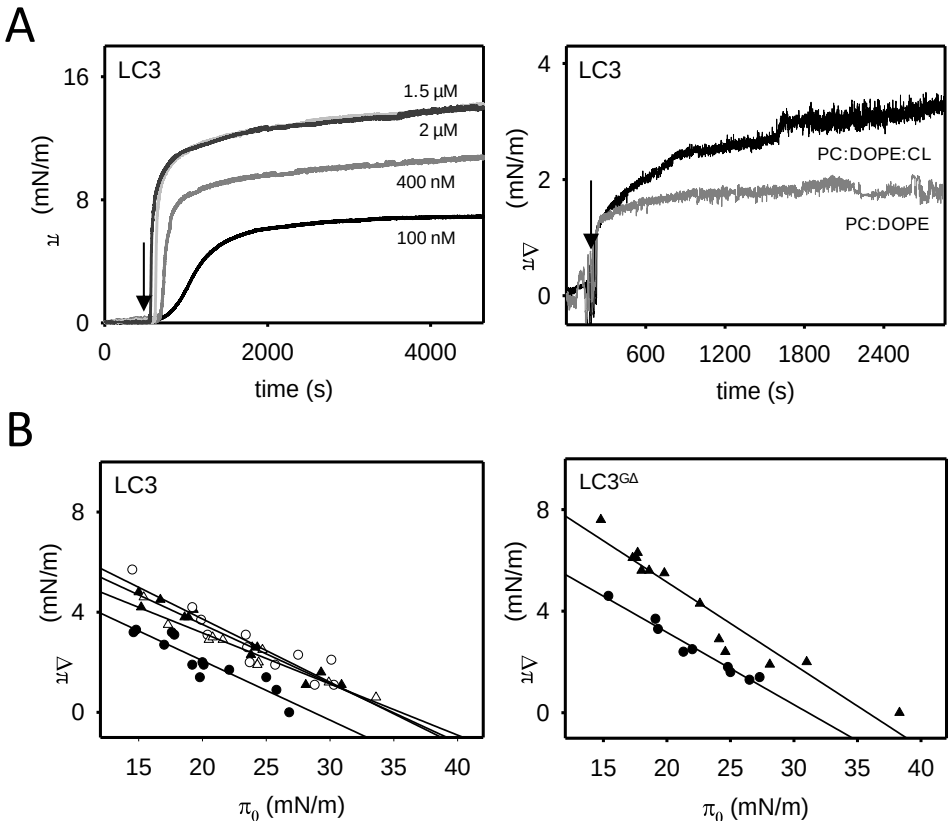

Figure 3.6. LC3B and LC3B^{GΔ} insertion into lipid monolayers. (**A**) Representative time courses of LC3B adsorption at the air-water interface (left-hand panel) and representative time courses of increase in lateral pressure after LC3B (1.5 µM) insertion into PC:DOPE (80:20 mol ratio) or PC:DOPE:CL (55:20:25 mol ratio) monolayers (right-hand panel) at 25ºC. (**B**) Maximum increase in lateral pressure after LC3B or LC3B^{GΔ} insertion into lipid monolayers at 25ºC. Lipids were: [●] PC:DOPE (80:20 mol ratio), [▲] PC:DOPE:CL, [○] PC:DOPE:PS and [Δ] PC:DOPE:PtdIns4 (55:20:25 mol ratio). Data reported as a function of initial lateral pressure π_0. Very similar results were obtained at 37ºC (data not shown).

Protein	Lipid Composition	π_c
LC3B	**PC:DOPE (80:20)**	28.7 mN/m (±0.40)
	PC:DOPE:CL (55:20:25)	35.0 mN/m (±0.30)
	PC:DOPE:PtdIns4P (55:20:25)	35.6 mN/m (±0.29)
	PC:DOPE:PS (55:20:25)	34.7 mN/m (±0.53)
LC3B^{GΔ}	**PC:DOPE (80:20)**	31.0 mN/m (±0.23)
	PC:DOPE:CL (55:20:25)	35.8 mN/m (±0.64)

Table 3.1. Critical pressures (π_c) for LC3B and LC3B^{GΔ} insertion into lipid monolayers. Data calculated from the straight lines in **Figure 3.6B**. The tendency line-associated standard error is given for each π_c.

The critical surface pressure is a measure of the penetration capacity of a protein entering a monolayer: if this pressure exceeds 30 to 32 mN/m, then the protein is considered to be capable of membrane insertion (see **Table 3.1**). This is based on the estimation of ~30 mN/m as the average physiological surface pressure in cell membranes (Marsh, 1996).

Thus, our data indicate that LC3B inserts at least part of its mass into the monolayer and that negatively-charged groups favor the insertion. This is compatible with the idea of CL stabilizing initial electrostatic interactions leading to a partial insertion of LC3B into the bilayer (Chu *et al.*, 2013).

To test whether LC3B-CL interaction would occur in a bilayer membrane vesicle in which lipids maintain a certain bilayer curvature and could form domains, we performed liposomal float-up assays. In these experiments, pure LC3B was incubated with liposomes of a defined curvature and lipid composition and protein association with liposomes was assessed by the protein ability to float with the vesicles after equilibrium sucrose gradient centrifugation. Equivalent amounts of the top (T) and bottom (B) fractions of the gradient, corresponding respectively to proteoliposomes and to unbound protein, were then subjected to SDS-PAGE and western blot analysis. The immunoblot response of LC3B was quantified at different protein concentrations by densitometry and the data were linearly fitted by the least-squares method (**Figure 3.7A**). The LC3B maximal binding response was observed with CL-containing LUVs, while it did not bind PC:DOPE vesicles. Interestingly, LC3B did not bind either PtdIns4P-containing liposomes, although those vesicles had the same net negative charge as the CL-containing ones (**Figure 3.8A**). Furthermore, considering that LC3B exhibited strong binding affinity for Chol in PLO assays (**Figure 3.5A**), we also analyzed the binding of LC3B to model membranes containing both CL and Chol. However cholesterol inclusion in CL-enriched membranes did not lead to a higher binding response of the protein (**Figure 3.8A**). Moreover, no LC3B binding was observed with LUVs or SUVs composed of PC:DOPE:Chol (50:20:30) (data not shown). Thus the presence of Chol in those lipid compositions did not significantly affect LC3B binding to liposomes. We also analyzed the protein dose-dependence of the interaction by incubating liposomes with LC3B at 3 different protein concentrations. As shown in **Figure 3.8B**, little or no increase in LC3B binding to CL-containing vesicles was detected above 10 μM protein. Finally, **Figure 3.8C** shows the dose-dependent binding of LC3B to CL-containing membranes; half-maximal binding occurred at 1.65 ± 0.2 mM total lipid. This suggests that the observed association of LC3B with PC:DOPE:CL vesicles is specific. Indeed, no protein binding was observed with

PC:DOPE vesicles even at the highest lipid concentration. These results suggest that LC3B is not an integral membrane protein but that it binds membranes through an interaction with acidic phospholipids, in agreement with the hypothesis proposed above that LC3B inserts only part of its mass into the membrane and that negatively-charged groups favor its insertion.

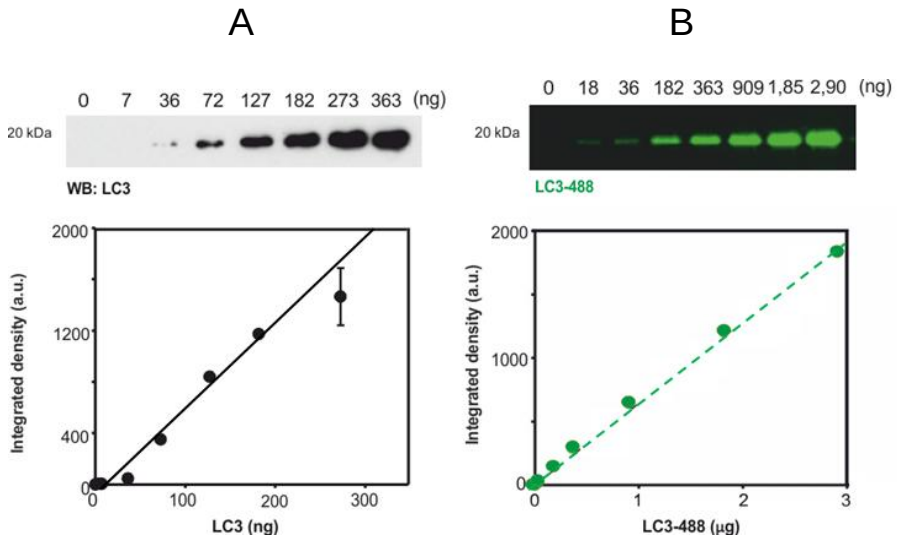

Figure 3.7. Least-squares linear fit to the experimental data. (**A**) Plot of immunoblot response of LC3B quantified by densitometry versus protein concentration. Line represents least-squares linear fit to the experimental data (R^2 = 0.972). (**B**) Plot of Alexa 488 fluorescence of LC3B quantified by densitometry versus protein concentration. Dashed line represents least-squares linear fit to the experimental data (R^2 = 0.997).

Moreover we have investigated the possible effect of changes in environmental pH on LC3B binding to model CL-containing membranes. CL is supposed to have only one negative charge below pH 7.5 (Kates *et al.*, 1993). In that case the electrostatic repulsion between CL phosphate groups might be reduced which together lowers the effective size of the headgroup and the smaller size of the polar headgroup should enhance the propensity of CL to form inverted nonlamellar lipid phases (Lewis & McElhaney, 2009). Regarding the pH effect on LC3B, the protein has a theoretical pI of 8.89 thus a net positive charge under our experimental conditions, with the charge becoming more positive as pH is lowered. As predicted, *in vitro* interaction of LC3B with CL-containing bilayers appeared to be highest at lower pH (**Figure 3.8D**).

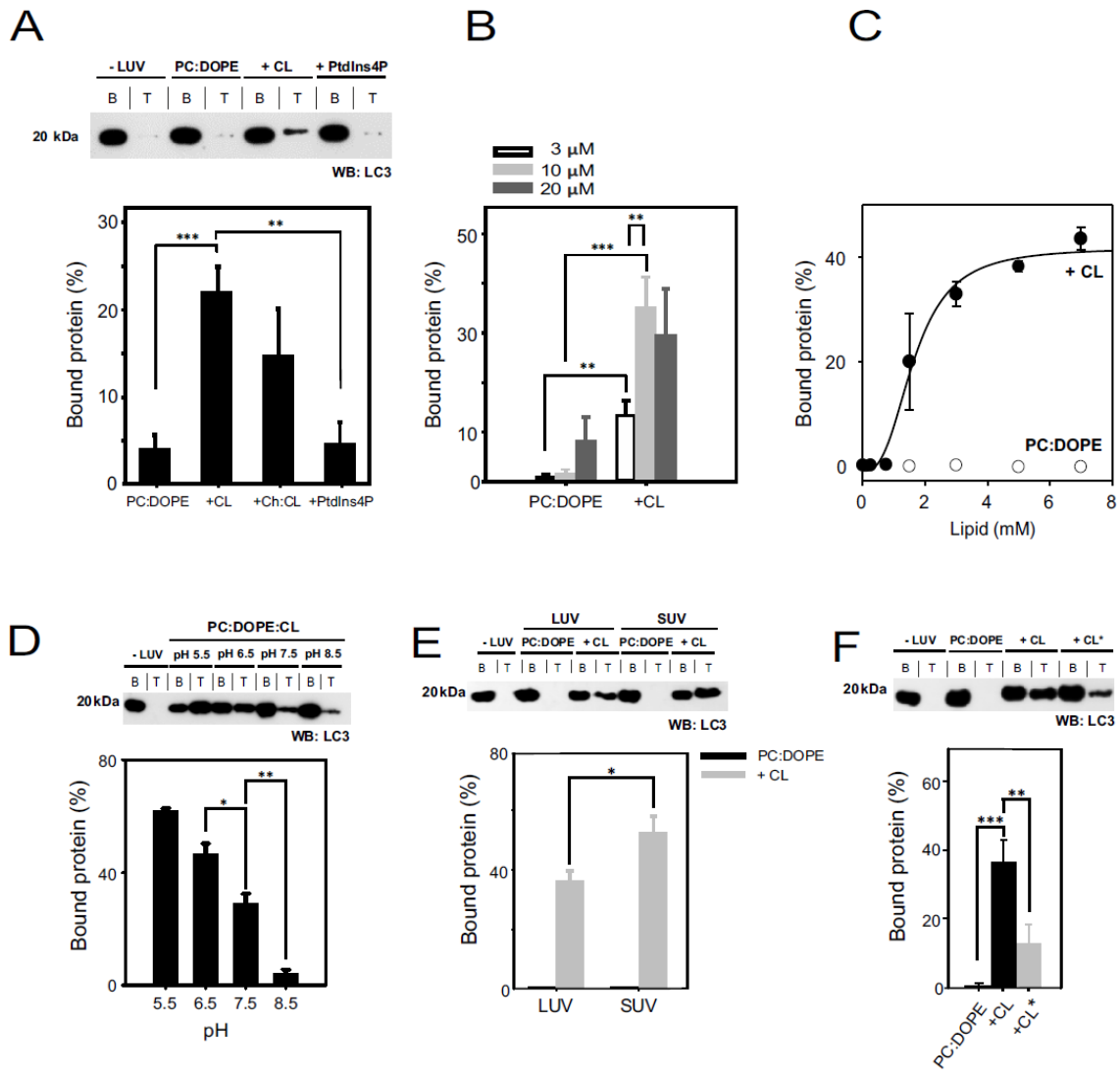

Figure 3.8. LC3B interacts preferentially with CL-containing liposomes. The liposome-bound protein fraction was analyzed after flotation in a sucrose density gradient by SDS-PAGE/immunoblot analysis and quantified by densitometric integration of the dots. (**A**) 10 µM LC3B was incubated with 3 mM LUVs composed of either PC:DOPE (80:20 mol ratio), PC:DOPE:CL (50:20:30 mol ratio), PC:DOPE:Chol:CL (30:14:33:23 mol ratio) or PC:DOPE:PtdIns4P (50:20:30 mol ratio). Molecular mass is shown in kDa on the left-hand side. Data shown as mean ± SEM (n = 3); **P = 0.001 to 0.01, ***P < 0.001. (**B**) LC3B dose-dependence analysis using 3, 10 and 20 µM protein and 3 mM liposomes. Data shown as mean ± SD (n = 3); **P = 0.001 to 0.01, ***P < 0.001. (**C**) Protein:lipid ratio effect on LC3B binding to PC:DOPE or PC:DOPE:CL vesicles. The continuous line represents the best fit of the data, assuming an EC50 of 1.65 ± 0.2 mM for binding to PC:DOPE:CL vesicles. Data shown as mean ± SEM from at least 3 independent experiments. (**D**) Effect of pH on LC3B (10 µM) binding to PC:DOPE:CL large vesicles (3 mM). Data shown as mean ± SEM (n = 3); *P = 0.01 to 0.05, **P = 0.001 to 0.01. (**E**) 10 µM LC3B was incubated with 3 mM LUV or SUV to analyze vesicle size effect on the interaction. Data shown as mean ± SD (n = 3); *P = 0.01 to 0.05. (**F**) Comparison between heart bovine (CL) and *E. coli* (CL*) cardiolipins in the interaction. 10 µM LC3B was incubated with 3 mM LUV of either composition. Data shown as mean ± SD (n = 3); **P = 0.001 to 0.01, ***P < 0.001.

Membrane curvature is increasingly being reported to play an important role during autophagy (Fan *et al.*, 2011; Rostislavleva *et al.*, 2015; Antonny, 2011; Horenkamp *et al.*, 2015). Mitophagy is preceded by mitochondrial fission, which divides elongated mitochondria into smaller pieces of manageable size for encapsulation, and lipidation of LC3 has been recently proposed to occur preferentially on small, highly curved membranes *in vivo* and *in vitro* (Nath *et al.*, 2014). To address the effect of vesicle radius on LC3 membrane binding, we examined the interaction of LC3B with PC:DOPE and PC:DOPE:CL vesicles of 3 different sizes: SUV (~60 nm), LUV (~100 nm) and GUV (5-100 µm). As shown in **Figures 3.8E and 3.13B**, we observed almost no binding of LC3B to PC:DOPE vesicles independently of their size. However LC3B bound CL-enriched SUVs better than LUVs and did not bind CL-containing GUVs. These results support the notion that interaction of LC3B with CL is promoted in the context of a curved membrane.

Apart from containing net negative charges CL is also characterized by a high degree of unsaturation of its acyl chains. This confers a high degree of flexibility to the membrane and the latter may in turn promote LC3 association. To evaluate this particular issue we analyzed LC3B binding to liposomes containing CL from *E.coli* which presents relatively short and fully-saturated or mono-unsaturated acyl chains. As shown in **Figure 3.8F**, LC3B bound significantly less the more rigid vesicles containing bacterial CL.

Additionally to the float-up assays, we used NBD-conjugated monocysteine LC3B mutants ($LC3B^{Q15C}$ and $LC3B^{S101C}$) for studying LC3B interaction with CL-containing membranes. To enhance the efficiency of covalent modification with NBD, Cys substitutions were made at sites in LC3B with SASA values greater than 45% (**Table 3.2**). Since the protein was labeled in each case with a unique NBD moiety, this approach allowed us to characterize the association to the membrane of specific sites of the protein. We first examined the spectral properties of the NBD-labeled $LC3B^{Q15C}$ mutant in the absence (black line) and presence (green line) of PC:DOPE, PC:DOPE:CL and PC:DOPE:PtdIns liposomes (**Figure 3.9A**). In the absence of liposomes, $LC3B^{Q15C\text{-}NBD}$ displayed NBD $\lambda_{em(max)}$ values around 550 nm indicating a predominantly solvent-exposed NBD environment. No changes in the NBD spectrum were observed upon incubation with SUVs composed of PC:DOPE or LUVs composed of PC:DOPE:PtdIns, in agreement with the low affinity of the protein observed for liposomes that did not contain CL (**Figure 3.8A**). However incubation with CL-containing liposomes produced a substantial increase in $LC3B^{Q15C\text{-}NBD}$ fluorescence intensity and blue-shifts in $\lambda_{em(max)}$ values, the change observed in the presence of CL-

enriched SUVs being larger than with LUVs (**Figure 3.9A**). As shown in **Figure 3.9B**, virtually no change in the emission spectrum of $LC3B^{S101C\text{-}NBD}$ was observed upon addition of large or small vesicles containing CL (red line), unlike the situation found with the $LC3B^{Q15C}$ mutant. Based on these data, we propose a structural model in which residue C101, which is located within the C terminus of the protein, remains in a hydrophilic environment before and after LC3B binding to CL-containing liposomes, while residue C15, which is localized within the N terminus, moves from a hydrophilic to a hydrophobic environment upon LC3B membrane binding (**Figure 3.9C**).

Protein	Residue	Localization	Modification	SASA (%)
LC3B	Q15	N terminus	Mutation to Cys and NBD labeling	47.0
	S101	C terminus	Mutation to Cys and NBD labeling	71.9
GABARAP	S16	N terminus	Mutation to Cys and NBD labeling	58.0
	S88	C terminus	Mutation to Cys and NBD labeling	90.8
GABARAPL2	C15	N terminus	NBD labeling	40.4

Table 3.2. Characterization of NBD-labeled protein forms. SASA values were obtained from GETAREA for PDB: 1UGM (LC3), 1GNU (GABARAP) and 1EO6 (GABARAPL2).

To sum up, results obtained using 4 independent lipid-interaction assays (lipid dot-blot, lipid monolayer surface pressure measurements, liposome flotation and NBD fluorescence spectroscopic analysis) concur in suggesting that (i) LC3B interacts preferentially with CL over other anionic phospholipids, (ii) LC3B-CL interaction relies on both electrostatic and other CL-mediated changes in membrane properties, e.g. bilayer fluidity and (iii) LC3B C terminus remains exposed to the hydrophilic environment after protein binding to CL-enriched membranes.

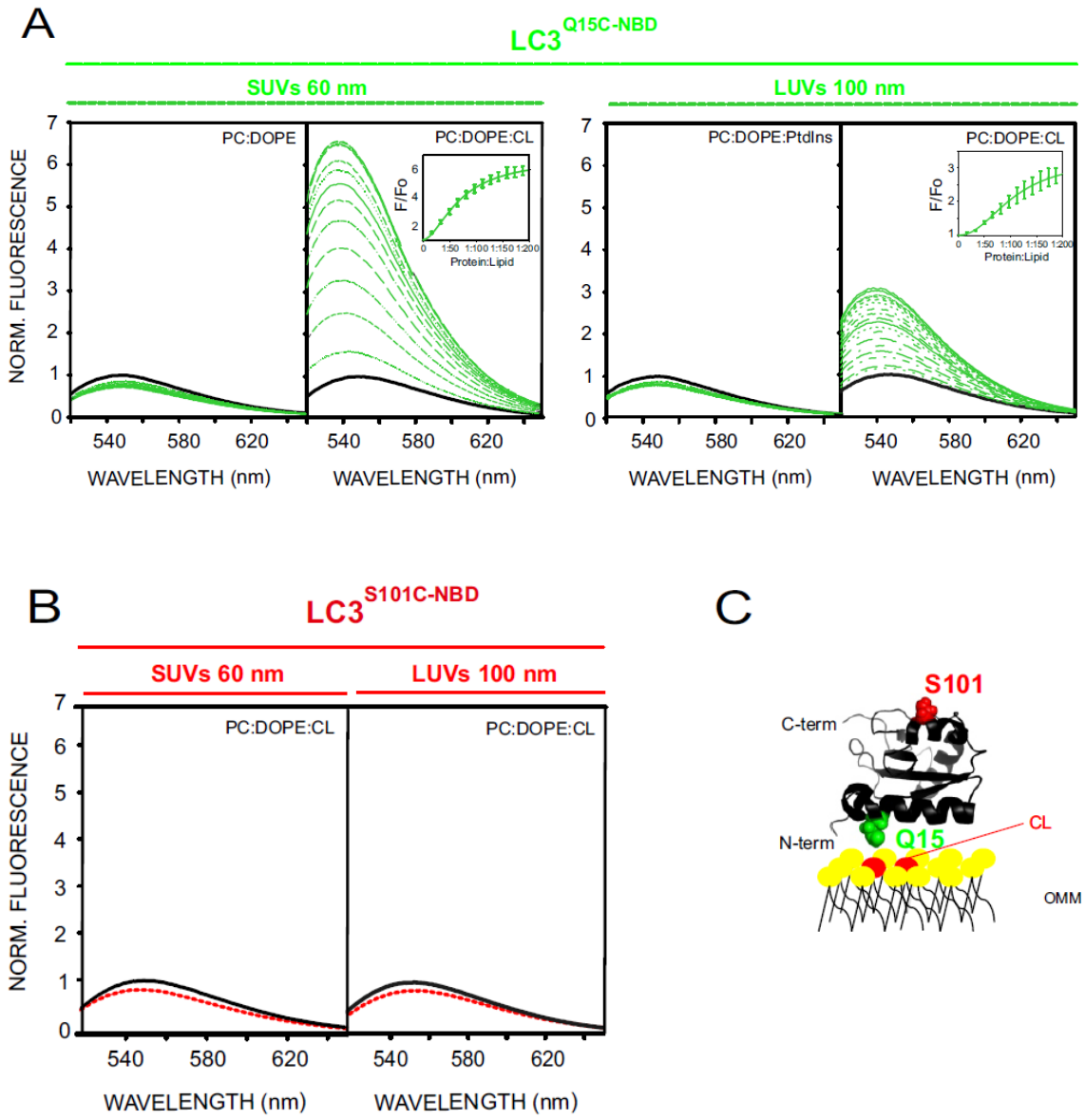

Figure 3.9. LC3B C terminus remains exposed to the hydrophilic environment after protein binding to CL-enriched membranes. Representative NBD fluorescence emission spectra of (**A**) LC3B$^{Q15C\text{-}NBD}$ (1 μM) in the absence or presence of increasing amounts of liposomes containing either PC:DOPE (80:20 mol ratio), PC:DOPE:CL or PC:DOPE:PtdIns (50:20:30 mol ratio); and (**B**) LC3B$^{S101C\text{-}NBD}$ (1 μM) in the absence or presence of PC:DOPE:CL liposomes. In each case, fluorescence was normalized to the peak intensity of the protein spectrum in the absence of liposomes. (**C**) Structural model generated with PyMol depicting the 2 LC3B residues that were individually mutated to cysteine obtaining single-cysteine LC3B mutants. The environmentally sensitive fluorophore NBD was used to label each of these single cysteine residues. PDB: 1UGM.

3.3.3 GABARAPL2 and GABARAP Interaction with CL-containing Membranes

To determine whether mechanisms underlying LC3-CL interaction are protein-specific or else they are the same for all human orthologs, we analyzed GABARAPL2 and GABARAP interaction with CL-enriched membranes (Antón *et al.*, 2016).

First, estimations of the electrostatic surface potential of Atg8 orthologs in solution revealed that the predicted CL-interacting region was markedly less basic for GABARAPL2 and GABARAP than for LC3B (**Figure 3.10**).

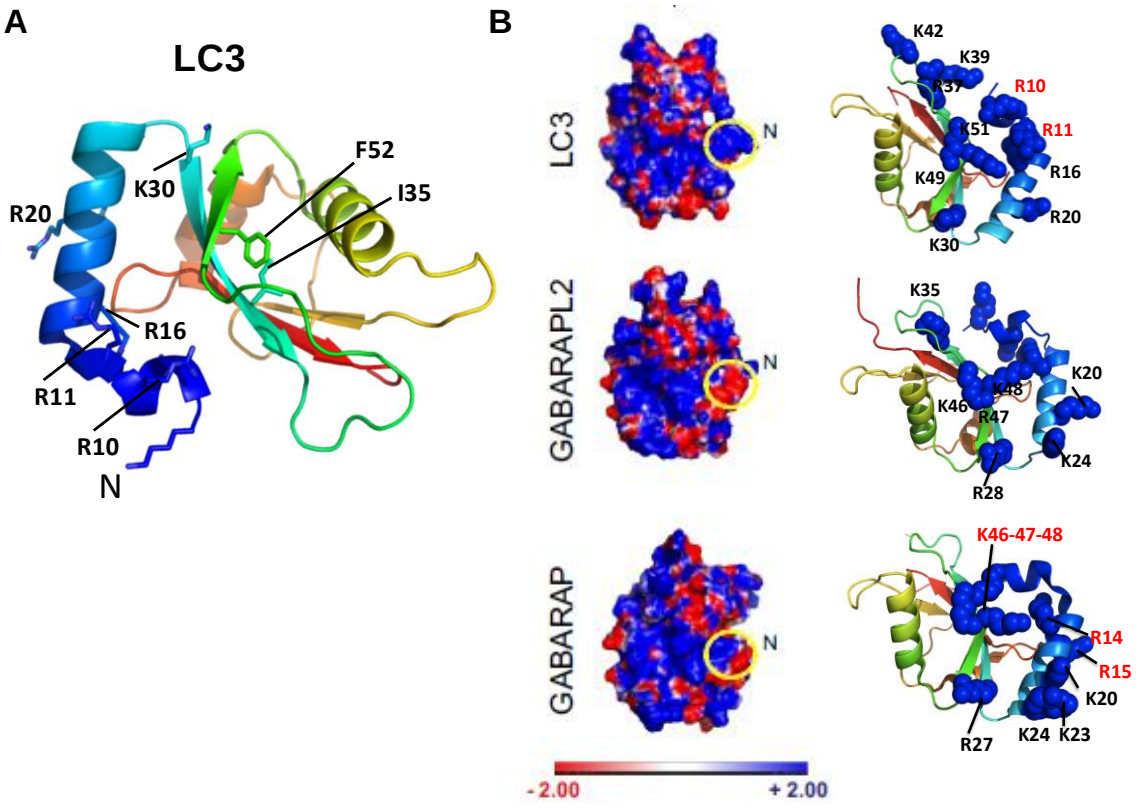

Figure 3.10. Location of the predicted cardiolipin-binding site in Atg8 orthologs. (**A**) Crystal structure of LC3, rainbow colored (blue N terminus to red C terminus) generated with PyMOL. The side chains of the N-terminal positively charged amino acids (Arg10, Arg11, Arg16, Lys30 and Lys51) are shown. These residues are concentrated on a basic patch that is predicted to interact with cardiolipin (Chu *et al.*, 2013). The side chains of Phe52 and Ile35 are also shown. These amino acids are located in the LC3 central globular domain and might be involved in ceramide-binding (Sentelle *et al.,* 2012). (**B**) Electrostatic surface diagram of each LC3 paralog in solution. Electrostatic potential surface was calculated using the Poisson-Boltzmann equation and displayed with PyMOL. The predicted cardiolipin-binding site is highlighted in yellow, and the color code is indicated below (left-hand panel). Right-hand panel shows locations of positively charged residues in two ribbon representation of Atg8 ortholog three-dimensional structures. Residues in LC3B and GABARAP that were mutated to alanine are highlighted in red. PDB: 1UGM (LC3), 1EO6 (GABARAPL2), 1GNU (GABARAP).

To test whether these structural features affected the lipid-binding profile of each LC3 paralog we first decided to explore the ability of GABARAP and GABARAPL2 to interact and insert into lipid monolayers using a Langmuir balance. In both cases an increase in π at the air-water interface similar to that of LC3B was observed after protein injection into the aqueous phase (**Figure 3.11A, left-hand panel**), also reaching a plateau value of ~15 mN/m at 1.5 μM protein concentration. Moreover, monolayer insertion of GABARAPL2 and GABARAP was also facilitated by the presence of CL or PtdIns4P [**Figure 3.11A (right-hand panel) and B**]. PS however did not distinctly modify the insertion of these 2 homologs, resulting in a change in lateral pressure equivalent to that observed with PC:DOPE (See **Table 3.3**).

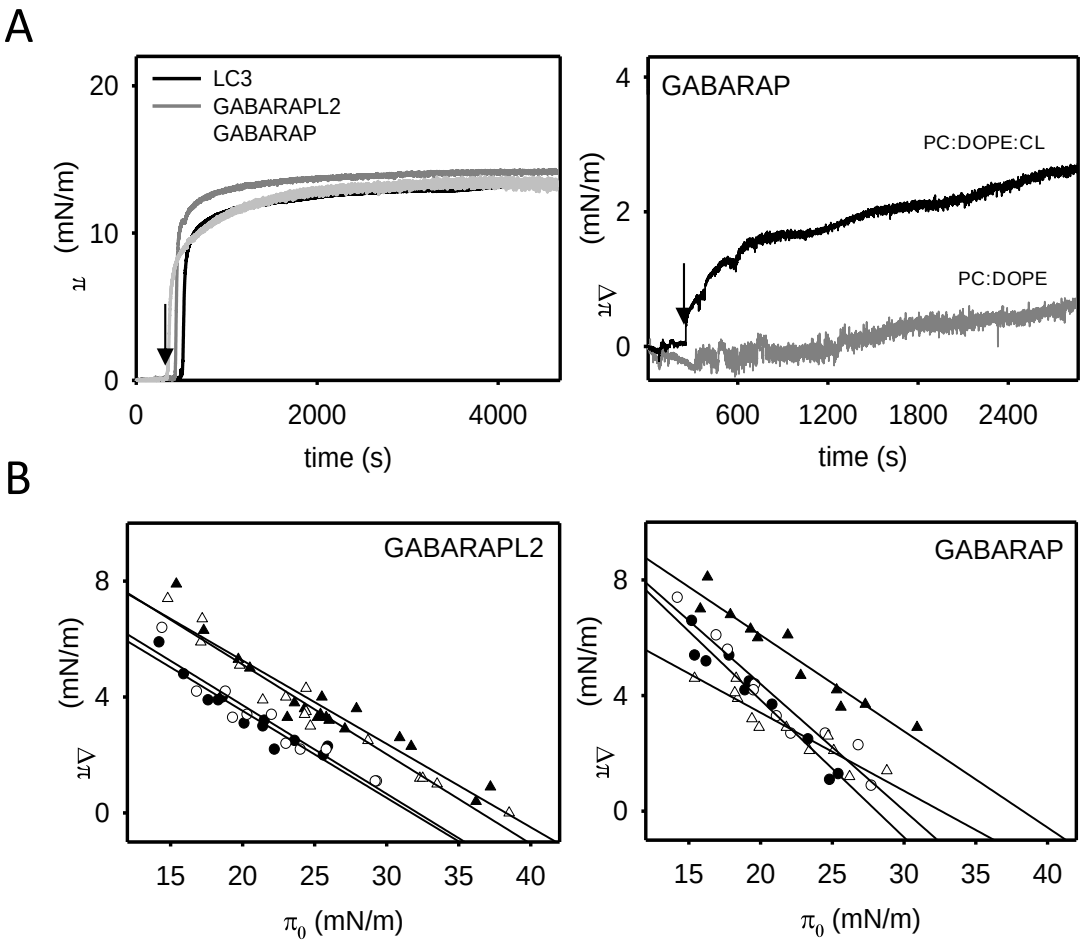

Figure 3.11. GABARAPL2 and GABARAP insertion into lipid monolayers. (**A**) Representative time courses of adsorption of LC3B, GABARAPL2 and GABARAP (1.5 μM) at the air-water interface (left-hand panel) and representative time courses of increase in lateral pressure after GABARAP (1.5 μM) insertion into PC:DOPE (80:20 mol ratio) or PC:DOPE:CL (55:20:25 mol ratio) monolayers (right-hand panel) at 25ºC. (**B**) Maximum increase in lateral pressure after GABARAPL2 and GABARAP insertion into lipid monolayers at 25ºC. Lipids were: [●] PC:DOPE (80:20 mol ratio), [▲] PC:DOPE:CL, [○] PC:DOPE:PS and [Δ] PC:DOPE:PtdIns4P (55:20:25 mol ratio). Data reported as a function of initial lateral pressure π_0. Very similar results were obtained at 37ºC (data not shown).

Protein	Lipid Composition	π_c
GABARAPL2	**PC:DOPE (80:20)**	31.8 mN/m (±0.39)
	PC:DOPE:CL (55:20:25)	38.2 mN/m (±0.57)
	PC:DOPE:PtdIns4P (55:20:25)	36.6 mN/m (±0.48)
	PC:DOPE:PS (55:20:25)	32.1 mN/m (±0.49)
GABARAP	**PC:DOPE (80:20)**	28.1 mN/m (±0.43)
	PC:DOPE:CL (55:20:25)	38.3 mN/m (±0.48)
	PC:DOPE:PtdIns4P (55:20:25)	32.5 mN/m (±0.42)
	PC:DOPE:PS (55:20:25)	30.0 mN/m (±0.55)

Table 3.3. Critical pressures (π_c) for GABARAPL2 and GABARAP insertion into lipid monolayers. Data calculated from the straight lines in **Figure 3.11B**. The tendency line-associated standard error is given for each π_c.

Furthermore, we assessed the binding of GABARAPL2 and GABARAP to PC:DOPE and PC:DOPE:CL vesicles by liposomal float-up assays. As depicted in **Figure 3.12**, GABARAP displayed a significantly lesser CL-binding response compared to that of LC3B and even less GABARAPL2 was observed to bind CL-containing liposomes.

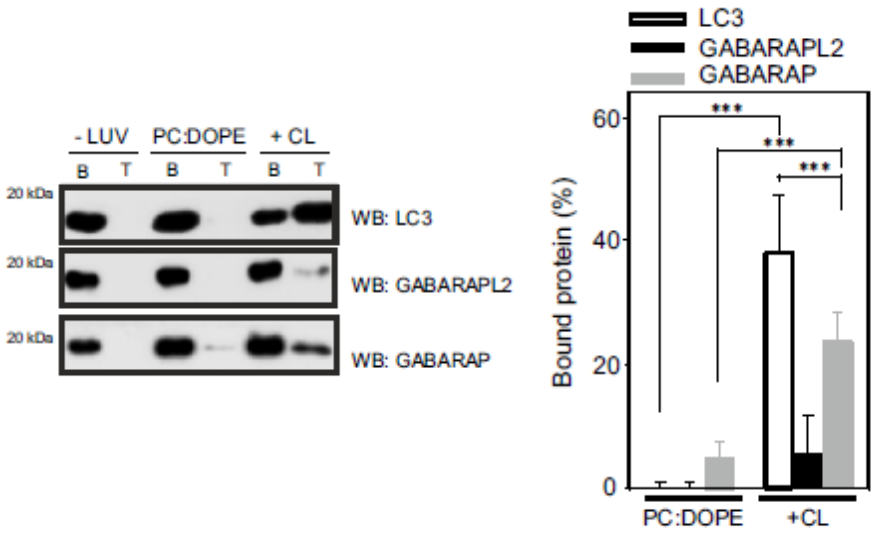

Figure 3.12. Different CL-interacting properties among human Atg8 orthologs. Each ortholog (10 µM) was incubated with 3 mM LUVs composed of PC:DOPE (80:20 mol ratio) or PC:DOPE:CL (50:20:30 mol ratio) followed by flotation of the liposomes by gradient centrifugation. Bound protein fraction was quantified by SDS-PAGE/immunoblot analysis using anti-LC3, GABARAPL2 and GABARAP antibodies. Molecular masses are shown in kDa on the left-hand side. Data shown as mean ± SD ($n \geq 3$); ***$P < 0.001$.

Additionally, as mentioned above, LC3B bound significantly less the more rigid vesicles containing bacterial CL (**Figure 3.8F**) and this is in agreement with a decrease in LC3B, but not GABARAP, membrane association with a higher saturation degree of CL fatty acyl chains (**Figure 3.13A**).

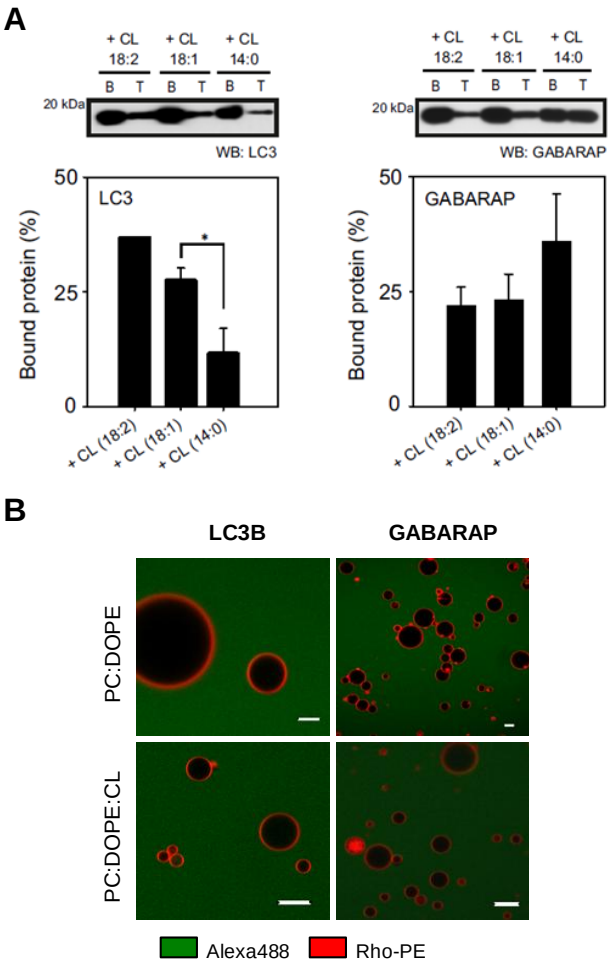

Figure 3.13. LC3B and GABARAP interaction with CL-enriched vesicles. (**A**) A higher degree of CL acyl chain unsaturation may facilitate LC3B, but not GABARAP membrane association. LC3B or GABARAP (10 μM) were incubated with 3 mM LUVs composed of PC:DOPE:CL (CL 18:2), PC:DOPE:TOCL (CL 18:1) or PC:DOPE:TMCL (CL 14:0) (50:20:30 mol ratio) followed by flotation. Bound protein fraction was quantified by SDS-PAGE/immunoblot analysis using anti-LC3 or anti-GABARAP antibodies. Molecular masses are shown in kDa on the left-hand side. Data shown as mean ± SEM (n = 3); *P = 0.01-0.05. (**B**) LC3B and GABARAP do not interact with GUVs composed of PC:DOPE:CL (50:20:30 mol ratio). Membrane and protein labeled with Rho-PE and Alexa 488 respectively. Lipid composition is given at the left-hand side. Bar: 10 μm.

We also compared the effect of liposomes containing CL on GABARAPL2 and GABARAP labeled at equivalent positions with NBD. To this aim, GABARAP^{S16C} and GABARAP^{S88C} mutants and GABARAPL2, on its endogenous C15 cysteine, were specifically labeled with NBD. To enhance the efficiency of covalent modification with NBD, Cys substitutions were made at sites in GABARAP with SASA values greater

than 45% (**Table 3.2**). For each monocysteine mutant, a structural model is shown in **Figure 3.14B** indicating the location of the Cys-substituted amino acid which was labeled with NBD. A representative NBD spectrum for each mutant in the absence (black line) or presence (green line) of PC:DOPE and PC:DOPE:CL is also shown. In solution, the $\lambda_{em(max)}$ values of NBD attached to monocysteine GABARAPL2 or GABARAP mutants were similar to those of LC3B mutants. The magnitude of NBD spectral changes induced by the presence of CL-enriched liposomes was somewhat smaller for GABARAP^{S16C} than for LC3B^{Q15C} (**Figure 3.14A**) and even smaller for GABARAPL2^{C15}, in correlation with the electrostatic surface potential of each protein and the flotation experiments shown above (**Figures 3.10B and 3.12**). Moreover, no increase in the emission spectrum of GABARAP$^{S88C\text{-}NBD}$ was observed upon its incubation with CL-containing large vesicles (red line) (**Figure 3.14A**). On the basis of the previously observed NBD spectral changes upon moving from solution to CL-containing liposomes, both LC3B and GABARAP would interact with CL-enriched membranes while exposing their C terminus to the hydrophilic environment (**Figures 3.9C and 3.14B**).

To further confirm the observed lack of effect of cardiolipin on GABARAPL2, we examined the protein tertiary structure by Trp fluorescence spectra analysis. GABARAPL2 is the only human ortholog studied in this work to contain Trp residues, namely two Trp residues in helix 1 and helix 3 (**Figure 3.15A**). In solution, the average Trp fluorescence emission of GABARAPL2 displayed a maximum value (Trp $\lambda_{em(max)}$) of 349 nm. The addition of both PC:DOPE and PC:DOPE:CL liposomes gave rise to a small increase in Trp fluorescence intensity (~1.2-fold increase) but it was not accompanied by a blue shift in Trp $\lambda_{em(max)}$ (**Figure 3.15B**). The observations from NBD and Trp fluorescence, as evident from the float-up assays (**Figure 3.12**), indicate that CL-containing membranes do not cause significant conformational rearrangements in GABARAPL2.

Taken together, these results strongly suggest that differences shown in the electrostatic surface potential of LC3 family proteins may lead to lipid-binding specificities among them.

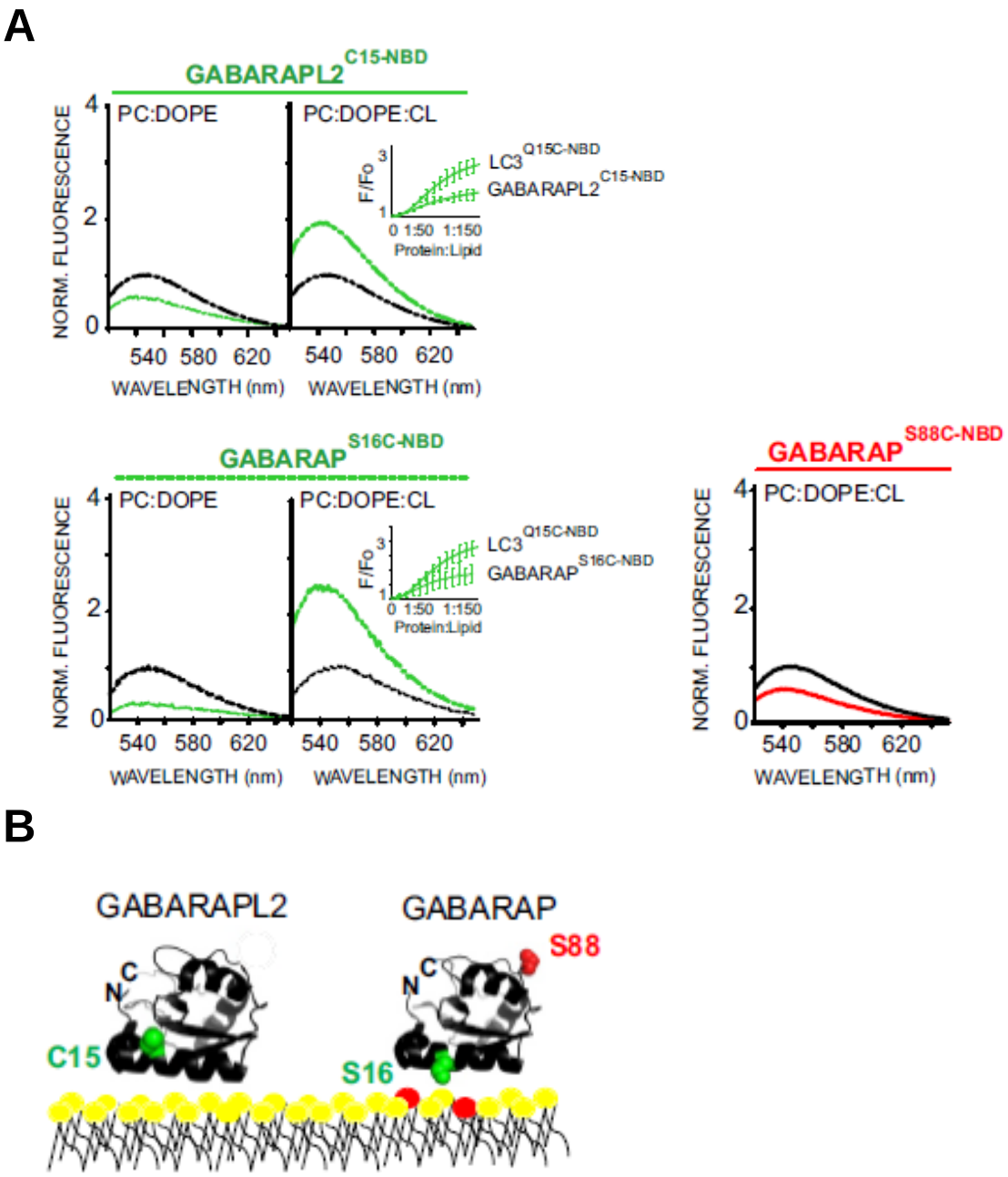

Figure 3.14. Effect of CL-containing liposomes on NBD-labeled GABARAPL2 and GABARAP. (**A**) Representative NBD fluorescence emission spectra of GABARAPL2$^{C15\text{-}NBD}$ and GABARAP$^{S16C\text{-}NBD}$ (1 μM) in the absence or presence of increasing amounts of liposomes containing PC:DOPE (80:20 mol ratio) or PC:DOPE:CL (50:20:30 mol ratio); and GABARAP$^{S88C\text{-}NBD}$ (1 μM) in the absence or presence of PC:DOPE:CL liposomes. In each case, fluorescence was normalized to the peak intensity of the protein spectrum in the absence of liposomes. (**B**) A structural model generated with PyMol is also shown depicting the 2 GABARAP residues that were individually mutated to cysteine obtaining single-cysteine GABARAP mutants and the endogenous cysteine of GABARAPL2. The environmentally sensitive fluorophore NBD was used to label each of these single cysteine residues. PDB: 1EO6 (GABARAPL2), 1GNU (GABARAP). CL is colored in red.

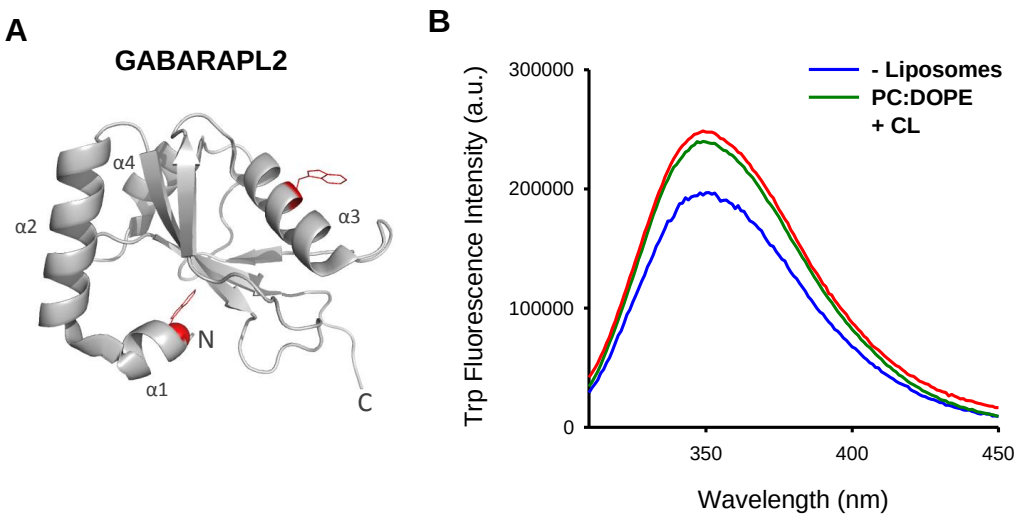

Figure 3.15. Trytophan fluorescence analysis of GABARAPL2 conformation. (**A**) Structural model of GABARAPL2 generated with PyMol displaying the side chains of Trp (W) residues that served as spectroscopic probes of protein conformational changes in the presence of liposomes. Red color highlights the location of W3 in helix 1, and of W62 in helix 3. PDB: 1EO6. (**B**) Representative Trp fluorescence spectra of GABARAPL2 (2 µM) incubated for 1 h at 37ºC in the absence or presence of SUVs (0.6 mM) composed of PC:DOPE (80:20 mol ratio) or PC:DOPE:CL (50:20:30 mol ratio). In all cases, 2 µM protein was excited at 295 nm and the fluorescence spectra were collected from 310 nm to 450 nm. Lines represent the average corrected emission spectra from three replicate experiments.

In their study, Kagan and colleagues (Chu *et al.*, 2013) have determined that cardiolipin recognition for mitophagy depended on N-terminal amino acids (R10 and R11) of LC3B (see **Figure 3.10**). To further validate our liposome-binding assay, we mutated those residues to alanine in LC3B and evaluated the LC3B^{R10,11A} capacity to bind CL-enriched liposomes (**Figure 3.16A**). Substitution of those residues did not produce structural changes in the protein as tested by secondary structure examination of both WT and mutant LC3B forms using far-UV circular dichroism spectroscopy (**Figure 3.3B**). Mutating those 2 residues made the anti-LC3 antibody unable to recognize LC3B in western blots (data not shown). To circumvent this we decided to label both LC3B and LC3B^{R10,11A} with Alexa Fluor 488. The Alexa Fluor 488 fluorescence of LC3B-A488 was quantified at different protein concentrations by densitometry and the data were linearly fitted by the least-squares method (**Figure 3.7B**). Consistent with a critical role of these 2 basic amino acids in the interaction of LC3 with CL (see **Figure 3.10**), the RR to AA mutation clearly decreased LC3B^{R10,11A} affinity for CL (**Figures 3.16B and C**).

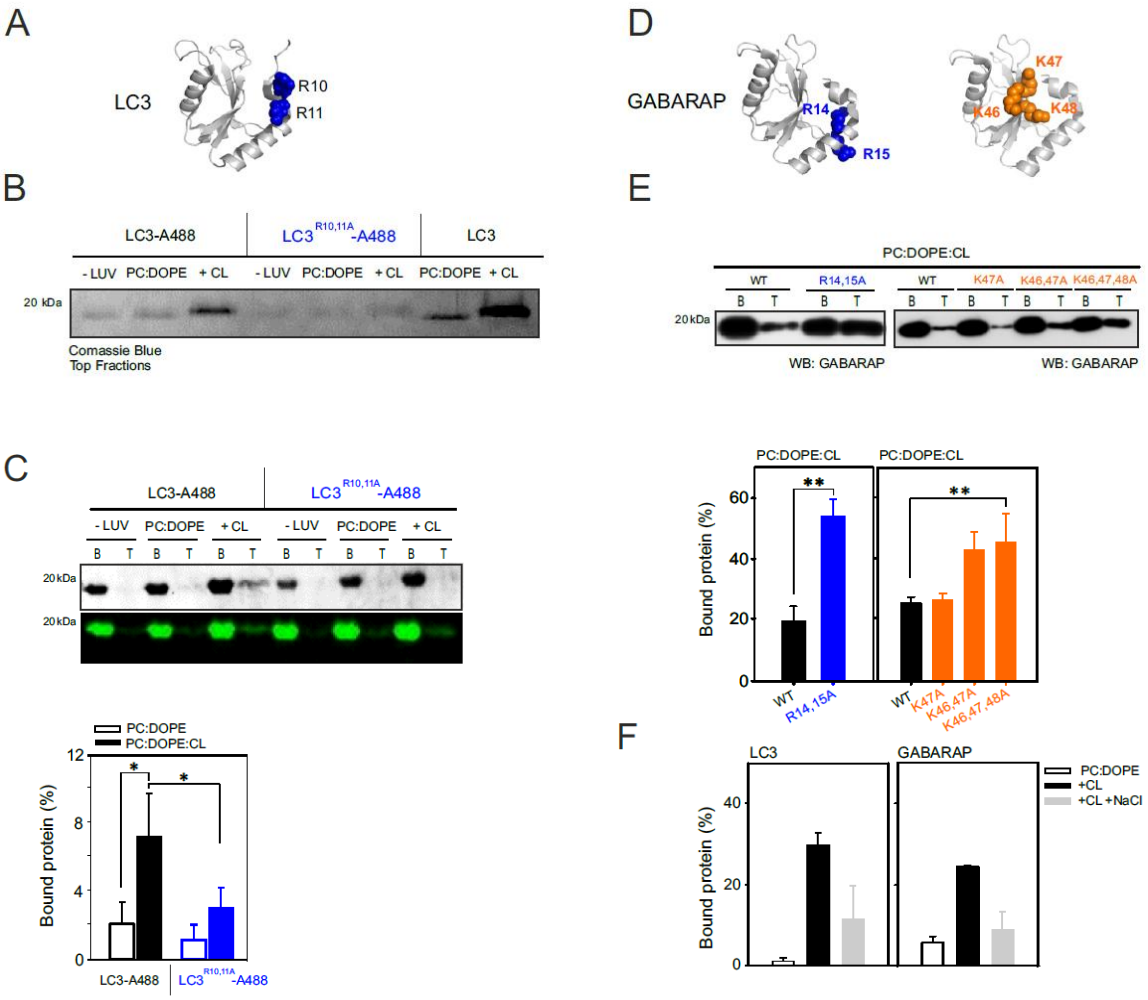

Figure 3.16. N-terminal RR to AA mutation reduces LC3B, but not GABARAP, ability to interact with CL. (**A**) Crystal structure of LC3 displaying the N-terminal residues (R10 and R11, colored in blue) that were mutated to alanine. PDB: 1UGM. (**B**) Control experiment comparing liposome-binding of unlabelled LC3B with labelled LC3B and LC3B^{R10,11A} under the same experimental conditions. (**C**) 10 µM LC3B- or LC3B^{R10,11A}-A488 were incubated with 3 mM LUV composed of PC:DOPE (80:20 mol ratio) or PC:DOPE:CL (50:20:30 mol ratio) followed by flotation in a sucrose density gradient. Liposome-bound protein fraction was quantified by SDS-PAGE and Alexa Fluor 488 fluorescence. Molecular masses are shown in kDa on the left-hand side. Data shown as mean ± SD (n = 3); *P = 0.01 to 0.05. (**D**) Crystal structures of GABARAP displaying the N-terminal residues (R14 and R15, colored in blue and K46, K47 and K48, colored in orange) that were mutated to alanine. PDB: 1GNU. (**E**) 10 µM GABARAP, GABARAP^{R14,15A}, GABARAP^{K47A}, GABARAP^{K46,47A} or GABARAP^{K46,47,48A} were incubated with 3 mM LUV composed of PC:DOPE:CL (50:20:30 mol ratio) followed by flotation in a sucrose density gradient. Liposome-bound protein fraction was quantified by SDS-PAGE and immunoblot analysis. Molecular mass is shown in kDa on the left-hand side. Data shown as mean ± SD (n = 3); **P = 0.001 to 0.01. (**F**) LC3B or GABARAP (10 µM) binding to liposomes (3 mM) composed of PC:DOPE or PC:DOPE:CL with/without addition of 300 mM NaCl. Data shown as mean ± SEM (n = 3).

In order to test whether these N-terminal residues are also involved in GABARAP interaction with CL-containing membranes, R14 and R15 GABARAP amino acids equivalent to the ones in LC3B, and K46, K47, K48 amino acids, that are also

within the proposed interaction patch (see **Figure 3.10B**), were mutated to alanines (**Figure 3.16D**). Note that K46, K47 and K48 are highly conserved basic amino acids (see **Figure 3.1A**) that have been shown to interact with amino acids present in the conserved LIR of the different cargo receptors during selective autophagy (Stolz *et al.*, 2014). Notably, all GABARAP mutants were still capable of recognizing CL, some of them with an even higher affinity than WT GABARAP (**Figure 3.16E**). Taking into account that substitution of the positively charged residues R10 and R11 had a negative effect on LC3B but not on GABARAP binding to CL, the contribution of electrical charge to each protein-CL interaction was further analyzed. To this aim, the interaction of LC3B and GABARAP with CL-enriched liposomes was examined in the presence of 300 mM NaCl (**Figure 3.16F**). We found that increasing the ionic strength of the medium both LC3B and GABARAP binding to CL-containing liposomes decreased, suggesting that in both cases the interaction depends at least in part on an electrostatic component. Given that R14, R15, K46, K47 and K48 residues are not essential for GABARAP binding to CL, other N-terminal residues may be involved in the protein interaction with CL.

3.4 Discussion

The expansion of the Atg8 family proteins in higher eukaryotes has been proposed to facilitate differential cargo handling during selective autophagy (Schreiber & Peter, 2014; Stolz *et al.*, 2014). The components of the ULK1/ULK2 complex, for instance, bind preferentially GABARAP-like over LC3-like proteins (Alemu *et al.*, 2012; Joachim *et al.*, 2015) whereas the receptor protein FYCO1 displays a strong preference for LC3 (Pankiv *et al.*, 2010). Structural studies have highlighted the importance of specific features of individual members in determining these preferential bindings. Importantly while most ubiquitin-directed autophagy receptors (SQSTM1, NBR1, and OPTN) interact with both GABARAP and LC3 subfamily proteins (**Figure 3.1**) (Sugawara *et al.*, 2005; Kirkin *et al.*, 2009a; Wild *et al.*, 2011), specific binding of CALCOCO2 to LC3C (and not the other LC3 isoforms) is crucial for innate immunity during xenophagy (von Muhlinen *et al.*, 2012). Again structural analysis revealed that the selectivity of CALCOCO2 for LC3C is conferred by a noncanonical LIR in CALCOCO2, in which the lack of an aromatic residue is balanced by specific interactions within the N-terminal region of LC3C. In addition to its role in microbial clearance, LC3C has been related to a unique anticarcinogenic activity (Mikhaylova *et al.*, 2012) whereas LC3B promotes tumor growth. While it is very likely that this

opposite effect is related to differential recruitment of critical autophagy targets, the identity of these cargos and the structural basis for these specific interactions are still elusive.

Selective elimination of mitochondria by mitophagy regulates not only the steady-state mitochondrial number required for changing metabolic demands, but also maintains cell quality control by removing damaged organelles. Although mitochondria can be engulfed nonselectively along with other cytosolic contents during bulk autophagy, different lines of evidence indicate that mitophagy can be mechanistically differentiated from other forms of autophagy, and mitophagy-specific mechanisms are now beginning to emerge (Randow & Youle, 2014).

Yeast genetic screening identified Atg11 as an important mitophagy regulator. By binding to Atg32 at the OMM and to Atg8 at the growing phagophore, Atg11 recruits the canonical autophagic machinery to the mitochondria and primes mitochondria for degradation (Okamoto *et al.*, 2009; Sakakibara *et al.*, 2015). In mammals, the ubiquitin-binding adaptor SQSTM1 is thought to act in the same way as Atg11 (Geisler *et al.*, 2010) and during erythrocyte differentiation mitochondrial resident BNIP3L functions as a mitophagy receptor at least in part by binding to LC3 homologs (Novak *et al.*, 2010).

Alternatively, upon mitochondrial membrane depolarization, PINK1 accumulates at the OMM and recruits the E3 ubiquitin-protein ligase PARK2 from the cytosol specifically to the damaged mitochondrion (Lazarou *et al.*, 2015). PARK2 then induces mitochondrial degradation through both ubiquitin-dependent and -independent pathways. The genes encoding PINK and PARK2 were found to be mutated in certain forms of autosomal recessive Parkinson disease (Valente et al., 2004; Vives-Bauza *et al.*, 2010) and loss of either protein in *Drosophila* results in mitochondrial dysfunction (Narendra *et al.*, 2010a). Nevertheless, pink1- or park2-knockout mice appear largely normal and have only subtle phenotypes, suggesting that in the absence of PINK1or PARK2 other factors can sustain effective mitophagy. In this line, it has been recently shown that exposed CL on the surface of the OMM combines with LC3 and gives rise to the recognition of injured mitochondria (Chu *et al.*, 2013). The process was not accompanied by membrane depolarization and was independent of PINK1 or PARK2. Interestingly, CL has also been reported to interact with other mitophagy-related proteins including DNM1L (Bustillo-Zabalbeitia *et al.*, 2014), human IRGM (Singh *et al.*, 2010) and Beclin 1 (Huang *et al.*, 2012), making CL an essential lipid in this process for both cargo reception and protein function regulation.

3.4.1 LC3B-CL Interaction

The aim of this study was to characterize the association of the autophagy protein LC3 with CL-containing membranes. In this work, we have described novel molecular mechanisms underlying this protein-lipid interaction (Antón *et al.*, 2016). Using several compositionally defined *in vitro* reconstituted systems we show that LC3B avidly interacts with CL, both when CL was spread onto nitrocellulose membranes in the context of a PLO assay and in CL-enriched model membranes (**Figures 3.5 to 3.9**). LC3B binds preferentially CL over other anionic lipids such as PtdIns4P, even though the latter also carries 2 negative charges and has been related to certain types of selective autophagy. Furthermore, we show that association of LC3B with CL predominantly relies on electrostatic interactions (**Figures 3.10 to 3.12 and 3.14**). These results are consistent with the notion that the interaction is mediated by basic patches at LC3 surface that stabilize the phosphate moieties of CL (Chu *et al.*, 2013). Our results with the $LC3B^{R10,11A}$ mutant (**Figure 3.16**) strongly support the idea that some of the residues within those patches are essential for LC3-CL interaction, modulating the binding capacity of the protein (see **Figure 3.10**). Moreover, molecular docking analyses of LC3B upon binding to CL-containing membranes implicate N-terminal Arg10 and Arg11 in the initial interactions of LC3 with CL (Chu *et al.*, 2013). In the *in silico* model the C terminus of LC3, which becomes crosslinked to autophagosome membranes through a conserved glycine residue (see **Figure 3.1A**, black arrow) is predicted to remain exposed to the solvent. Here, using site-specific NBD labeling coupled to NBD fluorescence spectroscopic analysis, we provide experimental data supporting this model in which the N- and C-terminal regions would bind mitochondria and autophagosomal membranes respectively (**Figure 3.9**). This membrane-interacting surface of LC3B located at the N-terminal domain would approach the hydrophobic region of the bilayer and directly interact with CL in the lipid bilayer. This N-terminal interaction with CL may induce a conformational rearrangement in LC3 that would lead to an enhancement of LC3 autophagic activity via its C terminus binding the autophagosomal membrane. Moreover, our previous study has found that fusion induced by LC3 human orthologs is facilitated by the presence of CL in model membranes (Landajuela *et al.*, 2016). Therefore, CL-mediated modulation of LC3B function would occur via changes in both membrane and protein properties. However, whether or not the CL effects on LC3B will affect the role of the LC3 conjugation system in autophagy needs to be clarified. Furthermore, the relative bilayer depth or surface exposure of LC3B potential membrane interacting sites could also be examined by the analysis of NBD fluorescence quenching. Indeed, the Atg8

orthologs membrane insertion degree still remains poorly characterized. Membrane insertion could be distinguished from peripheral association with the membrane by quenching of (i) intrinsic fluorescence by brominated lipids, and (ii) NBD fluorescence by doxyl/nitroxide moieties located at different depths in the bilayer.

Additionally, LC3B interaction with CL-containing membranes would be facilitated in an acidic environment (**Figure 3.8D**), which is in agreement with LC3 interacting with CL in the OMM of damaged mitochondria. Indeed inhibition of the mitochondrial ATP synthase could induce a higher proton concentration in the intermembrane space that would finally cause a local cytosolic pH decrease. When the mitochondrial respiratory chain is blocked lactic acid fermentation could also be activated as an alternative for the cell to obtain energy, and lactic produced in that process would tend to acidify the intracellular environment, thus to facilitate LC3-CL interaction. However the relationship between pH, CL net charge and LC3-CL binding may not be straightforward. Changing the environmental pH would change the protonation state of CL, but also the protein net charge, and CL packaging in the membrane (Khalifat *et al.*, 2011; Lemmin *et al.*, 2013). Since at lower pH CL would have a smaller negative charge, less binding of LC3B to CL would be expected, but at the same time LC3 charge would become more positive, and this would facilitate LC3 electrostatic interaction with CL. Moreover we must take into account that this interaction relies only partially on electrostatic forces, thus CL negative charge is just one of the several membrane properties that facilitate the interaction. Instituting an artificial pH gradient in CL-containing giant unilamellar vesicles (pH 4 to 5 outside) generates profound invaginations, potentially enriched in CL that would mimic mitochondrial cristae (Khalifat *et al.*, 2008). If these are indeed CL-enriched microdomains, they would facilitate the local binding of LC3.

LC3B preferential binding to smaller and more curved CL-containing liposomes may suggest that vesicle curvature is another factor increasing LC3 affinity for CL (**Figure 3.8E**). Indeed, LC3B does not interact with GUVs (**Figure 3.13B**) suggesting that LC3B interaction with membranes requires a vesicle curvature (GUV curvature is almost zero). This could be a mechanism of recognition of previously processed mitochondria, which would have been converted into pieces of manageable size for their engulfment by autophagosomes. Studies in different mammalian cells have shown that after DNM1L-mediated fission, depolarized mitochondrial products are much less likely to fuse and are eventually autophagocytosed (Twig *et al.*, 2008). Moreover, inhibition of DNM1L prevents both mitochondrial fragmentation and mitophagy, indicating that fission is related to efficiency of mitophagy. Therefore, mitochondrial

shape and size appear to be critical for LC3-CL interaction and targeted mitochondrial degradation. Note in this respect that the negative intrinsic curvature of the lipid CL is conceptually different from the geometrical curvature of a vesicle, in fact lipids with an intrinsic negative curvature can exist in vesicles, e.g. SUVs, with a high geometrical curvature (small radius) (Goñi, 2014).

CL isolated from heart cells displays not only a unique tandem head group arrangement but also a high degree of unsaturation in the acyl chains, linoleic (C18:2) being the most abundant fatty acid. This structural feature contributes to a high degree of flexibility within the membrane that may facilitate LC3 insertion and association. In support of this idea, LC3B binding to CL was significantly lower with vesicles enriched in bacterial CL that contains more saturated acyl chains leading to a more rigid membrane (**Figure 3.8F**). Thus bilayer rigidity would be another regulative mechanism in LC3B association with CL-enriched membranes. Indeed, lipid oxidation increases markedly mitochondrial membrane rigidity observed in aging animals (Chen & Yu, 1994). Hence free radical reaction-induced decrease in membrane fluidity would affect LC3 recognition of damaged mitochondria and this would be an aging-related process (García-Prat *et al.*, 2016).

3.4.2 GABARAPL2 and GABARAP

Since most studies have been focused on LC3, the role of other human Atg8 orthologs in mitophagy is less well characterized. LC3 family proteins have different specificities guiding the selective recruitment of different LIR-containing proteins (Weidberg *et al.*, 2010).

CL-binding assays and electrostatic surface potentials shown in this study revealed that human Atg8 orthologs also differ in their lipid-binding affinities (**Figures 3.10 to 3.16**). In contrast to LC3B and GABARAP, GABARAPL2 hardly binds CL-containing membranes (**Figures 3.12 to 3.15**). Therefore, LC3B, GABARAPL2 and GABARAP may play different roles during selective and nonselective autophagy, and there might be different mechanisms involved in the regulation of mitophagy pathways depending on the cellular and physiological context. The data presented in the next chapter may have important implications for the understanding of LC3B, GABARAP and GABARAPL2 localization in bulk autophagy and rotenone-dependent mitophagy *in vivo*.

Chapter 4

Rotenone-dependent regulation of Atg8-ortholog mitochondrial recruitment during mitophagy

CHAPTER 4:

Rotenone-dependent regulation of Atg8-ortholog mitochondrial recruitment during mitophagy

4.1 Introduction

Macroautophagy (referred to hereafter as autophagy) is an intracellular degradation pathway conserved in all eukaryotes (Klionsky, 2007; Mizushima & Komatsu, 2015). This process does not only provide nutrients to maintain vital cellular functions under amino acid limiting conditions, but also plays an important role in a wide range of physiological processes (Boya *et al.*, 2013). During macroautophagy, cytoplasmic material including entire organelles are sequestered by a double membrane-bound organelle called autophagosome. Eventually, autophagosome fuses with membranes of the endocytic and lysosomal pathways for cargo degradation and recycling (Shibutani & Yoshimori, 2014; Shen & Mizushima, 2014). One outstanding question is how the autophagosomal membrane is formed and elongated. The most widely accepted hypotheses propose the sequential recruitment of a series of regulatory proteins to a specialized site on the ER known as the autophagosome assembly site or "isolation membrane", upon which adhesion and fusion of further membrane structures would occur (Ktistakis & Tooze, 2016; Mi *et al.*, 2015).

Mitophagy is the specific turnover of mitochondria via a selective autophagy pathway (Hamacher-Brady & Brady, 2016; Randow & Youle, 2014) and inhibition of this process is found to cause mitochondria accumulation and excessive exposure to ROS (Rouschop *et al.*, 2009). LC3/GABARAP family proteins play a key role in the

recognition and engulfment of specific mitochondria through interaction with autophagy adaptor proteins that bind both the mitochondria and LC3/GABARAP family proteins through their LIRs (Wild *et al.*, 2014). Certain lipids such as cardiolipin or ceramide can also act as cargo receptors for the autophagy machinery (Dany & Ogretmen, 2015; Maguire *et al.*, 2016). For instance, Chu and colleagues proposed that the OMM-localized CL acts as a mitochondrial receptor for LC3 triggering mitophagy in cortical neurons and neuroblastoma cells treated with the electron transport chain complex I inhibitor rotenone (Chu *et al.*, 2013). However, much remains to be elucidated regarding the regulation and molecular mediators involved in cargo selection during selective autophagy pathways.

This area of research has attracted considerable attention recently as the mitophagy process is found to play an important role in multiple human pathological states including not only neurodegeneration (Nixon, 2013; Aufschnaiter *et al.*, 2016; Vidal *et al.*, 2014) but also cancer (Lu *et al.*, 2013) and myopathies (Kubli & Gustafsson, 2012). However, how the specific LC3/GABARAP subfamily protein members modulate the targeting and removal of damaged mitochondria in different cell-types and stress conditions remains largely unexplored. In this study, the previously described relevance of the LC3-CL interaction (Antón *et al.*, 2016; see Chapter 3), was further evaluated in several human cell lines, namely U87MG human glioblastoma cells, RPE1 cells and iPSC-derived human cortical neurons expressing LC3B, GABARAP, GABARAPL1, or GABARAPL2 proteins. Various imaging methods (light microscopy, confocal microscopy and CLEM) were used to gain further insight into the kinetics of mitophagy and the specific roles of different human Atg8 orthologs in selective targeting and removal of damaged mitochondria during PARK2-independent rotenone-induced mitophagy. Here CL translocation to the OMM induced by rotenone (Chu *et al.*, 2013), but not by other bulk autophagy-inducing signals, such as THC and AZD8055 treatments or nutrient starvation conditions, was found to induce LC3B translocation to mitochondria and its subsequent delivery to lysosomes in U87MG glioma cells and RPE1 cells. On the basis of these observations, CLEM was used next to locate and analyze the structure of mitophagic compartments within RPE1 cells using stage-specific fluorescently-tagged autophagosome markers. Ultrastructural analysis of LC3B recruitment to mitochondria via lipid attachments in different stages of the process upon rotenone treatment revealed mitochondria surrounded by large autophagosomal structures indicating the targeting and engulfment of mitochondria and fusion events between autophagosomes. By contrast, unlike the situation found with LC3B, neither GABARAPL2 nor GABARAP were found to be translocated to mitochondria upon

rotenone treatment in U87MG cells. Moreover, GABARAPL1-labeled autophagosomes were observed to be grouped in mitochondria-rich areas in rotenone-treated RPE1 cells but, contrary to that found for LC3B, GAPARAPL1 punctae were not observed in the vicinity of mitochondria in cortical neurons upon rotenone exposure.

Location of ATG5 puncta as a marker for isolation membranes or preautophagosomes was also evaluated upon induction of both nonselective and selective autophagy processes with the aim of determining whether LC3B lipidation is necessary for its recruitment to mitochondria. Induction of nonselective bulk autophagy was found to cause a significant increase in steady state puncta counts for GFP-ATG5 which was also significant for PARK2-dependent and -independent mitophagy induced by the mitochondrial uncoupler CCCP and rotenone, respectively. However, ATG5-positive preautophagosomes were not notably located to mitochondria under rotenone-induced mitophagy conditions in human RPE1 cells.

Together, the *ex vivo* studies presented in this chapter shed light on the specific regulation and function of the LC3/GABARAP family proteins in mitochondria recognition during mitophagy and provide evidence indicating that mechanisms for selective targeting and recruitment of individual family members may depend on environmental factors (e.g., metabolic or stress conditions) and reflect cell-specific functions.

4.2 Materials and Methods

4.2.1 Materials

Unless otherwise stated, all reagents were obtained from Sigma-Aldrich. Leupeptin and THC were prepared in H_2O and in an alcohol base, and were used at a final concentration of 20 and 4 µM, respectively. Rotenone, CCCP, and AZD8055 were prepared in DMSO and unless otherwise indicated were used at a final concentration of 1 or 5 µM, 20 µM, and 1 nM, respectively.

The following antibodies were used: anti-LAMP2 (1:100; BD Biosciences, San Jose, CA, USA), anti-LC3B (1:1000), and anti-TOMM20 (Santa Cruz Biotechnology) in experiments with U87MG cells; and anti-HSP60 (1:200), anti-ATPB (1:100), and anti-LC3B (1:400) for immunostaining of RPE1 cells.

4.2.2 Molecular Cloning

The construct containing the MTS, MTS-CFP, used for mitochondrial staining of RPE1 cells, was subcloned by insertion of MTS fragment into a peCFP-N1 vector, cut from the MTS-peGFP construct (from Ms G. Mulally) using EcoRI and BamHI. The ligation product was used to transform *E. coli* competent cells to select the colonies that contained the peCFP-N1 with the MTS inside and was further confirmed by electrophoresis (**Figure 4.7A**).

4.2.3 Cell Culture

U87MG cells were cultured in DMEM (Lonza, Basel, Switzerland) containing 10% FBS and penicillin/streptomycin (5 µg/mL) (Lonza). When required, cells were seeded at a density of 5000 to 10000 cells/cm^2 and transferred to medium containing 0.5% FBS, 18 h before performing the different treatments. For nutrient deprivation experiments, cells were incubated in EBSS medium (Lonza). RPE1 cells were grown in DMEM with 4.5 g/L glucose (high glucose) and 2 mM L-glutamine supplemented with 10% FBS (Gibco, Life Technologies), sodium pyruvate and HEPES. Cells were starved for 2 h in a pre-warmed serum-free media previously described by the group of N. Ktistakis (140 mM NaCl, 1 mM $CaCl_2$, 1 mM $MgCl_2$, 5 mM glucose and 20 mM HEPES at pH 7.4 supplemented with 1% (w/v) fresh BSA and filter sterilized) (Axe *et al.*, 2008). iPSC-derived human cortical neurons were cultured in N2B27 containing 1:1 Neurobasal (Life Technologies) and DMEM/F-12 with glutamax (Life Technologies) previously described in Nistor *et al.,* 2015. Neuronal cells were cultured either in 4-well plates (Thermo Fisher Scientific) or in live-cell imaging dishes (MatTek Corp.).

4.2.4 Transfection and Viral Transduction

Transfections of expression vectors GABARAPL2-GFP and GABARAP-GFP (from Dr. A. Simonsen) into U87MG cells and of plasmids MTS-CFP (sub-cloned from MTS-peGFP) and Mito-DsRed (from Dr. J. Lane) into RPE1 cells were carried out using the Lipofectamine®2000 transfection reagent (Invitrogen) according to the manufacturer's instructions. iPSC-derived human cortical neurons were transduced with lentiviral vectors containing the sequences for LC3B and GABARAPL1 with N-terminal GFP tags (from Dr. J. Lane).

4.2.5 Fluorescence Microscopy

Standard protocols for immunofluorescence microscopy were used. Incubation with appropriate Alexa Fluor 488-, Alexa Fluor 594- or Alexa Fluor 647-conjugated

secondary antibodies (Invitrogen) was performed in the dark at room temperature for 20-90 min.

U87MG cells were observed in a Leica TCS SP2 confocal microscope (Leica Microsystems CMS GmbH). Wide-field fluorescence imaging of RPE1 cells was performed using an Olympus IX-71 inverted microscope (Olympus UK Ltd.) driven by MetaMorph software (Molecular Devices). For live-cell imaging, RPE1 cells and iPSC-derived human cortical neurons were seeded in 35 mm glass-bottomed live-cell imaging dishes (MatTek Corp.). In case of cortical neurons, mitochondrial staining was performed using MitoTracker® Red CMXRos (Molecular Probes, Life Technologies). All live-cell imaging was performed at 37ºC and 5% CO_2.

4.2.6 Autophagic Flux Analysis by LC3B, GABARAPL1 or ATG5 Puncta Counting

Tandem fluorescent-tagged LC3B or GABARAPL1 and GFP-tagged ATG5 were used as a tool to analyze autophagic flux based on the principles described previously (Kimura *et al.*, 2007). Fixed RPE1 cells stably expressing mCherry-GFP-LC3B, mCherry-GFP-GABARAPL1 or GFP-ATG5 puncta were imaged using an Olympus IX-71 inverted microscope (Olympus UK Ltd.). An automated tandem LC3B-, tandem GABARAPL1- or GFP-ATG5-labelled autophagosome scoring was performed using the TopHat morphology filter in MetaMorph software, selecting for round objects of diameter 5 pixels (=1 μm) or less, on images taken at an optimal but constant exposure for a whole experiment. Individual items selected by the morphology filter were counted automatically by MetaMorph using fixed fluorescence thresholds, determined on images of the positive and negative controls for each experiment. Thresholds were set manually for each channel and experimental data set, and the MetaMorph “count cells” plugin was used to automatically count the number of puncta/field.

4.2.7 Correlative Light and Electron Microscopy (CLEM)

mCherry-GFP-LC3B stably expressing RPE1 cells plated in 35 mm glass-bottomed dishes with finder grids (MatTek Corp.) were first imaged by wide-field fluorescence and phase contrast microscopy (live-cell imaging) using an Olympus IX-71 inverted microscope (Olympus UK Ltd.) and then processed using chemical fixation and embedding in Epon resin for TEM. Resin blocks were trimmed and 70 nm serial sections were cut and stained. Images were obtained using a Tecnai-12-FEI 120kV BioTwin Spirit Transmission Electron Microscope (FEI Europe). Details of sample processing can be found in Section 2.12.

4.2.8 Statistical Analyses

Statistical analyses were performed by ANOVA with a *post hoc* analysis by the Student-Neuman-Keuls test.

4.3 Results

The conversion of the soluble form of LC3 (LC3-I) to the lipidated and autophagosome-associated form (LC3-II) is considered to be one of the hallmarks of autophagy. In intact cells, formation of LC3-II is associated with the appearance of LC3 puncta readily detected by conventional fluorescence microscopy. The mitochondrial complex I inhibitor rotenone and other promitophagic stimuli have been shown to increase the number of LC3 puncta and the level of colocalization with mitochondria. Interestingly, rotenone treatment also induced externalization of CL to the mitochondrial surface (Chu *et al.*, 2013).

4.3.1 CL Translocation to the OMM Leads to LC3B, but not GABARAP or GABARAPL2, Mitochondrial Localization in U87MG Glioblastoma Cells

U87MG cells were selected as a cellular model to investigate, in collaboration with Dr. G. Velasco, the activation of autophagy and mitophagy by different stimuli. In addition it is known that autophagy plays an important role in cancer cells and therefore the mechanism of regulation of mitochondria degradation studied in this cell line could also be relevant in the control of cancer cell survival. Cells were treated with rotenone for 4 h and colocalization of mitochondria with endogenous LC3B puncta was examined. In control experiments, nutrient starvation or THC were used as nonselective autophagy inducers. In agreement with Kagan and coworkers, rotenone treatment elicited robust colocalization of mitochondria with LC3B puncta, indicative of LC3B translocation to the organelle (**Figure 4.1A**). In parallel experiments, both THC and nutrient starvation caused potent LC3B puncta formation consistent with reports indicating that THC and nutrient deprivation induce autophagy-mediated death and protective autophagy, respectively (Salazar *et al.*, 2009; Weidberg *et al.*, 2011). Nevertheless, LC3B puncta formed under these treatment conditions did not exhibit mitochondrial colocalization unlike the situation observed with rotenone. Rotenone-induced mitophagy was further confirmed by colocalization of both mitochondria

(**Figure 4.1B**) and LC3B (**Figure 4.1C**) with lysosomes. Finally, consistent with THC and nutrient starvation not inducing mitophagy, LC3B puncta (**Figure 4.1C**) but not mitochondria (**Figure 4.1B**) exhibited lysosomal colocalization. Altogether, these results indicate that rotenone, but not other well-characterized autophagy inducers (THC, nutrient starvation) elicited mitophagy in U87MG human glioblastoma cells.

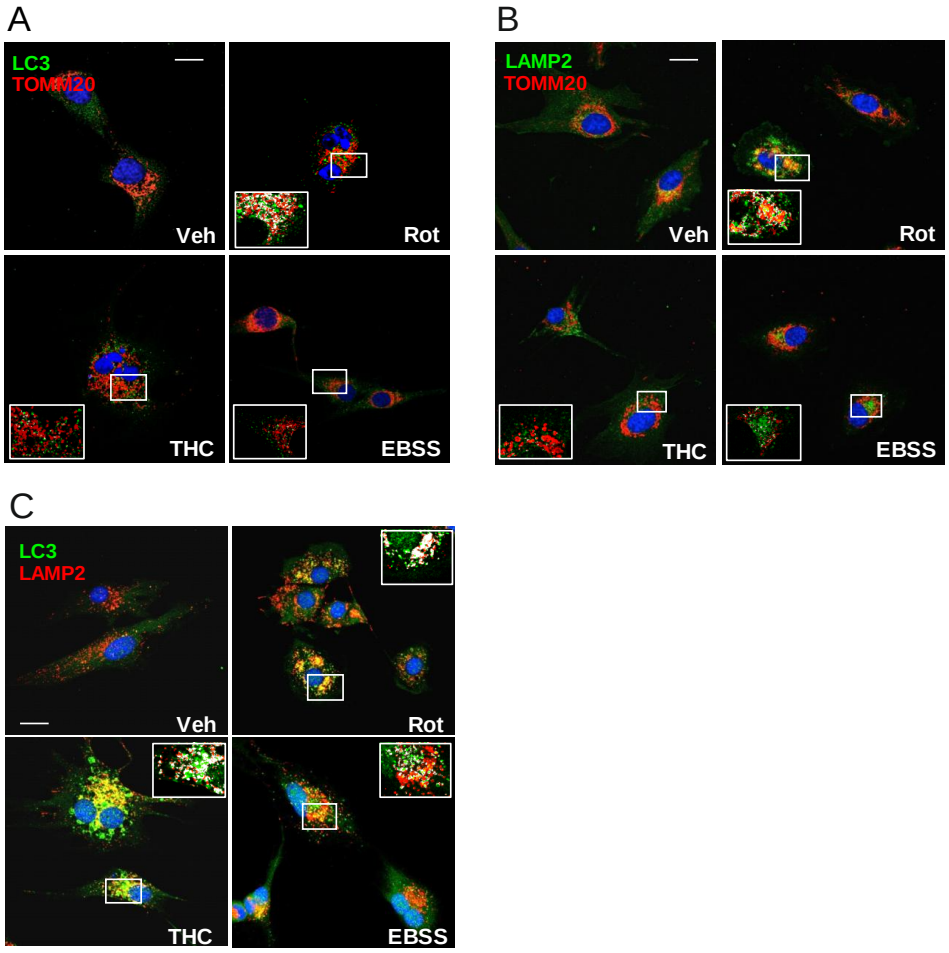

Figure 4.1. Rotenone, but not THC or nutrient starvation, elicits mitophagy in U87MG human glioblastoma cells. (**A**) Analysis of endogenous LC3B puncta colocalization with TOMM20-stained mitochondria in response to Rot (1 μM; 4 h) or THC (4 μM; 6 h) treatments, or to nutrient deprivation (EBSS) conditions in U87MG cells. (**B**) Rotenone, but not THC or EBSS, increased delivery of TOMM20-stained mitochondria to LAMP2-stained lysosomes in U87MG cells. (**C**) LC3B puncta colocalization with lysosomes (LAMP2) in response to Rot (1 μM; 4 h) or THC (4 μM; 6 h) treatments, or to nutrient deprivation (EBSS) conditions in U87MG cells. Insets from the same cells showing colocalization pixels in white are also shown. Bars: 20 μm.

Next, in order to analyze the functional implications of the previously observed differences among human orthologs *in vitro* (see Chapter 3), the possible rotenone-induced GABARAPL2 and GABARAP translocation to mitochondria was examined in glioblastoma cells. To this aim, U87MG cells were transiently transfected with plasmids expressing GFP-tagged human GABARAPL2 or GABARAP, and subjected to either nutrient starvation, THC or rotenone treatments. As shown in **Figure 4.2A and B**, all

treatments elicited an increase in GABARAPL2- and GABARAP-GFP puncta within cells. However GABARAP- or GABARAPL2-labeled autophagosomes did not exhibit mitochondrial colocalization after rotenone treatment. Thus, LC3B translocation to mitochondria in response to externalized CL might play a specific role in this cell line, different from that of GABARAPL2 and GABARAP.

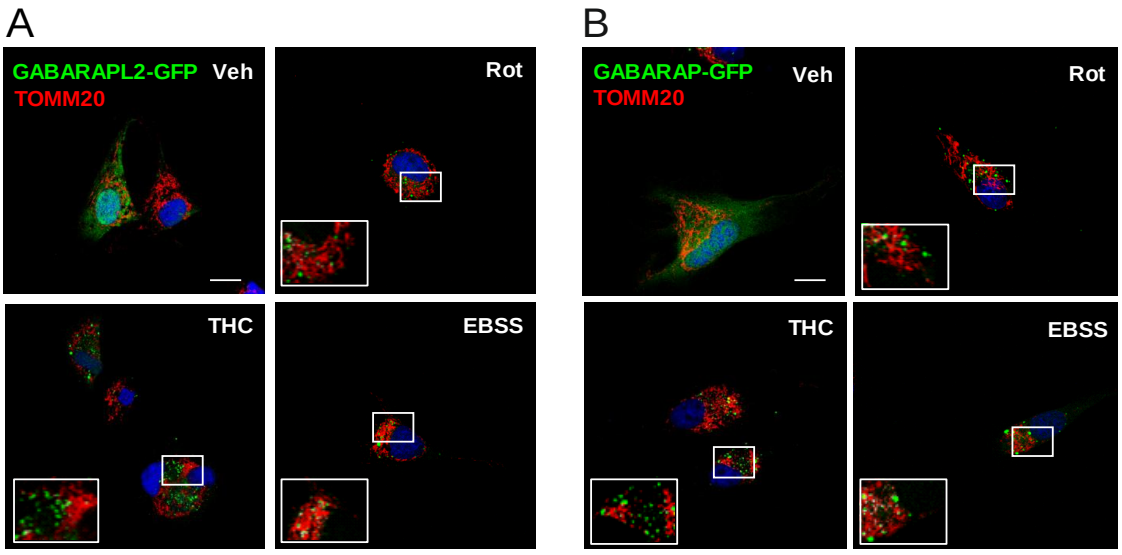

Figure 4.2. Neither GABARAPL2 nor GABARAP exhibit mitochondrial colocalization after rotenone treatment in U87MG cells. (**A-B**) Analysis of GABARAPL2-GFP or GABARAP-GFP puncta colocalization with TOMM20-stained mitochondria in response to rotenone (1 μM; 4 h) or THC (4 μM; 6 h) treatments, or to nutrient deprivation conditions in U87MG cells. Bars: 20 μm.

4.3.2 LC3B, GABARAPL1 and ATG5 Mitochondrial Recruitment during Mitophagy in Human RPE1 Cells

Mitochondrial complex I inhibition and CL externalization to the outer mitochondrial membrane act as signals for LC3B in U87MG human glioblastoma cells triggering the recruitment of the protein to mitochondria and leading to the selective removal of damaged mitochondria via autophagy (**Figure 4.1**; Antón *et al.,* 2016). However, whether this mechanism and pathway are specific for certain cell types and/or for LC3B, remains a matter of investigation.

4.3.2.1 LC3B, GABARAPL1 and ATG5 Intracellular Localization during Mitophagy

As a first approach to investigate the possibility of the previously observed LC3B mitochondrial recruitment during rotenone-induced mitophagy (Chu *et al.,* 2013; Antón *et al.,* 2016) to be a cell type-dependent process, a stable RPE1 cell line expressing tandem-tagged mCherry-GFP-LC3B was employed to examine the mitochondrial

localization of the LC3B-labelled autophagosomes (**Figure 4.3A**). Autophagosome maturation can be tracked by using the mCherry-GFP-LC3 fusion construct as, upon lysosomal fusion, GFP is quenched in a pH-dependent manner whereas mCherry resists the acidic lysosomal environment (Kimura *et al.*, 2007). As a result, late autolysosomes fluoresce red only, but earlier autophagosomes are decorated both green and red, thus appearing as yellow puncta when green and red channels are overlaid. As an example, during steady autophagy induction the number of autophagosomes (yellow) and autolysosomes (red) are expected to increase concurrently, however if autophagic flux is inhibited, only the autophagosomes (yellow) will increase in number. In the context of this project this method was used to quantitatively analyze LC3B puncta recruitment to mitochondria during nonselective bulk autophagy or mitophagy.

The predominant cellular response to rotenone exposure depends largely on dose and exposure time, as well as on the prior condition of the cells (Fleming *et al.*, 2004; Maurya *et al.*, 2015; Meurers *et al.*, 2009; Zhu *et al.*, 2004). Indeed, in some cases low doses have only mild toxic effects, as indicated by a high cell survival rate (Frank *et al.*, 2012; Shaikh & Nicholson, 2009), but a prolonged exposure or higher concentrations of rotenone can induce excessive accumulation of ROS, inclusion body formation or apoptosis, e.g. in dopaminergic neurons and striatal neurons (Höglinger *et al.*, 2003; Lapointe *et al.*, 2004; Maurya *et al.*, 2015; Shaikh & Nicholson, 2009; Zhu *et al*., 2004). Chu and coworkers have shown that rotenone, under sublethal or prelethal conditions (involving low doses), elicits mitophagy in primary rat cortical neurons and SH-SY5Y neuroblastoma cells. Moreover under these early, mitophagy-inducing treatment conditions no increased CL peroxidation products were detected (Chu *et al.,* 2013). Thus cell response to rotenone highly depends on experimental conditions and also varies with cell types.

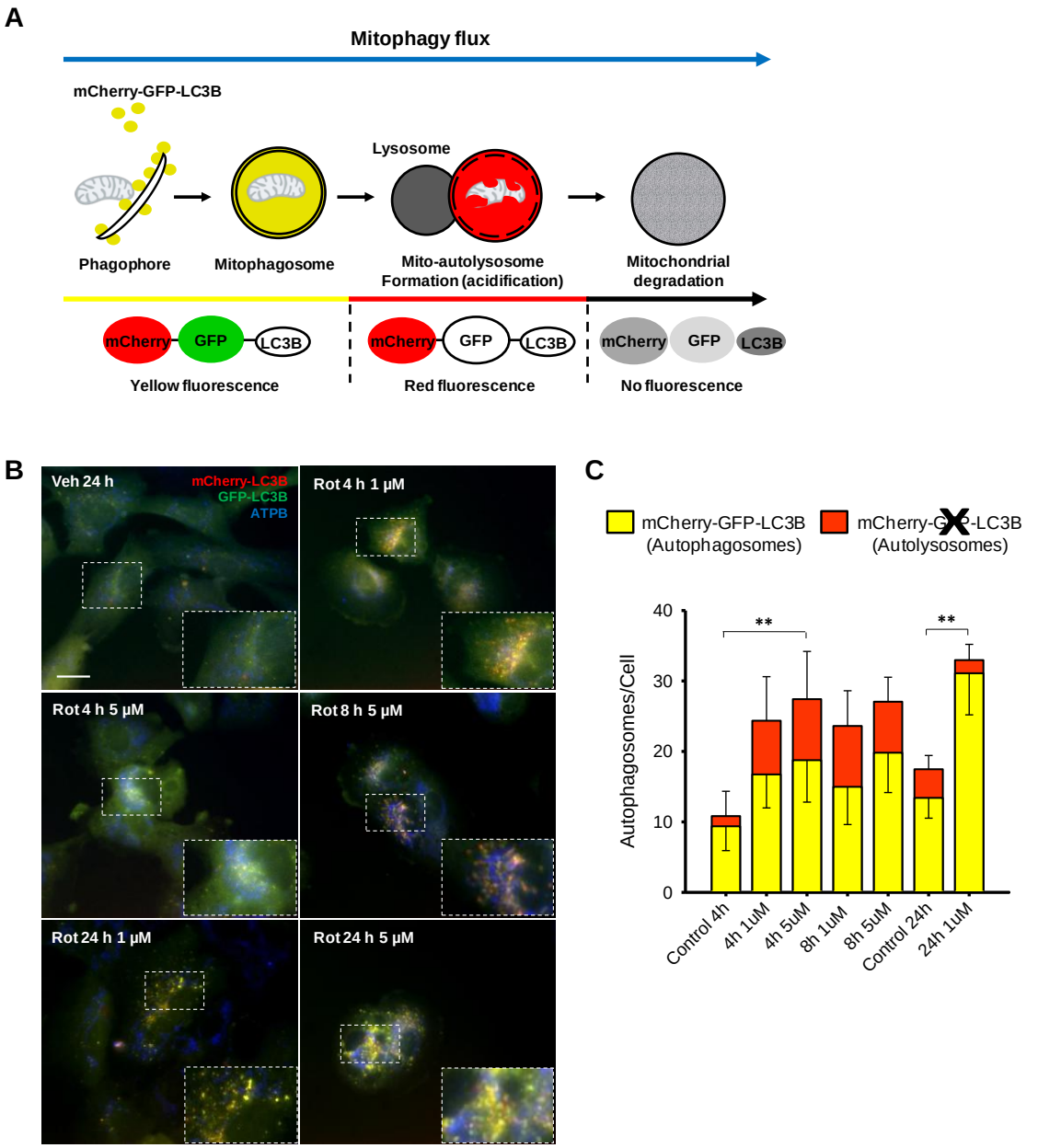

Figure 4.3. Rotenone shortest treatment and lowest dose for a mitochondrial colocalization of tandem LC3B in RPE1 cells. (**A**) Outline of mitophagy flux analysis using the mCherry-GFP-LC3B tandem tag. By merging green and red channels as shown, autophagosomes were identifiable as yellow puncta and autolysosomes as red puncta. (**B**) Colocalization analysis of mCherry-GFP-LC3B with ATPB-stained mitochondria in response to rotenone 1 or 5 µM, 4 h; 5 µM, 8 h and 1 or 5 µM, 24 h treatments in RPE1 cells. (**C**) mCherry-GFP-LC3B puncta quantitation of >400 cells/condition across n = 3 experiments are shown. Yellow bars represent red/green autophagosomes; red bars represent red-only autolysosomes (control = vehicle; upward error bars are SD of the red-only puncta and downward error bars are SD for green/red puncta; **P = 0.001 to 0.01). Bar: 20 µm.

In this study rotenone treatment dose and duration were designed to minimize the exposure length of rotenone-treated cells and cell damage, with the goal of avoiding the relatively acute cell death induced by higher doses or prolonged exposures to the

reagent, which would likely bias the analysis at a late stage in the process (Betarbet *et al.*, 2000; Höglinger *et al.*, 2003; Maurya *et al.*, 2015). To determine the minimum rotenone dose and exposure time sufficient to trigger LC3B puncta colocalization with mitochondria (mitophagy), an optimization experiment was first performed in mCherry-GFP-LC3B expressing RPE1 cells (**Figure 4.3**). Cell mitophagy response to varying concentrations of rotenone for 4, 8 and 24 h was measured, whereupon a statistically significant increment in autophagosome-bound LC3B localized to mitochondria was detected in rotenone-treated cells as compared to non-treated control cells (**Figure 4.3B, C**).

To confirm that induction of mitophagy would lead to LC3B localization in the outer mitochondrial membrane by a mechanism specific for this pathway, four different autophagy- or mitophagy-inducers were tested in the mCherry-GFP-LC3B cell line, namely nutrient deprivation, or AZD8055, CCCP or rotenone treatments. As previously shown for U87MG glioblastoma cells (**Figure 4.1**), amino acid/growth factor starvation is known to induce nonselective autophagy and LC3B dots formed under this treatment do not exhibit mitochondrial colocalization (Antón *et al.*, 2016; Hernández-Tiedra *et al.*, 2016). AZD8055 is an ATP-competitive mTOR kinase inhibitor that induces robust bulk autophagy (Chan *et al.*, 2012; Egan *et al.*, 2015; Hsieh *et al.*, 2012). For a positive mitophagy control, CCCP – a protonophore that causes an uncoupling of the respiratory chain and a loss of mitochondrial membrane potential by increasing permeability to protons (Betin *et al.*, 2012; Perry *et al.*, 2011) – was used. CCCP exposure is generally used to simulate mitochondrial dysfunction and induces PARK2-mediated mitophagy (Rüb *et al.*, 2016). Finally, low rotenone doses induce CL externalization to the OMM, LC3 translocation to mitochondria and mitophagy (Chu et al., 2013). In neurons and SH-SY5Y cells, in contrast to the effects observed with strong depolarizing agents such as CCCP (Kondapalli *et al.*, 2012), rotenone causes no more than 15% decrease of mitochondrial membrane potential and PINK1/PARK2 translocation is not observed (Chu *et al.*, 2013; Chu *et al.*, 2014).

LC3B intracellular localization was examined and LC3B puncta numbers were measured during nonselective autophagy, using nutrient starvation or AZD8055 treatment, or during CCCP- or rotenone-induced selective mitophagy (**Figure 4.4**). Correspondingly, in RPE1 cells expressing mCherry-GFP-LC3B, AZD8055 administration or starvation conditions caused a dramatically increased LC3B puncta numbers (~4.7-fold) (**Figure 4.4B**) that were largely diffuse in the cytoplasm, but no translocation to mitochondria was observed (**Figure 4.4A**). CCCP also caused a strong cell response (4.5-fold LC3B puncta) and in this case LC3B predominantly localized in

the surrounding mitochondria. Cells treated with 5 µM rotenone do not give rise to a particularly strong stress-induced autophagy response (**Figure 4.4B**), however they clearly induced LC3B translocation to mitochondria (**Figure 4.4A**).

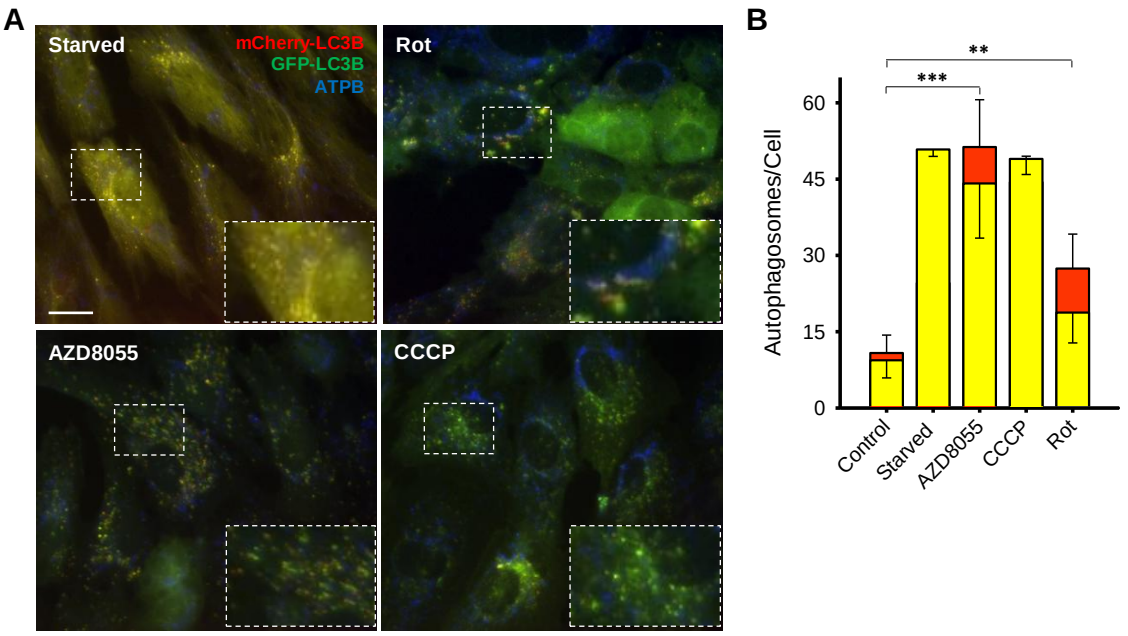

Figure 4.4. Rotenone induces less, larger puncta but more LC3B mitochondrial localization in human RPE1 cells. (**A**) Representative images of mCherry-GFP-LC3B colocalization analysis with ATPB-stained mitochondria and (**B**) tandem LC3B puncta quantitation are shown in response to AZD8055 (1 nM; 2 h), rotenone (5 µM; 4 h) or CCCP (20 µM; 4 h) treatments, or to nutrient deprivation conditions in RPE1 cells. Yellow bars represent red/green autophagosomes; red bars represent red-only autolysosomes (control = vehicle; upward error bars are SD of the red-only puncta and downward error bars are SD for green/red puncta; **P = 0.001 to 0.01, ***P < 0.001). Quantitation of >400 cells/condition across n = 3 experiments. Bar: 20 µm.

Although the above data were useful in determining the mCherry-GFP-LC3B response to both non-selective and selective autophagy inductions in RPE1 cells, a comparison with another LC3/GABARAP family member was needed to see whether this response was specific for LC3B in this human cell line. mCherry-GFP-GABARAPL1 expressing RPE1 cells were therefore treated with rotenone and CCCP as mitophagy inducers and AZD8055 was also included as a bulk nonselective autophagy inducer. In control non-treated cells, most of the mCherry-GFP-GABARAPL1 fluorescent signal was cytoplasmic with a few small puncta (**Figure 4.5**). The strongest responses in terms of number of autophagosomes were observed for AZD8055 and CCCP treatments (**Figure 4.5B**). Importantly, GABARAPL1 also localized to the outer mitochondrial membrane in response to rotenone administration in human RPE1 cells. This differs from the previous results with the other GABARAP subfamily proteins,

GABARAP and GABARAPL2, which were not recruited to mitochondria after rotenone treatment in U87MG glioma cells (**Figure 4.2**). Thus, human Atg8 orthologs may play different roles during damage-induced mitophagy in different cell types.

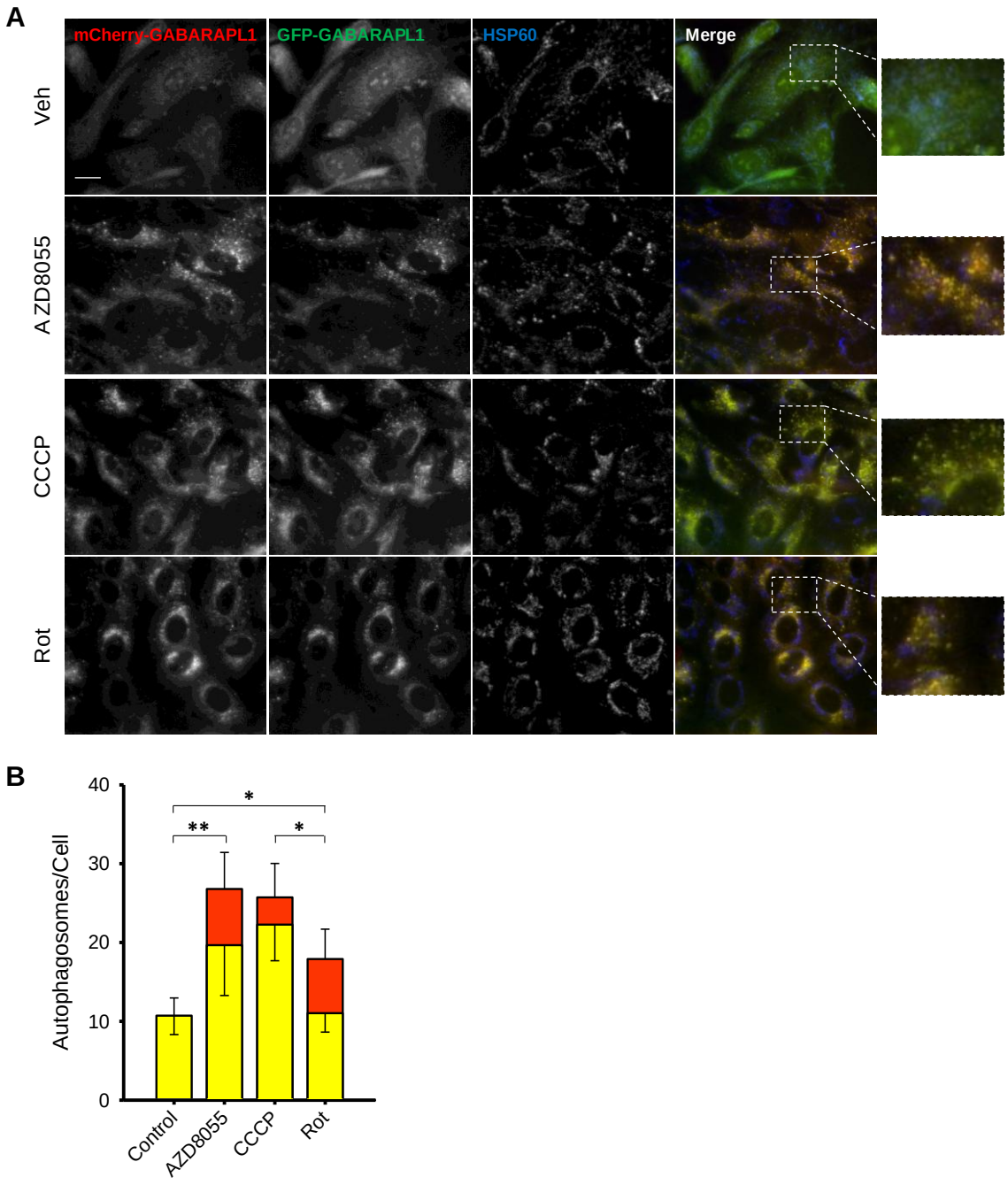

Figure 4.5. Rotenone-induced tandem GABARAPL1 mitochondrial recruitment in RPE1 cells. (**A**) Colocalization analysis of mCherry-GFP-GABARAPL1 with HSP60-stained mitochondria in response to AZD8055 (1 nM; 2 h), CCCP (20 μM; 4 h) or rotenone (5 μM; 4 h) treatments in RPE1 cells. (**B**) mCherry-GFP-GABARAPL1 puncta quantitation of >400 cells/condition across n = 3 experiments are shown. Yellow bars represent red/green autophagosomes; red bars represent red-only autolysosomes (control = vehicle; upward error bars are SD of the red-only puncta and downward error bars are SD for green/red puncta; *P = 0.01 to 0.05, **P = 0.001 to 0.01). Bar: 20 μm.

Next a RPE1 cell-line stably expressing GFP-ATG5 was used. ATG5 is a key component of an E3-like ATG12-ATG5-ATG16 protein complex that catalyzes conjugation of LC3 to lipids (Matsushita *et al.*, 2007). ATG5 plays a crucial role in the early stages of autophagosome formation controlling autophagic vesicle formation and expansion. ATG5 localizes to the PAS or "isolation membrane", together with ATG12 and ATG16L1 (Mizushima *et al.*, 2003; Mizushima *et al.*, 2001; Suzuki *et al.*, 2001), making this target a useful potential marker for the isolation membrane or assembly site. When the isolation membrane elongates and fuses to form the autophagosome, ATG5 detaches from the membrane. Therefore, GFP-ATG5 can be detected only on nascent autophagosomes, but not on completely formed ones (Mizushima *et al.*, 2001). In the context of this study, the rationale for the assessment of ATG5 intracellular localization was to see whether translocation of CL to the OMM would cause the recruitment of assembly sites, as detected by the mitochondrial localization of GFP-ATG5-positive structures during rotenone-induced mitophagy. Moreover, both early and late autophagosomal structures were labeled using immunostaining for LC3B in RPE1 cells exposed to AZD8055, CCCP or rotenone (**Figure 4.6**). Labeling of endogenous LC3B with antibodies is often used to identify autophagosomes and to quantify autophagy (number of puncta by fluorescence imaging or LC3B cytoplasmic/membrane-bound ratio by immunoblotting). Both methods can be used to measure autophagy at steady state or to monitor autophagy flux (Klionsky *et al.*, 2008). As shown in **Figure 4.6B**, CCCP and the mTOR catalytic inhibitor AZD8055 caused a significant increase in GFP-ATG5 puncta numbers (4.4 and 6.8-fold increase, respectively) with respect to the non-treated control cells. In contrast, under the same conditions 5 μM rotenone administration caused a lower increase in GFP-ATG5 puncta numbers. LC3B puncta signals were also increased and dispersed by AZD8055 treatment in GFP-ATG5 expressing cells (**Figure 4.6**), as in mCherry-GFP-LC3B expressing RPE1 cells (**Figure 4.4**). Furthermore, after rotenone-induced mitophagy, LC3B also localized to mitochondria in this cell line. Thus as shown above in **Figure 4.4** for mCherry-GFP-LC3B, the data in GFP-ATG5 expressing RPE1 cells indicate that rotenone is a weaker autophagy inducer than AZD8055 or CCCP. However, GFP-ATG5 colocalization with mitochondria was difficult to determine due to GFP-ATG5 puncta being far less frequent (<5 per cell) than LC3B ones.

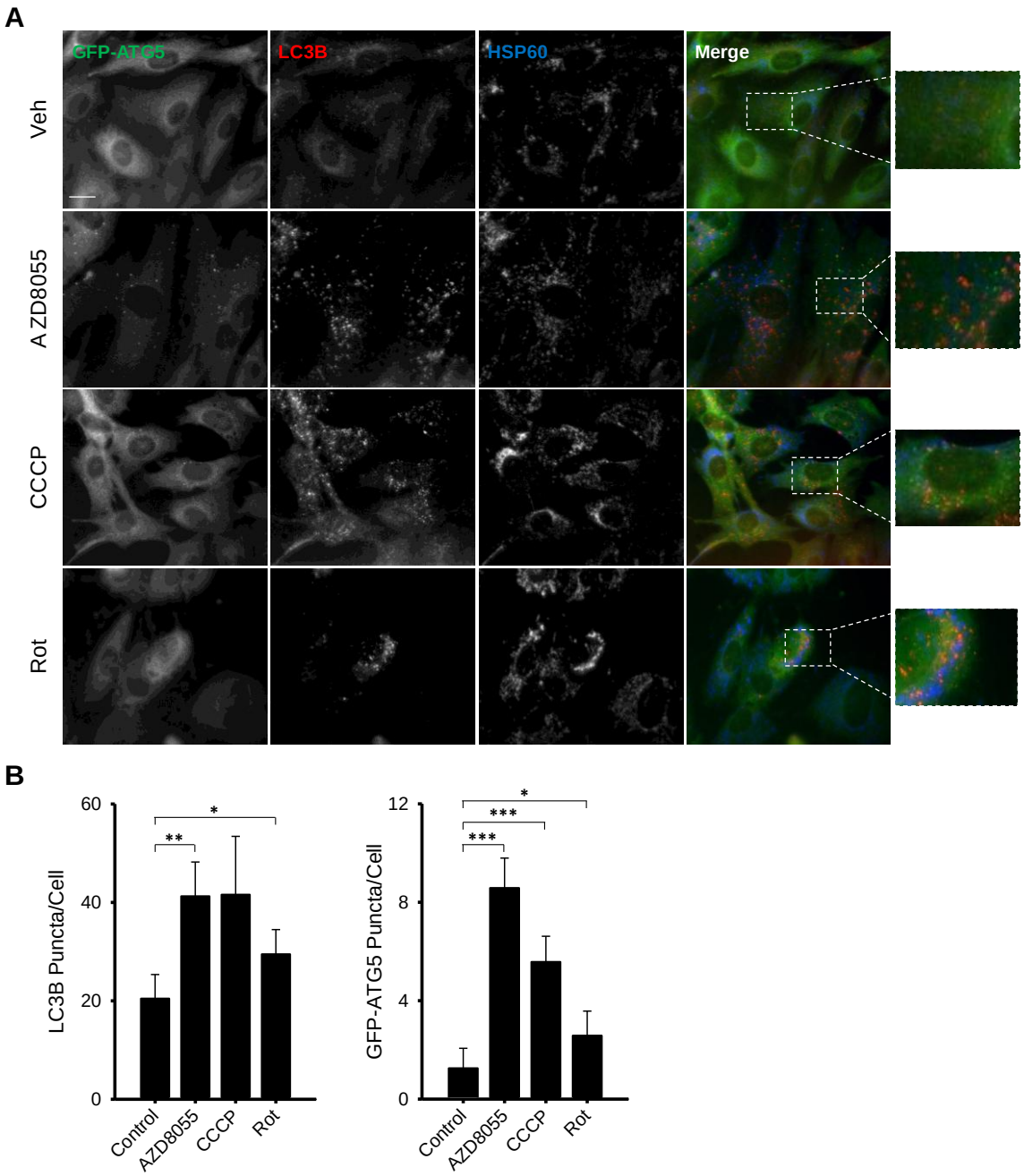

Figure 4.6. GFP-ATG5 as an early marker for preautophagosome localization after rotenone-induced mitophagy in RPE1 cells. (**A**) Colocalization analysis of GFP-ATG5 and LC3B with HSP60-stained mitochondria in response to AZD8055 (1 nM; 2 h), CCCP (20 μM; 4 h) or rotenone (5 μM; 4 h) treatments in RPE1 cells. (**B**) Measurements of LC3B and GFP-ATG5 puncta of >400 cells/condition across n = 3 experiments are shown (control = vehicle; error bars are SD; *P = 0.01 to 0.05, **P = 0.001 to 0.01, ***P < 0.001). Bar: 20 μm.

Taken together, the data obtained using three different fixed RPE1 cell-lines showed that mCherry-GFP-LC3B, mCherry-GFP-GABARAPL1, and GFP-ATG5 puncta numbers increased after AZD8055 and CCCP treatments indicating an autophagy cell response (**Figures 4.4B, 4.5B and 4.6B**). Rotenone treatment also significantly increased LC3B, GABARAPL1 and ATG5 puncta numbers, albeit less dramatically. In addition, induction of selective removal of mitochondria by CCCP or rotenone caused

LC3B and GABARAPL1 mitochondrial recruitment in fixed RPE1 cells (**Figures 4.4A, 4.5A and 4.6A**). In contrast, the autophagic structures labeled for the early autophagy marker ATG5 were not clearly localized to mitochondria after mitophagy induction (**Figure 4.6A**). Remarkably, LC3B- and GABARAPL1-labeled autophagosomes were far more perinuclear and clustered after 4 h rotenone treatment compared to other treatments in human RPE1 cells. The significance of altered autophagosome localization with regard to mitophagy efficiency is unclear, although admittedly the clustering of puncta may have caused an underestimation of automated autophagosome counts in rotenone-treated cells. Autophagosomes are normally delivered to the perinuclear region for fusion with the lysosomes thus there might be greater autophagosomal degradation in cells with perinuclear clustered autophagosomes (Korolchuk & Rubinsztein, 2011).

4.3.2.2 Dynamics of LC3B- or ATG5-labeled Autophagic Structures in Rotenone-treated RPE1 Cells

As mentioned above, the cellular response to rotenone treatment depends on the dose and exposure time, cell type and prior cell conditions (Zhu *et al.*, 2004; Meurers *et al.*, 2009; Maurya *et al.*, 2016). Indeed high concentrations of rotenone or prolonged low rotenone doses are found to induce cell death in some cell types (Shaikh & Nicholson, 2009; Höglinger *et al.*, 2003; Lapointe *et al.*, 2004). To find out at which point LC3B-mediated mitophagy is susceptible to 5 µM rotenone treatment, live-cell imaging of mCherry-GFP-LC3B or GFP-ATG5 stably expressing RPE1 cells was conducted (**Figures 4.7 to 4.9**). Time-lapse imaging of LC3B-labeled autophagosomes by wide-field or confocal imaging can be used to observe autophagosome or mitophagosome dynamics in living cells (Karanasios *et al.*, 2013; Kimura *et al.*, 2008; Maday *et al.*, 2012; Wang *et al.*, 2013; Yang & Yang, 2013). Here this technique was used to follow autophagosomes and capture uptake events of labeled mitochondria by autophagosomes during rotenone-induced mitophagy, analyzing variations at the ultrastructural level using correlative light and electron microscopy (see Section 4.3.2.3). In the following time-lapse experiments, mCherry-GFP-LC3B stably expressing RPE1 cells were transiently transfected with MTS-CFP for mitochondrial staining (**Figures 4.7 and 4.8**).

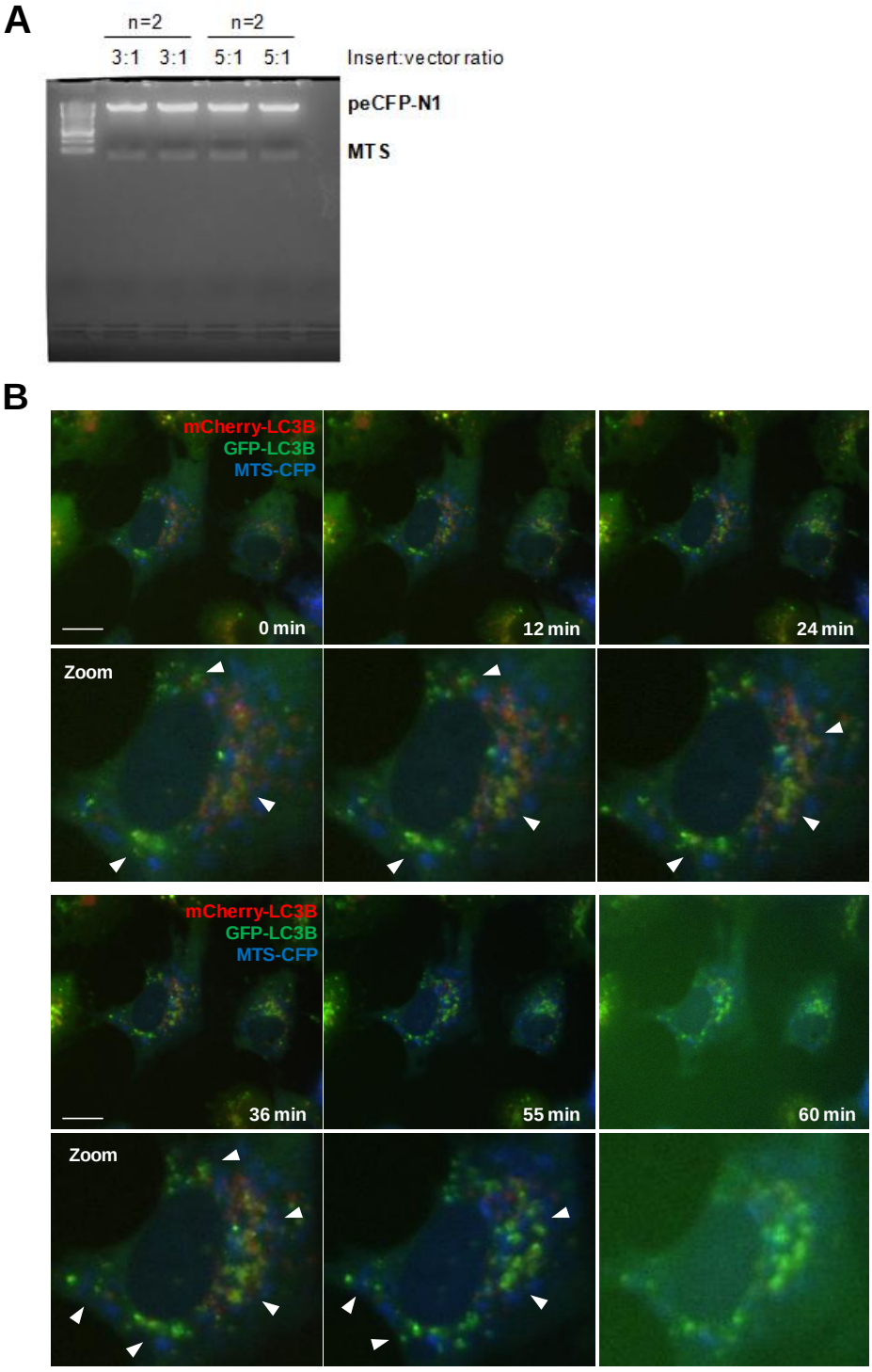

Figure 4.7. Tandem LC3B recruitment to damaged (rotenone-treated) mitochondria in RPE1 cells transfected with MTS-CFP. (**A**) The construct containing the MTS, MTS-peCFP-N1, was sub-cloned in this work from the construct MTS-peGFP. Confirmation of the presence of the MTS in the peCFP-N1 vector by agarose gel is shown. Various insert:vector ratios were used in the ligation reaction, and 3:1 and 5:1 ligation products containing bacteria colonies were selected. (**B**) mCherry-GFP-LC3B stably expressing RPE1 cells were transiently transfected using DNA samples with a 3:1 insert:vector ratio and treated with rotenone. Representative images from cell time-lapse experiments are shown (see Supplemental Movies 4.7 and 4.11). Arrow heads indicate changes observed for LC3B punctae surrounding mitochondria. The sequence starts (0 min) 1 h after rotenone addition to cells. 60 min: cells were fixed with 2% glutaraldehyde for CLEM (see Section 4.3.2.3). Bars = 20 μm.

This sequence may suggest (i) the targeting and engulfment of mitochondria by autophagosomes, (ii) fusion events between autophagosomes and (iii) a slow turnover of autophagosomes in human RPE1 cells (note that the imaging periods were about 60 min) (**Figure 4.7B**). Moreover, as shown above for rotenone-fixed cells (see previous Section 4.3.2.1), a perinuclear localization of LC3B puncta-decorated mitochondria was observed after rotenone treatment in living RPE1 cells (see arrows in **Figure 4.7B**).

To further confirm that mCherry-GFP-LC3B RPE1 cells remove their damaged mitochondria via mitophagy and for a better ultrastructural analysis of mitophagosomes using CLEM (see next section), a complete inhibition of lysosomal proteases and therefore of autophagosome degradation was induced using the acidic protease inhibitor leupeptin (**Figure 4.8**). The lysosome is the ultimate degradative autophagic compartment in the cell and leupeptin is a naturally occurring protease inhibitor that inhibits cysteine, serine and threonine peptidases (Yang *et al.*, 2013). It blocks autophagy at the step of degradation of the lysosome-enclosed cytoplasm and causes the accumulation of autolysosomes (see **Figure 4.8**) and/or many cytoplasmic inclusions in the central vacuoles (Kominami *et al.*, 1983; Moriyasu & Inoue, 2008). The V-ATPase inhibitor BafA1 is another autophagy inhibitor that is also used to study mitophagy flux. BafA1 acts as a pharmacological inhibitor of V-ATPase, and appears to prevent autophagosome maturation by blocking lysosome acidification and hindering the fusion of autophagosomes with lysosomes (Klionsky *et al.*, 2008). In the presence of BafA1 cells are unable to deliver mitochondria to lysosomes for degradation. However, as BafA1-induced lysosomal inhibition blocks lysosome acidification, it also affects pH thus the green-red fluorescence shift would not be observed in mCherry-GFP-LC3B expressing cells.

After treatment with both rotenone and leupeptin, mitochondrial colocalization with LC3B-labeled autophagosomes was also detected and perinuclear accumulation of autolysosomes was observed (**Figure 4.8**). Thus in the presence of the lysosomal inhibitor leupeptin, mitochondrial mass reduction is blocked at the basal state and after mitophagy induction.

In summary live-cell imaging of mCherry-GFP-LC3B expressing cells revealed that 2 h rotenone treatment was sufficient to trigger LC3B translocation to the mitochondria in RPE1 cells, confirming that 5 µM rotenone induces LC3B mitochondrial recruitment in this cell type. Interestingly, most autophagosomes were grouped in a mitochondria-rich area and persisted throughout the imaging period, about 60 min – a comparatively long time when the half-life of an autophagosome is thought to be on

average 6-9 min in several rat or mice tissues (Kovács *et al.*, 1987; Pfeifer, 1978) (**Figures 4.7 and 4.8**).

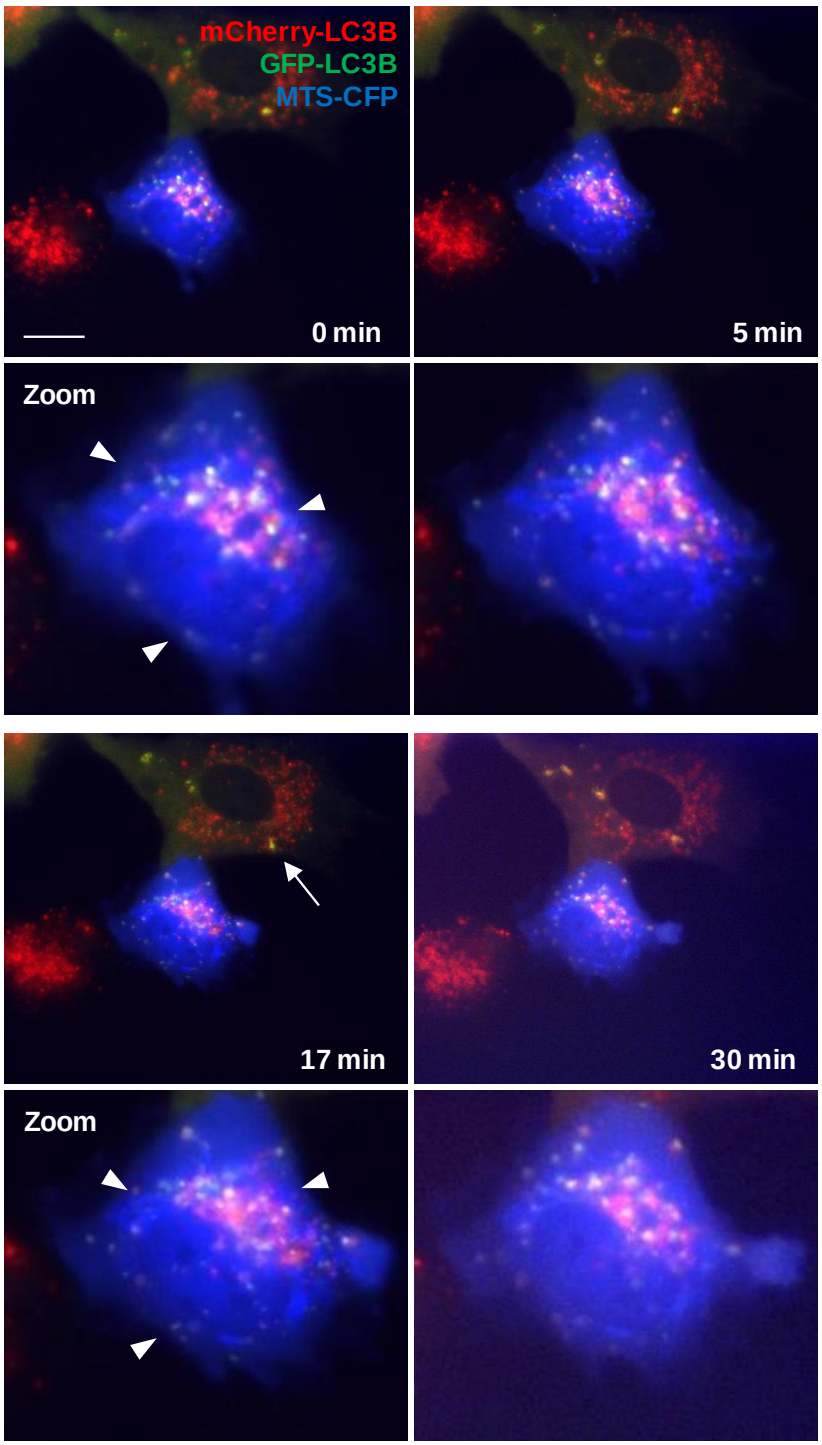

Figure 4.8. Inhibition of autophagic lysosomal degradation during rotenone-induced mitophagy in RPE1 cells stably expressing tandem LC3B. Live-cell imaging of mCherry-GFP-LC3B recruitment to mitochondria in RPE1 cells transfected with MTS-CFP and treated with 5 µM rotenone and 20 µM leupeptin (see Supplemental Movie 4.8). Arrow heads indicate localization of LC3B puncta-decorated mitochondria and lysosome inhibition-caused perinuclear accumulation of autolysosomes (see also arrow in the adjacent non-transfected cell). The sequence starts (0 min) 2 h after rotenone and leupeptin addition to cells. 30 min: cells were fixed with 2% glutaraldehyde for CLEM (see Section 4.3.2.3). Bar = 20 µm.

The next step was to study early stages of autophagosomal formation in a PARK2-independent rotenone-induced mitophagy background through analysis of GFP-ATG5 dynamics at the assembly site. To identify the autophagosome assembly site, or “isolation membrane” and its possible mitochondrial location, human RPE1 cells stably expressing GFP-ATG5 and cotransfected with Mito-DsRed were used (**Figure 4.9**).

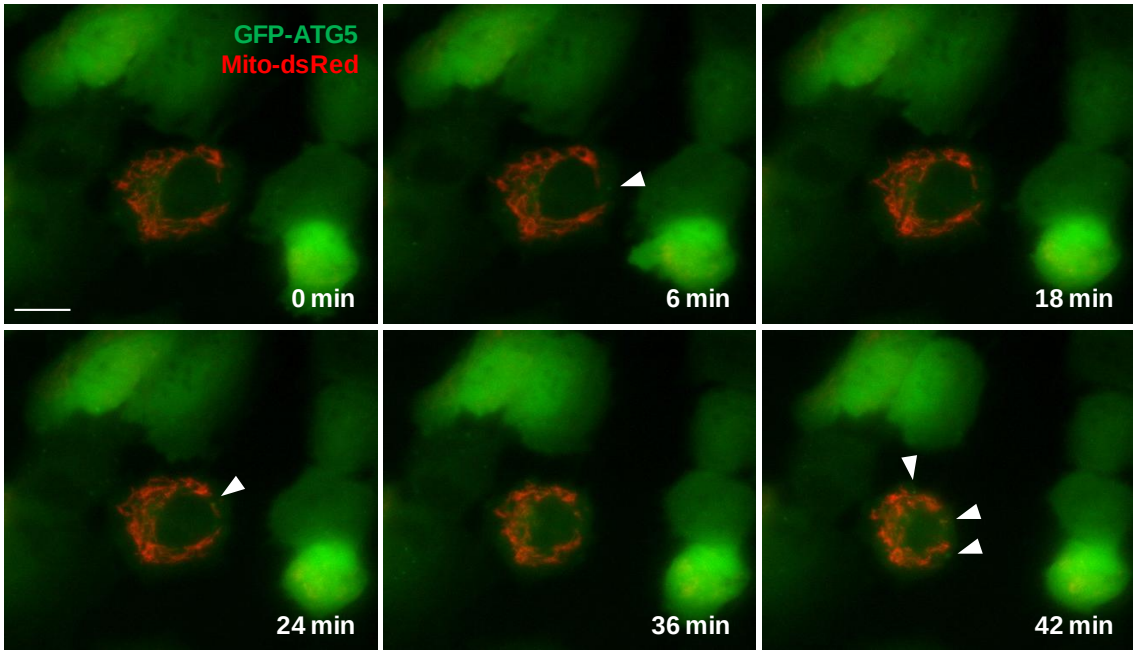

Figure 4.9. Recruitment of ATG5-positive isolation membranes to rotenone-treated mitochondria in RPE1 cells coexpressing Mito-DsRed. Arrow heads indicate cell zones where transient GFP-ATG5 punctae were observed (see Supplemental Movie 4.9). The sequence starts (0 min) 1 h 30 min after rotenone addition to cells. Bar = 20 µm.

Unfortunately, clear evidence of GFP-ATG5 recruitment to mitochondria was not detected in rotenone-treated RPE1 cells (**Figure 4.9**), despite the previously observed mitophagy response of this cell type to rotenone administration using the same dose and exposure time (**Figure 4.7**). These results suggest that preautophagosome localization to mitochondria might not be required for LC3B attachment to the outer mitochondrial membrane via LC3B-CL interaction. Note however that the lifetime of ATG5-positive structures was shorter than LC3B punctae and that GFP-ATG5 signal was primarily cytosolic, making ATG5 recruitment to mitochondria difficult to be determined in this early, mitophagy-inducing treatment conditions involving low doses of rotenone.

4.3.2.3 CLEM for Ultrastructural Characterization of LC3B Recruitment to Mitochondria in Rotenone-treated Cells

One of the aims of this project was to examine the ultrastructure of mitochondrial or/and autophagosomal membrane remodeling after LC3B recruitment to mitochondria and to examine possible changes in mitochondrial membrane morphology or structure after LC3B binding. For that purpose, EM was used following time-lapse imaging of rotenone-treated human RPE1 cells expressing mCherry-GFP-LC3B.

Autophagy was discovered and described as a lysosomal degradation pathway using EM. The discovery of autophagy factors involved at different stages of autophagosome formation and maturation from the 1990s allowed fluorescent labeling of these compartments and opened new possibilities for study, especially concerning autophagosome dynamics. CLEM links live-cell imaging with EM and provides crucial information to understand complex cellular events in all their dimensions including temporal information (van Rijnsoever *et al.*, 2008; Spiegelhalter *et al.*, 2014; Karreman *et al.*, 2016) – e.g. ultrastructural connections between phagophores and endoplasmic reticulum (Axe *et al.*, 2008; Hayashi-Nishino *et al.*, 2009; Ylä-Anttila *et al.*, 2009) or the colocalization of several proteins on the same autophagosomal structure (Ravikumar *et al.*, 2010). In this technique living cells are fixed at a selected time point of the time-lapse experiment following examination of the cellular architecture using EM imaging. In the context of this project, CLEM was used to study rotenone-induced mitophagy as it allowed identification and characterization of the mitochondria engulfed by autophagosomes and sent for degradation through this pathway. It was also a good alternative to EM to explore the stepwise events during rotenone-mediated cardiolipin exposure and mitophagy. Moreover, the prior immunofluorescence inspection of the sample – in this case using the autophagosome-specific antigen, mCherry-GFP-LC3B – allowed us to identify early and late autophagosomes involved in this pathway. Finally, CLEM provided us information about the ultrastructure of whole rotenone-treated RPE1 cells (e.g. distorted ER, pinocytic events, mitochondria and ER contact sites, transitional ER, lysosomal degradative compartments, or multivesicular bodies).

As mentioned above samples are fixed at a selected time point for CLEM. Aldehyde fixation is a widely used EM fixation technique adapted to most tissues and used in many autophagy studies (Eskelinen *et al.*, 2011). However, it is known to be associated with several artefacts including the possible collapse of membrane structures during dehydration (van Weering *et al.*, 2010). For this project glutaraldehyde fixation was used (see **Figure 4.10** for representative images of the cell of interest and

organelles fixed with glutaraldehyde). This fixation permitted a good identification of organelles and also had the strong advantage of generating highly contrasted ultrastructure (**Figures 4.10 to 4.12**). Despite the shape of cells and their organelles being sometimes irregular upon glutaraldehyde fixation, CLEM allowed the observation and identification of many autophagosomal structures (**Figures 4.10B, 4.11B and 4.12C**) – indicating an autophagic cell response induced by rotenone administration – and also other cellular organelles presented along this section. This included Golgi apparatus, intracellular trafficking vesicles, ER or mitochondria (**Figures 4.10A and 4.12A,B**).

Identification of the membrane-bound mitochondrion involved in the mitophagic pathway was essential for the purpose of this study. Labeling for LC3B, as a specific marker of autophagic vesicles, and the use of defined ultrastructural characteristics of their content based on criteria established by previous EM studies (Eskelinen *et al.*, 2011; Kent *et al.*, 1966), allowed us to classify early and late autophagosomes and mitophagosomes. Cells treated with the electron transport chain complex I inhibitor rotenone (**Figures 4.10 to 4.13**) or rotenone and leupeptin (**Figures 4.14 and 4.15**) were analyzed to confirm the extent and kinetics of mitophagy induction and mitochondrial removal in mCherry-GFP-LC3B expressing cells.

Green and red LC3B punctae observed with FM were clearly correlated with early and late autophagosome structures by EM imaging of the same cell regions (**Figure 4.11**). The autophagosome assembly site, or “isolation membrane” is a transient structure, with a characteristic ultrastructural morphology in aldehyde-fixed samples in Epon resin, consisting of closely opposed double membranes that appear electron dense (**Figure 4.11B**). This should ideally be the main criterion for recognizing these organelles; however, as EM studies have repeatedly mentioned (Eskelinen *et al.*, 2011), the two lipid bilayers delimitating autophagosomes cannot always be distinguished. Therefore, autophagosomes were also routinely identified by their cytoplasmic and/or organelle content and by FM observation of LC3B puncta. A large proportion of autophagosomes contained undefined cytoplasmic content, but larger organelles such as mitochondria could also be seen within (or close to) these compartments (**Figures 4.10B and 4.11B**). Supporting the observation made from light microscopy images that rotenone induced larger LC3B puncta compared to other autophagy inducers (**Figures 4.4A and 4.7B**), a portion of the autophagosomes observed by EM were larger and/or with varied content, possibly generated by homotypic fusion of several autophagosomes, or heterotypic fusion of autophagic and endocytic compartments, and could therefore be considered as amphisomes (**Figure**

4.11). Finally, together with the labeling for LC3B red puncta, the late autophagic compartments or autolysosomes, which represent the latest stage of this pathway, were identified by their fully degraded content (less electrodense and without the double membrane) (**Figures 4.10B, 4.11B and 4.12C**).

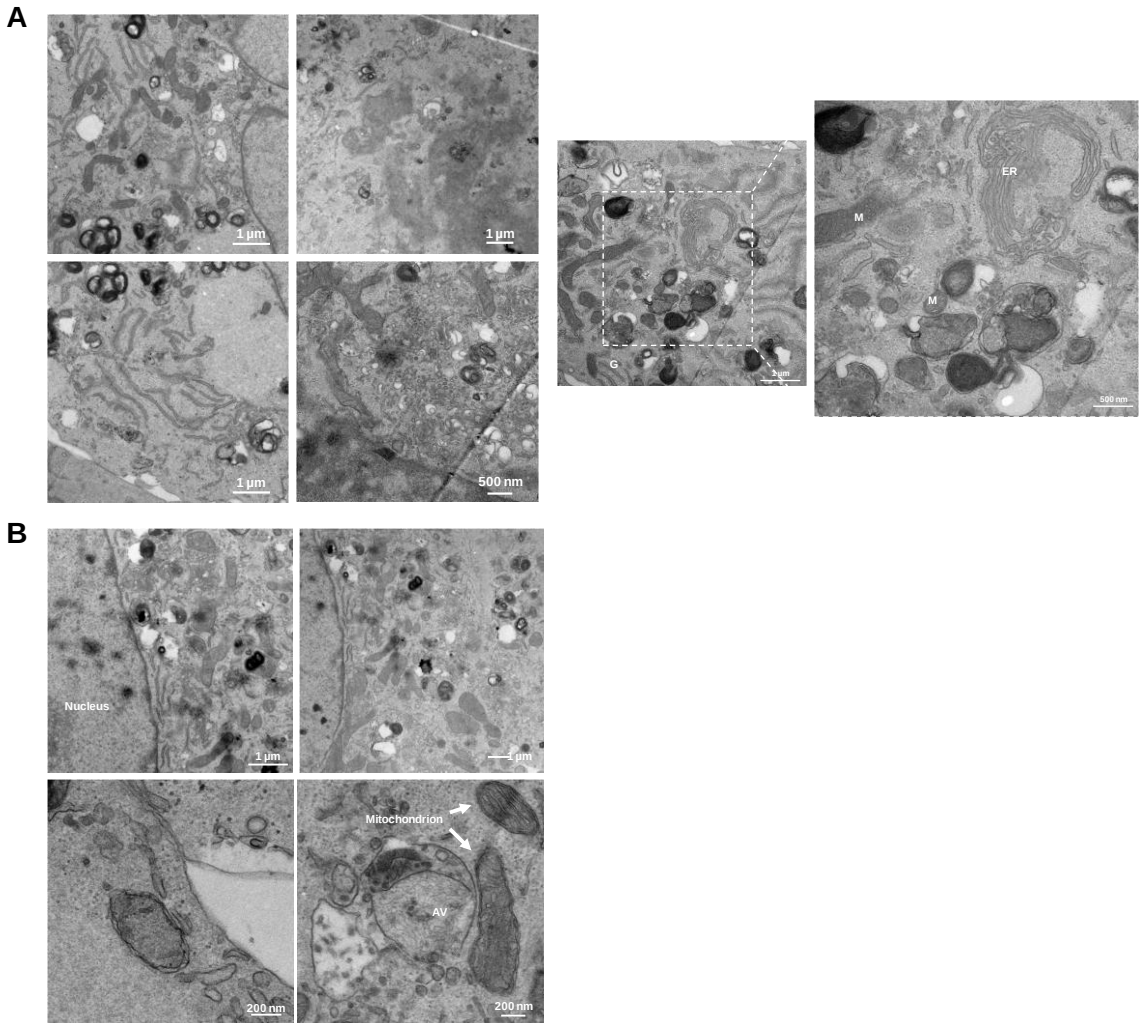

Figure 4.10. Ultrastructure of rotenone-treated human RPE1 cells expressing mCherry-GFP-LC3B fixed with glutaraldehyde. (**A**) Representative images of rotenone-treated mCherry-GFP-LC3B expressing cells following fixation with 2% glutaraldehyde. Glutaraldehyde-fixed cellular components were highly contrasted but often distorted. A large number of organelles could be identified by their ultrastructure on EM images as shown by examples of a RPE1 cell mitochondrion (M), ER, Golgi apparatus (G) or nucleus. (**B**) Representative images of organelles involved in the autophagy pathway in rotenone-treated and glutaraldehyde-fixed RPE1 cells. Early and late autophagosomes were observed, in correlation with green and red LC3B punctae previously observed by FM, and some of them were close to mitochondria.

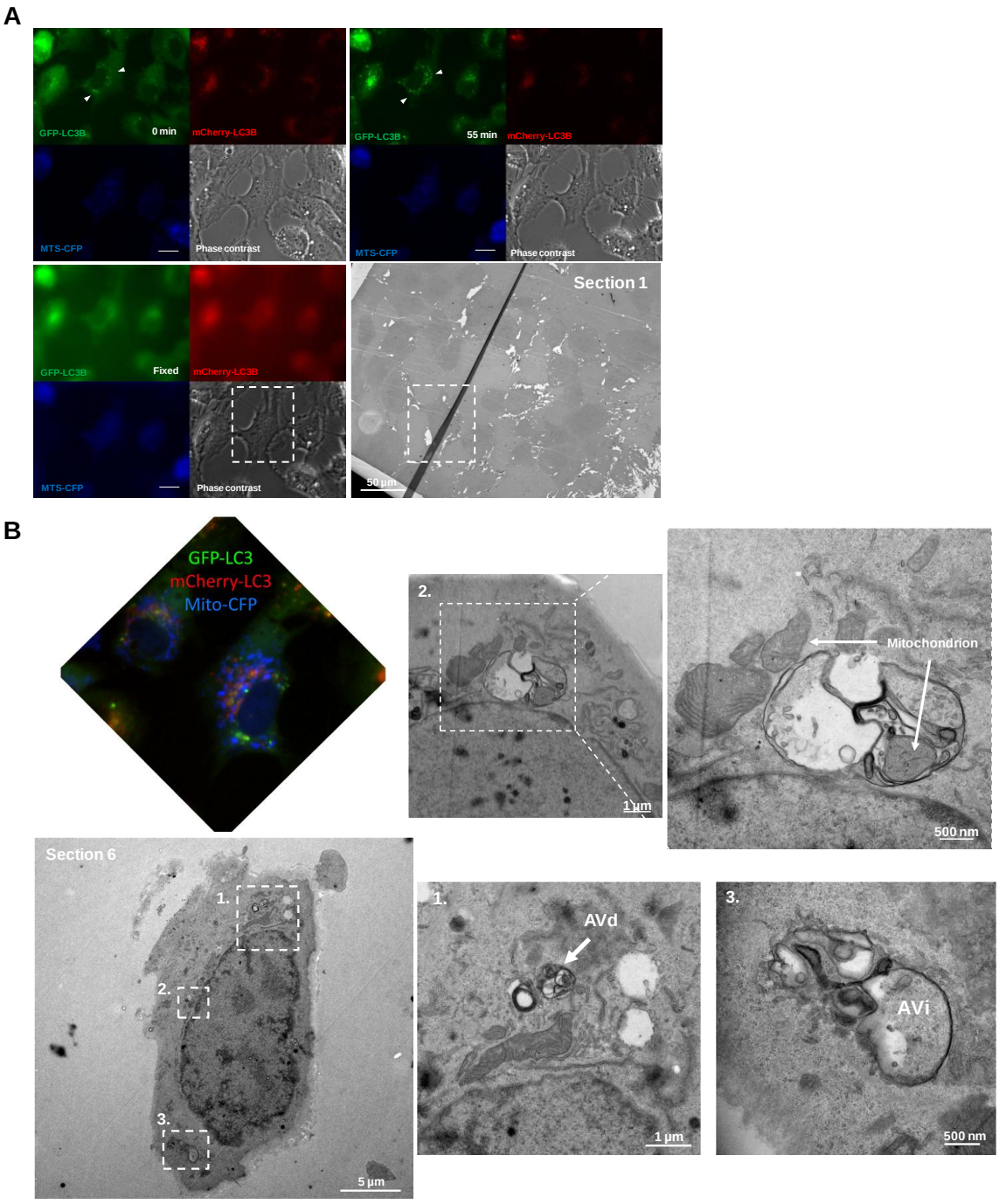

Figure 4.11. CLEM of rotenone-treated RPE1 cells stably expressing mCherry-GFP-LC3B transfected with MTS-CFP (Mito-CFP). (**A**) Cells were treated with rotenone for 2-3 h and, after live-cell imaging (see Supplemental Movies 4.7 and 4.11), were fixed and processed as described in Section 4.2.7. A representative image of the first section with the location of the cell of interest is shown (note white zones in the EM image due to the first sample section being thinner than later sections). Bars = 20 µm. (**B**) CLEM of rotenone-treated tandem LC3B expressing cell. The cell of interest is shown in the same orientation in both FM and EM images. Several cell regions were selected (1-3) for EM imaging considering live-cell imaging results for LC3B-positive structures and mitochondria.

Distorted ER structures were also observed by EM imaging suggesting ER stress induced by rotenone treatment (**Figure 4.12A**). Excessive ROS production is the major mediator of ER-stress among numerous pathological conditions (Hotamisligil, 2010). ER-stress response is afflicted with an adaptive signaling cascade known as the UPR (Hotamisligil, 2010). Excess ROS generation mediates unfolded or misfolded protein aggregation, which stimulates the prolonged UPR (Hotamisligil, 2010). ER-stress mediated prolonged UPR leads to general translational attenuation and hindrance in ER-associated degradation of unfolded or misfolded proteins (Hotamisligil, 2010; Xu *et al.*, 2005). This phenomenon promotes accumulation of high molecular weight ubiquitinated proteins and impaired UPS (Xu *et al.*, 2005). PDI is a chaperone protein that remains in the ER-lumen and assists in the maturation and transport of unfolded protein via thiol disulfide exchange. Previous work has shown that rotenone can lead to S-nitrosylation of PDI (catalytically inactive form), initiating misfolded protein aggregation (Uehara *et al.*, 2006). Moreover, Pal and coworkers have also shown that rotenone induces calcium-dependent oxidative stress in the ER in SHSY-5Y cells (Pal *et al.*, 2014), which correlates with observations in rotenone-treated human RPE1 cells (**Figure 4.12A**).

In the particular cell shown in **Figure 4.13**, a large number of autophagic processes were observed. However, the mitochondrion appeared relatively undamaged suggesting that damaged mitochondria had been already removed. Indeed, after mitophagy initiation mitochondria are rapidly degraded by autolysosomes. Therefore to be sure of analyzing cells in the mitophagy stage previous to mitochondrial degradation by autolysosomes, mitophagy and mitochondria removal were examined using CLEM in leupeptin-treated cells (**Figures 4.14 and 4.15**). Multivesicular bodies were observed that could be fused autophagosomes (autophagic structure) or endosomes. In addition, an autophagosome with mitochondria inside was also observed which could be a late mitophagosome (fused autophagosomes, internal vesicles) or an early mitophagosome (content similar to cytoplasm) (**Figure 4.13**). Finally, vacuoles and late autophagosomes located in the vicinity of the nucleus, and lysosomal degradative compartments (black circular dots) were identified.

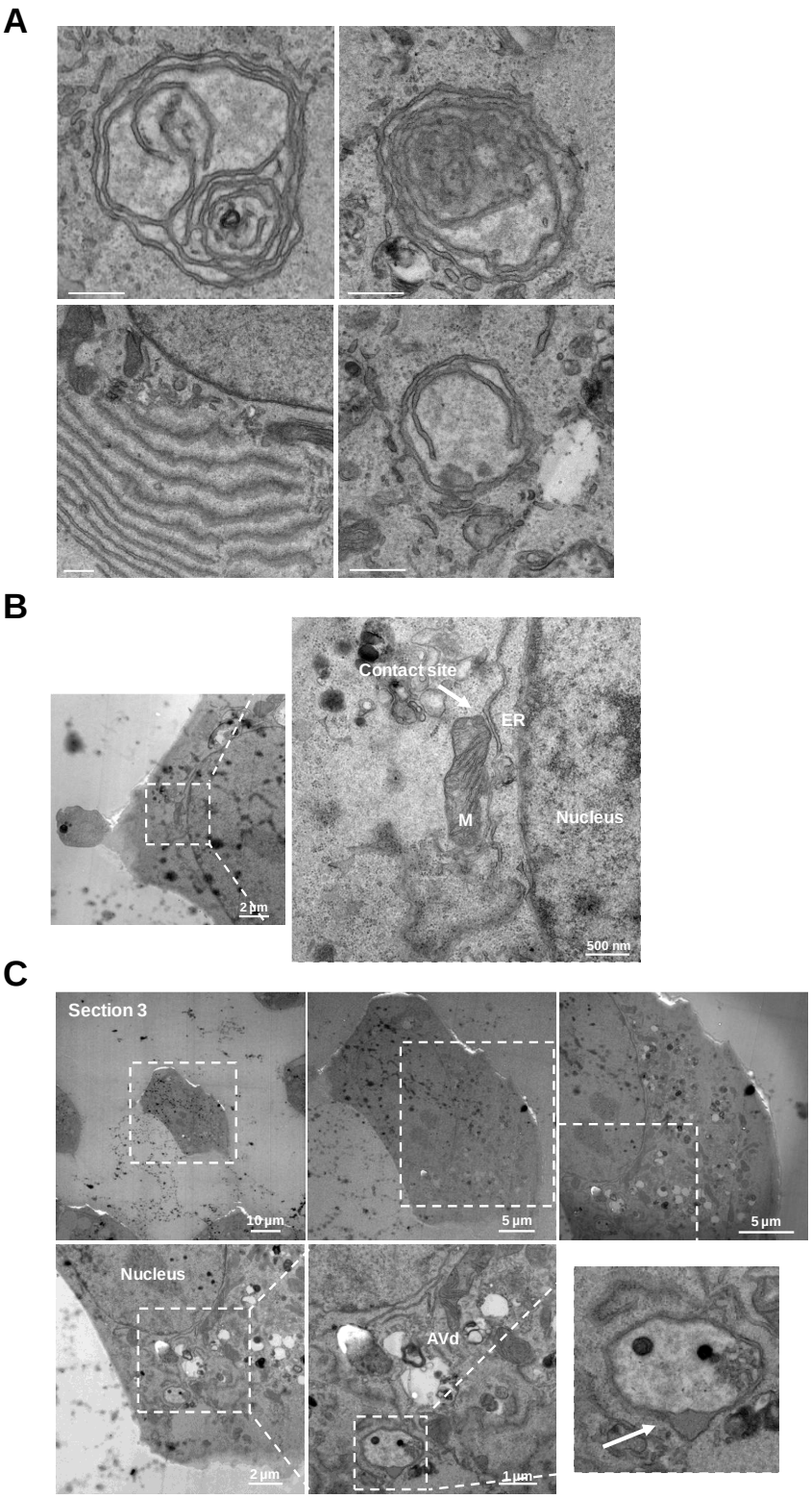

Figure 4.12. Representative images of different structures observed in rotenone-treated RPE1 cells. (**A**) Rotenone-mediated ER stress in human RPE1 cells. Representative images of distorted ER organization seen in rotenone-treated RPE1 cells are shown. Bars = 500 nm. (**B**) Representative image of a mitochondria (M)-ER contact site. (**C**) Representative images of the third section. Black deposits were observed formed during sample processing for EM. An autophagosome-like double membrane structure is also shown that eventually was not classified as an autophagosome due to the zone indicated with an arrow.

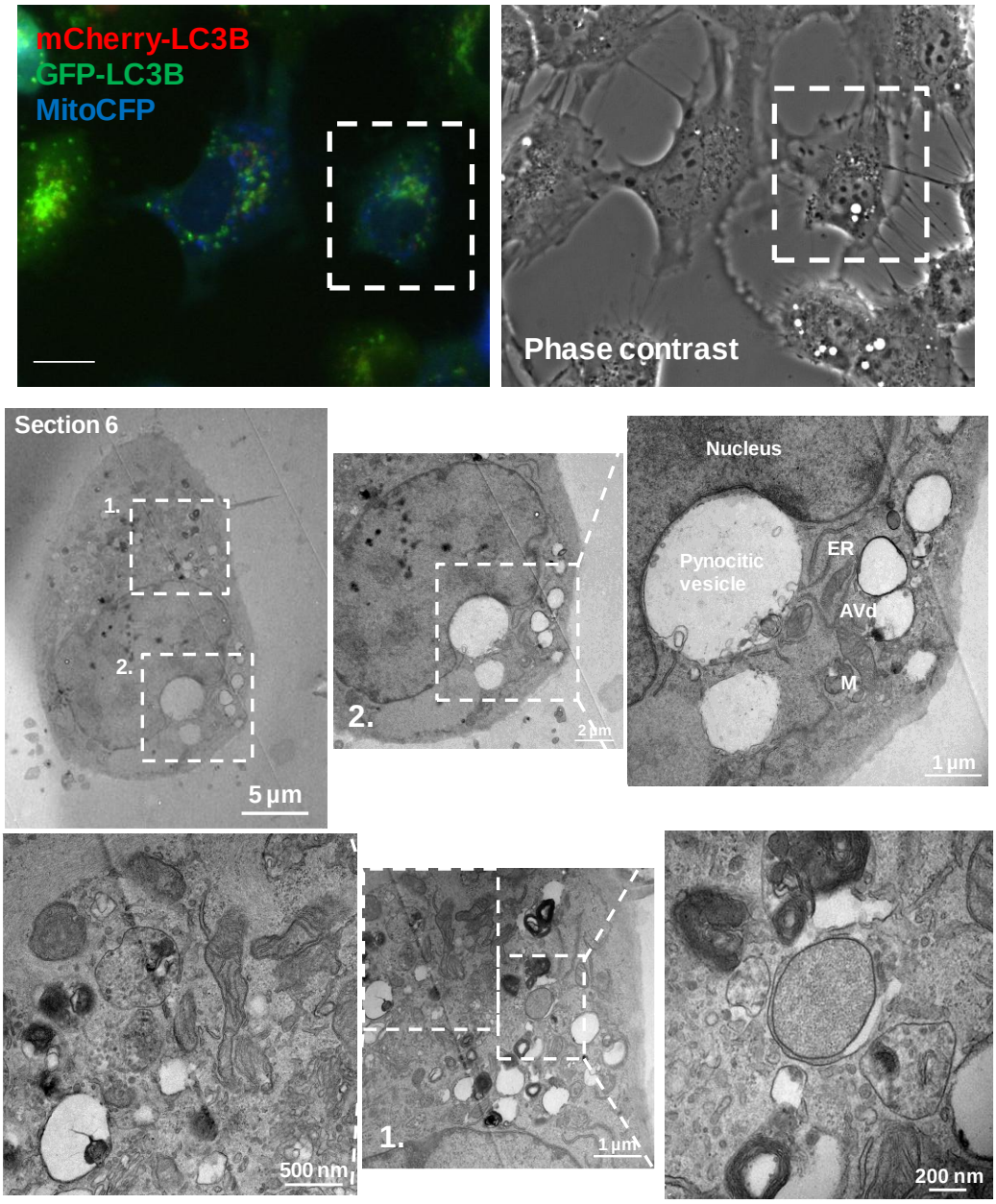

Figure 4.13. CLEM of rotenone-treated tandem LC3B expressing human RPE1 cells transfected with MTS-CFP. Cells were treated with rotenone for 2-3 h and after live-cell imaging were fixed and processed as described in Section 4.2.7. Bar = 20 µm. Representative image of the sixth section of the cell of interest is shown. The cell of interest is shown in the same orientation in both FM and EM images. (**1**) Multivesicular bodies, Golgi apparatus, AV with mitochondria inside and transitional ER and (**2**) pinocytic vesicles, mitochondrion (M), ER, early autophagosomes, AVd and lysosomal degradative compartments were observed.

As expected, many lysosomal structures were observed in rotenone- and leupeptin-treated cells, reflecting LC3B-labeled autolysosomes (red LC3B puncta) observed previously by light microscopy (**Figure 4.14**) – leupeptin inhibits lysosomal degradation but does not affect lysosome formation. The use of ethanol in sample processing for CLEM causes cell dehydration and in some cases lysosomes are less electrodense (white vesicles). HPF is a very useful alternative fixation technique to

avoid distortions in ultrastructure of specimens and introduces minimal artefacts (Studer *et al.*, 2008).

Double membrane vesicles were also observed in some cases with another membrane inside these structures, which could be mitochondria, or cytoplasmic material (**Figure 4.14**). In some sections parallel lines were observed probably caused by an occasional defect in the diamond knife used to cut the block face for sections (see arrow heads in **Figures 4.14 and 4.15**).

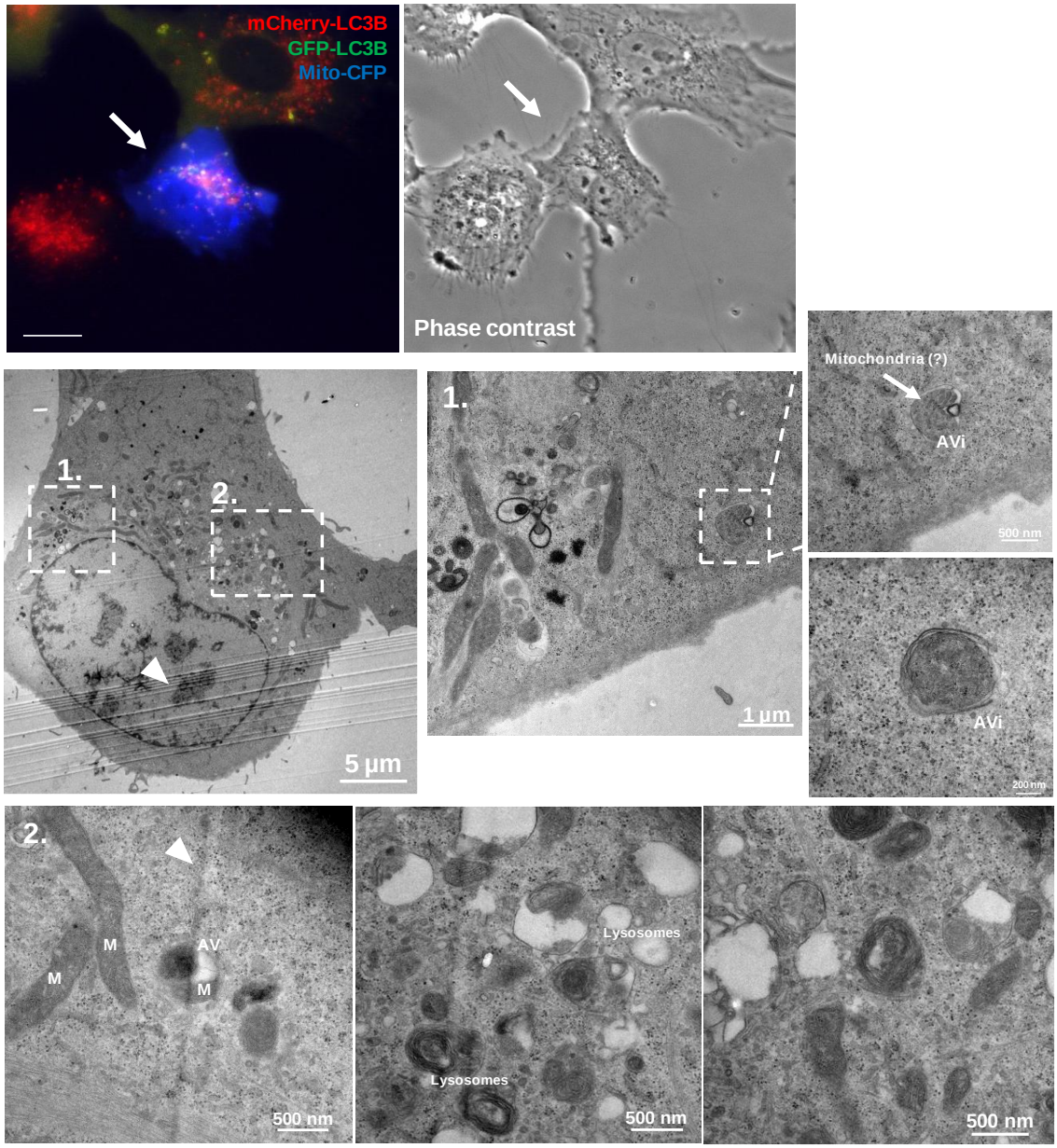

Figure 4.14. CLEM of rotenone- and leupeptin-treated RPE1 cells stably expressing mCherry-GFP-LC3B and transfected with MTS-CFP. Cells were treated with rotenone for 2-3 h and processed as described in Section 4.2.7. Arrows indicate which cell was examined by EM imaging. Bar = 20 µm. Representative images of (**1**) early autophagosomes (with double membrane), (**2**) an autophagosome engulfing a mitochondrion (M), and lysosomes are shown.

In the CLEM experiment shown in **Figure 4.14**, EM analysis was limited by the fact that it was not a flat cell and therefore some information was lost through serial sectioning. To circumvent this problem the adjacent flatter cell was next examined by EM and many double-membrane autophagic structures and autolysosomes were observed containing different cytoplasmic materials (**Figure 4.15**). In some cases it was hard to identify the intravesicular content in the autophagic compartments, as shown e.g. by an early autophagosome that was close to rough ER decorated with ribosomes (**Figure 4.15B**). Since ribosomes (black dots) were not observed within this compartment it could not be determined whether it was an ER- or mitochondria-containing autophagosome. In addition, a possible mitochondrial fission event was observed (**Figure 4.15B**). It is generally accepted that mitochondrial fission is a prerequisite for mitophagy in many mammalian cell types (MacVicar & Lane, 2014; Ni *et al.*, 2015; Hsu & Shi, 2016; Twig *et al.*, 2008; Frank *et al.*, 2012). Indeed, it would be expected for an elongated mitochondrion of over 5 µm in length to be chopped up prior to engulfment by 0.5 µm diameter autophagosomes (Gomes & Scorrano, 2011). But it could also be the result of different heights along the section upon sample processing.

Together, CLEM results confirmed that rotenone notably affects the behavior of cellular membranes. Autophagosome assembly sites in the vicinity of mitochondria observed by EM (**Figures 4.10, 4.11, 4.14 and 4.15**) clearly correlated with mitochondria-rich regions where numerous GFP-LC3B puncta were observed by light microscopy (**Figure 4.7B**). Moreover, large compartments (autophagosomes with large organelles and amphisomes) possibly formed by fusion of several autophagic compartments observed by EM imaging (**Figure 4.11B**) closely correlated with large LC3B green/red punctae observed by fluorescence microscopy (**Figure 4.7**). Finally, mitochondrial degradation was blocked by co-treatment with the acidic protease inhibitor leupeptin and rotenone, and consequently, a greater number of mitophagosomes were observed in cells co-treated with the two reagents (**Figures 4.14 and 4.15**) as compared to rotenone-only treated cells (**Figures 4.11 to 4.13**).

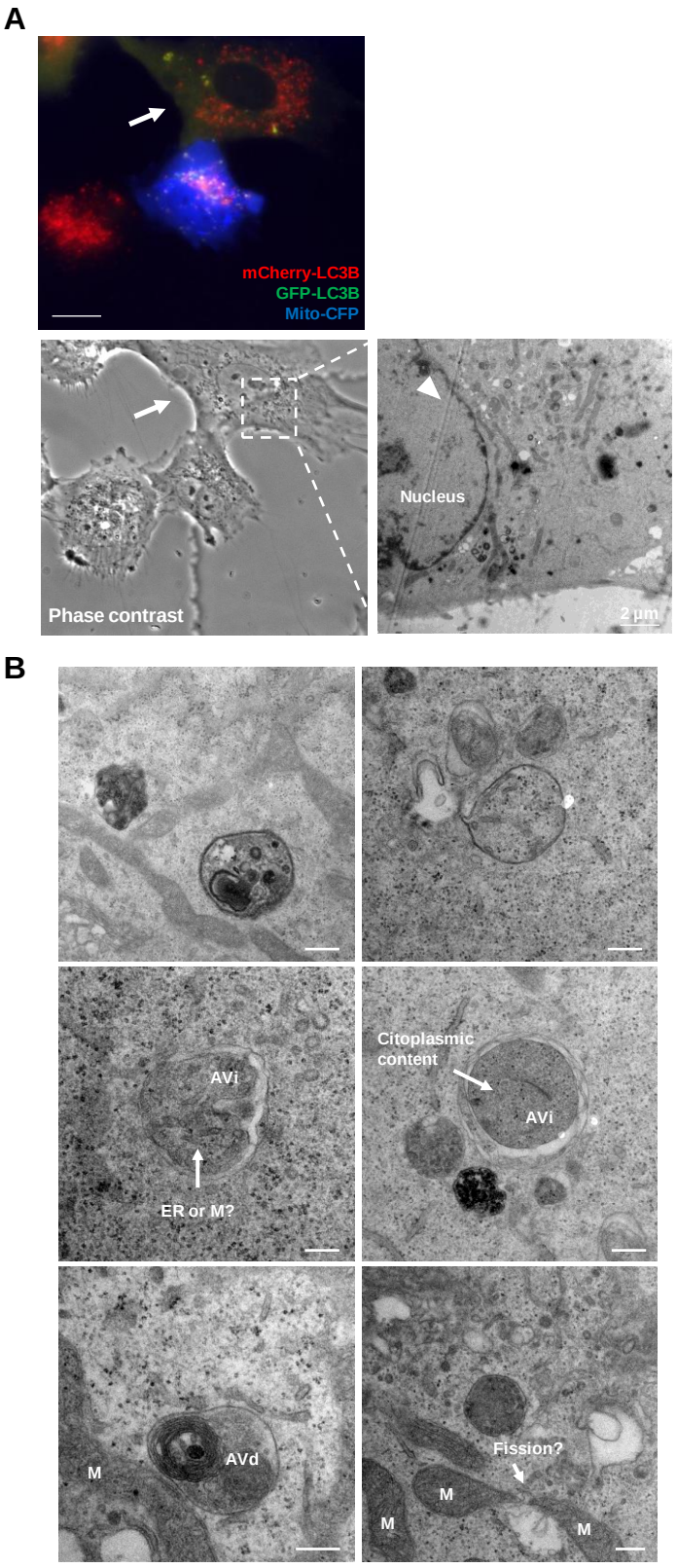

Figure 4.15. CLEM of rotenone and leupeptin-treated RPE1 cells stably expressing mCherry-GFP-LC3B and transfected with MTS-CFP. (**A**) Cells were treated with rotenone for 2-3 h and processed as described in Section 4.2.7. Arrows indicate the cell that was examined by EM imaging. Bar = 20 µm. (**B**) Examples of isolation membranes (AVi) and late autophagosomes (AVd) adjacent to mitochondria (M), and a possible mitochondrial fission event are shown. Note that the isolation membrane is very electron dense. Bars = 200 nm.

4.3.3 LC3B and GABARAPL1 Intracellular Location during Mitophagy in iPSC-derived Cortical Neurons

Mitochondria play a very important role in neurons supplying energy to sustain neuronal activity and are highly exposed to stress conditions such as high Ca^{2+} influx or oxidative stress over time (Grenier *et al.*, 2013). The majority of mitochondria are located at distal axons, whereas lysosomes occur in the soma. Synapses represent regions of high energy demand and protein turnover; they contain abundant mitochondria and polyribosomes which make them more susceptible to the consequences of dysfunctional autophagy (Lee *et al.*, 2013; Nixon, 2013; Aufschnaiter *et al.*, 2016; Vidal *et al.*, 2014). In addition, the fact that neurons are postmitotic and do not replicate in general might predispose them to the accumulation of toxic proteins and damaged organelles that would become diluted through cell division in replicating cells.

Damaged mitochondria accumulate with age and neuronal autophagy is essential for the turnover of dysfunctional mitochondria in the pathogenesis of Parkinson disease, in which the failure to induce mitophagy may underlie the selective dopaminergic neuronal loss. Thus, stimulating the proper induction of mitophagy in neurons may serve as a therapeutic target to slow disease progression in PD (Gautier *et al.*, 2008; Greene *et al.*, 2003; Son *et al.*, 2012). Previously, recessive mutations in the ubiquitin E3 ligase PARK2 had been identified as a cause of early onset, familial PD. PARK2 is shown to be selectively recruited to damaged mitochondria, that have low membrane potential in mammalian cells (Narendra *et al.*, 2010a; Geisler *et al.*, 2010). However, the precise role of PARK2 in mitochondria is unknown. Moreover, so far, whether damaged mitochondria have to be translocated to the soma to be degraded remains unclear. Ashrafi and coworkers have proposed that they might be locally sequestered in autophagosomes before their retrograde transport to the soma or may even be degraded outside the soma (Ashrafi & Schwarz 2013; Ashrafi *et al.*, 2014).

Exposure to rotenone, a widely used pesticide, increases the risk of developing neurodegenerative disorders (Pal *et al.*, 2011; Uehara *et al.*, 2006). Rotenone is known to inhibit complex 1 of the mitochondrial respiratory chain, and to regulate Nox activity, increasing oxidative stress in neuronal cells and leading to neurodegeneration (Uehara *et al.*, 2006; Xia *et al.*, 2007; Zhou *et al.*, 2012). As already mentioned, rotenone has also been implicated as a potential inducer of CL externalization to the OMM in primary rat cortical neurons and human neuroblastoma cells (SH-SY5Y) (Chu *et al.*, 2013). The OMM-localized CL acts as a mitochondrial receptor for LC3 triggering mitophagy *via* a

pathway that may be different from the PINK1/PARK2 pathway upstream of the damage mechanisms (Chu *et al.*, 2013; Chu *et al.*, 2014). Indeed, the LC3-CL pathway shows less than 15% depolarization in mitochondria, and in PARK2-dependent mitophagy PARK2 is found to be recruited, in a PINK1-dependent fashion, to depolarized mitochondria (Narendra *et al.*, 2008; Narendra *et al.*, 2010a; Rüb *et al.*, 2016).

As most information about selective autophagy pathways has been established in non-neural cell lines, mitophagy triggered by LC3/GABARAP family proteins in neurons needs to be further examined. This project aimed at studying LC3B and GABARAPL1 recruitment to mitochondria during rotenone-induced mitophagy in cortical neurons to gain further insight into the ability of different human Atg8 orthologs to mediate selective mitochondrial targeting in neural cells. The extreme sensitivity to *ex vivo* manipulation and very limited availability of mature human neurons, as well as the limited differentiation potential of neural progenitors, are significant constraining factors in the study of neuronal processes such as aging or degeneration. Therefore, the *ex vivo* use of mature neurons generated from induced-pluripotent stem cells became a good alternative approach. Adult cells converted “back to pluripotency” also termed hIPS, are pluripotent cells derived from adult donors which allow both *ex vivo*, highly reproducible studies of specific diseases, as well as transplantation back into the patient, free of host-versus-graft reaction. Nistor and colleagues have adapted the current protocols for differentiating human pluripotent cells towards neuronal lineages (Chambers *et al.*, 2009, 2012; Shi *et al.*, 2012), generating an improved protocol for neuronal differentiation from hIPSs (Nistor *et al.*, 2015). In this study, iPSC-derived cortical neurons were then transduced with a lentiviral system carrying GFP-LC3B or GFP-GABARAPL1 in a pxlg3 vector to follow GFP-tagged autophagosomes upon rotenone exposure. Expression of LC3 tagged at its N terminus with a fluorescent protein (e.g. GFP), is frequently used to monitor autophagosome numbers and dynamics using direct fluorescence imaging, especially in living cells (Klionsky *et al.*, 2008). In this case, GFP is observed on forming and maturing autophagosomes but not autolysosomes, as LC3 is thought to be removed from the outer membrane of autophagosomes during maturation (Tanida *et al.*, 2004a), and, as mentioned above, the GFP fluorescence bound to the inner membrane of autophagosomes gets quenched by acidification of these compartments (autolysosomes: ~pH 4.7, whereas GFP has a pKa of 6.0) (Shaner *et al.*, 2004).

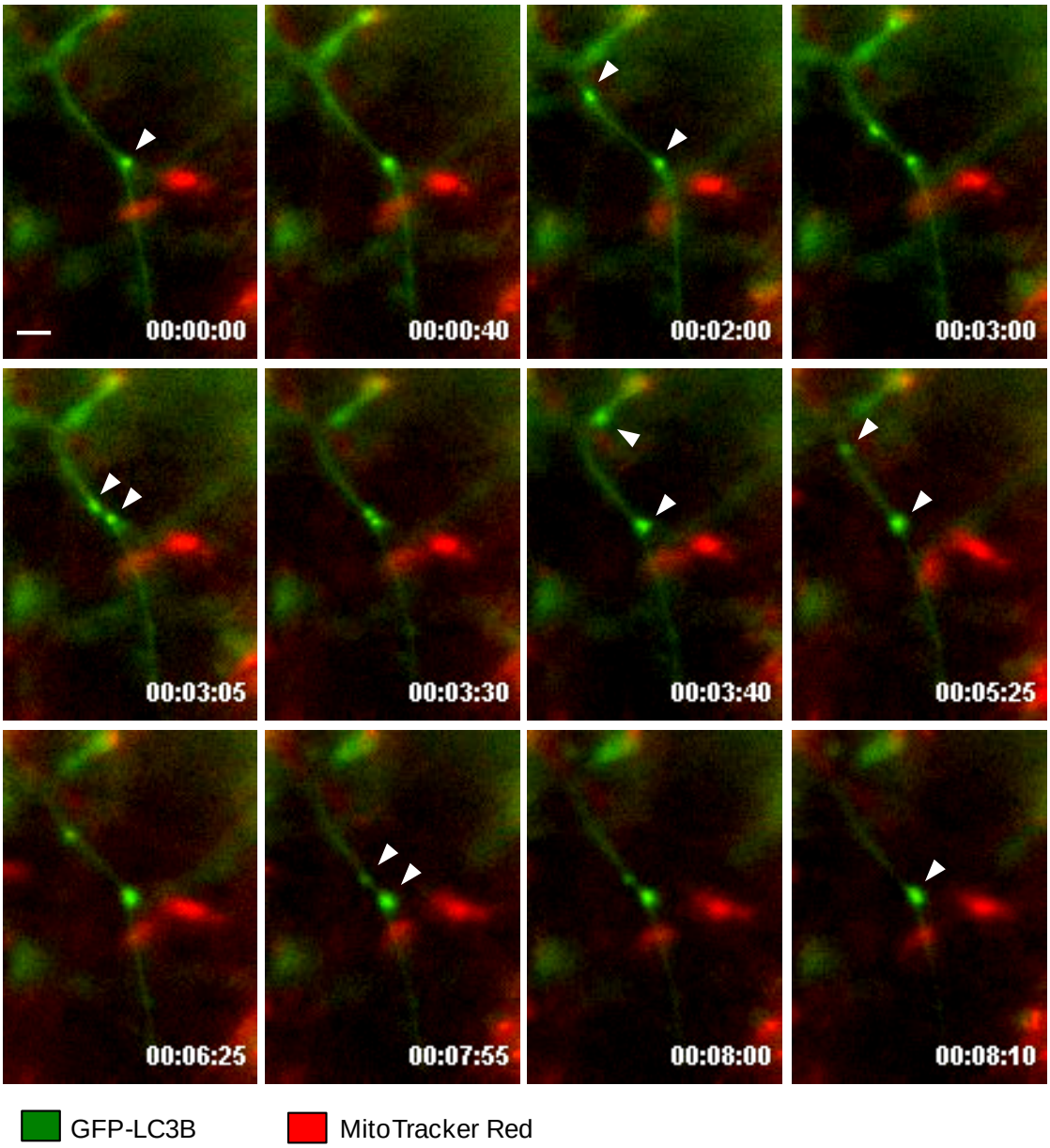

Figure 4.16. Autophagosome fusion events in iPSC-derived human cortical neurons expressing GFP-LC3B after 5 µM rotenone treatment. Cortical neurons were transduced with the autophagosomal marker GFP-LC3B using lentiviruses. Representative images are shown of the distribution of GFP-LC3B (cytoplasmic and bound to autophagosomal membranes/puncta – arrow heads) in a neuronal axon at the indicated filming time points (see Supplemental Movie 4.16). Bar = 2 µm.

A preliminary study using iPSC-derived human cortical neurons stably expressing GFP-LC3B or GFP-GABARAPL1 was performed in the presence of a mitochondrial marker (MitoTracker® Red) with the aim of precisely determining LC3B- or GABARAPL1-labeled autophagosome localization and possible recruitment to damaged mitochondria at various stages of the rotenone-induced mitophagy process. Time-lapse imaging of the described iPSC-derived cortical neurons allowed visualization of fusion processes of LC3B-positive structures upon rotenone treatment,

leading to the autophagosome growth as indicated by larger GFP-LC3B puncta (**Figure 4.16**). Unfortunately, in this particular experiment the mitochondrial marker (MitoTracker® Red) was unspecific and had a high background fluorescence (**Figure 4.16**). After rotenone administration to neurons expressing GFP-LC3B, most of the GFP-LC3B fluorescent signal was cytoplasmic with a few small puncta (**Figures 4.16 and 4.17**). Nonetheless, consistent with the previous results in U87MG glioblastoma cells and fixed and living RPE1 cells indicating that LC3B-positive autophagosomes are recruited to mitochondria after rotenone treatment, autophagosomes (GFP-puncta) were observed in the vicinity of mitochondria and seemed to follow mitochondria along the neuronal axon (**Figure 4.17**).

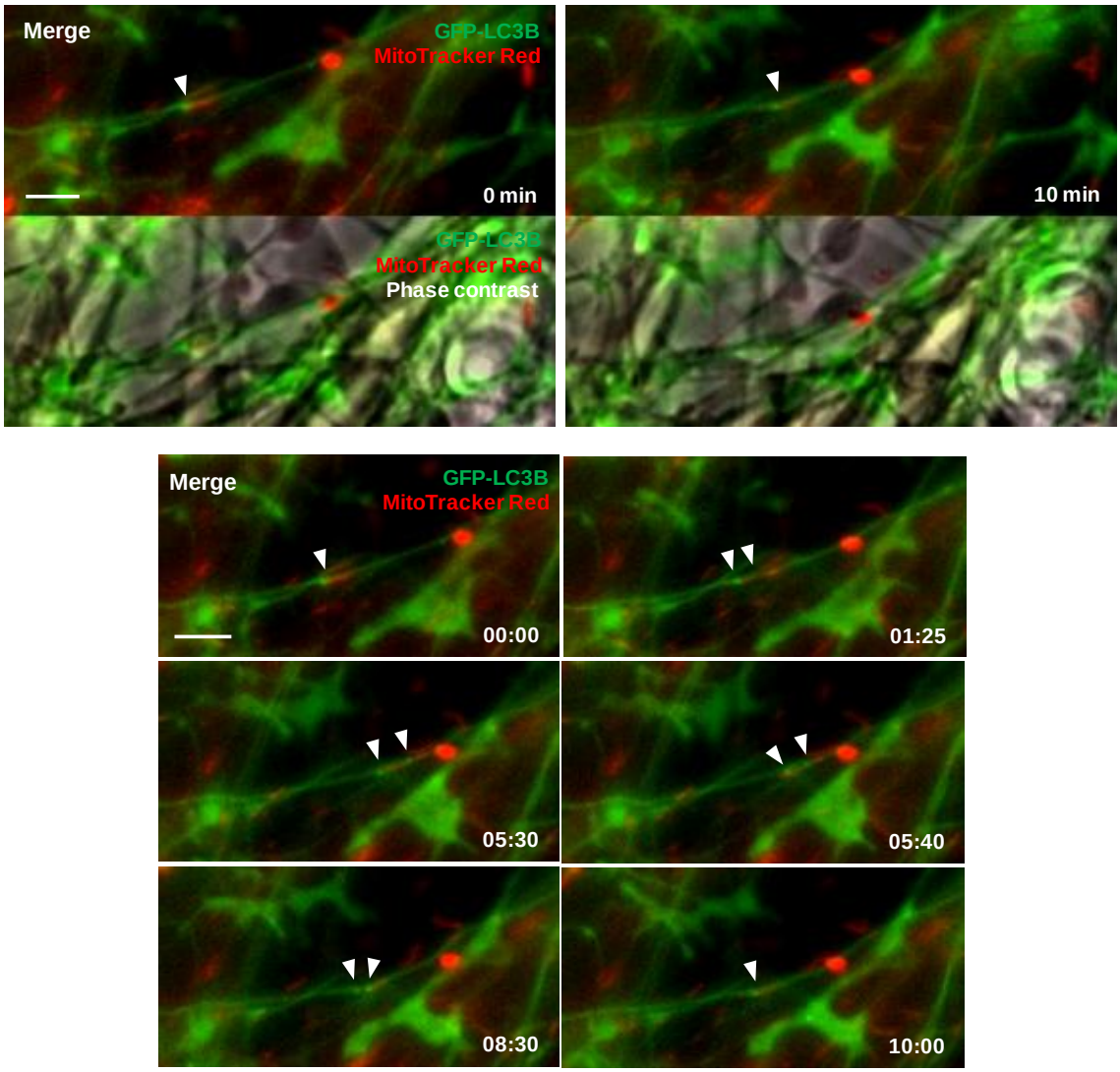

Figure 4.17. Autophagosome dynamics in GFP-LC3B expressing iPSC-derived human cortical neurons treated with 5 µM rotenone. Cortical neurons were virally transduced with GFP-LC3B and filmed 3 days later by time-lapse imaging. Mitochondria were stained with MitoTracker® Red CMXRos. Pictures follow several autophagosomes (arrow heads) possibly engulfing mitochondria in one neuronal axon at the indicated filming time points during a period of 10 min (see Supplemental Movie 4.17). Bars = 4 µm.

Live-cell imaging experiments with GFP-LC3B may suggest the targeting and engulfment of mitochondria by autophagosomes (**Figure 4.17**), fusion events between autophagosomes (**Figure 4.16**), and a rapid turnover of autophagosomes in human cortical neurons (note that the imaging periods were of about 10 min). Conversely, under these conditions, 5 µM rotenone treatment of cortical neurons virally transduced with GFP-GABARAPL1 had no effect on the number of GABARAPL1 puncta or mitochondrial recruitment (data not shown). This differs from previous results in human RPE1 cells that GABARAPL1 localized to outer mitochondrial membrane in response to rotenone administration (**Figure 4.5**).

This study using iPSC-derived cortical neurons was started late in this project (so that there was limited time to pursue it), but it could provide an interesting final read-out for future experiments following modulation of mitophagy in human cortical neurons. Overall, some obstacles need to be overcome, e.g. decrease the LC3B background fluorescence optimizing the protocol for GFP-LC3B lentiviral transduction, using formaldehyde fixation instead of methanol fixation, or using a photoactivatable GFP, to confirm and quantify the results obtained in cortical neurons and compare them with other LC3/GABARAP family proteins.

4.4 Discussion

4.4.1 LC3B, but not GABARAP or GABARAPL2, Translocation to Mitochondria in U87MG Glioblastoma Cells

Data presented in the previous chapter described novel molecular mechanisms underlying the association of the autophagy protein LC3 with CL-containing membranes (Antón *et al.*, 2016). Using several compositionally defined *in vitro* reconstituted systems LC3B has been shown to avidly interact with CL in CL-enriched model membranes (**Figures 3.5 to 3.9**). Moreover, site-specific NBD labeling coupled to NBD fluorescence spectroscopic analysis supported the model proposed by Chu and colleagues in which the N- and C-terminal regions would bind mitochondria and autophagosomal membranes respectively (Chu *et al.*, 2013; Antón *et al.,* 2016). Consistent with this, results presented in this work show that LC3B translocates to mitochondria upon mild rotenone treatment in U87MG glioblastoma cells, resulting in targeted removal of damaged mitochondria through the action of lysosomes (**Figure 4.1**). Nevertheless, nutrient deprivation did not elicit translocation of LC3B to mitochondria or targeting of mitochondria to lysosomes. These results are consistent

with reports indicating that in higher eukaryotes mitochondria are in fact spared from autophagy during starvation. In yeast however mitochondrial degradation occurs upon nutrient depletion and/or mitochondrial damage and there is no experimental evidence that mitophagy selects damaged, but not intact, mitochondria for degradation (Kiššova *et al.*, 2007). Moreover, yeast proteins mediating this process have no mammalian orthologs. Therefore the molecular mechanisms involved in selective mitophagy appear to be fairly different in yeast and mammals.

Furthermore, unlike LC3B, GABARAP and GABARAPL2 do not translocate to mitochondria upon mitophagy induction in U87MG cells (**Figure 4.2**), suggesting different regulatory mechanisms between orthologs. Even though GABARAP is able to interact with CL *in vitro*, though with less affinity than LC3B, it does not show mitochondrial localization after rotenone treatment (Antón *et al.,* 2016). Thus the possibility remains that its capacity to interact with CL simply relies on its structural homology with LC3B, in such a way that translocation of GABARAP to mitochondria would occur via a different mechanism.

4.4.2 Dynamics of LC3B-, GABARAPL1- and ATG5-positive Autophagic Structures during Mitophagy in RPE1 Cells

The aim of this study was not only to observe, but also to extensively quantify and structurally analyze mitochondrial targeting and degradation processes in several human cell lines. The average outcome of rotenone administration in RPE1 cells expressing mCherry-GFP-LC3B or -GABARAPL1 was a significant increase in puncta numbers compared to nontreated control cells, and a mitochondrial recruitment of both human Atg8 orthologs. These data suggest that rotenone-induced CL externalization triggers mitophagy via the recruitment of both proteins leading to the removal of damaged mitochondria (**Figures 4.3 to 4.7**). In addition, experiments with fixed human RPE1 cells indicate that the mTOR catalytic inhibitor AZD8055 exposure has the strongest influence on the autophagic cell response, which is similar to that of CCCP on PARK2-dependent mitophagy. LC3B and GABARAPL1 puncta numbers are also significantly increased after rotenone treatment but this causes a weaker cell response and a lower increase in puncta numbers as compared to other inducers (**Figures 4.4 to 4.6**). Furthermore rotenone treatment leads to larger LC3B punctae while in nutrient deprivation conditions LC3B-labeled structures are smaller and dispersed throughout the cytoplasm of RPE1 cells (**Figures 4.3 and 4.4**). This observation could indicate (i) that LC3B-positive autophagosomes formed after rotenone-treatment contain mitochondria (a large organelle inside autophagosomes, larger puncta), or (ii) that

ATG4-mediated LC3B delipidation is dysfunctional under conditions of rotenone administration, therefore LC3B would not only be inside the autophagic vesicle (small and bright puncta) but it would also localize outside the autophagosome (larger puncta). It should also be considered that when using mCherry-GFP tagged LC3B or labeling of endogenous LC3B in immunofluorescence microscopy, differences in puncta size might also be due to the space occupied by the antibodies (**Figures 4.4 and 4.6**). The latter could also be the reason for differences observed in LC3B puncta quantitation between tandem tagged LC3B expressing cells and endogenous LC3B labeled by antibodies. However, in both cases similar cell response patterns were observed with the different autophagy and mitophagy inducers (**Figures 4.4B and 4.6B**).

Identification and positional analysis of the autophagosome assembly site, or "isolation membrane" using GFP-ATG5 expressing human RPE1 cells suggest that rotenone causes a low but significant increase in ATG5 puncta numbers (**Figure 4.6B**), however a significant mitochondrial recruitment was not observed for ATG5-positive preautophagosomes (**Figures 4.6A and 4.9**). These data suggest that the PAS recruitment to mitochondria may not be required for the selective mitochondrial targeting mediated by LC3B and/or GABARAPL1 during mitophagy and therefore the molecular machinery for autophagosome assembly is not likely to be localized in the mitochondria, at least at this stage of the process. Hence, experiments with soluble LC3B and CL-enriched vesicles described in the previous chapter (Antón *et al.*, 2016), together with that observed for GFP-ATG5 expressing cells, suggest rather that both soluble and autophagosome-bound LC3 forms would be recruited to mitochondria after CL translocation for targeting of damaged mitochondria in RPE1 cells. However these observations have to be considered carefully due to the low number of ATG5-positive structures present and measured (less than 5 puncta per cell for cells treated with rotenone) (**Figure 4.6B**). The ATG5-positive autophagosome assembly site being a transient structure (ATG5 punctae were shorter-lived than LC3B punctae), and the early, mitophagy-inducing treatment conditions involving low doses of rotenone used would make GFP-ATG5 positive with isolation membrane puncta hardly detectable in rotenone-treated RPE1 living cells (**Figures 4.6 and 4.9**).

CLEM was another method of choice to study how the recruitment process takes place during mitophagy, with the purpose of first studying the process dynamics by time-lapse imaging and subsequently ultrastructurally indentifying interesting events after adaptating cell samples to this method (**Figures 4.10 to 4.15**). Since the study of early autophagosome, late autophagosome or mitophagosome morphology could not be pursued by fluorescent-labeling of resident LC3B, CLEM approach was expected to

be more informative. This study confirmed that green and red LC3B puncta observed by light microscopy can be closely correlated with early and late autophagosome structures by EM imaging in the same cell regions (**Figure 4.11**). Rotenone-induced larger LC3B puncta formation observed by immunofluorescence (**Figures 4.4, 4.7 and 4.8**) was supported by the observation in EM images that a fraction of the autophagosomes were larger and/or exhibited heterogeneous content (**Figures 4.10, 4.11 and 4.15**). In addition, in rotenone- and leupeptin-treated cells, a large number of lysosomal structures were also observed reflecting red LC3B punctae previously observed by fluorescence microscopy (**Figures 4.8, 4.14 and 4.15**). Finally, GFP-LC3B puncta located to mitochondria-rich regions (**Figure 4.7B**) appear to correlate with early autophagosomal vesicles observed in the vicinity of mitochondria by EM (**Figures 4.10, 4.11, 4.14 and 4.15**). In order to preserve the ultrastructure and size of cells and their organelles, the HPF technique could be used under conditions thought to introduce minimal artefacts as compared to direct chemical fixation used in this work.

4.4.3 LC3B-mediated Mitochondrial Targeting in Rotenone-treated iPSC-derived Cortical Neurons

Defective autophagy in the brain causes accumulation of damaged mitochondria and protein aggregates, leading to neurodegeneration (Lee *et al.*, 2013; Vidal *et al.*, 2014; Aufschnaiter *et al.*, 2016; Nixon, 2013). In contrast to the protonophores FCCP or CCCP (Kondapalli *et al.*, 2012), that cause a severe loss of mitochondrial membrane potential in neuronal cells, sublethal doses of rotenone do not distinctly affect the mitochondrial membrane potential and induce LC3, but not PINK1/PARK2 translocation to mitochondria in rat cortical neurons and human neuroblastoma cells (Chu *et al.*, 2013). However, as previously mentioned, rotenone-induced cell response can vary depending on treatment conditions and cell type.

This preliminary study suggests that rotenone induces autophagy and GFP-LC3B translocation to mitochondria in iPSC-derived human cortical neurons (**Figures 4.16 and 4.17**). In addition, LC3B puncta formation observed upon rotenone treatment could not be repeated in GFP-GABARAPL1 expressing cortical neurons (data not shown). However, analysis of much larger data sets would be required to confirm the statistical significance of these results. Moreover, to further determine the involvement of the PINK1/PARK2 pathway mentioned above in this rotenone-induced mitophagy response, PARK2-deficient cells could be used. Several obstacles will need to be overcome to pursue this study of autophagosome dynamics and mitochondrial targeting by time-lapse microscopy in human cortical neurons. First, GFP-LC3B background

fluorescence in live-cell imaging of neuronal samples is higher than in RPE1 cells (**Figures 4.16 and 4.17**). This high background fluorescence makes it harder to trace the formation and location of GFP-LC3B puncta. Furthermore, to continue the study of LC3B mitochondrial recruitment and to obtain quantitative data of the process, preliminary experiments were performed with fixed neurons using GFP-LC3B lentiviral transduction or LC3B immunostaining. However, as a result of the LC3B background fluorescence, few GFP-LC3B punctae were detected after rotenone or CCCP treatment in fixed neural cells (data not shown). Second, *ex vivo* cultured cortical neurons proved to be very sensitive to e.g. light exposure, addition of toxins or immunolabeling, influencing either their distinctive morphological features of cortical neurons or their health and viability, a strong limitation for live-cell imaging techniques. Moreover, neuronal cell cultures are built up by neurons as a 3D network, and conventional microscopy collects data from individual planes and cannot therefore simultaneously image neurons across different focal planes and fields of view. Finally, mitochondrial labeling rapidly appeared diffuse and in some cases was non-specific (**Figures 4.16 and 4.17** – in red). A more reliable method of mitochondrial labeling would be necessary – e.g. co-transduction of fluorescently-labeled mitochondrial markers such as MTS-CFP, previously used in this project for LC3B colocalization analysis with mitochondria in RPE1 cells (**Figure 4.7**).

In conclusion this study has confirmed that rotenone-induced CL externalization promotes LC3B translocation to mitochondria and the subsequent induction of mitophagy in U87MG glioblastoma cells and human RPE1 cells, while other proautophagy stimuli lead to nonselective autophagy. However the specific factors, distinct from bulk autophagy, required for individual mitochondria to be distinguished within the mitochondrial network are still to be determined. Moreover data described in this chapter indicate that specific LC3/GABARAP protein family members are recruited to mitochondria in a cell-type dependent manner that could also be stress-specific (Antón *et al.*, 2016). There is still an underlying layer of complexity when it comes to LC3/GABARAP family protein recruitment, which is found to be executed by multiple protein and lipid receptors, and remains a matter of investigation.

Chapter 5

Novel mechanisms for ceramide-mediated cancer cell death: Lethal autophagy versus lethal mitophagy

CHAPTER 5:

Novel mechanisms for ceramide-mediated cancer cell death: Lethal autophagy versus lethal mitophagy

5.1 Introduction

There are several types of autophagy, among which are microautophagy, chaperone-mediated autophagy and macroautophagy. Macroautophagy, hereafter named autophagy, was first described in mammals, where it was observed that complete organelles could be sequestered into double-membrane vesicles called autophagosomes. The autophagosome fuses with lysosomes, after which the sequestered content is degraded rapidly (Boya *et al.*, 2013; Klionsky *et al.*, 2012; Rubinsztein *et al.*, 2007). The membrane source from which autophagosomes are derived is still debated, it has been proposed that it could be derived either from *de novo* synthesized lipids or generated by vesicle budding from the ER, Golgi apparatus or endosomes (He & Klionsky, 2009; Juhasz & Neufeld, 2006), or the plasma membrane (Ravikumar *et al.*, 2010). In particular, an ER-derived structure termed the omegasome has been proposed as an origin of the phagophore membrane (Juhasz & Neufeld, 2006; Reggiori & Klionsky, 2005). Autophagy is the major source of nutrients and biosynthetic precursors when the supply of nutrients to cells is insufficient (Boya *et al.*, 2005; Green & Levine, 2014; Liu & Levine, 2015; Marino *et al.*, 2014). However, stimulation of autophagy can also have a cytotoxic effect. For example, several anticancer agents activate autophagy-associated cell death (Green & Levine, 2014; Liu & Levine, 2015; Marino *et al.*, 2014; Galluzzi *et al.*, 2015). However, the molecular

mechanisms that determine the outcome of autophagy activation for the survival or death of cancer cells remain to be clarified (reviewed in Galluzzi *et al.*, 2015).

Furthermore, specific autophagy can take place in the presence of nutrients, to remove damaged organelles or to assist in cell differentiation (i.e. in the erythrocyte maturation process), or simply to direct organelle replacement. For instance, in the selective process called mitophagy, cells turn over mitochondria through autophagy for quality control and to adapt to cellular needs (Kiššova *et al.*, 2004; Tal *et al.*, 2007; Youle & Narendra, 2011). Defects in mitophagy (mitochondria-specific autophagy) have been linked to multiple human pathological states including neurodegeneration, e.g. Parkinson disease (Valente *et al.*, 2004), myopathies, and cancer (Aufschnaiter *et al.*, 2016; Kubli & Gustafsson, 2012; Lu *et al.*, 2013; Nixon, 2013).

An unresolved question is how the autophagosome membrane forms and elongates. The most widely accepted hypothesis proposes *de novo* formation from a PAS, from which the adhesion and fusion of new membranes would be produced. Autophagosome elongation would be catalyzed by specific proteins and would involve their interaction with membrane lipids. Approximately 35 Atg proteins have been identified in mammals, which are essential in the initial stages of the PAS formation and autophagosome elongation (Boya *et al.*, 2013; Rubinsztein *et al.*, 2007; Klionsky *et al.*, 2012). Enlargement of this compartment to form the autophagosome requires the participation of 2 ubiquitin-like conjugation systems, one involving the conjugation of ATG12 to ATG5, and the other requiring conjugation of phosphatidylethanolamine to LC3 (Rubinsztein *et al.*, 2007). The first discovered member of the Ubl family was Atg8 from *S. cerevisiae.* Several Atg8 orthologs are known in mammalians, divided into LC3 and GABARAP subfamilies. These proteins are proteolyzed by ATG4B, causing the exposure of a C-terminal Gly. After proteolysis, LC3, GABARAP, and GABARAPL2 are activated by ATG7 (ubiquitin E1-like) and transferred to ATG3 (ubiquitin E2-like), after which they are able to conjugate with PS or PE. This protein-lipid covalent binding is essential for autophagosome elongation, but its mechanism remains unknown (Mizushima *et al.*, 2011; Landajuela *et al.*, 2016). The final outcome of autophagy activation is highly dependent on the cellular context and on the strength and duration of the stress-inducing signals.

THC, the main active component of *Cannabis sativa* (Pertwee *et al.*, 2010), exerts a wide variety of biological effects by mimicking endogenous substances — the endocannabinoids anandamide (Devane *et al.*, 1992) and 2-AG (Mechoulam *et al.*, 1995; Sugiura *et al.*, 1995) that engage specific cell-surface G protein-coupled

cannabinoid receptors (Pertwee *et al.*, 2010). So far, 2 major cannabinoid-specific receptors, CNR1/CB1 (brain) and CNR2/CB2 (macrophage), have been cloned and characterized from mammalian tissues (Matsuda *et al.*, 1990; Munro *et al.*, 1993). Previous findings from the group of Velasco have unraveled that cannabinoid administration induces autophagy in different types of tumor cells, including glioma/astrocytoma and pancreatic cancer cells, whereas they do not activate this cellular process in non-transformed cells of interest (Salazar *et al.*, 2009). Pharmacological or genetic inhibition of autophagy prevents cannabinoid-induced cell death as well as apoptosis, whereas abrogation of apoptosis prevents cell death but not autophagy as induced by these agents (Salazar *et al.*, 2009). These observations allowed them to conclude that induction of autophagy is part of the mechanism by which cannabinoids promote the apoptotic death of cancer cells (Velasco *et al.*, 2012). They have investigated the molecular mechanisms responsible for the activation of autophagy upon THC administration and have found that THC binds cannabinoid receptors, leading to the stimulation of *de novo* sphingolipid synthesis and the subsequent activation of an ER stress-related signaling route that involves the up-regulation of the transcriptional co-activator NUPR1/p8 (transcriptional regulator) and its effector TRIB3 (Armstrong *et al.*, 2015; Carracedo *et al.*, 2006a; Carracedo *et al.*, 2006b; Velasco *et al.*, 2012). The stimulation of this pathway promotes in turn autophagy via TRIB3-mediated inhibition of the AKT-MTORC1 axis, which is essential for the proapoptotic and antitumoral action of cannabinoids (Salazar *et al.*, 2009, 2013).

A lipidomic study of human glioma cells after THC administration supports that the effect is related to differences in sphingolipid composition of autophagosomes, particularly an increased content of 14:0 and 16:0 dihydroceramides (Hernández-Tiedra *et al.*, 2016). Moreover, treatment with THC also promotes the release of cathepsins by autolysosomes. These effects may be due to the increased levels of those sphingolipids, which would alter the structure of autolysosomal or autophagosomal membranes, making them more unstable or permeable and allowing the release of cathepsins. On the basis of these observations, the study in this work has attempted to gain further insight into the molecular mechanism underlying the activation of autophagy-mediated cancer cell death by modeling the behavior of membranes with different ratios of dihydroceramide to test the above hypothesis. With this purpose, we have performed experiments in which ceramides and dihydroceramides were added to model liposomal membranes of controlled compositions, and their ability to induce membrane destabilization was assayed. We have also explored the implication of ceramide and dihydroceramide domain formation by generating them enzymatically

after *B. cereus* nSMase action (Hernández-Tiedra *et al.*, 2016). Using this experimental approach, we found that (i) dihydroceramide forms primarily dihydroceramide-rich rigid regions that melt at temperatures well above those generated by ceramide; (ii) dihydroceramides form rigid domains in GUV which are morphologically similar to those formed by ceramides; and (iii) dihydroceramide causes release of contents in liposomes based on PC and Chol. Release of vesicular aqueous contents induced by dihydroceramide appears to be larger and faster than that induced by ceramide. Thus, the alteration of the balance between different molecular species of ceramides and dihydroceramides in the microsomal fraction of cancer cells induced by THC administration can promote the permeabilization of autophagosomal and autolysosomal membranes leading to the release of cathepsins to the cytoplasm and the subsequent activation of apoptotic cell death.

Moreover, as mentioned in the Introduction, recent studies have shown that ceramide in the mitochondrial membrane acts as a receptor for LC3B (Sentelle *et al.*, 2012; Dany & Ogretmen, 2015). Mutagenesis and docking analyses indicated that ceramide has a higher affinity to the PE-conjugated LC3 than to soluble LC3 (Sentelle *et al.*, 2012). In the present work we examined this interaction, using the vesicle flotation approach, to test whether some of the features observed in LC3B interaction with cardiolipin (see Chapter 3) also play a role in its interaction with ceramide. Our results with the soluble form of the protein strongly support the idea that previous lipidation of the autophagic protein is essential for LC3-Cer interaction, modulating the binding capacity of the protein.

5.2 Materials and Methods

5.2.1 Materials

PC and PE from egg yolk were purchased from Lipid Products. Bovine heart CL (90% TLCL, 5% TOCL, 5% unknown), DOPE, Chol/Ch, Cer16/C16Cer, C16dhCer, Cer18, Cer24:1 and egg SM were from Avanti Polar Lipids. dhSM (86% C16dhSM) was synthesized by Gemma Fabrias (Department of Biomedical Chemistry, iQAC, Barcelona) from egg SM (Avanti Polar Lipids). SMase (EC 3.1.4.12) from *Bacillus cereus* and o-phenanthroline were supplied by Sigma-Aldrich. ANTS and DPX were supplied by Molecular Probes. Anti-LC3 monoclonal antibody was from MBL International (Medical & Biological laboratories Co. Ltd.).

5.2.2 Recombinant Protein Expression and Purification

A plasmid for expression of the human Atg8 ortholog LC3B was kindly provided by Dr. I. Tanida. Note that this Atg8 ortholog is a truncated form ending in the reactive C-terminal Gly such that no ATG4-mediated preprocessing is necessary. LC3B was purified from soluble fractions of bacterial extracts obtained in the absence of detergents, and was >90% pure as evaluated by Coomassie Blue-stained SDS-PAGE. *E.coli* BL21(DE3) cells were transformed with the LC3B plasmid and cells were grown to OD_{600} 0.8 and induced with 0.5 mM IPTG (Sigma-Aldrich) for 3 h at 37ºC. Following centrifugation at 4,500 x g for 15 min, the pellet was resuspended and sonicated in breaking buffer [10 mM PBS, 20 mM Tris-HCl, pH 7, 150 mM NaCl, supplemented with freshly prepared 1 mg/mL lysozyme (Sigma-Aldrich), 1 mM DTT (Sigma-Aldrich), bacterial protease inhibitors (Roche) and 2.5 µg/mL DNase (Sigma-Aldrich)]. After removal of cellular debris by centrifugation at 30,000 x g for 30 min at 4ºC, the sample supernatant fraction was incubated with 1 mL glutathione Sepharose 4B (GE Healthcare) for 3 h at 4°C to bind GST-tagged proteins. Then PreScission Protease (GE Healthcare) was added at 100 units/mL in a 2-bed volume of PreScission Buffer (50 mM Tris-HCl pH 7.5, 150 mM NaCl, 1 mM EDTA) freshly prepared with 1 mM DTT and cleavage was performed for 4 h at 4°C. Cleaved protein was eluted and concentrated. Recombinant LC3B was stored in 20% glycerol at -80°C.

5.2.3 Liposome Preparation

The appropriate lipids were mixed in organic solution [chloroform:methanol (2:1 v/v)] and the solvent was evaporated to dryness under a N_2 stream. Then the sample was kept under vacuum for 2 h to remove solvent traces and the lipids were swollen in

a buffer solution for MLV preparation. In the present study, when preparing “complex” MLVs, i.e. those presenting several lipid components or those having lipids with high main phase transition temperatures, hydration was performed in a slightly different way. Briefly, instead of adding the aqueous solution at once, hydration was performed by adding increasing amounts of the aqueous solution while maintaining the temperature above that of the lipid with the highest main phase transition temperature, and helping dispersion by stirring with a glass rod. Finally, the generated vesicles were homogenized by passing the sample 50-100 times between two syringes through a narrow tubing (0.5 mm internal diameter, 10 cm long) at the same temperature of the hydration process.

LUVs of diameters 100–150 nm were prepared from swollen lipids, subjected to 10 freeze/thaw cycles, and then extruded using a LIPEX Liposome Extrusion System (Transferra Nanosciences) equipped with 0.1-mm pore diameter Nuclepore filters (Whatman) at 65ºC (as described in Mayer *et al.*, 1986). By using a circulating water bath, the extruder was maintained at the desired temperature. Vesicle size was checked by quasi-elastic light scattering using a Malvern Zeta-Sizer 4 spectrometer (Malvern Instruments). Phospholipid concentration was measured in terms of lipid phosphorus.

5.2.4 Differential Scanning Calorimetry (DSC)

Previously degassed buffer solutions (20mM PIPES, 150mM NaCl, 1mM EDTA, pH 7.4) were introduced into both reference and sample cells of a VP-DSC high-sensitivity scanning microcalorimeter (MicroCal) to obtain the buffer reference thermogram. Then, in order to determine the specific thermodynamic parameters, at least three heating scans were performed with the lipid sample in the form of MLV. Lipid concentration of the sample was determined by phosphate analysis. In all cases, background thermograms from samples lacking lipid were substracted from the thermograms obtained with lipid containing samples. Sample concentration was normalized and the specific parameters determined. Data treatment was performed using the ORIGIN 7.0 (MicroCal).

5.2.5 Release of Vesicle Contents

Leakage of LUV contents was assayed with the ANTS/DPX fluorescence system (Ellens *et al.*, 1985; Nieva *et al.*, 1989; Goñi *et al.*, 2003). LUVs were prepared as previously described in the following buffer: 20 mM ANTS, 70 mM DPX, 40 mM NaCl, 10 mM HEPES, 10mM $CaCl_2$ and 2mM $MgCl_2$, pH 7. A high DPX/ANTS ratio was

used to ensure complete quenching inside vesicles. The vesicle suspension was passed through a Sephadex G-25 column to remove non-entrapped ANTS and DPX molecules. A previously adjusted isosmotic buffer solution consisting of 150 mM NaCl, 10 mM HEPES, 10mM $CaCl_2$ and 2mM $MgCl_2$, pH 7 was used for this process.

Ceramide or SMase was added to vesicles and leakage was followed in terms of ANTS fluorescence in a QuantaMaster spectrofluorometer (Photon Technology International) at 37ºC and 520 nm. The excitation wavelength was set at 355 nm and the band-pass was 2 nm. A 470 nm cut-off filter was placed between the sample and the emission monochromator to avoid scattering interference. Since commercial sphingomyelinase preparations may contain phospholipase C impurities, 2 mM o-phenanthroline (Sigma-Aldrich) was routinely added in all our enzyme assays. Lipid concentration was 0.3 mM and sphingomyelinase was used at 0.15 units/mL. Lipid concentration was determined by phosphate analysis. To establish the 100% leakage signal, Triton X-100 was added to a 0.1% (v/v) final concentration.

5.2.6 Sucrose Gradient Centrifugation of Liposomes

Recombinant LC3B (10 µM) was incubated with 3 mM liposomes (containing 0.05 mol percent Rho-PE for detection) for 1 h at 37ºC in 200 µL PreScission buffer. 125 µl protein/lipid mix was diluted to 300 µL in PreScission buffer containing 2.4 M sucrose (Sigma-Aldrich). Then the reaction mix was transferred to a centrifuge tube. The 1.4 M sucrose layer was overlaid with 400 µL PreScission buffer containing 0.8 M sucrose and 300 µL PreScission buffer containing 0.5 M sucrose. Sucrose step gradients were centrifuged in a TLA-120.2 rotor (Beckman Coulter) at 356,160 x g for 3 h at 4ºC. Four 250-µL fractions were pipetted, starting from the bottom. The T fraction, containing liposomes as indicated by the rhodamine fluorescence, and the B fraction containing the unbound protein were analyzed by SDS-PAGE and western blotting.

5.2.7 GUV Preparation

GUVs were prepared using the electroformation method described previously (Montes *et al.*, 2007), using a homemade chamber (Industrias Tecnicas ITC) that allows direct visualization under the microscope. Stock solutions of lipids (0.2 mM total lipid containing 0.3 mol% Rho-PE) were prepared in chloroform:methanol (2:1, v/v) and 5 µl of the lipid stocks were added onto the surface of platinum electrodes. Then solvent traces were removed by evacuating the chamber under high vacuum for at least 2 h. The platinum electrodes were covered with 400 µl of 25 mM HEPES and 150 mM NaCl, pH 7.5, buffer previously equilibrated at 65ºC, and connected to an electric wave

generator (TG330 function generator, Thurlby Thandar Instruments) under AC field conditions (500 Hz, 0.08V for 6 min; 500 Hz, 1.0 V for 20 min, and 500 Hz, 3.0 V for 1 h 30 min) at 65ºC. Vesicles remain attached to the platinum wire and are left to equilibrate for 1 h at room temperature after switching off the generator and water bath.

5.2.8 Fluorescence Microscopy

In the present work, laser scanning confocal microscopy has been applied to the characterization of lipid domains in GUVs under thermodynamic equilibrium conditions. After GUV electroformation, the chamber was placed on an inverted confocal fluorescence microscope (Nikon D-ECLIPSE C1, Nikon). The excitation wavelength was 561 nm for Rho-PE. The images were collected using band-pass filter of 593 ± 20 nm. Image treatment was performed using the EZ-C1 3.20 software (Nikon).

5.2.9 Statistical Analyses

Statistical analyses were performed by ANOVA with a *post hoc* analysis by the Student-Neuman-Keuls test.

5.3 Results

Previous reports by Velasco and coworkers show that THC triggers an early accumulation of *de novo*-synthesized sphingolipids (an event that takes place in the ER) and inhibits the transport of sphingolipids from the ER to the Golgi, which leads in turn to ER stress response and is involved in the induction of autophagy-mediated cancer cell death (Carracedo *et al.*, 2006a; Salazar *et al.*, 2009; Velasco *et al.*, 2012). To investigate the potential relevance of changes observed in the sphingolipid composition of autophagosomes and autolysosomes, and specifically of the increased dihydroceramide levels in THC-treated cells, we undertook a series of experiments to analyze the role of these lipids in model vesicles. The main objective was the verification that dihydroceramide exhibits a transition temperature similar to that of ceramide, forms rigid domains and causes release of contents in the same way as ceramides. Mass spectrometry studies of the subcellular fraction (microsomes) of human glioma cells had shown that the main change induced by THC treatment was a decrease in C16Cer and a concomitant increase in C16dhCer (Hernández-Tiedra *et al.*, 2016). Therefore, experiments were conducted using 16:0 sphingolipids. Moreover, in microsomes it had been observed that PC species predominated, together with some Chol, so PC:Chol (95:5, mol ratio) was used as the basic lipid composition.

Differential scanning calorimetry, fluorescence confocal microscopy and fluorescence spectroscopy were applied to the characterization of membranes based on egg PC with different ratios of dihydroceramide in MLVs, GUVs and LUVs at 37ºC.

5.3.1 Ceramide-Domain Formation Experiments

As a first approach to investigate the molecular mechanisms responsible for the activation of autophagy-mediated cancer cell death we analyzed the formation of ceramide domains which has been previously described in our group by DSC (as different domains have different transition temperatures) and by IR spectroscopy, using both natural ceramides (brain, egg) and synthetic phospholipids. Measurements in monolayers have shown that the potential dipole may play an important role in the lateral phase separation (Goñi & Alonso, 2009). Thus, the ceramide-PC dipolar pairing would favor strong interactions while unfavorable pairings would explain phase segregation in ceramide-rich domains. Moreover, epifluorescence studies of sphingomyelin monolayers and the quantification of the area occupied by the different domains after SMase addition revealed that domain formation is related to the activity of the enzyme. It seems therefore that decoupling of the chains is an important factor

that regulates phase separation. However, the causes of domain formation can be very diverse, although the most important is probably the ability of ceramides (and sphingolipids in general) to form hydrogen bonds. While glycerophospholipids can only act as hydrogen acceptors, sphingolipids (such as sphingomyelin and ceramides) may act as acceptors and also as donors through their hydroxyl and amide groups (see **Figure 5.10**) (Goñi & Alonso, 2009).

In the present study, experiments focused on the formation of dihydroceramide domains included DSC assays that determined the thermodynamic parameters for the lipid phase transition induced by temperature changes. For that purpose, 2 mM MLV of the following mixtures were analyzed: pure ePC, ePC:C16Cer (80:20, mol ratio), and ePC:C16dhCer (80:20, mol ratio) (**Figure 5.1**).

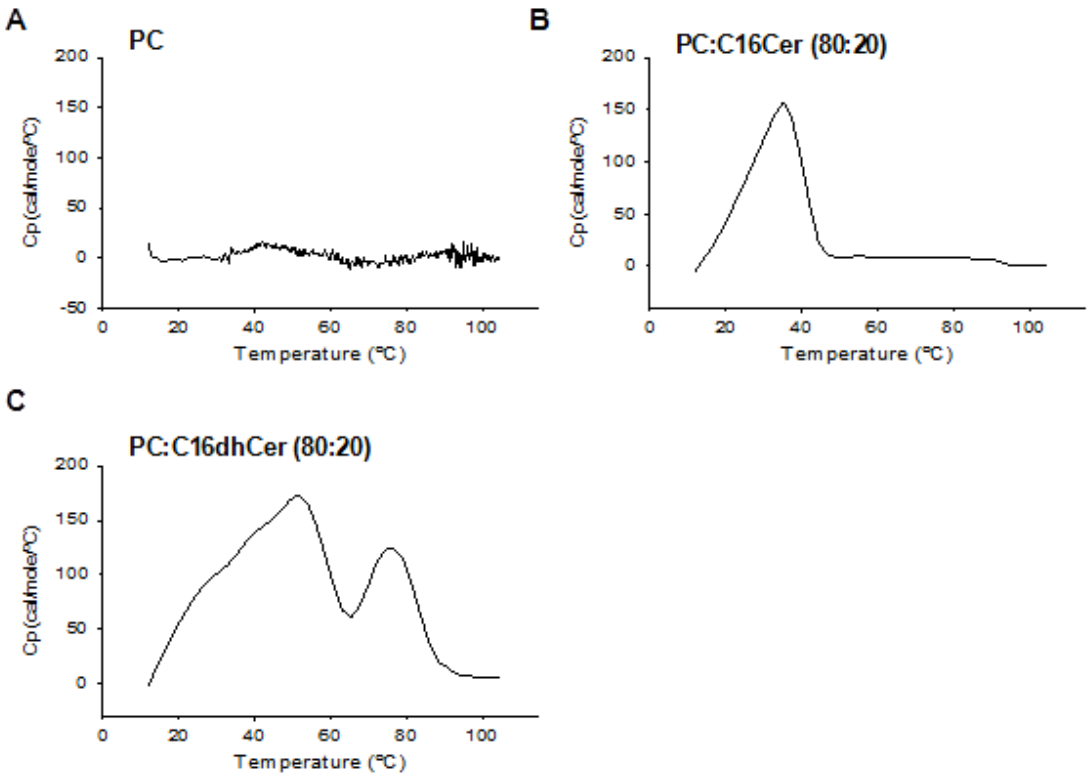

Figure 5.1. Effect of C16 ceramides and C16 dihydroceramides on the gel-to-fluid phase transition of lipid membranes. DSC thermograms of (**A**) pure PC, (**B**) PC:C16Cer (80:20, mol ratio) and (**C**) PC:C16dhCer (80:20, mol ratio). Representative thermograms of three independent experiments are shown.

In the control sample thermogram (PC) no peak appeared as its phase transition occurs at about -3°C, i.e. below our experimentally accessible temperature range (**Figure 5.1A**). In the PC:C16dhCer thermogram two zones can be observed: we suggest that the first is associated with dihydroceramide mixed with PC resulting in dihydroceramide-rich rigid regions that melt at ~52°C; the same phenomenon can be observed in PC:C16Cer samples at ~40°C (**Figure 5.1B**). The second peak would correspond to regions primarily formed of dihydroceramide (~77ºC) that contain small amounts of PC (**Figure 5.1C**).

This calorimetric phase transition experiments indicate that C16dhCer, prepared in a mixture with egg PC, exhibited a more complex transition (extending over higher temperatures) than C16Cer, i.e. the membrane rigidifying effect of C16dhCer is higher than that of C16Cer. These observations suggest that an enhanced proportion of dihydroceramide facilitates the formation of more rigid domains than ceramide in biological membranes, so there should be larger fluidity differences between ePC-rich areas and dihydroceramide domains than in the case of ceramide domains. This in turn would lead to the greater release ratios observed with dihydroceramide in the leakage experiments described below (see **Figures 5.5 and 5.6** and **Tables 5.1 and 5.2**).

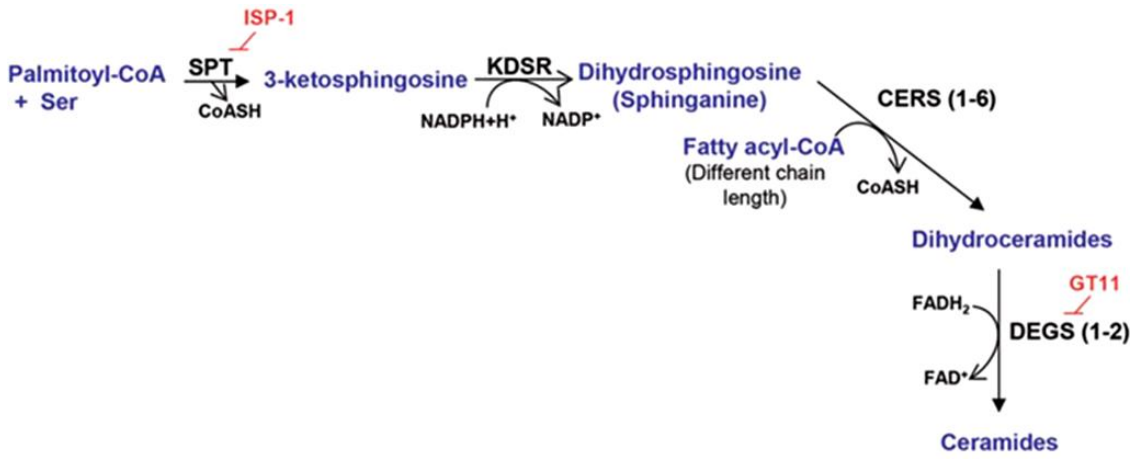

Figure 5.2. The pathway of *de novo* sphingolipid synthesis. SPT catalyzes the condensation of serine and palmitoyl-CoA to produce 3-ketosphinganine. KDSR catalyzes the reduction of 3-ketosphinganine to dihydrosphingosine (sphinganine). The next reaction is catalyzed by CERS1 to CERS6 (each isoform of this enzyme has selectivity for fatty acyl-CoAs with different chain length). CERSs convert dihydrosphingosine into the different molecular species of dihydroceramides, which are subsequently transformed into ceramides by the insertion of a 4, 5-*trans* double bond catalyzed by the enzymes DEGS1 and DEGS2. ISP-1 and GT11 are pharmacological inhibitors of SPT and DEGS, respectively.

As mentioned above, analysis of the sphingolipid composition of autophagosome-enriched fractions derived from human glioma cells have shown that PC species predominate together with some Chol and that THC treatment produces an increase in the levels of different species of dihydroceramides (Hernández-Tiedra *et al.*, 2016; see **Figure 5.2**). It should be noted that ceramide levels were 6- to 10-fold higher than those of dihydroceramides in vehicle-treated cells. Thus, the observed THC-triggered increase in dihydroceramides led to a striking modification of the ratio of both sphingolipid types in the microsomal fraction, specifically the C16Cer:C16dhCer ratio varied from 6:1 to 2:1 (Hernández-Tiedra *et al.*, 2016).

Thus, after studying by DSC phase transitions in samples with both ceramide and dihydroceramide, the formation and morphology of domains were monitored by direct confocal microscopy of individual vesicles. For this purpose, 0.2 mM GUV were electroformed attached to a platinum wire composed of PC:Chol (95:5, mol ratio) to which either 30 mol% of C16Cer:C16dhCer (6:1, mol ratio) or 30 mol% of C16Cer:C16dhCer (2:1, mol ratio) were added (73:4:23, final mol ratio) (**Figures 5.3 and 5.4**). A buffer was used (25 mM HEPES, 150 mM NaCl, pH 7.5) with which large, non-overlapping vesicles were obtained.

Morphological examination of GUVs indicated that the control GUVs (PC:Chol) failed to show lateral domain formation (**Figure 5.3**). In contrast domains can be observed in ceramide- and dihydroceramide-containing vesicles, in accordance with the results obtained by DSC (**Figures 5.3 and 5.4**). We noticed that some of the ceramide-containing vesicles lacked Cer/dhCer-rich domains, which suggests sample heterogeneity.

PC:Chol (95:5)

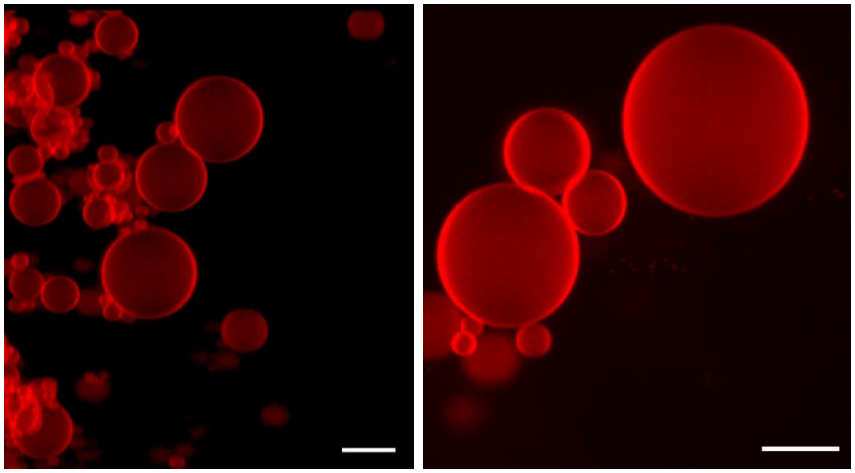

PC:Chol (95:5) + 30 additional mol% Cer:dhCer (2:1)

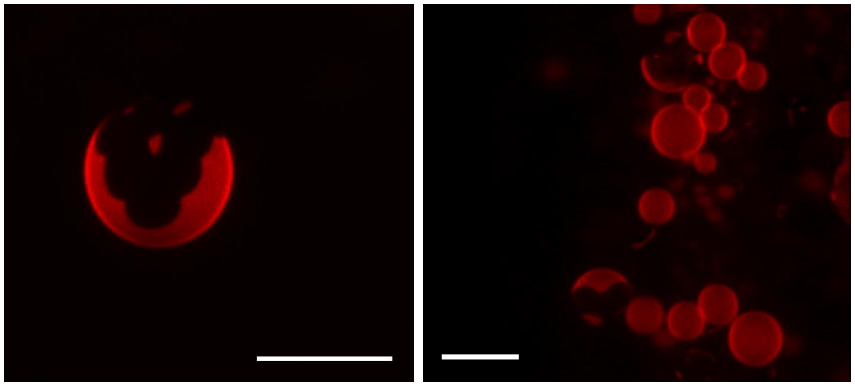

Figure 5.3. Generation of ceramide rigid domains in C16 ceramide:dihydroceramide-containing GUVs. Upper panel: a control experiment with GUVs composed of PC:Chol (95:5, mol ratio) that does not give rise to domains under these conditions. Lower panel: Ceramide rigid domains in bilayers containing PC (a fluid phospholipid), Chol, C16 ceramide, and C16 dihydroceramide (73:4:15:8, final mol ratio). Bars: 10 µm.

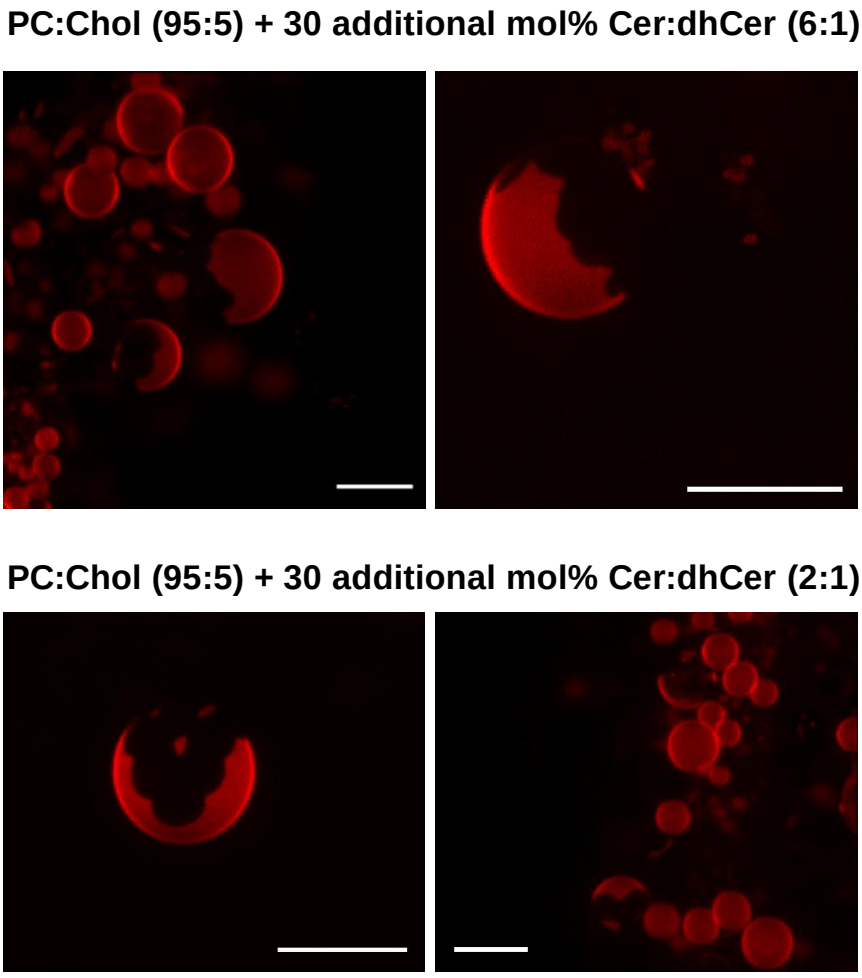

Figure 5.4. Effect of the C16Cer:C16dhCer ratio modification in the formation and morphology of ceramide domains. Upper panel: Ceramide rigid domains in bilayers containing PC (a fluid phospholipid), Chol, C16 ceramide, and C16 dihydroceramide (73:4:20:3, final mol ratio). Lower panel: Ceramide rigid domains in bilayers containing PC (a fluid phospholipid), Chol, C16 ceramide, and C16 dihydroceramide (73:4:15:8, final mol ratio). Bars: 10 μm.

5.3.2 Vesicle Contents Leakage Assays

Next we analyzed whether the domains observed in ceramide-enriched vesicles could contribute to membrane destabilization. Changes in membrane stability of vesicles can be determined by measuring the release of the vesicles aqueous contents. This technique measures the ability of individual molecules to permeabilize the vesicle lipid bilayer. In the present study, the permeabilising effects of ceramide and dihydroceramide were tested in LUVs by following the externalization of the well-known low molecular weight and water-soluble fluorescent dye ANTS and its quencher DPX.

As mentioned in the Introduction, ceramide can be synthetized in at least two different ways: (i) *de novo* by condensation of serine and palmitoyl-CoA forming 3-

oxosphinganine, dihydroceramide in the final step being oxidized by dihydroceramide reductase to form ceramide by the introduction of a *trans* double bond in position 4-5; and (ii) by the action of enzymes involved in the hydrolysis of SM, called sphingomyelinases (Goñi *et al.*, 2012).

Six types of sphingomyelinases are considered, namely acidic, secretory, Mg^{2+}-dependent neutral (integral membrane proteins in mammals and soluble proteins in bacteria), Mg^{2+}-independent neutral (cytosolic), alkaline, and bacterial enzymes with both phospholipase C and sphingomyelinase activity. nSMase is involved in several cellular processes including differentiation, cell cycle arrest and programmed cell death (apoptosis) through the generation of ceramide. It has been proposed that mammalian nSMase1 is localized predominantly in microsomal fractions (ER and Golgi) (Tomiuk *et al.*, 2000). Moreover, it has been shown that when bacterial SMase is directed to mitochondria the cell undergoes apoptosis (Birbes *et al.*, 2001). These enzymes have been found in *Bacillus cereus, Staphylococcus aureus* (β-toxin), *Listeria ivanovii, Leptospira interrogans, Cromobacterium violaceum, Helicobacter pylori* and *Pseudomonas TK4*. The best known of these enzymes is the nSMase from *B. cereus*. It was the first one cloned in *E. coli* and it is a secreted enzyme of 37 kDa (306 amino acids), which depends on Mg^{2+} and is activated by TNF, ligand-bound Fas, CD-95, oxidized LDL and various chemotherapeutic agents (for a recent review see Goñi *et al.*, 2012).

In this work, ceramides and dihydroceramides were generated enzymatically by the action of *Bacillus cereus* nSMase. Alternatively ceramides and dihydroceramides were added in organic solvents to the preformed liposome suspensions (see **Figure 5.10**).

As a first approach to analyze the effect of acute increases in ceramide and/or dihydroceramide on membrane stability, ceramide and/or dihydroceramide were formed *in situ* in the membrane by addition of bacterial sphingomyelinase at 37°C (**Figures 5.5 and 5.6** and **Tables 5.1 and 5.2**). Tests were performed with 0.3 mM LUV containing different proportions of C16 sphingomyelin and C16 dihydrosphingomyelin to which 0.15 U/mL SMase was added. In all enzymatic assays 2 mM *o*-phenanthroline, a phospholipase C inhibitor, was added as sphingomyelinase commercial preparations may contain phospholipase C impurities. Phospholipase C induces aggregation and fusion of vesicles composed of PC:PE:Chol (2:1:1, mol ratio) (Goñi & Alonso, 2006). Fusion induced by SMase is also possible, although the mechanism is probably different from the fusion elicited by phospholipase C.

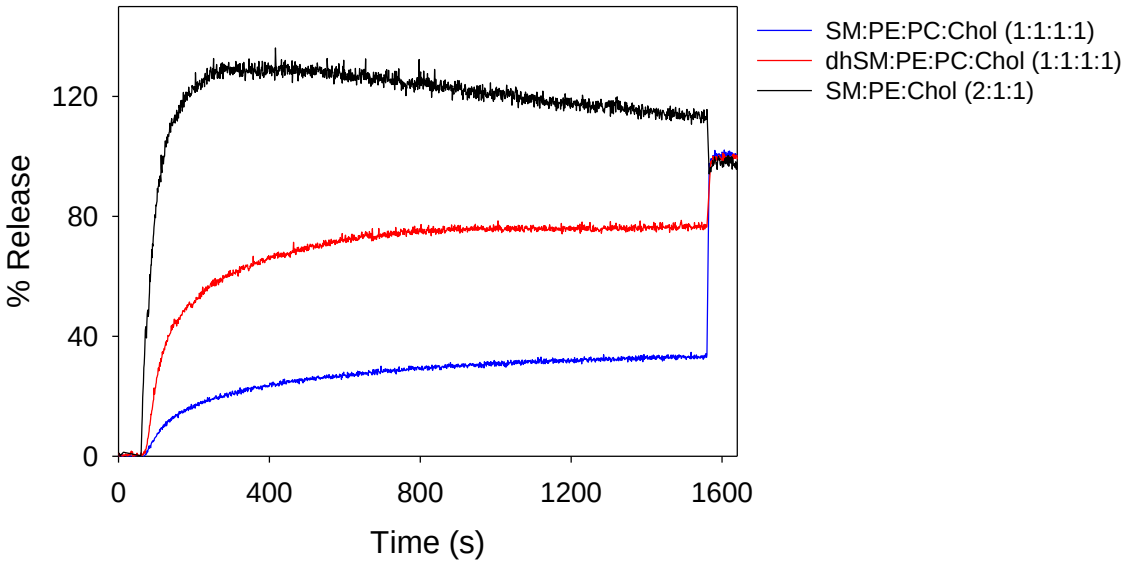

Figure 5.5. Release of vesicular aqueous contents induced by C16 ceramide and C16 dihydroceramide. Ceramides were generated by the action of sphingomyelinase on LUVs composed of SM:PE:Chol (2:1:1, mol ratio), SM:PE:PC:Chol (1:1:1:1, mol ratio); and dhSM:PE:PC:Chol (1:1:1:1, mol ratio). Representative time courses of three independent experiments are shown.

	SM:PE:Chol (2:1:1)	SM:PE:PC:Chol (1:1:1:1)	dhSM:PE:PC:Chol (1:1:1:1)
Initial slope 1	1.90	0.25	0.45
Initial slope 2	1.90	0.20	0.49
Initial slope 3	0.74	0.30	0.59
Mean	1.50	0.25	0.51
SD	0.65	0.052	0.072
Size (n)	3	3	3

Table 5.1. Individual and average values obtained from time courses of *in situ*-generated Cer- and/or dhCer-induced leakage of vesicle contents as shown in Fig. 5.5.

There are few studies regarding the effect of lipids on sphingomyelinase activity, and most of them have used model membranes as substrates. It has been shown that human recombinant SMase activity is enhanced by lysosomal lipids and that sphingomyelinase binding to lipid bilayers is enhanced by certain types of lipids (anionic) (Goñi *et al.*, 2012). It has been observed that SMase from *B. cereus* is little active on SM bilayers in the gel state. Including egg PC or PE in the composition of the

bilayer at 37°C, sphingomyelinase activity (practically zero in pure sphingolipid bilayers) increases, together with a decrease in the transition temperature of sphingomyelin (Goñi *et al.*, 2012). Thus, as glycerophospholipids are added to the membrane composition, the amount of sphingomyelin in the fluid state at 37°C also increases, making easier the enzyme hydrolysis. Therefore, sphingomyelinase requires the substrate to be in bilayer form and in the fluid state for optimum activity. Lateral organization of lipids also influences SMase activity (Fanani *et al.*, 2002) since the enzyme induces phase separation, which changes the surface topography. These topographical changes in turn act as feedback regulators in the kinetics of the enzyme.

After treatment of large unilamellar vesicles composed of SM:PE:Chol (2:1:1, mol ratio), SM:PE:PC:Chol (1:1:1:1, mol ratio) and dhSM:PE:PC:Chol (1:1:1:1, mol ratio) with sphingomyelinase, ceramides were generated in the lipid bilayers resulting from sphingomyelin hydrolysis. Vesicles were packed with soluble fluorescent probes under isotonic conditions, so that probe release could be observed. Probe release occurs simultaneously with the production of ceramides. As shown in **Figure 5.5**, increasing SM, thus ceramide ratio in the bilayer [SM:PE:Chol (2:1:1, mol ratio)], the maximum release increased. This result demonstrates that release is very sensitive to ceramide concentration in the bilayer. Moreover the release of vesicle aqueous contents induced by C16dhCer generated by SMase [dhSM:PE:PC:Chol (1:1:1:1, mol ratio)] was larger and faster than that induced by C16Cer [SM:PE:PC:Chol (1:1:1:1, mol ratio)]. In terms of initial slopes (see **Table 5.1**), SM:PE:PC:Chol mixture exhibited an initial slope of 0.25 ± 0.030, lower than that of dhSM:PE:PC:Chol 0.51 ± 0.041 (n = 3; *P = 0.019).

Next, we prepared vesicles with lipid compositions that mimicked the microsomal and autophagosome-enriched fraction of cells treated with THC or EBSS (containing sphingomyelin and dihydrosphingomyelin in the same proportion as those of ceramides and dihydroceramides after treatment with THC or EBSS) (Hernández-Tiedra *et al.*, 2016). Addition of sphingomyelinase to these membranes showed that a higher proportion of dihydroceramides resulted in a more rapid and extensive release of aqueous contents from these vesicles (see **Figure 5.6 and Table 5.2**).

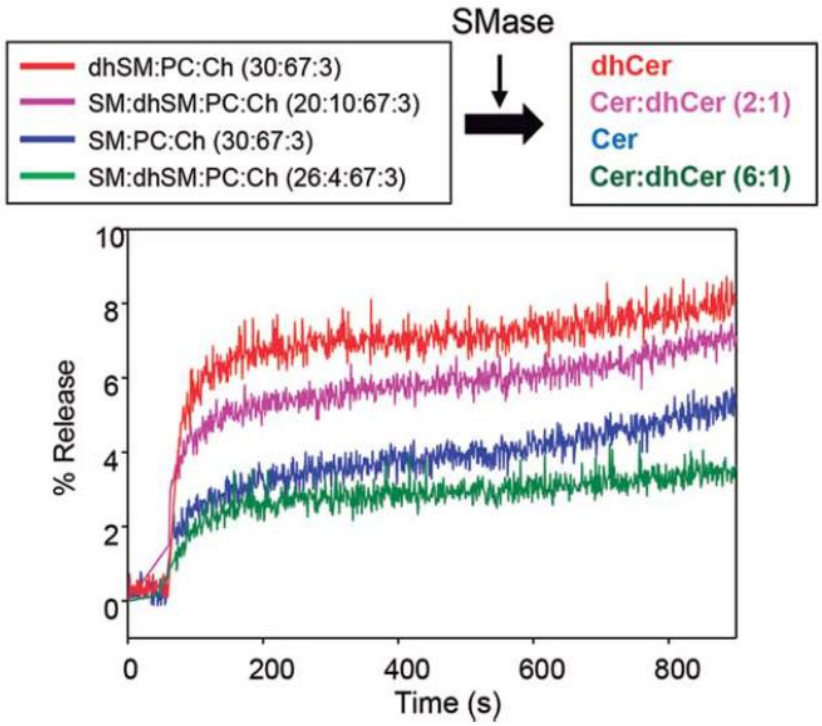

Figure 5.6. Release of vesicular aqueous contents induced by ceramides. Effect of the different proportions of C16 ceramide:C16 dihydroceramide generated by the action of sphingomyelinase on LUVs composed of dhSM:PC:Ch (30:67:3; red); SM:dhSM:PC:Ch (20:10:67:3; magenta); SM:PC:Ch (30:67:3; blue); and SM:dhSM:PC:Ch (26:4:67:3; green). A representative example of 3 closely similar experiments is shown.

	SM:PC:Chol (30:67:3)	dhSM:PC:Chol (30:67:3)	SM:dhSM:PC:Chol (26:4:67:3)
Initial slope (Mean)	0.044	0.25	0.030
SD	0.048	0.021	0.010
Size (n)	3	3	3

Table 5.2. Individual and average values obtained from time courses of *in situ*-generated Cer- and/or dhCer-induced leakage of vesicle contents as shown in Fig. 5.6.

In order to mimic these conditions, we also performed leakage assays by externally adding different amounts of ceramide and dihydroceramide at 37°C (**Figures 5.7 and 5.8**). To 0.3 mM PC:Chol (95:5, mol ratio) LUV 15 mol% and 30 mol% of C16Cer:C16dhCer (83:4:13, mol ratio and 73:4:23, mol ratio) in 6:1 and 2:1 proportions were added dissolved in DMSO or dodecane/ethanol (2:98 v/v). Results of release induced by externally-added ceramides are summarized in **Tables 5.3 to 5.6**. In all cases control experiments (0% ceramide in **Tables 5.5 and 5.6**) were performed in which only the organic solvent was added.

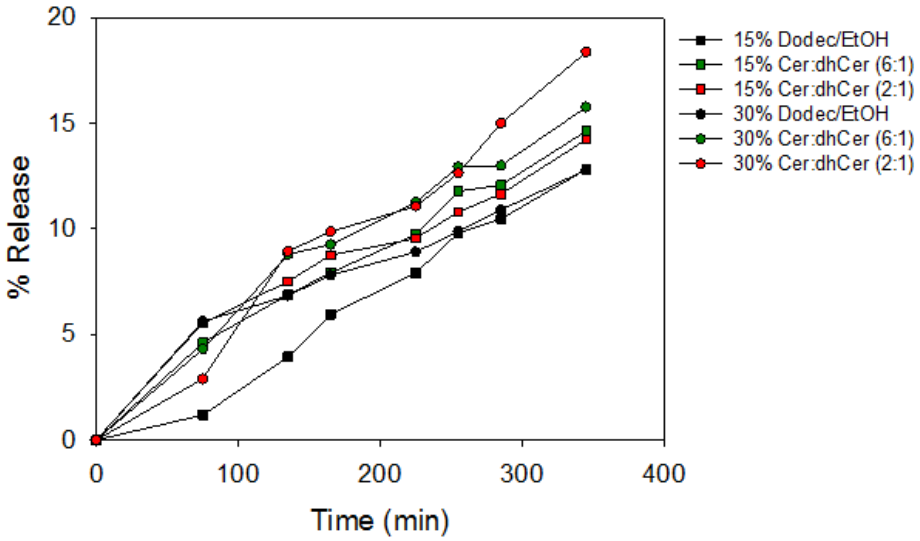

Figure 5.7. Time-course of ANTS/DPX release. Long-chain ceramides were added dissolved in dodecane/ethanol (2:98 v/v) to the preformed PC:Chol (95:5, mol ratio) vesicles.

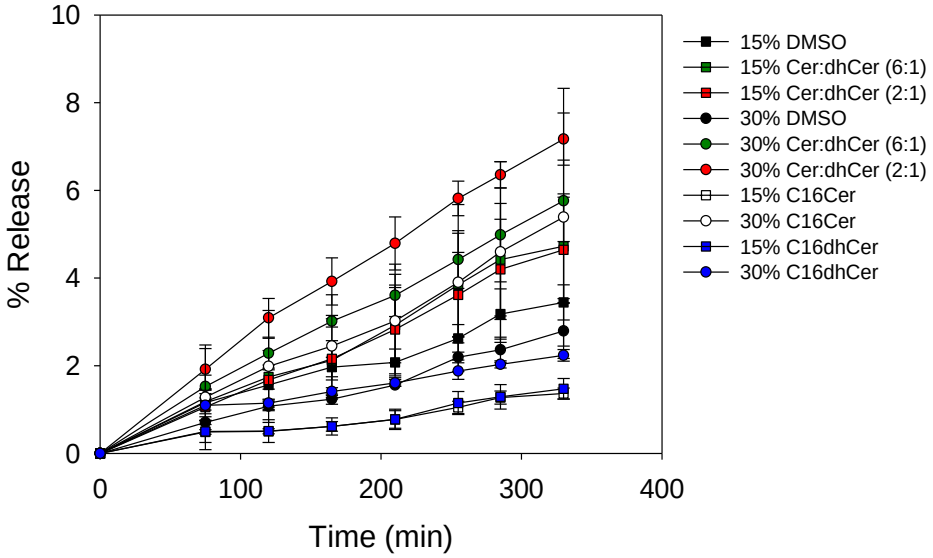

Figure 5.8. Time-course of ANTS/DPX release. Long-chain ceramides were added dissolved in DMSO to the preformed PC:Chol (95:5, mol ratio) vesicles.

When ceramides were added to preformed liposomes, the solvent was an important issue. We observed that dodecane/ethanol caused a high release of contents by itself (**Figure 5.7**). For this reason, DMSO was chosen as a more convenient solvent than dodecane/ethanol to perform this kind of experiments (**Figure 5.8** and **Tables 5.5 and 5.6**).

As shown in **Figure 5.8**, release of ANTS was observed after adding ceramides to bilayers even though at lower rates and extents than in the case of enzymatically-generated ceramides.

Regarding the release caused by externally-added ceramides dissolved in DMSO, it was found that Cer-induced ANTS/DPX release was dose-dependent (**Figure 5.8**). Furthermore mixed ceramides (C16Cer:C16dhCer), both in 6:1 and in 2:1 proportion, appeared to cause higher release than when added in the pure form.

The highest release was found for the samples containing a higher proportion of C16dhCer, i.e. 30 mol% of the Cer:dhCer 2:1 mixture (**Figure 5.8, Tables 5.3 and 5.4**). This confirms the higher permeabilizing ability of dhCer as compared to Cer, in agreement with the results obtained with *in situ* Cer generation (**Figures 5.5 and 5.6**).

Time (min)	15% DMSO	15% Cer:dhCer (6:1)	15% Cer:dhCer (2:1)	15% Cer	15% dhCer
0	0 ± 0	0 ± 0	0 ± 0	0 ± 0	0 ± 0
75	1.158 ± 0.322	1.182 ± 0.277	1.056 ± 0.308	0.489 ± 0.055	0.501 ± 0.251
120	1.562 ± 0.345	1.742 ± 0.274	1.675 ± 0.671	0.505 ± 0.058	0.510 ± 0.260
165	1.969 ± 0.222	2.125 ± 0.449	2.157 ± 0.916	0.617 ± 0.109	0.616 ± 0.196
210	2.075 ± 0.306	2.926 ± 0.858	2.827 ± 1.012	0.776 ± 0.200	0.778 ± 0.232
255	2.624 ± 0.315	3.844 ± 1.177	3.618 ± 0.966	1.050 ± 0.140	1.150 ± 0.263
285	3.179 ± 0.573	4.420 ± 1.283	4.198 ± 1.142	1.274 ± 0.151	1.291 ± 0.280
330	3.445 ± 0.401	4.727 ± 1.194	4.643 ± 1.202	1.367 ± 0.125	1.474 ± 0.236

Table 5.3. Vesicle contents leakage induced by externally added 15% Cer or dhCer. Average values ± S.D. (n = 3).

Time (min)	30% DMSO	30% Cer:dhCer (6:1)	30% Cer:dhCer (2:1)	30% Cer	30% dhCer
0	0 ± 0	0 ± 0	0 ± 0	0 ± 0	0 ± 0
75	0.706 ± 0.048	1.524 ± 0.260	1.917 ± 0.476	1.280 ± 1.195	1.097 ± 0.107
120	1.077 ± 0.102	2.286 ± 0.340	3.093 ± 0.442	1.985 ± 1.278	1.147 ± 0.090
165	1.238 ± 0.115	3.016 ± 0.134	3.923 ± 0.539	2.450 ± 1.170	1.412 ± 0.088
210	1.559 ± 0.028	3.605 ± 0.481	4.790 ± 0.606	3.022 ± 1.295	1.609 ± 0.074
255	2.194 ± 0.327	4.423 ± 0.660	5.816 ± 0.394	3.903 ± 1.773	1.878 ± 0.189
285	2.364 ± 0.288	4.985 ± 1.072	6.354 ± 0.300	4.595 ± 2.061	2.031 ± 0.082
330	2.793 ± 0.628	5.762 ± 0.929	7.170 ± 0.595	5.389 ± 2.940	2.236 ± 0.132

Table 5.4. Vesicle contents leakage induced by externally added 30% Cer or dhCer. Average values ± S.D. (n = 3).

Bilayer composition	Ceramide % in the bilayer	Initial slope (% release/min)
PC:Chol (95:5)	**0%**	11.5
	15% C16Cer:C16dhCer (6:1)	11.8
	15% C16Cer:C16dhCer (2:1)	10.7
PC:Chol (95:5)	**0%**	9.6
	30% C16Cer:C16dhCer (6:1)	12.8
	30% C16Cer:C16dhCer (2:1)	15.1

Table 5.5. Release of vesicle aqueous contents induced by ceramides dissolved in dodecane/ethanol. Vesicles contained ANTS/DPX. Total lipid concentration was 0.3 mM.

Bilayer composition	Ceramide % in the bilayer	Initial slope (% release/min)
PC:Chol (95:5)	**0%**	3.8
	15% C16Cer	1.4
	15% C16dhCer	1.5
	15% C16Cer:C16dhCer (6:1)	5.1
	15% C16Cer:C16dhCer (2:1)	4.5
PC:Chol (95:5)	**0%**	3.0
	30% C16Cer	5.6
	30% C16dhCer	1.8
	30% C16Cer:C16dhCer (6:1)	5.9
	30% C16Cer:C16dhCer (2:1)	6.5

Table 5.6. Release of vesicle aqueous contents induced by ceramides dissolved in DMSO. Vesicles contained ANTS/DPX. Total lipid concentration was 0.3 mM.

In summary data obtained from contents leakage experiments indicate that the presence of long-chain dihydroceramides induces release of contents through membranes, the release being higher and faster when dihydroceramides are enzymatically produced by SMase than when they are externally added.

Lysosomal membrane permeabilization produces cell death as a consequence of the release of lysosomal proteases to the cytoplasm (Aits & Jäättelä, 2013; Boya & Kroemer, 2008). Therefore, considering the above-described membrane permeabilizing effect of dihydroceramide, Velasco's group investigated whether the cell death promoting activity of THC relies on a sphingolipid-dependent induction of LMP. In line with this idea, treatment with THC produced an increase in cytosolic CTSB and CTSL activity and caused the appearance of CTSB in the cytosol of both U87MG cells and the melanoma cell line SK-MEL-28, these events being prevented by the pharmacological inhibition of *de novo* sphingolipid synthesis (Hernández-Tiedra *et al.*, 2016). Moreover, they found that THC-induced CTSB release was abrogated in U87MG and SK-MEL-28 cells and in oncogene-transformed MEFs in which autophagy had been genetically inhibited (Hernández-Tiedra *et al.*, 2016), indicating that autophagy stimulation is required for THC induced LMP. Collectively these observations suggest

that the increase in dihydroceramide autophagosomal content that triggers THC leads to autolysosomal membrane destabilization, LMP and cathepsin release (see **Figure 5.9**).

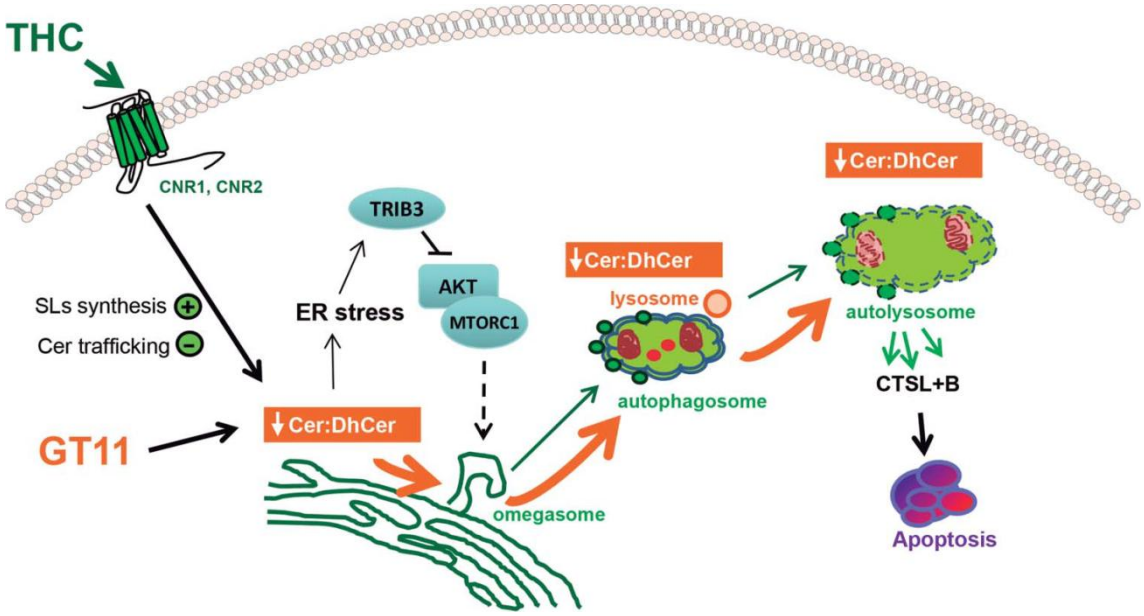

Figure 5.9. Proposed model of a mechanism by which the intracellular increase of dihydroceramide would promote glioma cell death. THC binding to CNR1 and CNR2 stimulates *de novo* synthesis of ceramide and inhibits the transport of ceramide from the ER to the Golgi inducing a modification on the ER sphingolipid composition. This event triggers: (i) the induction of an ER stress response that leads to a TRIB3-dependent inhibition of the AKT-MTORC1 axis and the subsequent induction of autophagy and (ii) a modification of the ceramide to dihydroceramide (Cer:dhCer) ratio in the ER. The DEGS1 inhibitor GT11 produces a similar decrease on the ratio Cer:dhCer. The alteration in the Cer:dhCer ratio triggered by THC or GT11 is transmitted to autophagosomes and autolysosomes, thus modifying the permeability of the membranes, facilitating LMP, cathepsin release and the subsequent activation of apoptosis and cell death (Hernández-Tiedra *et al.*, 2016).

LMP triggers the activation of the mitochondrial apoptotic pathway although it can also lead to necrotic cell death (Aits & Jäättelä, 2013; Boya *et al.*, 2003; Serrano-Puebla & Boya, 2015). In agreement with Velasco and coworkers previous findings showing that autophagy is upstream of apoptosis in the mechanism of cannabinoid induced cell death (Salazar *et al.*, 2009), they found that treatment with THC induced apoptosis and did not lead to a significant increase in necrotic cell death (Hernández-Tiedra *et al.*, 2016). Moreover, THC treatment promoted mitochondrial CYCS release (an event that is closely associated with the activation of the intrinsic apoptotic pathway), an event which was prevented by the pharmacological inhibition of sphingolipid biosynthesis and CTSB activity (Hernández-Tiedra *et al.*, 2016). Likewise, genetic inhibition of autophagy prevented THC-induced CTSB and CYCS release.

Furthermore, pharmacological inhibition of cathepsins prevented THC-induced cell death. Therefore THC-induced autophagy appears to promote LMP and the subsequent activation of the mitochondrial apoptotic pathway in a sphingolipid biosynthesis- and autophagy-dependent manner.

Taken together, the data described in this section support the notion that an increase in *de novo*-synthesized sphingolipids, specifically a decrease in the ceramide: dihydroceramide ratio (similar to that induced by THC in the microsomal and autophagosome-enriched fraction of live cells), leads to the formation of specific membrane domains and to a subsequent destabilization (increased permeability) of the membrane. In collaboration with Velasco and coworkers we found that this is an important factor in the activation of cytotoxic autophagy by THC (Hernández-Tiedra *et al.*, 2016) and therefore pharmacological manipulation of dihydroceramide levels could be used as a strategy to stimulate autophagy-mediated *in vivo* cancer cell death.

5.3.3 LC3B Interaction with Ceramide-containing Membranes

Cer18 has been recently reported as a receptor for anchoring LC3-II to mitochondrial membranes, through direct interaction of Cer18 with LC3-II, but not with LC3-I (Sentelle *et al.*, 2012; Dany & Ogretmen, 2015). Based on these data, we decided to study the molecular mechanisms of Cer-LC3B interaction which leads to LC3B-II autophagosomes targeting to mitochondrial membranes. For this purpose, the binding of the soluble form of LC3B to ceramides with different fatty acid chain lengths (see **Figure 5.10**) was examined using the flotation assay, in which lipids maintain a certain bilayer curvature and could form domains.

We observed that LC3B-I did not interact with membranes containing ceramide (**Figure 5.11**). Thus while LC3 lipidation appears to be important for Cer18 interaction, it is not required for LC3B binding to CL (see Chapter 3). This may suggest that ceramide interaction involves the central hydrophobic domain of LC3, which has similarities to the CERT domain that binds C16- and C18-ceramides, while CL would bind the N-terminal domain, as predicted by docking analysis (Sentelle *et al.*, 2012; Chu *et al.*, 2013; Antón *et al.*, 2016). Moreover, LC3B-I binding was not detectable neither with Cer18 nor with Cer16 or Cer24:1 (**Figures 5.10 and 5.11**).

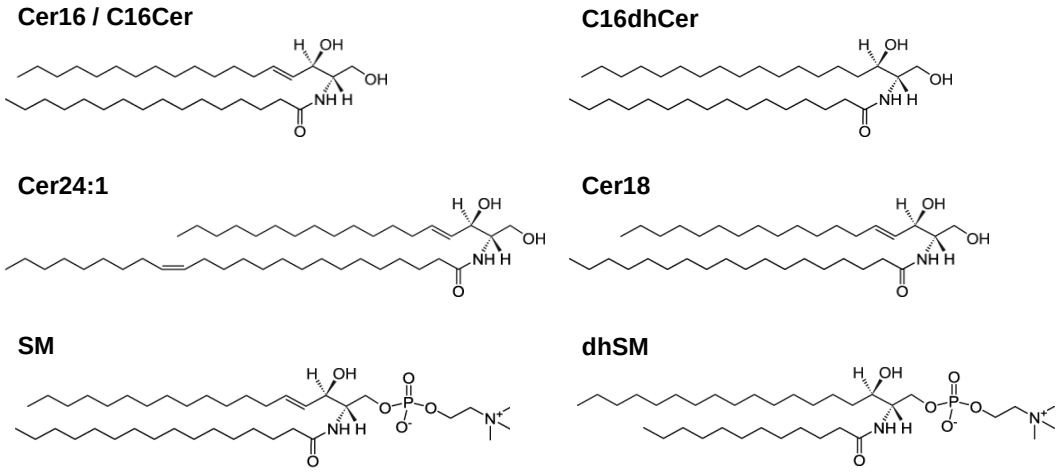

Figure 5.10. Structure of sphingolipid metabolites used in this thesis. Cer16 or C16Cer, N-palmitoyl-D-erythro-sphingosine; Cer18, N-octadecanoyl-D-erythro-sphingosine; Cer24:1, N-nervonoyl-D-erythro-sphingosine; C16dhCer, N-palmitoyl-D-erythro-sphinganine; SM, sphingomyelin from egg chicken (systematic name of predominant species, N-palmitoyl-D-sphingomyelin); dhSM, Dihydrosphingomyelin (representative structure of commercial C12dhSM, N-lauroyl-D-erythro-sphinganylphosphorylcholine). Note that dhSM used in this work was synthesized by G. Fabrias and was 86% C16dhSM. Images provided by Avanti Polar Lipids.

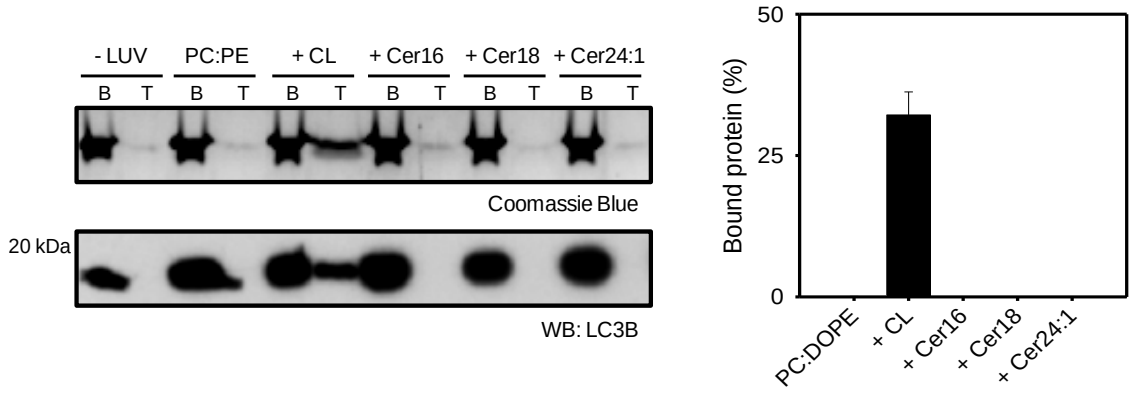

Figure 5.11. LC3B binding to ceramides of different fatty acid chain lengths. 10 µM LC3B was incubated with 3 mM LUVs composed of PC:DOPE (80:20 mol ratio), PC:DOPE:CL, PC:DOPE:Cer16, PC:DOPE:Cer18 or PC:DOPE:Cer24:1 (50:20:30 mol ratio). The liposome-bound protein fraction was analyzed after flotation in a sucrose density gradient by SDS-PAGE/immunoblot analysis and quantified by densitometric integration of the dots. Molecular mass is shown in kDa on the left-hand side. Data shown as mean ± SEM from at least 3 independent experiments.

5.4 Discussion

Velasco and coworkers described previously that cannabinoid action (specifically THC) induces autophagy-mediated cell death through stimulation of ER stress in human glioma cells (Salazar *et al.*, 2009). In agreement with the notion that autophagosomal membranes are derived, at least in part and under many cellular settings, from the ER (Juhasz & Neufeld, 2006; Axe *et al.*, 2008), and that the enzymes involved in the synthesis of ceramides are located in this organelle, they have also found that changes induced by THC in the ER sphingolipid composition are transmitted to the autophagosomes during the process that gives origin to the phagophore/omegasome, and, in turn, to the autolysosome (Hernández-Tiedra *et al.*, 2016).

To investigate the molecular mechanisms that determine the cytotoxic outcome of this autophagy activation, in collaboration with the above group, we constructed a model system for autophagy-mediated cancer cell death in which we compared the effect of different ratios of ceramide and dihydroceramide that are modified after THC administration. Our findings show that THC-triggered changes in the ER sphingolipid composition (especially the increase in dihydroceramide:ceramide ratio) play a crucial role in the stimulation of autophagy-mediated cancer cell death by THC. Specifically, data support the hypothesis that dihydroceramide-promoted destabilization of autolysosomes is based on their ability to (i) form dihydroceramide and dihydroceramide-rich regions that melt at temperatures well above those generated by ceramide, (ii) form rigid domains, and (iii) cause release of vesicular aqueous contents that is more extensive and faster than that induced by ceramide (Hernández-Tiedra *et al.*, 2016). However, the precise regulatory mechanisms by which binding of THC to cannabinoid receptors triggers these changes in the sphingolipid metabolism of cancer cells have not been clarified as yet.

In parallel ceramide has also been proposed to induce lethal mitophagy, anchoring LC3B-II-autophagosomes to mitochondrial membranes, leading to tumor suppression (Sentelle *et al.*, 2012; Dany & Ogretmen, 2015). Based on this observation we performed experiments in order to characterize the association of the autophagy protein LC3 with ceramide-containing membranes (Antón *et al.*, 2016).

5.4.1 Dihydroceramide Accumulation Leads to Autolysosome Destabilization during Lethal Autophagy

In this set of experiments we examined in more detail the observation that, in cannabinoid-induced autophagy and subsequent apoptosis, the proportion of dihydroceramides (lacking the 4-5 double bond of sphingosine) was considerably increased (Salazar *et al.*, 2009; Hernández-Tiedra *et al.*, 2016). Since apoptosis is accompanied by the release of proteins, specifically cathepsins, to the cytosol, it was tempting to test the capacity of dihydroceramides, as compared to that of ceramides, to increase membrane permeability. The above authors had observed a change in the ceramide/dihydroceramide ratio from 6:1 to 2:1 in the cannabinoid-induced autophagy-apoptosis. Thus a study was warranted comparing the membrane properties of ceramides and dihydroceramides, in particular their respective effects on membrane permeability (Hernández-Tiedra *et al.*, 2016).

Contents release assays described in this chapter show that, apart from ceramides, dihydroceramides also induce reorganization of the lipid bilayers, whatever the method used to insert them into the membrane (**Figures 5.5 to 5.8** and **Tables 5.1 to 5.6**). However there are significant differences in the kinetics and release rate, depending on the experimental procedures used. Therefore there are two main issues in this context: the mechanism of membrane restructuring and the concordance between different experimental methods.

When measuring release some methodological aspects must be taken into account. For example, dodecane/ethanol produces more efflux than DMSO probably for reasons related to the solubility of ceramides (**Figures 5.7 and 5.8**). But even in controls release is higher by using dodecane/ethanol as solvent. Moreover, the fact that ceramides generated by the action of sphingomyelinase results in a greater and more rapid release as compared with ceramides introduced in an organic solvent is also important (**Figures 5.5 and 5.6**). This, coupled with the large release observed at higher proportions of dihydroceramide suggests that the dihydroceramide enzymatic production is a localized process that occurs whenever a sphingomyelinase molecule binds to the membrane and goes along the lag phase (Ruiz-Argüello *et al.*, 2002). The rapid hydrolysis generates a dihydroceramide-rich microdomain and therefore an inter-domain interface through which the release occurs. In contrast addition of dihydroceramides in an organic solvent would result in a more regular distribution of the lipid in the bilayer and thus release would be a secondary process which would occur as a result of lateral segregation of dihydroceramides and domain formation.

An important mechanism that explains release is the lateral segregation of ceramide-rich domains in the membrane plane (Huang *et al.*, 1996). Ceramides have melting temperatures much higher than SM (80°C versus 40°C), so at 37°C, dihydroceramide-rich domains constitute rigid isolated islands in a fluid lipid sea (Goñi & Alonso, 2009). This fact has been corroborated in this work, both with calorimetric studies of ceramide and dihydroceramide mixtures and with GUV images in which dihydroceramide domains were observed with morphology similar to those formed by ceramide (**Figures 5.1 to 5.4**). It is known that the coexistence of gel and fluid domains is a condition that allows release to occur (Ruiz-Argüello *et al.*, 1996). Therefore, the appearance of interfaces between dihydroceramide-rich and -poor regions could be responsible for the observed release of vesicle contents. The fact that release induced by enzymatically-generated dihydroceramides is much faster supports the hypothesis that the lateral segregation of dihydroceramide-rich domains is one of the causes of release.

Local changes in the concentration of different species of sphingolipids (and specifically of ceramides) produce membrane permeabilization through the formation of rigid structures in biological membranes (Goñi *et al.*, 2014; Vieira et al., 2010). Data presented in this section show now that an increase in dihydroceramide proportion strongly enhances this effect. Moreover from the above results using model vesicles, the conclusion can be reached that a local increase in the dihydroceramide:ceramide ratio (similar to that induced by THC in the microsomal and autophagosome-enriched fraction of U87MG cells) leads to the formation of specific membrane domains and to increased permeability of biological membranes (Hernández-Tiedra *et al.*, 2016). Membrane restructuration produced by dihydroceramides could be explained taking into account their tendency to induce lateral segregation. From this point of view the release of vesicular solutes would not occur through well-structured channels but preferably through transient and irregular interfaces between dihydroceramide-rich and -poor domains or through local points of destabilization. It has been recently shown that manipulation of the activity of SMPD1 (acid lysosomal; a hydrolytic enzyme located primarily in the lysosomes) leads to LMP and stimulation of cancer cell death (Aits & Jäättelä, 2013; Petersen *et al.*, 2013), suggesting that changes in the sphingolipid composition of lysosomes can affect the stability of this organelle. Results obtained in collaboration with Velasco's group now show that autophagy is required for THC-induced LMP and support the idea that the fusion of dihydroceramide-enriched autophagosomes with lysosomes leads in turn to a local increase in the proportion of dihydroceramides in specific subdomains of autolysosomes and lysosomes, thereby

leading to membrane destabilization, LMP and the subsequent release of cathepsins into the cytoplasm of cancer cells.

5.4.2 LC3B-Ceramide Interaction for Mitochondrial Targeting during Lethal Mitophagy

It has been shown that the selective targeting of mitochondria by LC3B-II-containing phagophores occurs through direct interaction between ceramide and LC3B-II (Sentelle *et al.*, 2012; Dany & Ogretmen, 2015). The globular domain of LC3B was found to be structurally similar to the ceramide-binding domain of COL4A3BP44 (that can also bind C16dhCer) (Kumagai *et al.*, 2005). It is therefore tempting to speculate that, in addition to regulating membrane stability and the activity of the above-described ER stress-related signaling pathway, local changes in the content and subcellular distribution of C16dhCer or other dihydrosphingolipids might be able to modulate autophagy via selective binding to LC3B or other autophagy regulatory proteins.

Here using several compositionally defined *in vitro* reconstituted systems we show that the soluble form of LC3B does not interact with ceramide (**Figure 5.11**). These results are consistent with the molecular docking analyses of LC3 upon binding to Cer-containing membranes implicating LC3 N-terminal, opposite to where PE is conjugated, in the interaction of the protein with Cer (Sentelle *et al.*, 2012). Indeed, docking simulations indicate that conjugation of LC3-I to PE hides a low-affinity ceramide-binding sites allowing ceramide to bind selectively to the opposite end of the protein. Thus, as observed for CL (see Chapter 3), the C terminus of LC3 would be crosslinked to the autophagosome through the conserved glycine residue after protein binding to the outer mitochondrial membrane. Furthermore, we show that association of soluble LC3B with ceramides does not change with the ceramide fatty acid chain length (**Figures 5.10 and 5.11**). This is in agreement with the proposed importance of the mitochondrial localization of endogenous ceramides, and not their fatty acid chain length *per se*, to determine their distinct biological actions during mitophagy (Sentelle *et al.*, 2012).

As mentioned above, THC increases sphingolipid synthesis in the ER, eventually contributing to autophagy-mediated cancer cell death (Salazar *et al.*, 2009; Hernández-Tiedra *et al.*, 2016). It is worth noting that ceramides had been previously implicated in autophagy-associated cell death via induction of lethal mitophagy (Sentelle *et al.*, 2012; Dany & Ogretmen, 2015). THC-induced autophagy-mediated

LMP also leads to cell death via stimulation of the mitochondrial apoptotic pathway rather than necrotic cell death (Hernández-Tiedra *et al.*, 2016). However, a significant increase in mitophagy upon treatment with THC was not found indicating that this mechanism is not responsible for the stimulation of autophagy-mediated cell death in response to treatment with this cannabinoid. These findings are in agreement with previous results showing that autophagy is upstream of apoptosis in the mechanism of cannabinoid induced glioma cell death (Salazar *et al.*, 2009) and with the notion that LMP can activate apoptosis (Aits & Jäättelä, 2013; Boya *et al.*, 2003). Moreover, mitochondrial localization of endogenous ceramides and previous lipidation of LC3 have been suggested to be essential for LC3-ceramide association during mitophagy (Sentelle *et al.*, 2012), the latter being in agreement with our experimental data (Antón *et al.*, 2016). In the previous chapter we have also shown that THC induces potent bulk autophagy but no mitochondria were targeted to degradation in U87MG cells (Antón *et al.*, 2016). THC-induced, autophagy-mediated cell death is mediated by ceramide accumulation which stimulates the ER stress-related signaling route (Salazar *et al.*, 2009; Hernández-Tiedra *et al.*, 2016). However, during bulk THC-promoted autophagy, direct LC3 interaction with ceramide has not yet been described.

In summary, findings described in this chapter support the concept that the stimulation of autophagy-mediated cancer cell death by THC relies on a modification of the sphingolipid composition of the endoplasmic reticulum of glioma cells that is transmitted to autophagosomes and autolysosomes thereby leading to lysosomal membrane permeabilization, cathepsin release and the subsequent activation of apoptotic cell death (Hernández-Tiedra *et al.*, 2016) (**Figure 5.9**). Moreover, we have described novel molecular mechanisms underlying human LC3B interaction with ceramide that regulate lethal mitophagy, leading to tumor suppression (Antón *et al.*, 2016). We consider that these observations further support the biological relevance of sphingolipid metabolites in the regulation of autophagy and emphasize the potential therapeutic implications of modulating the levels of dihydrosphingolipids such as dihydroceramides for the treatment of cancer. Furthermore, defining the molecular details of sphingolipid-protein binding such as the putative ceramide-LC3B-II complex, will help to understand the mechanisms by which ceramide regulates lethal versus survival autophagy.

Chapter 6

Overview and Conclusions

CHAPTER 6:

Overview and Conclusions

Overview

Autophagy is the main lysosomal pathway for degradation of bulk or selected cytoplasmic material and organelles in mammalian cells (Mizushima & Komatsu, 2015; Mochida *et al.*, 2015). The key roles for autophagy in a wide range of physiological processes (Boya *et al.*, 2013), including the provision of nutrients and biosynthetic precursors (Green & Levine, 2014; Marino *et al.*, 2014), is reflected in the increasing number of disorders linked to a lack or inhibition of autophagy, e.g. neurodegenerative diseases (Nixon, 2013; Aufschnaiter *et al.*, 2016). Furthermore, this process is not only associated with cell survival but also cell death (Galluzzi *et al.*, 2015), as in autophagy-mediated cancer cell death (Salazar *et al.*, 2009; Velasco *et al.*, 2012).

Autophagy involves the formation of a double-membrane structure, named isolation membrane or phagophore, upon which adhesion and fusion of further membrane structures and sequential recruitment of regulatory proteins would occur to form an organelle called autophagosome (Shibutani & Yoshimori, 2014). The autophagosome then fuses with lysosomes for content degradation and recycling (Klionsky *et al.*, 2012; Shen & Mizushima, 2014). Human LC3/GABARAP family proteins are processed to conjugate with PS or PE in the autophagosomal membrane (Kabeya *et al.*, 2000; Tanida *et al.*, 2002), and are essential for the autophagosome formation and cargo recognition (Shpilka *et al.*, 2011; Ktistakis & Tooze, 2016). Despite the high structural similarities, LC3/GABARAP family members differ in autophagosome conjugation (stress-induced regulation, dependent on vesicle curvature), binding partners, expression (via differential transcriptional regulation), and

post-translational regulation, making them unique in function (Landajuela *et al.*, 2016; Alemu *et al.*, 2012; Schaaf *et al.*, 2016).

Mitophagy is a selective autophagy pathway in which cells turn over mitochondria for quality control and adjustment to changing metabolic requirements (Hamacher-Brady & Brady, 2016; Randow & Youle, 2014). Impaired mitophagy causes accumulation of damaged mitochondria and protein aggregates, and excessive exposure to ROS, leading to a wide range of pathological conditions including neurodegeneration, e.g. Parkinson disease (Aufschnaiter *et al.*, 2016; Vidal *et al.*, 2014), cancer (Lu *et al.*, 2013) and myopathies (Kubli & Gustafsson, 2012). LC3/GABARAP family proteins play an essential role in the recognition and engulfment of damaged mitochondria through interaction with adaptor proteins or specific lipids (Hsu *et al.*, 2015; Maguire *et al.*, 2016). The latter include cardiolipin and ceramide, which act as cargo receptors for LC3B in the mitochondrial membrane leading to targeted removal of damaged mitochondria (Chu *et al.*, 2014; Dany & Ogretmen, 2015).

However, much remains to be elucidated regarding the extent of involvement and specific regulatory mechanisms of certain lipids in LC3/GABARAP proteins recruitment to damaged mitochondria during mitophagy and autophagy-mediated cell death. For this reason the main aim of this thesis has been to shed light on the molecular basis and relevance of specific lipids as cargo receptors and their effect on membrane properties for the mitochondrial recruitment of individual LC3/GABARAP family members during mitophagy and lethal autophagy pathways. To this aim quantitative biophysical approaches using model vesicles, and cell biology techniques have been applied to (i) study the physical interaction of the various human Atg8 orthologs with cardiolipin and to determine the structural and functional consequences of such interactions at the membrane level, (ii) to gain further insight into the role of this interaction as a regulatory mechanism for the mitochondrial recruitment of individual LC3/GABARAP proteins during rotenone-induced mitophagy, and (iii) to model the behavior of ceramides in THC-induced autophagic cancer cell death and to characterize the LC3B-ceramide interaction during mitophagy-mediated tumor suppression.

Mitochondrial Recruitment of LC3/GABARAP Family Proteins upon CL Externalization to the OMM is Stress-Specific and Cell Type-dependent

The expansion of the Atg8 protein family in higher eukaryotes facilitates differential functions and cargo handling during nonselective and selective autophagy (Stolz *et al.*, 2014; Schaaf *et al.*, 2016). Structural studies have highlighted the importance of specific features within LC3/GABARAP family members to determine preferential binding of certain interacting partners or receptor proteins (Alemu *et al.*, 2012; Joachim *et al.*, 2015). In the selective elimination of mitochondria by mitophagy several protein regulators act as specific receptors recruiting Atg8 orthologs to the mitochondria and priming mitochondria for degradation. Upon mitochondrial membrane depolarization, an alternative pathway can also be activated in which PINK1 specifically recruits PARK2 to the damaged mitochondrion (Lazarou *et al.*, 2015). In addition, some studies have described certain lipids as cargo receptors during selective mitochondrial autophagy (Chu *et al.*, 2013; Sentelle *et al.*, 2012). Among them, the electron transport chain complex I inhibitor, rotenone, is shown to induce cardiolipin externalization to the OMM that acts as a signal for LC3, giving rise to the selection and removal of damaged mitochondria (Chu *et al.*, 2013). In contrast to the strong depolarizing agents such as the uncoupler CCCP (Kondapalli *et al.*, 2012), rotenone does not distinctly perturb the mitochondrial membrane potential and is independent of PINK1/PARK2-mediated mitophagy (Chu *et al.*, 2013).

The quantitative data on LC3B-CL interaction presented in this thesis show that LC3B interacts preferentially with CL over other di-anionic lipids and that LC3B-CL interaction relies on both electrostatic forces (**Figures 3.5 to 3.12, and 3.14**) and CL-specific changes in membrane properties. For instance, the high degree of unsaturation of CL contributes to a high degree of flexibility within the membrane that may also facilitate LC3B association and insertion (**Figure 3.8F**). Additionally, some residues within basic patches at LC3B surface are found to be essential for the interaction (**Figure 3.16**), modulating the binding capacity of the protein (**Figure 3.10**). Site-specific NBD labeling coupled to NBD fluorescence spectroscopic analysis support a model in which the LC3B N- and C-terminal regions would bind mitochondria and autophagosomal membranes respectively (**Figure 3.9**) (Chu *et al.*, 2013; Antón *et al.,* 2016). Moreover, LC3B interaction with CL-containing membranes would be facilitated in an acidic environment (**Figure 3.8D**) as a result of (i) inhibition of ATP synthase in damaged mitochondria which would cause a local cytosolic pH decrease, (ii) mitophagy induction during lactic acid fermentation, (iii) LC3 charge becoming more positive, or (iv) generation of CL-enriched microdomains (Lemmin *et al.*, 2013; Khalifat *et al.*,

2011). In addition, LC3B preferentially binds CL-containing smaller and more curved vesicles (**Figures 3.8E and 3.13B**) as a possible regulatory mechanism to recognize more efficiently smaller mitochondrial fragments, which would have been converted into pieces of manageable size for their engulfment by autophagosomes (Twig *et al.*, 2008).

Consistent with the above results, rotenone-induced CL translocation to the OMM (Chu *et al.*, 2013), but not other bulk autophagy-inducing signals, such as THC or AZD8055 treatments or nutrient starvation conditions, promotes LC3B translocation to mitochondria and its subsequent delivery to lysosomes in human U87MG glioma cells, RPE1 cells, and iPSC-derived cortical neurons (**Figures 4.1, 4.3, 4.4, 4.16 and 4.17)**. Ultrastructural analysis of rotenone-treated RPE1 cells stably expressing fluorescently-tagged LC3B by CLEM revealed mitochondria surrounded by large autophagosomal structures indicating the targeting and engulfment of mitochondria, and fusion events between autophagosomes (**Figures 4.11 and 4.13**). EM tomography and/or fluorescently labeled CL could be used to further investigate the ultrastructure of mitochondrial membrane remodeling after binding of LC3 and the possibility to be localized to CL microdomains. Co-treatment of RPE1 cells with rotenone and the lysosomal protease inhibitor leupeptin leads to formation of a large number of LC3B-labeled lysosomal structures (**Figures 4.14 and 4.15**). However, ATG5-positive assembly sites or isolation membranes are not located to mitochondria upon mitophagy induction in human RPE1 cells (**Figures 4.6 and 4.9**). These data, together with the described interaction of the soluble form of LC3B with CL-enriched vesicles (**Figures 3.5 to 3.12**), suggest that previous LC3B lipidation may not be required for its mitochondrial recruitment after CL translocation to the OMM. Intracellular location of other stage-specific fluorescently-tagged autophagosome markers would clarify the possible sequential recruitment of autophagy factors to mitochondria and whether LC3 recruitment occurs before or after autophagosome formation. In addition, further experiments in ATG5-null cells rescued with wild-type ATG5, with ATG5 mutants that cannot be conjugated to ATG12 and fail to make autophagosomes, with mutant forms of ATG4 to prevent LC3 lipidation/delipidation, or in cells treated with ATG7 siRNA, which is required for the conjugation of LC3 to PE, could confirm this hypothesis. LC3B cytoplasmic localization in cells with diminished levels or mutant forms of those essential autophagosome biogenesis factors would indicate a key role for LC3 lipidation in rotenone-induced mitophagy.

LC3/GABARAP family proteins not only have different specificities guiding the selective recruitment of different LIR-containing proteins (Weidberg *et al.*, 2010) but

they also differ in their lipid-binding affinities. Indeed, in contrast to LC3B and GABARAP, GABARAPL2 hardly binds CL-containing membranes (**Figures 3.10 to 3.16**). Furthermore, not all cell-types appear to conform to the same mechanism for the specific removal of mitochondria. In fact, in U87MG glioma cells, unlike the situation found with LC3B (**Figure 4.1**), neither GABARAP nor GABARAPL2 localize to mitochondria upon rotenone treatment (**Figure 4.2**). Additionally, in RPE1 cells rotenone exposure causes a weak autophagic cell response but elicits the mitochondrial recruitment of both LC3B and GABARAPL1 (**Figures 4.3 to 4.7**); however iPSC-derived human cortical neurons treated with rotenone resulted in LC3B, but not GABARAPL1 puncta location to mitochondria (**Figure 4.17**). Whether GABARAPL1 is directly involved in mitophagy or influences mitophagy through modulation of general autophagy activity needs to be further investigated. Moreover, given that only LC3B showed a biological correlation to the observed *in vitro* binding by translocation to mitochondria, it would be particularly informative to compare interaction of LC3A, B and C isoforms with CL and the subsequent mitochondrial targeting.

Ceramide in Autophagy and Mitophagy-mediated Cancer Cell Death: Novel Functions of Sphingolipids in the ER and Mitochondria

Different sphingolipids, and specifically ceramides, dihydroceramides and sphingosine 1-phosphate, have been proposed to regulate autophagy in cancer cells primarily by acting as upstream triggers of the signaling pathways that regulate this cellular process (Jiang & Ogretmen, 2013; Li *et al.*, 2014). Velasco and coworkers have found that the cannabinoid THC induces changes in the ER sphingolipid composition that are transmitted to the autolysosomes and elicit an ER stress-related pathway, finally leading to autophagy-mediated cell death in human glioma cells (Salazar *et al.*, 2009; Salazar *et al.*, 2013). In this thesis a model system for the autophagy-mediated cell death has been constructed to investigate the molecular events of the cytotoxic outcome of this autophagy pathway. On the basis of observations that during this cannabinoid-induced lethal autophagy dihydroceramide proportion was considerably increased, and was accompanied by the release of cathepsins (Salazar *et al.*, 2009), it was tempting to test the capacity of dihydroceramides, as compared to that of ceramides, to increase membrane permeability.

Contents release assays show that both externally added and *de novo* synthesized ceramides and dyhidroceramides induce lipid bilayer reorganization

(**Figures 5.5 to 5.8** and **Tables 5.1 to 5.6**). However, *in situ* generated ceramides lead to a more rapid and greater release of vesicular aqueous contents as compared to ceramides added in an organic solvent, dihydroceramide-promoted release being larger and faster than that induced by ceramides (**Figures 5.5 to 5.8**). These data suggest that dihydroceramide generated by sphingomyelinase action forms dihydroceramide-rich microdomains and therefore inter-domain interfaces through which the release occurs. In contrast previous lateral segregation of dihydroceramides and domain formation is necessary when adding them in an organic solvent due to the more regular distribution in the lipid bilayer, release being a secondary process (Goñi *et al.*, 2014). Moreover, calorimetric studies and confocal microscopy of model vesicles containing ceramide and dihydroceramide mixtures indicate the formation of dihydroceramide-rich regions that melt at temperatures well above those of ceramide, and the generation of rigid membrane domains by dihydroceramide with morphology similar to those formed by ceramide (**Figures 5.1 to 5.4**). These data, together with studies from Velasco and coworkers, support the notion that during THC-induced autophagy-mediated cancer cell death, alteration of the balance between different molecular species of ceramides and dihydroceramides in the microsomal fraction of cancer cells leads to the generation of specific subdomains and permeabilization of autolysosomal membranes, the latter event playing a crucial role in the subsequent release of cathepsins into the cytoplasm of cancer cells and determining the cell death-promoting fate of autophagy stimulation by cannabinoids (**Figure 5.9**; Hernández-Tiedra *et al.*, 2016). However, the precise regulatory mechanisms by which binding of THC to cannabinoid receptors triggers these changes in the sphingolipid metabolism of cancer cells have not been clarified as yet. Moreover, the experimental approach used in this study shows dihydroceramide-mediated release of low molecular weight molecules. Hence to test the starting hypothesis – i.e. that local increase in the proportion of ER dihydroceramides is the main cause of cathepsin release by autolysosomes after treatment of glioblastoma cells with THC – leakage assays could be performed with fluorescein-labeled dextrans, having a molecular weight similar to that of some cathepsins.

Ceramides had been previously implicated in tumor suppression via autophagy-associated cell death acting as a selective cargo receptor for the autophagosome-bound LC3B in the mitochondria and leading to lethal mitophagy (Sentelle *et al.*, 2012; Dany & Ogretmen, 2015). Therefore, in addition to the local changes in dihydrosphingolipid content and subcellular distribution regulating membrane stability in the above-described ER stress-related signaling pathway, this would be another novel mechanism for ceramide-mediated modulation of autophagy in cancer cells. Previous

molecular docking analyses of this protein-lipid interaction implicate the protein N terminus opposite to where PE is conjugated in the autophagosomal membrane (Sentelle *et al.*, 2012). Furthermore, previous LC3 lipidation and mitochondrial localization of endogenous ceramides, but not their fatty acid chain length *per se*, would be determinant for this distinct biological action during mitophagy (Sentelle *et al.*, 2012). In agreement with this the soluble form of LC3B does not interact with ceramides, and fatty acid chain lengths do not have an effect on the protein association to ceramide-containing membranes (**Figures 5.10 and 5.11**). These results, together with data presented in this thesis for LC3B-CL interaction, indicate that after protein recruitment to mitochondria by these lipid receptors during mitophagy, the C terminus would be conjugated to the autophagosome (Antón *et al.*, 2016).

In the THC-induced lethal autophagy described above, glioma cell death is also mediated by the mitochondria apoptotic pathway (Hernández-Tiedra *et al.*, 2016). Nevertheless, THC induces potent bulk autophagy but no mitochondria are found to be targeted to degradation in U87MG glioma cells (**Figure 4.1**). Hence this mechanism is not responsible for the stimulation of autophagy-mediated cell death in response to treatment with this cannabinoid. Moreover, in the THC-induced ER stress-related signaling route dihydroceramide might not act on the membrane in its free form but by forming complexes with certain proteins. However, during this bulk autophagy process, direct protein association with ceramides (e.g. LC3 or other autophagy regulatory proteins) has not been described yet. These observations would contribute to further understand the biological relevance and specific molecular mechanisms by which specific sphingolipid metabolites and autophagy regulatory proteins regulate lethal and survival autophagy. Moreover, these findings support the idea that the pharmacological manipulation of the sphingolipid content (and specifically of the levels of certain species of ceramides and dihydroceramides) may be exploited therapeutically to promote the activation of autophagy and tumor growth inhibition. In any case, further research should clarify whether similar differences in the organelle sphingolipid composition might play a role in determining the final outcome of the autophagic process stimulation in response to other stimuli.

In summary the findings in this thesis provide new insights on the molecular mechanisms underlying the recruitment of LC3/GABARAP family proteins to mitochondria during mitophagy and the specific roles of human Atg8 orthologs in different human cell lines. Cardiolipin function as a receptor for selection of damaged mitochondria is clearly modulated by factors including ionic strength, bilayer fluidity and membrane curvature. This lipid-protein electrostatic interaction would be specific for

mitophagy and would not occur in protective nonselective autophagy or THC-induced lethal autophagy. The data also imply that the individual human Atg8 orthologs respond differently to the presence of CL in model membranes, in accordance with the differences observed in their electrostatic surface potential. Moreover, specific LC3/GABARAP protein family members are recruited to mitochondria in a cell-type dependent manner that could also be stress specific (Antón *et al.*, 2016; Antón *et al.*, in preparation). Finally, findings described in this thesis support the concept that the stimulation of autophagy-mediated cancer cell death by THC relies on dihydroceramide accumulation in the ER that leads to autolysosome membrane permeabilization and subsequent activation of apoptotic cell death (Hernández-Tiedra *et al.*, 2016). Moreover, lipidation of LC3B modulates the ceramide-binding capacity of the protein in the mitochondrial membrane (Antón *et al.*, 2016), regulating lethal mitophagy and tumor suppression.

Conclusions

1) LC3B interaction with cardiolipin is modulated by particular membrane properties including ionic strength, bilayer fluidity and membrane curvature that could allow the specific recognition of impaired mitochondria. Structural differences in the various LC3/GABARAP family proteins lead to a specific response to the presence of CL in model membranes.

2) CL functions as a cargo receptor in a mechanism specific for mitophagy that may not occur in protective nonselective autophagy or THC-induced lethal autophagy. Individual LC3/GABARAP family members are recruited to mitochondria depending on the human cell type and on metabolic or stress conditions. ATG5-positive assembly sites are not localized to mitochondria during rotenone-induced mitophagy in RPE1 cells.

3) Ceramides play a crucial role in autophagy-mediated cancer cell death: (i) dihydroceramide behaviour and properties in membranes are very similar to those of ceramide, except that the dihydro derivatives are more active in permeabilizing the lipid bilayers. Dihydroceramide accumulation leads to autolysosome destabilization during lethal autophagy. (ii) Previous lipidation of the autophagy protein LC3B is essential for its interaction with ceramide in the mitochondrial membrane, modulating the binding capacity of the protein during lethal mitophagy.

References

References

Abramzon, Y., Johnson, J. O., Scholz, S. W., Taylor, J. P., Brunetti, M., Calvo, A., … Traynor, B. J. (2012). Valosin-containing protein (VCP) mutations in sporadic amyotrophic lateral sclerosis. *Neurobiol Aging*, *33*, 2231.e1–2231.e6.

Acehan, D., Khuchua, Z., Houtkooper, R. H., Malhotra, A., Kaufman, J., Vaz, F. M., … Schlame, M. (2009). Distinct effects of tafazzin deletion in differentiated and undifferentiated mitochondria. *Mitochondrion*, *9*, 86–95.

Aerbajinai, W., Giattina, M., Lee, Y. T., Raffeld, M., & Miller, J. L. (2003). The proapoptotic factor Nix is coexpressed with Bcl-xL during terminal erythroid differentiation. *Blood*, *102*, 712–717.

Aisenbrey, C., Michalek, M., Salnikov, E. S., & Bechinger, B. (2013). Solid-state NMR approaches to study protein structure and protein–lipid interactions. *Methods Mol Biol*, *974*, 357–387.

Aits, S., & Jäättelä, M. (2013). Lysosomal cell death at a glance. *J Cell Sci*, *126*, 1905–12.

Alemu, E. A., Lamark, T., Torgersen, K. M., Birgisdottir, A. B., Larsen, K. B., Jain, A., … Johansen, T. (2012). ATG8 family proteins act as scaffolds for assembly of the ULK complex: Sequence requirements for LC3-interacting region (LIR) motifs. *J Biol Chem*, *287*, 39275–39290.

Allen, T. M., & Cullis, P. R. (2013). Liposomal drug delivery systems: from concept to clinical applications. *Adv Drug Deliv Rev*, *65*, 36–48.

Angelova, M. I., & Dimitrov, D. S. (1986). Liposome electroformation. *Faraday Discuss Chem Soc*, *81*, 303–311.

Angelova, M. I., & Tsoneva, I. (1999). Interactions of DNA with giant liposomes. *Chem Phys Lipids*, *101*, 123–137.

Angelova, M., Soleau, S., Meleard, P., Faucon, F., & Bothorel, P. (1992). Preparation of giant vesicles by external AC electric fields. Kinetics and applications. *Trends Coll Interf Sci VI*, 127–131.

Antón, Z., Landajuela, A., Hervás, J. H., Montes, L. R., Hernández-Tiedra, S., Velasco, G., … Alonso, A. (2016). Human Atg8-cardiolipin interactions in mitophagy: Specific properties of LC3B, GABARAPL2 and GABARAP. *Autophagy*, *12*, 2386–2403.

Antonny, B. (2011). Mechanisms of membrane curvature sensing. *Annu Rev Biochem*, *80*, 101–123.

Ardail, D., Privat, J. P., Egret-Charlier, M., Levrat, C., Lerme, F., Louisot, P., & Biolow, M. (1990). Mitochondrial contact sites. Lipid composition and dynamics. *J Biol Chem*, *265*, 18797–18802.

Armstrong, J. L., Hill, D. S., McKee, C. S., Hernandez-Tiedra, S., Lorente, M., Lopez-Valero, I., … Lovat, P. E. (2015). Exploiting cannabinoid-induced cytotoxic autophagy to drive melanoma cell death. *J Invest Dermatol*,*135*, 1629–1637.

Asanuma, K., Tanida, I., Shirato, I., Ueno, T., Takahara, H., Nishitani, T., … Tomino, Y. (2003). MAP-LC3, a promising autophagosomal marker, is processed during the differentiation and recovery of podocytes from PAN nephrosis. *FASEB J*, *17*, 1165–1167.

Ashrafi, G., Schlehe, J. S., LaVoie, M. J., & Schwarz, T. L. (2014). Mitophagy of damaged mitochondria occurs locally in distal neuronal axons and requires PINK1 and Parkin. *J Cell Biol*, *206*, 655–670.

Ashrafi, G., & Schwarz, T. L. (2013). The pathways of mitophagy for quality control and clearance of mitochondria. *Cell Death Differ*, *20*, 31–42.

Aufschnaiter, A., Kohler, V., Diessl, J., Peselj, C., Carmona-Gutierrez, D., Keller, W., & Büttner, S. (2016). Mitochondrial lipids in neurodegeneration. *Cell Tissue Res*. http://dx.doi.org/10.1007/s00441-016-2463-1

Axe, E. L., Walker, S. A., Manifava, M., Chandra, P., Roderick, H. L., Habermann, A., … Ktistakis, N. T. (2008). Autophagosome formation from membrane compartments enriched in phosphatidylinositol 3-phosphate and dynamically connected to the endoplasmic reticulum. *J Cell Biol, 182*, 685–701.

Azad, M. B., Chen, Y., Henson, E. S., Cizeau, J., McMillan-Ward, E., Israels, S. J., & Gibson, S. B. (2008). Hypoxia induces autophagic cell death in apoptosis-competent cells through a mechanism involving BNIP3. *Autophagy*, *4*, 195–204.

Baehrecke, E. H. (2003). Autophagic programmed cell death in Drosophila. *Cell Death Differ*, *10*, 940–945.

Bagatolli, L. A. (2003). Thermotropic behavior of lipid mixtures studied at the level of single vesicles: giant unilamellar vesicles and two-photon excitation fluorescence microscopy. *Methods Enzymol*, *367*, 233–53.

Baile, M. G., Whited, K., & Claypool, S. M. (2013). Deacylation on the matrix side of the mitochondrial inner membrane regulates cardiolipin remodeling. *Mol Biol Cell*, *24*, 2008–2020.

Bakás, L., Ostolaza, H., Vaz, W. L., & Goñi, F. M. (1996). Reversible adsorption and nonreversible insertion of Escherichia coli alpha-hemolysin into lipid bilayers. *Biophys J*, *71*, 1869–76.

Bangham, A. D., & Horne, R. W. (1964). Negative staining of phospholipids and their

structural modification by surface-active agents as observed in the electron microscope. *J Mol Biol, 8*, 660–668.

Barde, I., Rauwel, B., Marin-florez, R. M., Corsinotti, A., Verp, S., Offner, S., … Kapopoulou, A. (2013). A KRAB / KAP1-miRNA cascade regulates erythropoiesis through stage-specific control of mitophagy. *Science*, *340*, 350–353.

Bartke, N., & Hannun, Y. A. (2009). Bioactive sphingolipids: metabolism and function. *J Lipid Res*, *50*, S91-6.

Bartlett, G. R. (1959). Phosphorus Assay in Column Chromatography. *J Biol Chem*, *234*, 466–468.

Becker, D., Richter, J., Tocilescu, M. A., Przedborski, S., & Voos, W. (2012). Pink1 kinase and its membrane potential (Δψ)-dependent cleavage product both localize to outer mitochondrial membrane by unique targeting mode. *J Biol Chem*, *287*, 22969–22987.

Behrends, C., Sowa, M. E., Gygi, S. P., & Harper, J. W. (2010). Network organization of the human autophagy system. *Nature*, *466*, 68–76.

Bejarano, E., & Cuervo, A. M. (2010). Chaperone-mediated autophagy. *Proc Am Thorac Soc*, *7*, 29–39.

Berg, J. M., Tymoczko, J. L., & Stryer, L. (2002). Biochemistry. W H Freeman.

Bergamini, E., Cavallini, G., Donati, A., & Gori, Z. (2003). The anti-ageing effects of caloric restriction may involve stimulation of macroautophagy and lysosomal degradation, and can be intensified pharmacologically. *Biomed Pharmacother*, *57*, 203–8.

Betarbet, R., Sherer, T. B., Mackenzie, G., Garcia-osuna, M., Panov, A. V, & Greenamyre, J. T. (2000). Chronic systemic pesticide exposure reproduces features of Parkinson's disease. *Nat Neurosci*, *3*, 1301–1306.

Betin, V. M. S., & Lane, J. D. (2009). Caspase cleavage of Atg4D stimulates GABARAP-L1 processing and triggers mitochondrial targeting and apoptosis. *J Cell Sci*, *122*, 2554–66.

Betin, V. M. S., MacVicar, T. D. B., Parsons, S. F., Anstee, D. J., & Lane, J. D. (2012). A cryptic mitochondrial targeting motif in Atg4D links caspase cleavage with mitochondrial import and oxidative stress. *Autophagy*, *8*, 664–676.

Bhatia-Kiššova, I., & Camougrand, N. (2010). Mitophagy in yeast: Actors and physiological roles. *FEMS Yeast Res, 10,* 1023–34.

Birbes, H., El Bawab, S., Hannun, Y. A., & Obeid, L. M. (2001). Selective hydrolysis of a mitochondrial pool of sphingomyelin induces apoptosis. *FASEB J, 15*, 2669–79.

Bjørkøy, G., Lamark, T., Brech, A., Outzen, H., Perander, M., Øvervatn, A., … Johansen, T. (2005). p62/SQSTM1 forms protein aggregates degraded by

autophagy and has a protective effect on huntingtin-induced cell death. *J Cell Biol*, *171*, 603–614.

Böttcher, C. J. F., Van gent, C. M., & Pries, C. (1961). A rapid and sensitive sub-micro phosphorus determination. *Anal Chim Acta*, *24*, 203–204.

Boya, P., Andreau, K., Poncet, D., Zamzami, N., Perfettini, J. L., Metivier, D., … Kroemer, G. (2003). Lysosomal membrane permeabilization induces cell death in a mitochondrion-dependent fashion. *J Exp Med*, *197*, 1323–1334.

Boya, P., González-Polo, R.-A., Casares, N., Perfettini, J.-L., Dessen, P., Larochette, N., … Kroemer, G. (2005). Inhibition of macroautophagy triggers apoptosis. *Mol Cell Biol*, *25*, 1025–40.

Boya, P., & Kroemer, G. (2008). Lysosomal membrane permeabilization in cell death. *Oncogene*, *27*, 6434–6451.

Boya, P., Reggiori, F., & Codogno, P. (2013). Emerging regulation and functions of autophagy. *Nat Cell Biol*, *15*, 713–20.

Boyer-Guittaut, M., Poillet, L., Liang, Q., Bôle-Richard, E., Ouyang, X., Benavides, G. A., … Zhang, J. (2014). The role of GABARAPL1/GEC1 in autophagic flux and mitochondrial quality control in MDA-MB-436 breast cancer cells. *Autophagy*, *10*, 986–1003.

Bustillo-Zabalbeitia, I., Montessuit, S., Raemy, E., Basañez, G., Terrones, O., & Martinou, J. C. (2014). Specific interaction with cardiolipin triggers functional activation of dynamin-related protein 1. *PLoS One*, *9*, e102738.

Cao, J., Liu, Y., Lockwood, J., Burn, P., & Shi, Y. (2004). A novel cardiolipin-remodeling pathway revealed by a gene encoding an endoplasmic reticulum-associated acyl-CoA:lysocardiolipin acyltransferase (ALCAT1) in mouse. *J Biol Chem*, *279*, 31727–31734.

Cárdenas, C., Miller, R. A., Smith, I., Bui, T., Molgó, J., Müller, M., … Foskett, J. K. (2010). Essential Regulation of Cell Bioenergetics by Constitutive InsP3 Receptor Ca^{2+} Transfer to Mitochondria. *Cell*, *142*, 270–283.

Carquin, M., D'Auria, L., Pollet, H., Bongarzone, E. R., & Tyteca, D. (2016). Recent progress on lipid lateral heterogeneity in plasma membranes: From rafts to submicrometric domains. *Prog Lipid Res*, *62*, 1–24.

Carracedo, A., Gironella, M., Lorente, M., Garcia, S., Guzman, M., Velasco, G., & Iovanna, J. L. (2006a). Cannabinoids induce apoptosis of pancreatic tumor cells via endoplasmic reticulum stress-related genes. *Cancer Res*, *66*, 6748–6755.

Carracedo, A., Lorente, M., Egia, A., Blázquez, C., García, S., Giroux, V., … Velasco, G. (2006b). The stress-regulated protein p8 mediates cannabinoid-induced apoptosis of tumor cells. *Cancer Cell*, *9*, 301–312.

Cecconi, F., & Levine, B. (2008). The role of autophagy in mammalian development: cell makeover rather than cell death. *Dev Cell*, *15*, 344–357.

Chambers, S. M., Fasano, C. A., Papapetrou, E. P., Tomishima, M., Sadelain, M., & Studer, L. (2009). Highly efficient neural conversion of human ES and iPS cells by dual inhibition of SMAD signaling. *Nat Biotechnol*, *27*, 275–280.

Chambers, S. M., Qi, Y., Mica, Y., Lee, G., Zhang, X., Niu, L., … Studer, L. (2012). Combined small-molecule inhibition accelerates developmental timing and converts human pluripotent stem cells into nociceptors. *Nature Biotechnol*, *30*, 715–720.

Chan, D. C. (2006). Mitochondria: dynamic organelles in disease, aging, and development. *Cell*, *125*, 1241–52.

Chan, L. L. Y., Shen, D., Wilkinson, A. R., Patton, W., Lai, N., Chan, E., … Qiu, J. (2012). A novel image-based cytometry method for autophagy detection in living cells. *Autophagy*, *8*, 1371–1382.

Chen, C., Li, J. G., Chen, Y., Huang, P., Wang, Y., & Liu-Chen, L. Y. (2006). GEC1 interacts with the kappa opioid receptor and enhances expression of the receptor. *J Biol Chem*, *281*, 7983–7993.

Chen, C., Wang, Y., Huang, P., & Liu-Chen, L. Y. (2011). Effects of C-terminal modifications of GEC1 and GABARAP, two microtubules-associated proteins, on kappa opioid receptor expression. *The Journal of Biological Chemistry*, *8*, 1–21.

Chen, H., Vermulst, M., Wang, Y. E., Chomyn, A., Prolla, T. A., McCaffery, J. M., & Chan, D. C. (2010). Mitochondrial fusion is required for mtdna stability in skeletal muscle and tolerance of mtDNA mutations. *Cell*, *141*, 280–289.

Chen, J. J., & Yu, B. P. (1994). Alterations in mitochondrial membrane fluidity by lipid peroxidation products. *Free Radic Biol Med, 17*, 411–8.

Chen, Y., McMillan-Ward, E., Kong, J., Israels, S. J., & Gibson, S. B. (2007). Mitochondrial electron-transport-chain inhibitors of complexes I and II induce autophagic cell death mediated by reactive oxygen species. *J Cell Sci*, *120*, 4155–4166.

Chen, Y., McMillan-Ward, E., Kong, J., Israels, S. J., & Gibson, S. B. (2008). Oxidative stress induces autophagic cell death independent of apoptosis in transformed and cancer cells. *Cell Death Differ, 15*, 171–182.

Chen, Z. W., Chang, C. S. S., Leil, T. A., & Olsen, R. W. (2007). C-terminal modification is required for GABARAP-mediated GABA(A) receptor trafficking. *J Neurosci*, *27*, 6655–6663.

Cheong, H., Lindsten, T., Wu, J., Lu, C., & Thompson, C. B. (2011). Ammonia-induced autophagy is independent of ULK1/ULK2 kinases. *Proc Natl Acad Sci U S A*,

27108, 11121–11126.

Cherra, S. J., Kulich, S. M., Uechi, G., Balasubramani, M., Mountzouris, J., Day, B. W., & Chu, C. T. (2010). Regulation of the autophagy protein LC3 by phosphorylation. *J Cell Biol, 190*, 533–539.

Cherra, S. J., Steer, E., Gusdon, A. M., Kiselyov, K., & Chu, C. T. (2013). Mutant LRRK2 elicits calcium imbalance and depletion of dendritic mitochondria in neurons. *Am J Pathol*, *182*, 474–484.

Chew, L. H., & Yip, C. K. (2014). Structural biology of the macroautophagy machinery. *Front Biol (Beijing)*, *9*, 18–34.

Chistiakov, D. A., Sobenin, I. A., Revin, V. V., Orekhov, A. N., & Bobryshev, Y. V. (2014). Mitochondrial aging and age-related dysfunction of mitochondria. *BioMed Res Int, 2014,* 238463.

Choi, M. S., Kim, H. J., Ham, M., Choi, D. H., Lee, T. R., & Shin, D. W. (2016). Amber light (590 nm) induces the breakdown of lipid droplets through autophagy-related lysosomal degradation in differentiated adipocytes. *Sci Rep*, *6*, 28476.

Chu, C. T., Bayir, H., & Kagan, V. E. (2014). LC3 binds externalized cardiolipin on injured mitochondria to signal mitophagy in neurons: Implications for Parkinson disease. *Autophagy*, *10*, 376–378.

Chu, C. T., Ji, J., Dagda, R. K., Jiang, J. F., Tyurina, Y. Y., Kapralov, A. A., … Kagan, V. E. (2013). Cardiolipin externalization to the outer mitochondrial membrane acts as an elimination signal for mitophagy in neuronal cells. *Nat Cell Biol*, *15*, 1197–205.

Clark, I. E., Dodson, M. W., Jiang, C., Cao, J. H., Huh, J. R., Seol, J. H., … Guo, M. (2006). Drosophila pink1 is required for mitochondrial function and interacts genetically with parkin. *Nature*, *441*, 1162–1166.

Claypool, S. M., & Koehler, C. M. (2012). The complexity of cardiolipin in health and disease. *Trends Biochem Sci*, *37*, 32–41.

Contreras, F. X., Ernst, A. M., Haberkant, P., Björkholm, P., Lindahl, E., Gönen, B., … Brügger, B. (2012). Molecular recognition of a single sphingolipid species by a protein's transmembrane domain. *Nature*, *481*, 525–529.

Contreras, F. X., Sánchez-Magraner, L., Alonso, A., & Goñi, F. M. (2010). Transbilayer (flip-flop) lipid motion and lipid scrambling in membranes. *FEBS Lett*, *584*, 1779–1786.

Contreras, F. X., Ernst, A. M., Wieland, F., & Brügger, B. (2011). Specificity of intramembrane protein-lipid interactions. *Cold Spring Harb Perspect Biol*, *3*, 1–18.

Cook, J. L., Re, R. N., DeHaro, D. L., Abadie, J. M., Peters, M., & Alam, J. (2008). The trafficking protein GABARAP binds to and enhances plasma membrane

expression and function of the angiotensin II type 1 receptor. *Circ Res*, *102*, 1539–1547.

Corcelle-Termeau, E., Vindeløv, S. D., Hämälistö, S., Mograbi, B., Keldsbo, A., Bräsen, J. H., … Jäättelä, M. (2016). Excess sphingomyelin disturbs ATG9A trafficking and autophagosome closure. *Autophagy*, *12*, 833–849.

Cortese, K., Diaspro, A., & Tacchetti, C. (2009). Advanced correlative light / electron microscopy : current methods and new developments using Tokuyasu cryosections. *Histochem*, *57*, 1103–1112.

Coyle, J. E., Qamar, S., Rajashankar, K. R., & Nikolov, D. B. (2002). Structure of GABARAP in two conformations: Implications for GABAA receptor localization and tubulin binding. *Neuron*, *33*, 63–74.

Cruz, A., & Pérez-Gil, J. (2007). Langmuir films to determine lateral surface pressure on lipid segregation. *Methods Mol Biol*, *400*, 439–57.

Cullis, P. R., de Kruijff, B., Verkleij, A. J., & Hope, M. J. (1986). Lipid polymorphism and membrane fusion. *Biochem Soc Trans*, *14*, 242–245.

Cuvillier, O., Pirianov, G., Kleuser, B., Vanek, P. G., Coso, O. A., Gutkind, S., & Spiegel, S. (1996). Suppression of ceramide-mediated programmed cell death by sphingosine-1-phosphate. *Nature*, *381*, 800–3.

Daido, S., Kanzawa, T., Yamamoto, a, Takeuchi, H., Kondo, Y., & Kondo, S. (2004). Pivotal role of the cell death factor BNIP3 in ceramide-induced autophagic cell death in malignant glioma cells. *Cancer Res*, *64*, 4286–4293.

Danson, C. M., Pocha, S. M., Bloomberg, G. B., & Cory, G. O. (2007). Phosphorylation of WAVE2 by MAP kinases regulates persistent cell migration and polarity. *J Cell Sci*, *120*, 4144–54.

Dany, M., & Ogretmen, B. (2015). Ceramide induced mitophagy and tumor suppression. *Biochim Biophys Acta*, *1853*, 2834–2845.

Daum, G., & Vance, J. E. (1997). Import of lipids into mitochondria. *Prog Lipid Res*, *36*, 103–30.

de Almeida, R. F. M., Fedorov, A., & Prieto, M. (2003). Sphingomyelin/phosphatidylcholine/cholesterol phase diagram: boundaries and composition of lipid rafts. *Biophys J*, *85*, 2406–2416.

de Duve, C. (1963). The lysosome. *Sci Am*, *208*, 64–72.

de Kroon, A. I. P. ., Dolis, D., Mayer, A., Lill, R., & de Kruijff, B. (1997). Phospholipid composition of highly purified mitochondrial outer membranes of rat liver and Neurospora crassa. Is cardiolipin present in the mitochondrial outer membrane? *Biochim Biophys Acta*, *1325*, 108–116.

Deas, E., Plun-Favreau, H., Gandhi, S., Desmond, H., Kjaer, S., Loh, S. H. Y., …

Wood, N. W. (2011). PINK1 cleavage at position A103 by the mitochondrial protease PARL. *Hum Mol Genet*, *20*, 867–879.

Debnath, J. (2009). Detachment-induced autophagy in three-dimensional epithelial cell cultures. *Methods Enzymol*, *452*, 423–39.

Decker, R. S. & Wildenthal, K. (1980). Lysosomal alterations in hypoxic and reoxygenated hearts: I. Ultrastructure and cytochemical changes. *Am J Pathol, 98*, 425–444.

Demaison, C., Parsley, K., Brouns, G., Scherr, M., Battmer, K., Kinnon, C., … Thrasher, A. J. (2002). High-level transduction and gene expression in hematopoietic repopulating cells using a human immunodeficiency [correction of imunodeficiency] virus type 1-based lentiviral vector containing an internal spleen focus forming virus promoter. *Hum Gene Ther*, *13*, 803–813.

Deretic, V. (2011). Autophagy in immunity and cell-autonomous defense against intracellular microbes. *Immunol Rev*, *240*, 92–104.

Deretic, V. (2012). Autophagy as an innate immunity paradigm: Expanding the scope and repertoire of pattern recognition receptors. *Curr Opin Immunol*, *24*, 21–31.

Devane, W. A., Hanus, L., Breuer, A., Pertwee, R. G., Stevenson, L. A., Griffin, G., … Mechoulam, R. (1992). Isolation and structure of a brain constituent that binds to the cannabinoid receptor. *Science*, *258*, 1946–9.

Ding, W. X., Ni, H. M., Gao, W., Hou, Y. F., Melan, M. A., Chen, X., … Yin, X. M. (2007). Differential effects of endoplasmic reticulum stress-induced autophagy on cell survival. *J Biol Chem*, *282*, 4702–10.

Ding, W. X., Ni, H. M., Li, M., Liao, Y., Chen, X., Stolz, D. B., … Yin, X. M. (2010). Nix is critical to two distinct phases of mitophagy, reactive oxygen species-mediated autophagy induction and Parkin-ubiquitin-p62-mediated mitochondrial priming. *J Biol Chem*, *285*, 27879–27890.

Dooley, H. C., Razi, M., Polson, H. E. J., Girardin, S. E., Wilson, M. I., & Tooze, S. A. (2014). WIPI2 links LC3 conjugation with PI3P, autophagosome formation, and pathogen clearance by recruiting Atg12–5-16L1. *Mol Cell*, *55*, 238–252.

Dowler, S., Kular, G., & Alessi, D. R. (2002). Protein lipid overlay assay. *Sci STKE*, *2002*, pl6.

Egami, Y., Kiryu-Seo, S., Yoshimori, T., & Kiyama, H. (2005). Induced expressions of Rab24 GTPase and LC3 in nerve-injured motor neurons. *Biochem Biophys Res Commun*, *337*, 1206–1213.

Egan, D. F., Chun, M. G. H., Vamos, M., Zou, H., Rong, J., Miller, C. J., … Shaw, R. J. (2015). Small molecule inhibition of the autophagy kinase ULK1 and identification of ULK1 substrates. *Mol Cell*, *59*, 285–297.

El Bawab, S., Roddy, P., Qian, T., Bielawska, A., Lemasters, J. J., & Hannun, Y. A. (2000). Molecular cloning and characterization of a human mitochondrial ceramidase. *J Biol Chem*, *275*, 21508–21513.

Ellens, H., Bentz, J., & Szoka, F. C. (1985). H^+- and Ca^{2+}-induced fusion and destabilization of liposomes. *Biochem*, *24*, 3099–3106.

Eng, C. H., Yu, K., Lucas, J., White, E., & Abraham, R. T. (2010). Ammonia derived from glutaminolysis is a diffusible regulator of autophagy. *Sci Signal*, *3*, ra31.

Engelman, D. M. (2005). Membranes are more mosaic than fluid. *Nature*, *438*, 578–80.

Epand, R. F., Schlattner, U., Wallimann, T., Lacombe, M. L., & Epand, R. M. (2007a). Novel lipid transfer property of two mitochondrial proteins that bridge the inner and outer membranes. *Biophys J*, *92*, 126–137.

Epand, R. F., Tokarska-Schlattner, M., Schlattner, U., Wallimann, T., & Epand, R. M. (2007b). Cardiolipin clusters and membrane domain formation induced by mitochondrial proteins. *J Mol Biol*, *365*, 968–980.

Epand, R. M. (1998). Lipid polymorphism and protein–lipid interactions. *Biochim Biophys Acta*, *1376*, 353–368.

Eskelinen, E. L. (2005). Maturation of autophagic vacuoles in Mammalian cells. *Autophagy*, *1*, 1–10.

Eskelinen, E. L., Reggiori, F., Baba, M., Kovács, A. L., & Seglen, P. O. (2011). Seeing is believing: The impact of electron microscopy on autophagy research. *Autophagy*, *7*, 935–56.

Esposti, M. D., Erler, J. T., Hickman, J. A., & Dive, C. (2001). Bid, a widely expressed proapoptotic protein of the Bcl-2 family, displays lipid transfer activity. *Mol Cell Biol*, *21*, 7268–7276.

Exner, N., Treske, B., Paquet, D., Holmström, K., Schiesling, C., Gispert, S., … Haass, C. (2007). Loss-of-function of human PINK1 results in mitochondrial pathology and can be rescued by parkin. *J Neurosci*, *27*, 12413–8.

Fan, W., Nassiri, A., & Zhong, Q. (2011). Autophagosome targeting and membrane curvature sensing by Barkor/Atg14(L). *Proc Natl Acad Sci U S A*, *108*, 7769–7774.

Fanani, M. L., Härtel, S., Oliveira, R. G., & Maggio, B. (2002). Bidirectional control of sphingomyelinase activity and surface topography in lipid monolayers. *Biophys J*, *83*, 3416–24.

Fidorra, M., Duelund, L., Leidy, C., Simonsen, A. C., & Bagatolli, L. A. (2006). Absence of fluid-ordered/fluid-disordered phase coexistence in ceramide/POPC mixtures containing cholesterol. *Biophys J*, *90*, 4437–4451.

Fisher, C. L., & Pei, G. K. (1997). Modification of a PCR-based site-directed mutagenesis method. *Biotechniques*, *23*, 570–574.

Fiske, C. H., & Subbarow, Y. (1925). The colorimetric determination of phosphorus. *J Biol Chem*, *66*, 375–400.

Fleming, S. M., Zhu, C., Fernagut, P. O., Mehta, A., DiCarlo, C. D., Seaman, R. L., & Chesselet, M. F. (2004). Behavioral and immunohistochemical effects of chronic intravenous and subcutaneous infusions of varying doses of rotenone. *Exp Neurol*, *187*, 418–429.

Frank, M., Duvezin-Caubet, S., Koob, S., Occhipinti, A., Jagasia, R., Petcherski, A., … Reichert, A. S. (2012). Mitophagy is triggered by mild oxidative stress in a mitochondrial fission dependent manner. *Biochim Biophys Acta*, *1823*, 2297–2310.

Frank, S., Gaume, B., Bergmann-Leitner, E. S., Leitner, W. W., Robert, E. G., Catez, F., … Youle, R. J. (2001). The role of dynamin-related protein 1, a mediator of mitochondrial fission, in apoptosis. *Dev Cell*, *1*, 515–525.

Friedman, J. R., Lackner, L. L., West, M., DiBenedetto, J. R., Nunnari, J., & Voeltz, G. K. (2011). ER tubules mark sites of mitochondrial division. *Science*, *334*, 358–362.

Fu, M., St-Pierre, P., Shankar, J., Wang, P. T. C., Joshi, B., & Nabi, I. R. (2013). Regulation of mitophagy by the Gp78 E3 ubiquitin ligase. *Mol Biol Cell*, *24*, 1153–62.

Fuller, M. (2010). Sphingolipids: the nexus between Gaucher disease and insulin resistance. *Lipids Health Dis*, *9*, 113.

Füllgrabe, J., Klionsky, D. J., & Joseph, B. (2014). The return of the nucleus: transcriptional and epigenetic control of autophagy. *Mol Cell Biol*, *15*, 65–74.

Gallet, P. F., Petit, J. M., Maftah, A., Zachowski, A., & Julien, R. (1997). Asymmetrical distribution of cardiolipin in yeast inner mitochondrial membrane triggered by carbon catabolite repression. *Biochem J*, *324*, 627–634.

Galluzzi, L., Pietrocola, F., Bravo-San Pedro, J. M., Amaravadi, R. K., Baehrecke, E. H., Cecconi, F., … Kroemer, G. (2015). Autophagy in malignant transformation and cancer progression. *EMBO J*, *34*, 856–880.

Gangoiti, P., Camacho, L., Arana, L., Ouro, A., Granado, M. H., Brizuela, L., … Gómez-Muñoz, A. (2010). Control of metabolism and signaling of simple bioactive sphingolipids: Implications in disease. *Prog Lipid Res*, *49*, 316–34.

García-Prat, L., Martínez-Vicente, M., Perdiguero, E., Ortet, L., Rodríguez-Ubreva, J., Rebollo, E., … Muñoz-Cánoves, P. (2016). Autophagy maintains stemness by preventing senescence. *Nature*, *529*, 37–42.

García-Ruiz, C., Colell, A., Marí, M., Morales, A., & Fernández-Checa, J. (1997). Direct effect of ceramide on the mitochondrial electron transport chain leads to generation of reactive oxygen species. Role of mitochondrial glutathione. *J Biol*

Chem, *272*, 11369–11377.

Garzotto, M., Haimovitz-Friedman, A., Liao, W. C., White-Jones, M., Huryk, R., Heston, W. D. W., … Fuks, Z. (1999). Reversal of radiation resistance in LNCaP cells by targeting apoptosis through ceramide synthase. *Cancer Res*, *59*, 5194–5201.

Garzotto, M., White-Jones, M., Jiang, Y., Ehleiter, D., Liao, W. C., Haimovitz-Friedman, A., … Kolesnick, R. (1998). 12-O-tetradecanoylphorbol-13-acetate-induced apoptosis in LNCaP cells is mediated through ceramide synthase. *Cancer Res*, *58*, 2260–2264.

Gautier, C. A., Kitada, T., & Shen, J. (2008). Loss of PINK1 causes mitochondrial functional defects and increased sensitivity to oxidative stress. *Proc Natl Acad Sci U S A*, *105*, 11364–11369.

Ge, L., Melville, D., Zhang, M., & Schekman, R. (2013). The ER-Golgi intermediate compartment is a key membrane source for the LC3 lipidation step of autophagosome biogenesis. *eLife*, *2013*, 1–23.

Gegg, M. E., Cooper, J. M., Chau, K. Y., Rojo, M., Schapira, A. H. V, & Taanman, J. W. (2010). Mitofusin 1 and mitofusin 2 are ubiquitinated in a PINK1/parkin-dependent manner upon induction of mitophagy. *Hum Mol Gene*, *19*, 4861–4870.

Geisler, S., Holmström, K. M., Skujat, D., Fiesel, F. C., Rothfuss, O. C., Kahle, P. J., & Springer, W. (2010). PINK1/Parkin-mediated mitophagy is dependent on VDAC1 and p62/SQSTM1. *Nat Cell Biol*, *12*, 119–131.

Gennis, R. B. (1989). *Biomembranes: molecular structure and function*. Springer-Verlag.

Gibbings, D., Mostowy, S., Jay, F., Schwab, Y., Cossart, P., & Voinnet, O. (2012). Selective autophagy degrades DICER and AGO2 and regulates miRNA activity. *Nat Cell Biol*, *14*, 1314–1321.

Gilbert, R. J. C. (2016). Protein-lipid interactions and non-lamellar lipidic structures in membrane pore formation and membrane fusion. *Biochim Biophys Acta*, *1858*, 487–499.

Glater, E. E., Megeath, L. J., Stowers, R. S., & Schwarz, T. L. (2006). Axonal transport of mitochondria requires milton to recruit kinesin heavy chain and is light chain independent. *J Cell Biol*, *173*, 545–557.

Gomes, L. C., Di Benedetto, G., & Scorrano, L. (2011a). During autophagy mitochondria elongate, are spared from degradation and sustain cell viability. *Nat Cell Biol*, *13*, 589–98.

Gomes, L. C., Di Benedetto, G., & Scorrano, L. (2011b). Essential amino acids and glutamine regulate induction of mitochondrial elongation during autophagy. *Cell Cycle*, *10*, 2635–9.

Gomes, L. C., & Scorrano, L. (2011). Mitochondrial elongation during autophagy: A stereotypical response to survive in difficult times. *Autophagy*, *7*, 1251–1253.

González-Polo, R. A., Boya, P., Pauleau, A. L., Jalil, A., Larochette, N., Souquère, S., … Kroemer, G. (2005). The apoptosis/autophagy paradox: autophagic vacuolization before apoptotic death. *J Cell Sci*, *118*, 3091–3102.

Gonzalvez, F., & Gottlieb, E. (2007). Cardiolipin: setting the beat of apoptosis. *Apoptosis*, *12*, 877–85.

Goñi, F. M. (2002). Non-permanent proteins in membranes: when proteins come as visitors. *Mol Membr Biol*, *19*, 237–45.

Goñi, F. M. (2014). The basic structure and dynamics of cell membranes: an update of the Singer-Nicolson model. *Biochim Biophys Acta*, *1838*, 1467–76.

Goñi, F. M., & Alonso, A. (2006). Biophysics of sphingolipids I. Membrane properties of sphingosine, ceramides and other simple sphingolipids. *Biochim Biophys Acta*, *1758*, 1902–1921.

Goñi, F. M., & Alonso, A. (2009). Effects of ceramide and other simple sphingolipids on membrane lateral structure. *Biochim Biophys Acta, 1788,* 169–77.

Goñi, F. M., Alonso, A., Bagatolli, L. A., Brown, R. E., Marsh, D., Prieto, M., & Thewalt, J. L. (2008). Phase diagrams of lipid mixtures relevant to the study of membrane rafts. *Biochim Biophys Acta, 1781*, 665–84.

Goñi, F. M., Montes, L. R., & Alonso, A. (2012). Phospholipases C and sphingomyelinases: Lipids as substrates and modulators of enzyme activity. *Prog Lipid Res*, *51*, 238–266.

Goñi, F. M., Sot, J., & Alonso, A. (2014). Biophysical properties of sphingosine, ceramides and other simple sphingolipids. *Biochem Soc Trans*, *42*, 1401–8.

Goñi, F. M., Villar, A. V, Nieva, J. L., & Alonso, A. (2003). Interaction of phospholipases C and sphingomyelinase with liposomes. *Methods Enzymol*, *372*, 3–19.

Grabenbauer, M., Geerts, W. J. C., Fernadez-Rodriguez, J., Hoenger, A., Koster, A. J., & Nilsson, T. (2005). Correlative microscopy and electron tomography of GFP through photooxidation. *Nat Methods*, *2*, 857–862.

Graef, M., & Nunnari, J. (2011). Mitochondria regulate autophagy by conserved signalling pathways. *EMBO J*, *30*, 2101–2114.

Grassmé, H., Riethmüller, J., & Gulbins, E. (2007). Biological aspects of ceramide-enriched membrane domains. *Prog Lipid Res*, *46*, 161–70.

Green, D. R., & Levine, B. (2014). To be or not to be? How selective autophagy and cell death govern cell fate. *Cell*, *157*, 65–75.

Green, F., O'Hare, T., Blackwell, A., & Enns, C. A. (2002). Association of human transferrin receptor with GABARAP. *FEBS Lett*, *518*, 101–106.

Greene, A. W., Grenier, K., Aguileta, M. a, Muise, S., Farazifard, R., Haque, M. E., … Fon, E. a. (2012). Mitochondrial processing peptidase regulates PINK1 processing, import and Parkin recruitment. *EMBO Rep*, *13*, 378–385.

Greene, J. C., Whitworth, A. J., Kuo, I., Andrews, L. A., Feany, M. B., & Pallanck, L. J. (2003). Mitochondrial pathology and apoptotic muscle degeneration in Drosophila parkin mutants. *Proc Natl Acad Sci U S A*, *100*, 4078–83.

Gregoriadis, G. (1978). Liposomes in the therapy of lysosomal storage diseases. *Nature*, *275*, 695–6.

Gregoriadis, G. (2008). Liposome research in drug delivery: the early days. *J Drug Target*, *16*, 520–4.

Grenier, K., McLelland, G. L., & Fon, E. A. (2013). Parkin- and PINK1-dependent mitophagy in neurons: Will the real pathway please stand up? *Front Neurol, 4,* 100.

Griffiths, R. E., Kupzig, S., Cogan, N., Mankelow, T. J., Betin, V. M. S., Trakarnsanga, K., … Lane, J. D. (2012). The ins and outs of human reticulocyte maturation: Autophagy and the endosome/exosome pathway. *Autophagy*, *8*, 1150–1.

Gudz, T. I., Tserng, K. Y., & Hoppel, C. L. (1997). Direct Inhibition of Mitochondrial Respiratory Chain Complex III by Cell-permeable Ceramide. *J Biol Chem*, *272*, 24154–24158.

Guo, J. Y., Chen, H. Y., Mathew, R., Fan, J., Strohecker, A. M., Karsli-Uzunbas, G., … White, E. (2011). Activated Ras requires autophagy to maintain oxidative metabolism and tumorigenesis. *Genes Dev*, *25*, 460–470.

Gutierrez, M. G., Master, S. S., Singh, S. B., Taylor, G. A., Colombo, M. I., & Deretic, V. (2004). Autophagy is a defense mechanism inhibiting BCG and Mycobacterium tuberculosis survival in infected macrophages. *Cell*, *119*, 753–766.

Hamacher-Brady, A., & Brady, N. R. (2016). Mitophagy programs: Mechanisms and physiological implications of mitochondrial targeting by autophagy. *Cell Mol Life Sci*, *73*, 775–795.

Hamasaki, M., Shibutani, S. T., & Yoshimori, T. (2013). Up-to-date membrane biogenesis in the autophagosome formation. *Curr Opin Cell Biol*, *25*, 455–60.

Hanna, R. A., Quinsay, M. N., Orogo, A. M., Giang, K., Rikka, S., & Gustafsson, Å. B. (2012). Microtubule-associated protein 1 light chain 3 (LC3) interacts with Bnip3 protein to selectively remove endoplasmic reticulum and mitochondria via autophagy. *J Biol Chem*, *287*, 19094–19104.

Hannun, Y. A., & Luberto, C. (2000). Ceramide in the eukaryotic stress response. *Trends Cell Biol*, *10*, 73–80.

Hara, T., Nakamura, K., Matsui, M., Yamamoto, A., Nakahara, Y., Suzuki-Migishima,

R., … Mizushima, N. (2006). Suppression of basal autophagy in neural cells causes neurodegenerative disease in mice. *Nature*, *441*, 885–9.

Harb, J. S., Comte, J., & Gautheron, D. C. (1981). Asymmetrical orientation of phospholipids and their interactions with marker enzymes in pig heart mitochondrial inner membrane. *Arch Biochem Biophys*, *208*, 305–318.

Hasegawa, J., Iwamoto, R., Otomo, T., Nezu, A., Hamasaki, M., & Yoshimori, T. (2016). Autophagosome-lysosome fusion in neurons requires INPP5E, a protein associated with Joubert syndrome. *EMBO J*, *35*, 1853–1867.

Hayashi-Nishino, M., Fujita, N., Noda, T., Yamaguchi, A., Yoshimori, T., & Yamamoto, A. (2009). A subdomain of the endoplasmic reticulum forms a cradle for autophagosome formation. *Nat Cell Biol*, *11*, 1433–1437.

He, C., & Klionsky, D. J. (2009). Regulation mechanisms and signaling pathways of autophagy. *Annu Rev Genet*, *43*, 67–93.

He, H., Dang, Y., Dai, F., Guo, Z., Wu, J., She, X., … Yu, L. (2003). Post-translational modifications of three members of the human MAP1LC3 family and detection of a novel type of modification for MAP1LC3B. *J Biol Chem*, *278*, 29278–29287.

He, Y., Liu, J., Grossman, D., Durrant, D., Sweatman, T., Lothstein, L., … Lee, R. M. (2007). Phosphorylation of mitochondrial phospholipid scramblase 3 by protein kinase C-δ induces its activation and facilitates mitochondrial targeting of tBid. *J Cell Biochem*, *101*, 1210–1221.

Heberle, F. A., & Feigenson, G. W. (2011). Phase separation in lipid membranes. *Cold Spring Harb Perspect Biol*, *3*, 1–13.

Heberle, F. A., Petruzielo, R. S., Pan, J., Drazba, P., Kučerka, N., Standaert, R. F., … Katsaras, J. (2013). Bilayer thickness mismatch controls domain size in model membranes. *J Am Chem Soc*, *135*, 6853–6859.

Hernández-Tiedra, S., Fabriàs, G., Dávila, D., Salanueva, Í. J., Casas, J., Montes, L. R., … Velasco, G. (2016). Dihydroceramide accumulation mediates aytotoxic autophagy of cáncer cells via autolysosome destabilization. *Autophagy*, *12*, 2213–2229.

Heuck, A. P., Hotze, E. M., Tweten, R. K., & Johnson, A. E. (2000). Mechanism of membrane insertion of a multimeric beta-barrel protein: perfringolysin O creates a pore using ordered and coupled conformational changes. *Mol Cell*, *6*, 1233–1242.

Hoch, F. L. (1992). Cardiolipins and biomembrane function. *Biochim Biophys Acta, 1113*, 71–133.

Hoepken, H. H., Gispert, S., Morales, B., Wingerter, O., Del Turco, D., Mülsch, A., … Auburger, G. (2007). Mitochondrial dysfunction, peroxidation damage and changes in glutathione metabolism in PARK6. *Neurobiol Dis*, *25*, 401–411.

Höglinger, G. U., Féger, J., Prigent, A., Michel, P. P., Parain, K., Champy, P., … Hirsch, E. C. (2003). Chronic systemic complex I inhibition induces a hypokinetic multisystem degeneration in rats. *J Neurochem*, *84*, 491–502.

Holthuis, J. C. M., & Menon, A. K. (2014). Lipid landscapes and pipelines in membrane homeostasis. *Nature*, *510*, 48–57.

Hong, S. B., Kim, B. W., Lee, K. E., Kim, S. W., Jeon, H., Kim, J., & Song, H. K. (2011). Insights into noncanonical E1 enzyme activation from the structure of autophagic E1 Atg7 with Atg8. *Nat Struct Mol Biol, 18*, 1323–1330.

Horenkamp, F. A., Kauffman, K. J., Kohler, L. J., Sherwood, R. K., Krueger, K. P., Shteyn, V., … Reinisch, K. M. (2015). The Legionella anti-autophagy effector RavZ targets the autophagosome via PI3P- and curvature-sensing motifs. *Dev Cell*, *34*, 569–576.

Hotamisligil, G. S. (2010). Endoplasmic reticulum stress and atherosclerosis. *Nat Med*, *16*, 396–9.

Hovius, R., Lambrechts, H., Nicolay, K., & De Kruijff, B. (1990). Improved methods to isolate and subfractionate rat liver mitochondria. Lipid composition of the inner and outer membrane. *Biochim Biophys Acta*, *1021*, 217–26.

Hruban, Z., Spargo, B., Swift, H., Wissler, R. W., & Kleinfeld, R. G. (1963). Focal cytoplasmic degradation. *The American Journal of Pathology*, *42*, 657–83.

Hsieh, A. C., Liu, Y., Edlind, M. P., Ingolia, N. T., Janes, M. R., Sher, A., … Ruggero, D. (2012). The translational landscape of mTOR signalling steers cancer initiation and metastasis. *Nature*, *485*, 55–61.

Hsu, P., Liu, X., Zhang, J., Wang, H. G., Ye, J. M., & Shi, Y. (2015). Cardiolipin remodeling by TAZ/tafazzin is selectively required for the initiation of mitophagy. *Autophagy*, *11*, 643–652.

Hsu, P., & Shi, Y. (2016). Regulation of autophagy by mitochondrial phospholipids in health and diseases. *Biochim Biophys Acta. http://dx.doi.org/10.1016/j.bbalip.2016.08.003*

Huang, H. W., Goldberg, E. M., & Zidovetzki, R. (1996). Ceramide induces structural defects into phosphatidylcholine bilayers and activates phospholipase A2. *Biochem Biophys Res Commun*, *220*, 834–838.

Huang, W., Choi, W., Hu, W., Mi, N., Guo, Q., Ma, M., … Shi, Y. (2012). Crystal structure and biochemical analyses reveal Beclin 1 as a novel membrane binding protein. *Cell Res, 22,* 473–89.

Hurley, J. H. (2006). Membrane binding domains. *Biochim Biophys Acta*, *1761*, 805–11.

Hurley, J. H., & Schulman, B. A. (2014). Atomistic autophagy: The structures of cellular

self-digestion. *Cell*, *157*, 300–311.

Ichimura, Y., Kumanomidou, T., Sou, Y. S., Mizushima, T., Ezaki, J., Ueno, T., … Komatsu, M. (2008). Structural basis for sorting mechanism of p62 in selective autophagy. *J Biol Chem*, *283*, 22847–22857.

Israelachvili, J. N., Marcelja, S., & Horn, R. G. (1980). Physical principles of membrane organization. *Q Rev Biophys*, *13*, 121–200.

Itakura, E., Kishi-Itakura, C., Koyama-Honda, I., & Mizushima, N. (2012). Structures containing Atg9A and the ULK1 complex independently target depolarized mitochondria at initial stages of Parkin-mediated mitophagy. *J Cell Sci*, *125*, 1488–1499.

Itakura, E., & Mizushima, N. (2011). p62 targeting to the autophagosome formation site requires self-oligomerization but not LC3 binding. *J Cell Biol*, *192*, 17–27.

Itoh, T., Kanno, E., Uemura, T., Waguri, S., & Fukuda, M. (2011). OATL1, a novel autophagosome-resident Rab33B-GAP, regulates autophagosomal maturation. *J Cell Biol*, *192*, 838–853.

Jacobson, K., Sheets, E. D., & Simson, R. (1995). Revisiting the fluid mosaic model of membranes. *Science*, *268*, 1441–2.

James, D. I., Parone, P. A., Mattenberger, Y., & Martinou, J. C. (2003). hFis1, a novel component of the mammalian mitochondrial fission machinery. *J Biol Chem*, *278*, 36373–36379.

Janmey, P. A., & Kinnunen, P. K. (2006). Biophysical properties of lipids and dynamic membranes. *Trends Cell Biol*, *16*, 538–546.

Jeong, H., Then, F., Melia, T. J., Mazzulli, J. R., Cui, L., Savas, J. N., … Krainc, D. (2009). Acetylation targets mutant huntingtin to autophagosomes for degradation. *Cell*, *137*, 60–72.

Jiang, S., Wells, C. D., & Roach, P. J. (2011). Starch-binding domain-containing protein 1 (Stbd1) and glycogen metabolism: Identification of the Atg8 family interacting motif (AIM) in Stbd1 required for interaction with GABARAPL1. *Biochemical and Biophys Res Commun*, *413*, 420–425.

Jiang, W., & Ogretmen, B. (2013). Ceramide stress in survival versus lethal autophagy paradox Ceramide targets autophagosomes to mitochondria and induces lethal mitophagy. *Autophagy*, *9*, 258–259.

Jin, S. M., Lazarou, M., Wang, C., Kane, L. A., Narendra, D. P., & Youle, R. J. (2010). Mitochondrial membrane potential regulates PINK1 import and proteolytic destabilization by PARL. *J Cell Biol*, *191*, 933–942.

Jin, S. M., & Youle, R. J. (2013). The accumulation of misfolded proteins in the mitochondrial matrix is sensed by PINK1 to induce PARK2/Parkin-mediated

mitophagy of polarized mitochondria. *Autophagy*, *9*, 1750–1757.

Joachim, J., Jefferies, H. B. J., Razi, M., Frith, D., Snijders, A. P., Chakravarty, P., … Tooze, S. A. (2015). Activation of ULK Kinase and Autophagy by GABARAP Trafficking from the Centrosome Is Regulated by WAC and GM130. *Molecular Cell*, *60*, 899–913.

Johansen, T., & Lamark, T. (2011). Selective autophagy mediated by autophagic adapter proteins. *Autophagy*, *7*, 279–96.

Johnson, A. E. (2005). Fluorescence approaches for determining protein conformations, interactions and mechanisms at membranes. *Traffic*, *6*, 1078–92.

Juhasz, G., & Neufeld, T. P. (2006). Autophagy: A forty-year search for a missing membrane source. *PLoS Biol, 4,* e36.

Juris, L., Montino, M., Rube, P., Schlotterhose, P., Thumm, M., Krick, R., … Rubinsztein, D. (2015). PI3P binding by Atg21 organises Atg8 lipidation. *EMBO J*, *34*, 955–973.

Kabeya, Y., Mizushima, N., Yamamoto, A., Oshitani-Okamoto, S., Ohsumi, Y., & Yoshimori, T. (2004). LC3, GABARAP and GATE16 localize to autophagosomal membrane depending on form-II formation. *J Cell Sci*, *117*, 2805–2812.

Kabeya, Y., Mizushima, N., Ueno, T., Yamamoto, A., Kirisako, T., Noda, T., … Yoshimori, T. (2000). LC3, a mammalian homologue of yeast Apg8p, is localized in autophagosome membranes after processing. *EMBO J*, *19*, 5720–5728.

Kagan, V. E., Chu, C. T., Tyurina, Y. Y., Cheikhi, A., & Bayir, H. (2014). Cardiolipin asymmetry, oxidation and signaling. *Chem Phys Lipids*, *179*, 64–69.

Kagan, V. E., Tyurin, V. A., Jiang, J., Tyurina, Y. Y., Ritov, V. B., Amoscato, A. A., … Borisenko, G. G. (2005). Cytochrome c acts as a cardiolipin oxygenase required for release of proapoptotic factors. *Nat Chem Biol*, *1*, 223–32.

Kagan, V. E., Tyurina, Y. Y., Bayir, H., Chu, C. T., Kapralov, A. A., Vlasova, I. I., … Jiang, J. (2006). The “pro-apoptotic genies” get out of mitochondria: Oxidative lipidomics and redox activity of cytochrome c/cardiolipin complexes. *Chem Biol Interact*, *163*, 15–28.

Kaiser, S. E., Qiu, Y., Coats, J. E., Mao, K., Klionsky, D. J., & Schulman, B. A. (2013). Structures of Atg7-Atg3 and Atg7-Atg10 reveal noncanonical mechanisms of E2 recruitment by the autophagy E1. *Autophagy*, *9*, 778–780.

Kane, L. A., Lazarou, M., Fogel, A. I., Li, Y., Yamano, K., Sarraf, S. A., … Youle, R. J. (2014). PINK1 phosphorylates ubiquitin to activate parkin E3 ubiquitin ligase activity. *J Cell Biol*, *205*, 143–153.

Kanki, T., Furukawa, K., & Yamashita, S. (2015). Mitophagy in yeast: Molecular mechanisms and physiological role. *Biochim Biophys Acta*, 1853, 2756–65.

Kanki, T., & Klionsky, D. J. (2008). Mitophagy in yeast occurs through a selective mechanism. *J Biol Chem*, *283*, 32386–32393.

Kanki, T., Wang, K., Cao, Y., Baba, M., & Klionsky, D. J. (2009). Atg32 Is a Mitochondrial Protein that Confers Selectivity during Mitophagy. *Dev Cell*, *17*, 98–109.

Karanasios, E., Stapleton, E., Walker, S. a, Manifava, M., & Ktistakis, N. T. (2013). Live cell imaging of early autophagy events: omegasomes and beyond. *J Vis Exp*, *77*, 1–9.

Karanasios, E., Walker, S. A., Okkenhaug, H., Manifava, M., Hummel, E., Zimmermann, H., … Ktistakis, N. T. (2016). Autophagy initiation by ULK complex assembly on ER tubulovesicular regions marked by ATG9 vesicles. *Nat Commun, 7*, 12420.

Karreman, M. A., Hyenne, V., Schwab, Y., & Goetz, J. G. (2016). Intravital correlative microscopy: Imaging life at the nanoscale. *Trends Cell Biol*, *26,* 848–863.

Karreman, M. A., Mercier, L., Schieber, N. L., Shibue, T., Schwab, Y., & Goetz, J. G. (2014). Correlating intravital multi-photon microscopy to 3D electron microscopy of invading tumor cells using anatomical reference points. *PLoS One*, *9*, 1–23.

Kates, M., Syz, J. Y., Gosser, D., & Haines, T. H. (1993). pH-dissociation characteristics of cardiolipin and its 2'-deoxy analogue. *Lipids*, *28*, 877–882.

Kazlauskaite, A., Kondapalli, C., Gourlay, R., Campbell, D. G., Ritorto, M. S., Hofmann, K., … Muqit, M. M. K. (2014). Parkin is activated by PINK1-dependent phosphorylation of ubiquitin at Ser65. *Biochem J*, *460*, 127–139.

Kelly, S. M., Jess, T. J., & Price, N. C. (2005). How to study proteins by circular dichroism. *Biochim Biophys Acta, 1751,* 119–39.

Kent, G., Minick, O. T., Volini, F. I., & Orfei, E. (1966). Autophagic vacuoles in human red cells. *Am J Pathol*, *48*, 831–57.

Khalifat, N., Fournier, J. B., Angelova, M. I., & Puff, N. (2011). Lipid packing variations induced by pH in cardiolipin-containing bilayers: The driving force for the cristae-like shape instability. *Biochim Biophys Acta*, *1808*, 2724–2733.

Khalifat, N., Puff, N., Bonneau, S., Fournier, J.-B., & Angelova, M. I. (2008). Membrane deformation under local pH gradient: mimicking mitochondrial cristae dynamics. *Biophys J*, *95*, 4924–33.

Khaminets, A., Heinrich, T., Mari, M., Grumati, P., Huebner, A. K., Akutsu, M., … Dikic, I. (2015). Regulation of endoplasmic reticulum turnover by selective autophagy. *Nature*, *522*, 354–358.

Kim, N. C., Tresse, E., Kolaitis, R. M., Molliex, A., Thomas, R. E., Alami, N. H., … Taylor, J. P. (2013). VCP is essential for mitochondrial quality control by

PINK1/Parkin and this function is impaired by VCP mutations. *Neuron*, *78*, 65–80.

Kim, P. K., Hailey, D. W., Mullen, R. T., & Lippincott-Schwartz, J. (2008). Ubiquitin signals autophagic degradation of cytosolic proteins and peroxisomes. *Proc Natl Acad Sci U S A*, *105*, 20567–74.

Kim, T.-H., Zhao, Y., Ding, W.-X., Shin, J. N., He, X., Seo, Y.-W., … Yin, X.-M. (2004). Bid-cardiolipin interaction at mitochondrial contact site contributes to mitochondrial cristae reorganization and cytochrome C release. *Mol Biol Cell*, *15*, 3061–3072.

Kimura, S., Noda, T., & Yoshimori, T. (2007). Dissection of the autophagosome maturation process by a novel reporter protein, tandem fluorescent-tagged LC3. *Autophagy*, *3*, 452–460.

Kimura, S., Noda, T., & Yoshimori, T. (2008). Dynein-dependent movement of autophagosomes mediates efficient encounters with lysosomes. *Cell Struct Funct*, *33*, 109–122.

Kirisako, T., Baba, M., Ishihara, N., Miyazawa, K., Ohsumi, M., Yoshimori, T., … Ohsumi, Y. (1999). Formation process of autophagosome is traced with Apg8/Aut7p in yeast. *J Cell Biol*, *147*, 435–446.

Kirkin, V., Lamark, T., Sou, Y. S., Bjørkøy, G., Nunn, J. L., Bruun, J. A., … Johansen, T. (2009a). A role for NBR1 in autophagosomal degradation of ubiquitinated substrates. *Mol Cell*, *33*, 505–516.

Kirkin, V., McEwan, D. G., Novak, I., & Dikic, I. (2009b). A role for ubiquitin in selective autophagy. *Mol Cell*, 34, 259–69.

Kirkland, R. A., Adibhatla, R. M., Hatcher, J. F., & Franklin, J. L. (2002). Loss of cardiolipin and mitochondria during programmed neuronal death: Evidence of a role for lipid peroxidation and autophagy. *Neuroscience*, *115*, 587–602.

Kiššova, I., Deffieu, M., Manon, S., & Camougrand, N. (2004). Uth1p is involved in the autophagic degradation of mitochondria. *J Biol Chem*, *279*, 39068–39074.

Kiššova, I., Salin, B., Schaeffer, J., Bhatia, S., Manon, S., & Camougrand, N. (2007). Selective and non-selective autophagic degradation of mitochondria in yeast. *Autophagy*, *3*, 329–336.

Kitada, T., Asakawa, S., Hattori, N., Matsumine, H., Yamamura, Y., Minoshima, S., … Shimizu, N. (1998). Mutations in the parkin gene cause autosomal recessive juvenile parkinsonism. *Nature*, *392*, 605–608.

Kittler, J. T., Rostaing, P., Schiavo, G., Fritschy, J. M., Olsen, R., Triller, a, & Moss, S. J. (2001). The subcellular distribution of GABARAP and its ability to interact with NSF suggest a role for this protein in the intracellular transport of GABA(A) receptors. *Mol Cell Neurosci*, *18*, 13–25.

Klionsky, D., Agholme, L., Agnello, M., Agostinis, P., Aguirre-ghiso, J. a, Ahn, H. J., …

Finkbeiner, S. (2012). Guidelines for the use and interpertation of assays for monitoring autophagy. *Autophagy*, *8*, 445–544.

Klionsky, D. J. (2007). Autophagy: from phenomenology to molecular understanding in less than a decade. *Mol Cell Biol*, *8*, 931–937.

Klionsky, D. J. (2008). Autophagy revisited: A conversation with Christian de Duve. *Autophagy*, *4*, 740–3.

Klionsky, D. J., Abeliovich, H., Agostinis, P., Agrawal, D. K., Aliev, G., Askew, D. S., … Pinkas-kramarski, R. (2008). Guidelines for the use and interpretation of assays for monitorig autophagy in higher eukaryotes. *Autophagy*, *4*, 151–175.

Kolotuev, I., Schwab, Y., & Labouesse, M. (2010). A precise and rapid mapping protocol for correlative light and electron microscopy of small invertebrate organisms. *Biol Cell*, *102*, 121–132.

Komatsu, M., Waguri, S., Ueno, T., Iwata, J., Murata, S., Tanida, I., … Chiba, T. (2005). Impairment of starvation-induced and constitutive autophagy in Atg7-deficient mice. *J Cell Biol*, *169*, 425–434.

Komatsu, M., Wang, Q. J., Holstein, G. R., Friedrich Jr., V. L., Iwata, J., Kominami, E., … Yue, Z. (2007). Essential role for autophagy protein Atg7 in the maintenance of axonal homeostasis and the prevention of axonal degeneration. *Proc Natl Acad Sci U S A*, *104*, 14489–14494.

Kominami, E., Hashida, S., Khairallah, E. A., & Katunuma, N. (1983). Sequestration of cytoplasmic enzymes in an autophagic vacuole-lysosomal system induced by injection of leupeptin. *J Biol Chem*, *258*, 6093–6100.

Kondapalli, C., Kazlauskaite, A., Zhang, N., Woodroof, H. I., Campbell, D. G., Gourlay, R., … Morrice, N. (2012). PINK1 is activated by mitochondrial membrane potential depolarization and stimulates Parkin E3 ligase activity by phosphorylating Serine 65. *Open Biol*, *2*, 120080.

Kondo-Okamoto, N., Noda, N. N., Suzuki, S. W., Nakatogawa, H., Takahashi, I., Matsunami, M., … Okamoto, K. (2012). Autophagy-related protein 32 acts as autophagic degron and directly initiates mitophagy. *J Biol Chem*, *287*, 10631–10638.

Koning, R. I., Kutchoukov, V. G., Hagen, C. W., & Koster, A. J. (2013). Nanofabrication of a gold fiducial array on specimen support for electron tomography. *Ultramicroscopy*, *135*, 99–104.

Korac, J., Schaeffer, V., Kovacevic, I., Clement, A. M., Jungblut, B., Behl, C., … Ashwell, J. D. (2013). Ubiquitin-independent function of optineurin in autophagic clearance of protein aggregates. *J Cell Sci*, *126*, 580–92.

Korolchuk, V. I., & Rubinsztein, D. C. (2011). Regulation of autophagy by lysosomal

positioning. *Autophagy*, *7*, 927–8.

Koukourakis, M. I., Kalamida, D., Giatromanolaki, A., Zois, C. E., Sivridis, E., Pouliliou, S., … Harris, A. L. (2015). Autophagosome proteins LC3A, LC3B and LC3C have distinct subcellular distribution kinetics and expression in cancer cell lines. *PLoS One*, *10*, 1–13.

Kouno, T., Mizuguchi, M., Tanidal, I., Uenol, T., Kanematsu, T., Mori, Y., … Kawano, K. (2005). Solution structure of microtubule-associated protein light chain 3 and identification of its functional subdomains. *J Biol Chem*, *280*, 24610–24617.

Kovács, J., Fellinger, E., Kárpáti, A. P., Kovács, A. L., László, L., & Réz, G. (1987). Morphometric evaluation of the turnover of autophagic vacuoles after treatment with Triton X-100 and vinblastine in murine pancreatic acinar and seminal vesicle epithelial cells. *Virchows Arch B Cell Pathol Incl Mol Pathol*, *53*, 183–190.

Koyano, F., Okatsu, K., Kosako, H., Tamura, Y., Go, E., Kimura, M., … Matsuda, N. (2014). Ubiquitin is phosphorylated by PINK1 to activate parkin. *Nature*, *510*, 162–6.

Kozlov, M. M., & Chernomordik, L. V. (2015). Membrane tension and membrane fusion. *Curr Opin Struct Biol*, *33*, 61–7.

Kraft, C. A., Garrido, J. L., Leiva-Vega, L., & Romero, G. (2009). Quantitative analysis of protein-lipid interactions using tryptophan fluorescence. *Sci Signal*, *2*, pl4.

Kraft, C., Kijanska, M., Kalie, E., Siergiejuk, E., Lee, S. S., Semplicio, G., … Peter, M. (2012). Binding of the Atg1/ULK1 kinase to the ubiquitin-like protein Atg8 regulates autophagy. *EMBO J*, *31*, 3691–703.

Krebs, J. J. R., Hauser, H., & Carafoli, E. (1979). Asymmetric distribution of phospholipids in the inner membrane of beef heart mitochondria. *J Biol Chem*, *254*, 5308–5316.

Ktistakis, N. T., & Tooze, S. A. (2016). Digesting the expanding mechanisms of autophagy. *Trends Cell Biol*, *26,* 624–35.

Kubli, D. A., & Gustafsson, Å. B. (2012). Mitochondria and mitophagy: The yin and yang of cell death control. *Circ Res*, 111, 1208–21.

Kuma, A., Hatano, M., Matsui, M., Yamamoto, A., Nakaya, H., Yoshimori, T., … Mizushima, N. (2004). The role of autophagy during the early neonatal starvation period. *Nature*, *432*, 1032–1036.

Kumagai, K., Yasuda, S., Okemoto, K., Nishijima, M., Kobayashi, S., & Hanada, K. (2005). CERT mediates intermembrane transfer of various molecular species of ceramides. *J Biol Chem*, *280*, 6488–6495.

Kumeta, H., Watanabe, M., Nakatogawa, H., Yamaguchi, M., Ogura, K., Adachi, W., … Inagaki, F. (2010). The NMR structure of the autophagy-related protein Atg8. *J*

Biomol NMR, *47*, 237–241.

Kundu, M., Lindsten, T., Yang, C. Y., Wu, J., Zhao, F., Zhang, J., … Thompson, C. B. (2008). Ulk1 plays a critical role in the autophagic clearance of mitochondria and ribosomes during reticulocyte maturation. *Blood*, *112*, 1493–1502.

Lakowicz, J. R. (2007). *Principles of fluorescence spectroscopy. 2nd edition*. *Plenum Publishing Corp.*

Lamb, C., Yoshimori, T., & Tooze, S. A. (2013). The autophagosome: origins unknown, biogenesis complex. *Nat Rev Mol Cell Biol*, *14*, 759–774.

Landajuela, A., Hervás, J. H., Antón, Z., Montes, L. R., Gil, D., Valle, M., … Alonso, A. (2016). Lipid geometry and bilayer curvature modulate LC3/GABARAP-mediated model autophagosomal elongation. *Biophys J*, *110*, 411–422.

Landeta, O., Landajuela, A., Gil, D., Taneva, S., DiPrimo, C., Sot, B., … Basañez, G. (2011). Reconstitution of proapoptotic BAK function in liposomes reveals a dual role for mitochondrial lipids in the BAK-driven membrane permeabilization process. *J Biol Chem*, *286*, 8213–8230.

Lang, T., Schaeffeler, E., Bernreuther, D., Bredschneider, M., Wolf, D. H., & Thumm, M. (1998). Aut2p and Aut7p, two novel microtubule-associated proteins are essential for delivery of autophagic vesicles to the vacuole. *EMBO J*, *17*, 3597–3607.

Langmuir, I. (1917). The constitution and fundamental properties of solids and liquids. *J Am Chem Soc*, *39*, 1848–1906.

Lapointe, N., St-Hilaire, M., Martinoli, M. G., Blanchet, J., Gould, P., Rouillard, C., & Cicchetti, F. (2004). Rotenone induces non-specific central nervous system and systemic toxicity. *FASEB J*, *18*, 717–719.

Lazarou, M., Jin, S. M., Kane, L. A., & Youle, R. J. (2012). Role of PINK1 binding to the TOM complex and alternate intracellular membranes in recruitment and activation of the E3 ligase Parkin. *Dev Cell*, *22*, 320–333.

Lazarou, M., Sliter, D. A., Kane, L. A., Sarraf, S. A., Wang, C., Burman, J. L., … Youle, R. J. (2015). The ubiquitin kinase PINK1 recruits autophagy receptors to induce mitophagy. *Nature*, *524*, 309–14.

Lee, K. M., Hwang, S. K., & Lee, J. A. (2013). Neuronal autophagy and neurodevelopmental disorders. *Exp Neurobiol*, *22*, 133–42.

Leil, T. A., Chen, Z. W., Chang, C. S., & Olsen, R. W. (2004). GABAA receptor-associated protein traffics GABAA receptors to the plasma membrane in neurons. *J Neurosci*, *24*, 11429–11438.

Lemmin, T., Bovigny, C., Lançon, D., & Dal Peraro, M. (2013). Cardiolipin models for molecular simulations of bacterial and mitochondrial membranes. *J Chem Theory*

Comput, *9*, 670–678.

Lemmon, M. A. (2008). Membrane recognition by phospholipid-binding domains. *Nat Rev Mol Cell Biol*, *9*, 99–111.

Lemmon, M. A., Ferguson, K. M., O'Brien, R., Sigler, P. B., & Schlessinger, J. (1995). Specific and high-affinity binding of inositol phosphates to an isolated pleckstrin homology domain. *Proc Natl Acad Sci U S A*, *92*, 10472–10476.

Levine, B., & Kroemer, G. (2008). Autophagy in the Pathogenesis of Disease. *Cell*, *132*, 27–42.

Lewis, R. N., & McElhaney, R. N. (2009). The physicochemical properties of cardiolipin bilayers and cardiolipin-containing lipid membranes. *Biochim Biophys Acta, 1788, 2069–79.*

Li, X. X., Tsoi, B., Li, Y. F., Kurihara, H., & He, R. R. (2015). Cardiolipin and its different properties in mitophagy and apoptosis. *J Histochem Cytochem*, *63*, 301–11.

Li, Y., Li, S., Qin, X., Hou, W., Dong, H., Yao, L., & Xiong, L. (2014). The pleiotropic roles of sphingolipid signaling in autophagy. *Cell Death Dis*, *5*, e1245.

Liang, X. H., Jackson, S., Seaman, M., Brown, K., Kempkes, B., Hibshoosh, H., & Levine, B. (1999). Induction of autophagy and inhibition of tumorigenesis by beclin 1. *Nature*, *402*, 672–676.

Lindahl, E., & Sansom, M. S. (2008). Membrane proteins: molecular dynamics simulations. *Curr Opin Struct Biol,18,* 425–431.

Liu, J., Dai, Q., Chen, J., Durrant, D., Freeman, A., Liu, T., … Lee, R. M. (2003). Phospholipid scramblase 3 controls mitochondrial structure, function, and apoptotic response. *Mol Cancer Res*, *1*, 892–902.

Liu, J., Epand, R. F., Durrant, D., Grossman, D., Chi, N. W., Epand, R. M., & Lee, R. M. (2008). Role of phospholipid scramblase 3 in the regulation of tumor necrosis factor-α-induced apoptosis. *Biochemistry*, *47*, 4518–4529.

Liu, L., Feng, D., Chen, G., Chen, M., Zheng, Q., Song, P., … Chen, Q. (2012). Mitochondrial outer-membrane protein FUNDC1 mediates hypoxia-induced mitophagy in mammalian cells. *Nat Cell Biol*, *14*, 177–85.

Liu, X., Mao, K., Yu, A. Y. H., Omairi-Nasser, A., Austin, J., Glick, B. S., … Klionsky, D. J. (2016). The Atg17-Atg31-Atg29 complex coordinates with Atg11 to recruit the Vam7 SNARE and mediate autophagosome-vacuole fusion. *Curr Biol*, *26*, 150–160.

Liu, Y., & Levine, B. (2015). Autosis and autophagic cell death: the dark side of autophagy. *Cell Death Differ*, *22*, 367–76.

Lokireddy, S., Wijesoma, I. W., Teng, S., Bonala, S., Gluckman, P. D., McFarlane, C., … Kambadur, R. (2012). The ubiquitin ligase Mul1 induces mitophagy in skeletal

muscle in response to muscle-wasting stimuli. *Cell Metab*, *16*, 613–624.

Lu, H., Li, G., Liu, L., Feng, L., Wang, X., & Jin, H. (2013). Regulation and function of mitophagy in development and cancer. *Autophagy*, *9*, 1720–1736.

Lutter, M., Fang, M., Luo, X., Nishijima, M., Xie, X., & Wang, X. (2000). Cardiolipin provides specificity for targeting of tBid to mitochondria. *Nat Cell Biol*, *2*, 754–761.

Lynch-Day, M. A., & Klionsky, D. J. (2010). The Cvt pathway as a model for selective autophagy. *FEBS Lett*, *584*, 1359–66.

MacVicar, T. D. B., & Lane, J. D. (2014). Impaired OMA1-dependent cleavage of OPA1 and reduced DRP1 fission activity combine to prevent mitophagy in cells that are dependent on oxidative phosphorylation. *J Cell Sci*, *127*, 2313–25.

Maday, S., Wallace, K. E., & Holzbaur, E. L. F. (2012). Autophagosomes initiate distally and mature during transport toward the cell soma in primary neurons. *Journal of Cell Biol*, *196*, 407–417.

Madrigal-Matute, J., & Cuervo, A. M. (2016). Regulation of Liver Metabolism by Autophagy. *Gastroenterology*, *150*, 328–39.

Maguire, J. J., Tyurina, Y. Y., Mohammadyani, D., Kapralov, A. A., Anthonymuthu, T. S., Qu, F., … Kagan, V. E. (2016). Known unknowns of cardiolipin signaling: The best is yet to come. *Biochim Biophys Acta. http://dx.doi.org/10.1016/j.bbalip.2016.08.001*

Mammucari, C., Milan, G., Romanello, V., Masiero, E., Rudolf, R., Del Piccolo, P., … Sandri, M. (2007). FoxO3 controls autophagy in skeletal muscle in vivo. *Cell Metab*, *6*, 458–471.

Mann, S. S., & Hammarback, J. A. (1994). Molecular characterization of light chain 3. A microtubule binding subunit of MAP1A and MAP1B. *J Biol Chem*, *269*, 11492–11497.

Mao, K., Wang, K., Liu, X., & Klionsky, D. (2013). The scaffold protein Atg11 recruits fission machinery to drive selective mitochondria degradation by autophagy. *Dev Cell*, *26*, 9–18.

Mari, M., Tooze, S. A., & Reggiori, F. (2011). The puzzling origin of the autophagosomal membrane. *F1000 Biol Rep*, *3*, 25.

Marino, G., Niso-Santano, M., Baehrecke, E. H., & Kroemer, G. (2014). Self-consumption: the interplay of autophagy and apoptosis. *Nat Rev Mol Cell Biol*, *15*, 81–94.

Mariño, G., Fernández, A. F., Cabrera, S., Lundberg, Y. W., Cabanillas, R., Rodríguez, F., … López-Otín, C. (2010). Autophagy is essential for mouse sense of balance. *J Clin Invest*, *120*, 2331–2344.

Mariño, G., Salvador-Montoliu, N., Fueyo, A., Knecht, E., Mizushima, N., & López-Otín,

C. (2007). Tissue-specific autophagy alterations and increased tumorigenesis in mice deficient in Atg4C/autophagin-3. *J Biol Chem*, *282*, 18573–18583.

Marsh, D. (1980). Molecular motion in phospholipid bilayers in the gel phase: long axis rotation. *Biochemistry*, *19*, 1632–7.

Marsh, D. (1996). Lateral pressure in membranes. *Biochim Biophys Acta*, *1286*, 183–223.

Marsh, D. (2008). Electron spin resonance in membrane research: Protein–lipid interactions. *Methods*, *46*, 83–96.

Martin, S. R., & Schilstra, M. J. (2008). Circular dichroism and its application to the study of biomolecules. *Methods Cell Biol*, *84*, 263–93.

Mathew, R., & White, E. (2011). Autophagy in tumorigenesis and energy metabolism: Friend by day, foe by night. *Curr Opin Genet Dev, 21*, 113–9.

Matsuda, L. A., Lolait, S. J., Brownstein, M. J., Young, A. C., & Bonner, T. I. (1990). Structure of a cannabinoid receptor and functional expression of the cloned cDNA. *Nature*, *346*, 561–564.

Matsuda, N., Sato, S., Shiba, K., Okatsu, K., Saisho, K., Gautier, C. A., … Tanaka, K. (2010). PINK1 stabilized by mitochondrial depolarization recruits Parkin to damaged mitochondria and activates latent Parkin for mitophagy. *J Cell Biol*, *189*, 211–221.

Matsushita, M., Suzuki, N. N., Obara, K., Fujioka, Y., Ohsumi, Y., & Inagaki, F. (2007). Structure of Atg5·Atg16, a complex essential for autophagy. *J Biol Chem*, *282*, 6763–6772.

Maurya, N., Agarwal, N. R., & Ghosh, I. (2015). Low-dose rotenone exposure induces early senescence leading to late apoptotic signaling cascade in human trabecular meshwork (HTM) cell line: An in vitro glaucoma model. *Cell Biol Int*, *40*, 107–120.

Mayer, L. D., Hope, M. J., & Cullis, P. R. (1986). Vesicles of variable sizes produced by a rapid extrusion procedure. *Biochim Biophys Acta*, *858*, 161–168.

Mechoulam, R., Ben-Shabat, S., Hanus, L., Ligumsky, M., Kaminski, N. E., Schatz, A. R., … Vogel, Z. (1995). Identification of an endogenous 2-monoglyceride, present in canine gut, that binds to cannabinoid receptors. *Biochem Pharmacol*, *50*, 83–90.

Meléndez, A., Tallóczy, Z., Seaman, M., Eskelinen, E.-L., Hall, D. H., & Levine, B. (2003). Autophagy genes are essential for dauer development and life-span extension in C. elegans. *Science*, *301*, 1387–91.

Meurers, B. H., Zhu, C., Fernagut, P. O., Richter, F., Hsia, Y. C., Fleming, S. M., … Chesselet, M. F. (2009). Low dose rotenone treatment causes selective transcriptional activation of cell death related pathways in dopaminergic neurons

in vivo. *Neurobiol Dis*, *33*, 182–192.

Mi, N., Chen, Y., Wang, S., Chen, M., Zhao, M., Yang, G., … Yu, L. (2015). CapZ regulates autophagosomal membrane shaping by promoting actin assembly inside the isolation membrane. *Nat Cell Biol*, *17*, 1112–23.

Miao, Y., Li, G., Zhang, X., Xu, H., & Abraham, S. N. (2015). A TRP channel senses lysosome neutralization by pathogens to trigger their expulsion. *Cell*, *161*, 1306–1319.

Mikhaylova, O., Stratton, Y., Hall, D., Kellner, E., Ehmer, B., Drew, A. F., … Czyzyk-Krzeska, M. F. (2012). VHL-regulated MiR-204 suppresses tumor growth through inhibition of LC3B-mediated autophagy in renal clear cell carcinoma. *Cancer Cell*, *21*, 532–546.

Misaka, T., Miyashita, T., & Kubo, Y. (2002). Primary structure of a dynamin-related mouse mitochondrial GTPase and its distribution in brain, subcellular localization, and effect on mitochondrial morphology. *J Biol Chem*, *277*, 15834–15842.

Mizushima, N. (2007). Autophagy: Process and function. *Genes Dev, 21, 2861–73.*

Mizushima, N., & Komatsu, M. (2015). Autophagy: Renovation of Cells and Tissues. *Cell*, *147*, 728–741.

Mizushima, N., Kuma, A., Kobayashi, Y., Yamamoto, A., Matsubae, M., Takao, T., … Yoshimori, T. (2003). Mouse Apg16L, a novel WD-repeat protein, targets to the autophagic isolation membrane with the Apg12-Apg5 conjugate. *J Cell Sci*, *116*, 1679–1688.

Mizushima, N., Levine, B., Cuervo, A. M., & Klionsky, D. J. (2008). Autophagy fights disease through cellular self-digestion. *Nature*, *451*, 1069–75.

Mizushima, N., Yamamoto, A., Hatano, M., Kobayashi, Y., Kabey, Y., Suzuki, K., … Yoshimori, T. (2001). Dissection of autophagosome formation using Apg5-deficient mouse embryonic stem cells. *J Cell Biol*, *152*, 657–667.

Mizushima, N., Yoshimori, T., & Ohsumi, Y. (2011). The role of Atg proteins in autophagosome formation. *Annu Rev Cell Dev Biol, 27,* 107–32.

Mochida, K., Oikawa, Y., Kimura, Y., Kirisako, H., Hirano, H., Ohsumi, Y., & Nakatogawa, H. (2015). Receptor-mediated selective autophagy degrades the endoplasmic reticulum and the nucleus. *Nature*, *522*, 359–62.

Montes, L. R., Alonso, A., Goñi, F. M., & Bagatolli, L. A. (2007). Giant unilamellar vesicles electroformed from native membranes and organic lipid mixtures under physiological conditions. *Biophys J*, *93*, 3548–54.

Morad, S. A., & Cabot, M. C. (2013). Ceramide-orchestrated signalling in cancer cells. *Nat Rev Cancer*, *13*, 51–65.

Morad, S. A. F., Messner, M. C., Levin, J. C., Abdelmageed, N., Park, H., Merrill, A. H.,

& Cabot, M. C. (2013). Potential role of acid ceramidase in conversion of cytostatic to cytotoxic end-point in pancreatic cancer cells. *Cancer Chemother Pharmacol*, *71*, 635–645.

Moravcevic, K., Mendrola, J. M., Schmitz, K. R., Wang, Y.-H., Slochower, D., Janmey, P. A., & Lemmon, M. A. (2010). Kinase associated-1 domains drive MARK/PAR1 kinases to membrane targets by binding acidic phospholipids. *Cell*, *143*, 966–77.

Moriyasu, Y., & Inoue, Y. (2008). *Use of protease inhibitors for detecting autophagy in plants. Methods Enzymol*, 451, 557–80.

Mowers, E. E., Sharifi, M. N., & Macleod, K. F. (2016). Autophagy in cancer metastasis. *Oncogene*. http://dx.doi.org/10.1038/onc.2016.333

Moyzis, A. G., Sadoshima, J., & Gustafsson, Å. B. (2015). Mending a broken heart: the role of mitophagy in cardioprotection. *Am J Physiol, 308*, H183-92.

Munro, S., Thomas, K. L., & Abu-Shaar, M. (1993). Molecular characterization of a peripheral receptor for cannabinoids. *Nature*, *365*, 61–65.

Münz, C. (2015). Of LAP, CUPS, and DRibbles - Unconventional use of autophagy proteins for MHC restricted antigen presentation. *Front Immunol, 6,* 200.

Murphy, M. P., Holmgren, A., Larsson, N. G., Halliwell, B., Chang, C. J., Kalyanaraman, B., … Winterbourn, C. C. (2011). Unraveling the biological roles of reactive oxygen species. *Cell Metab*, *13*, 361–6.

Nakatogawa, H., Ichimura, Y., & Ohsumi, Y. (2007). Atg8, a ubiquitin-like protein required for autophagosome formation, mediates membrane tethering and hemifusion. *Cell*, *130*, 165–178.

Nakatogawa, H., Ohbayashi, S., Sakoh-Nakatogawa, M., Kakuta, S., Suzuki, S. W., Kirisako, H., … Ohsumi, Y. (2012). The autophagy-related protein kinase Atg1 interacts with the ubiquitin-like protein Atg8 via the Atg8 family interacting motif to facilitate autophagosome formation. *J Biol Chem*, *287*, 28503–28507.

Narendra, D. P., Jin, S. M., Tanaka, A., Suen, D. F., Gautier, C. A., Shen, J., … Youle, R. J. (2010a). PINK1 is selectively stabilized on impaired mitochondria to activate Parkin. *PLoS Biol*, *8*, e1000298.

Narendra, D. P., Kane, L. A., Hauser, D. N., Fearnley, I. M., & Youle, R. J. (2010b). p62/SQSTM1 is required for Parkin-induced mitochondrial clustering but not mitophagy; VDAC1 is dispensable for both. *Autophagy*, *6*, 1090–1106.

Narendra, D., Tanaka, A., Suen, D. F., & Youle, R. J. (2008). Parkin is recruited selectively to impaired mitochondria and promotes their autophagy. *J Cell Biol*, *183*, 795–803.

Nath, S., Dancourt, J., Shteyn, V., Puente, G., Fong, W. M., Nag, S., … Melia, T. J. (2014). Lipidation of the LC3/GABARAP family of autophagy proteins relies on a

membrane-curvature-sensing domain in Atg3. *Nat Cell Biol*, *16*, 415–24.

Navarro-Yepes, J., Burns, M., Anandhan, A., Khalimonchuk, O., del Razo, L. M., Quintanilla-Vega, B., … Franco, R. (2014). Oxidative stress, redox signaling, and autophagy: cell death *versus* survival. *Antioxid Redox Signal*, *21*, 66–85.

Nemos, C., Mansuy, V., Vernier-Magnin, S., Fraichard, A., Jouvenot, M., & Delage-Mourroux, R. (2003). Expression of gec1/GABARAPL1 versus GABARAP mRNAs in human: Predominance of gec1/GABARAPL1 in the central nervous system. *Mol Brain Res*, *119*, 216–219.

Newman, A. C., Scholefield, C. L., Kemp, A. J., Newman, M., McIver, E. G., Kamal, A., & Wilkinson, S. (2012). TBK1 kinase addiction in lung cancer cells is mediated via autophagy of Tax1bp1/Ndp52 and non-canonical NF-κB signalling. *PLoS One*, *7*, e50672.

Ni, H. M., Williams, J. A., & Ding, W. X. (2015). Mitochondrial dynamics and mitochondrial quality control. *Redox Biol*, *4*, 6–13.

Nieva, J. L., Goñi, F. M., & Alonso, A. (1989). Liposome fusion catalytically induced by phospholipase C. *Biochemistry*, *28*, 7364–7.

Nishida, Y., Arakawa, S., Fujitani, K., Yamaguchi, H., Mizuta, T., Kanaseki, T., … Shimizu, S. (2009). Discovery of Atg5/Atg7-independent alternative macroautophagy. *Nature*, *461*, 654–658.

Nistor, P. A., May, P. W., Tamagnini, F., Randall, A. D., & Caldwell, M. A. (2015). Long-term culture of pluripotent stem-cell-derived human neurons on diamond - A substrate for neurodegeneration research and therapy. *Biomaterials*, *61*, 139–149.

Nixon, R. A. (2013). The role of autophagy in neurodegenerative disease. *Nat Med*, *19*, 983–97.

Noble, G. T., Stefanick, J. F., Ashley, J. D., Kiziltepe, T., & Bilgicer, B. (2014). Ligand-targeted liposome design: challenges and fundamental considerations. *Trends Biotechnol*, *32*, 32–45.

Noda, N. N., & Fujioka, Y. (2015). Atg1 family kinases in autophagy initiation. *Cell Mol Life Sci*, *72*, 3083–3096.

Noda, N. N., & Inagaki, F. (2015). Mechanisms of Autophagy. *Annu Rev Biophys, 44*, 101–122.

Noda, N. N., Ohsumi, Y., & Inagaki, F. (2010). Atg8-family interacting motif crucial for selective autophagy. *FEBS Lett, 584*, 1379–85.

Noda, N. N., Satoo, K., Fujioka, Y., Kumeta, H., Ogura, K., Nakatogawa, H., … Inagaki, F. (2011). Structural basis of Atg8 activation by a homodimeric E1, Atg7. *Mol Cell*, *44*, 462–475.

Novak, I., Kirkin, V., McEwan, D. G., Zhang, J., Wild, P., Rozenknop, A., … Dikic, I.

(2010). Nix is a selective autophagy receptor for mitochondrial clearance. *EMBO Rep*, *11*, 45–51.

Nowikovsky, K., Reipert, S., Devenish, R. J., & Schweyen, R. J. (2007). Mdm38 protein depletion causes loss of mitochondrial K^+/H^+ exchange activity, osmotic swelling and mitophagy. *Cell Death Differ*, *14*, 1647–1656.

O'Sullivan, G. A., Kneussel, M., Elazar, Z., & Betz, H. (2005). GABARAP is not essential for GABA receptor targeting to the synapse. *Eur J Neurosci*, *22*, 2644–2648.

Ogata, M., Hino, S., Saito, A., Morikawa, K., Kondo, S., Kanemoto, S., … Imaizumi, K. (2006). Autophagy is activated for cell survival after endoplasmic reticulum stress. *Mol Cell Biol*, *26*, 9220–9231.

Ogretmen, B., & Hannun, Y. A. (2004). Biologically active sphingolipids in cancer pathogenesis and treatment. *Nat Rev Cancer*, *4*, 604–616.

Okamoto, K. (2014). Organellophagy: Eliminating cellular building blocks via selective autophagy. *J Cell Biol*, *205*, 435–445.

Okamoto, K., Kondo-Okamoto, N., & Ohsumi, Y. (2009). Mitochondria-anchored receptor Atg32 mediates degradation of mitochondria via selective autophagy. *Dev Cell*, *17*, 87–97.

Orsi, A., Razi, M., Dooley, H. C., Robinson, D., Weston, A. E., Collinson, L. M., & Tooze, S. A. (2012). Dynamic and transient interactions of Atg9 with autophagosomes, but not membrane integration, are required for autophagy. *Mol Biol Cell*, *23*, 1860–73.

Osman, C., Voelker, D. R., & Langer, T. (2011). Making heads or tails of phospholipids in mitochondria. *J Cell Biol, 192*, 7–16.

Ostolaza, H., & Goñi, F. M. (1995). Interaction of the bacterial protein toxin alpha-haemolysin with model membranes: protein binding does not always lead to lytic activity. *FEBS Lett*, *371*, 303–306.

Otera, H., Ishihara, N., & Mihara, K. (2013). New insights into the function and regulation of mitochondrial fission. *Biochim Biophys Acta*, *1833*, 1256–68.

Otera, H., Wang, C., Cleland, M. M., Setoguchi, K., Yokota, S., Youle, R. J., & Mihara, K. (2010). Mff is an essential factor for mitochondrial recruitment of Drp1 during mitochondrial fission in mammalian cells. *J Cell Biol*, *191*, 1141–1158.

Pal, R., Miranda, M., & Narayan, M. (2011). Nitrosative stress-induced Parkinsonian Lewy-like aggregates prevented through polyphenolic phytochemical analog intervention. *Biochem Biophys Res Commun*, *404*, 324–329.

Pal, R., Monroe, T. O., Palmieri, M., Sardiello, M., & Rodney, G. G. (2014). Rotenone induces neurotoxicity through Rac1-dependent activation of NADPH oxidase in

SHSY-5Y cells. *FEBS Lett*, *588*, 472–481.

Palsdottir, H., & Hunte, C. (2004). Lipids in membrane protein structures. *Biochim Biophys Acta, 1666,* 2–18.

Pankiv, S., Alemu, E. A., Brech, A., Bruun, J. A., Lamark, T., Overvatn, A., … Johansen, T. (2010). FYCO1 is a Rab7 effector that binds to LC3 and PI3P to mediate microtubule plus end - Directed vesicle transport. *J Cell Biol*, *188*, 253–269.

Pankiv, S., Clausen, T. H., Lamark, T., Brech, A., Bruun, J. A., Outzen, H., … Johansen, T. (2007). p62/SQSTM1 binds directly to Atg8/LC3 to facilitate degradation of ubiquitinated protein aggregates by autophagy. *J BiolChem*, *282*, 24131–24145.

Park, J., Lee, S. B., Lee, S. B., Kim, Y., Song, S., Kim, S., … Chung, J. K. (2006). Mitochondrial dysfunction in Drosophila PINK1 mutants is complemented by parkin. *Nature*, *441*, 1157–1161.

Patsos, H. A., Greenhough, A., Hicks, D. J., Kharusi, M. A. L., Collard, T. J., Lane, J. D., … Williams, A. C. (2010). The endogenous cannabinoid, anandamide, induces COX-2-dependent cell death in apoptosis-resistant colon cancer cells. *Int J Oncol*, *37*, 187–193.

Pattingre, S., Bauvy, C., Levade, T., Levine, B., & Codogno, P. (2009). Ceramide-induced autophagy: To junk or to protect cells? *Autophagy*, *5*, 558–560.

Paz, Y., Elazar, Z., & Fass, D. (2000). Structure of GATE-16, membrane transport modulator and mammalian ortholog of autophagocytosis factor Aut7p. *J Biol Chem, 275*, 25445–25450.

Peddie, C. J., & Collinson, L. M. (2014). Exploring the third dimension: Volume electron microscopy comes of age. *Micron*, *61*, 9–19.

Peralta, E. R., & Edinger, A. L. (2009). Ceramide-induced starvation triggers homeostatic autophagy. *Autophagy*, *5*, 407–409.

Perry, S. W., Norman, J. P., Barbieri, J., Brown, E. B., & Gelbard, H. A. (2011). Mitochondrial membrane potential probes and the proton gradient: A practical usage guide. *Biotechniques, 50 ,* 98–115.

Pertwee, R. G., Howlett, A. C., Abood, M. E., Alexander, S. P., Di Marzo, V., Elphick, M. R., … Ross, R. A. (2010). International Union of Basic and Clinical Pharmacology. LXXIX. Cannabinoid receptors and their ligands: beyond CB(1) and CB(2). *Pharmacol Rev*, *62*, 588–631.

Petersen, N. H. T., Olsen, O. D., Groth-Pedersen, L., Ellegaard, A. M., Bilgin, M., Redmer, S., … Jäättelä, M. (2013). Transformation-associated changes in sphingolipid metabolism sensitize cells to lysosomal cell death induced by

inhibitors of acid sphingomyelinase. *Cancer Cell*, *24*, 379–393.

Pfeifer, U. (1978). Inhibition by insulin of the formation of autophagic vacuoles in rat liver. A morphometric approach to the kinetics of intracellular degradation by autophagy. *J Cell Biol*, *78*, 152–167.

Pickrell, A. M., & Youle, R. J. (2015). The roles of PINK1, Parkin, and mitochondrial fidelity in parkinson's disease. *Neuron*, *85*, 257–73.

Pike, L. J. (2006). Rafts defined: a report on the Keystone Symposium on Lipid Rafts and Cell Function. *J Lipid Res*, *47*, 1597–1598.

Polager, S., Ofir, M., & Ginsberg, D. (2008). E2F1 regulates autophagy and the transcription of autophagy genes. *Oncogene*, *27*, 4860–4864.

Polson, H. E. J., de Lartigue, J., Rigden, D. J., Reedijk, M., Urbé, S., Clague, M. J., & Tooze, S. A. (2010). Mammalian Atg18 (WIPI2) localizes to omegasome-anchored phagophores and positively regulates LC3 lipidation. *Autophagy*, *6*, 506–522.

Poot, M., Zhang, Y. Z., Kramer, J. A., Wells, K. S., Jones, L. J., Hanzel, D. K., … Haugland, R. P. (1996). Analysis of mitochondrial morphology and function with novel fixable fluorescent stains. *J Histochem Cytochem*, *44*, 1363–1372.

Pozuelo-Rubio, M. (2011). Regulation of autophagic activity by 14-3-3ζ proteins associated with class III phosphatidylinositol-3-kinase. *Cell Death Differ*, *18*, 479–92.

Priyadarshini, M., Orosco, L. A., & Panula, P. J. (2013). Oxidative stress and regulation of pink1 in zebrafish (Danio rerio). *PLoS One*, *8*, e81851.

Pryde, K. R., Smith, H. L., Chau, K. Y., & Schapira, A. H. V. (2016). PINK1 disables the anti-fission machinery to segregate damaged mitochondria for mitophagy. *J Cell Biol*, *213*, 163–171.

Pyo, J. O., Jang, M. H., Kwon, Y. K., Lee, H. J., Jun, J. Il, Woo, H. N., … Jung, Y. K. (2005). Essential roles of Atg5 and FADD in autophagic cell death: Dissection of autophagic cell death into vacuole formation and cell death. *J Biol Chem*, *280*, 20722–20729.

Qu, X., Yu, J., Bhagat, G., Furuya, N., Hibshoosh, H., Troxel, A., … Levine, B. (2003). Promotion of tumorigenesis by heterozygous disruption of the beclin 1 autophagy gene. *J Clin Invest*, *112*, 1809–1820.

Ragusa, M. J., Stanley, R. E., & Hurley, J. H. (2012). Architecture of the Atg17 Complex as a Scaffold for Autophagosome Biogenesis. *Cell*, *151*, 1501–1512.

Rambold, A. S., Kostelecky, B., Elia, N., & Lippincott-Schwartz, J. (2011). Tubular network formation protects mitochondria from autophagosomal degradation during nutrient starvation. *Proc Natl Acad Sci U S A*, *108*, 10190–10195.

Rana, A., Rera, M., & Walker, D. W. (2013). Parkin overexpression during aging

reduces proteotoxicity, alters mitochondrial dynamics, and extends lifespan. *Proc Natl Acad Sci U S A*, *110*, 8638–43.

Randow, F., & Youle, R. J. (2014). Self and nonself: How autophagy targets mitochondria and bacteria. *Cell Host Microbe*, *15*, 403–11.

Rao, Y., Perna, M. G., Hofmann, B., Beier, V., & Wollert, T. (2016). The Atg1-kinase complex tethers Atg9-vesicles to initiate autophagy. *Nat Commun*, *7*, 1–13.

Raunser, S., & Walz, T. (2009). Electron crystallography as a technique to study the structure on membrane proteins in a lipidic environment. *Annu Rev Biophys*, *38*, 89–105.

Ravikumar, B., Berger, Z., Vacher, C., O'Kane, C. J., & Rubinsztein, D. C. (2006). Rapamycin pre-treatment protects against apoptosis. *Hum Mol Genet*, *15*, 1209–1216.

Ravikumar, B., Duden, R., & Rubinsztein, D. C. (2002). Aggregate-prone proteins with polyglutamine and polyalanine expansions are degraded by autophagy. *Human Mol Genet*, *11*, 1107–1117.

Ravikumar, B., Moreau, K., Jahreiss, L., Puri, C., & Rubinsztein, D. C. (2010). Plasma membrane contributes to the formation of pre-autophagosomal structures. *Nat Cell Biol*, *12*, 747–757.

Read, R., Savelieva, K., Baker, K., Hansen, G., & Vogel, P. (2011). Histopathological and neurological features of Atg4b knockout mice. *Vet Pathol*, *48*, 486–494.

Reeves, J. P., & Dowben, R. M. (1969). Formation and properties of thin-walled phospholipid vesicles. *J Cell Physiol*, *73*, 49–60.

Reggiori, F., & Klionsky, D. J. (2005). Autophagosomes: Biogenesis from scratch? *Curr Opin Cell Biol*, *17*, 415–22.

Reggiori, F., Komatsu, M., Finley, K., & Simonsen, A. (2012). Autophagy: More than a nonselective pathway. *Int J Cell Biol*, *2012*, 219625.

Ren, M., Phoon, C. K. L., & Schlame, M. (2014). Metabolism and function of mitochondrial cardiolipin. *Prog Lipid Res, 55*, 1–16.

Reynolds, E. S. (1963). The use of lead citrate at high pH as an electron-opaque stain in electron microscopy. *J Cell Biol*, *17*, 208–212.

Rich, P. R., & Maréchal, A. (2010). The mitochondrial respiratory chain. *Essays Biochem*, *47*, 1–23.

Riley, B. E., Lougheed, J. C., Callaway, K., Velasquez, M., Brecht, E., Nguyen, L., … Johnston, J. A. (2013). Structure and function of Parkin E3 ubiquitin ligase reveals aspects of RING and HECT ligases. *Nat Commun*, *4*, 1982.

Romanov, J., Walczak, M., Ibiricu, I., Schüchner, S., Ogris, E., Kraft, C., & Martens, S. (2012). Mechanism and functions of membrane binding by the Atg5–Atg12/Atg16

complex during autophagosome formation. *EMBO J*, *31*, 4304–4317.

Rostislavleva, K., Soler, N., Ohashi, Y., Zhang, L., Pardon, E., Burke, J. E., … Williams, R. L. (2015). Structure and flexibility of the endosomal Vps34 complex reveals the basis of its function on membranes. *Science*, *350*, aac7365-aac7365.

Rouschop, K. M. A., Ramaekers, C. H. M. A., Schaaf, M. B. E., Keulers, T. G. H., Savelkouls, K. G. M., Lambin, P., … Wouters, B. G. (2009). Autophagy is required during cycling hypoxia to lower production of reactive oxygen species. *Radiother Oncol*, *92*, 411–416.

Rüb, C., Wilkening, A., & Voos, W. (2016). Mitochondrial quality control by the Pink1/Parkin system. *Cell Tissue Res*. http://dx.doi.org/10.1007/s00441-016-2485-8

Rubinsztein, D. C. (2006). The roles of intracellular protein-degradation pathways in neurodegeneration. *Nature*, *443*, 780–6.

Rubinsztein, D. C., Gestwicki, J. E., Murphy, L. O., & Klionsky, D. J. (2007). Potential therapeutic applications of autophagy. *Nat Rev Drug Discov*, *6*, 304–312.

Ruiz-Argüello, M. B., Basáñez, G., Goñi, F. M., & Alonso, A. (1996). Different effects of enzyme-generated ceramides and diacylglycerols in phospholipid membrane fusion and leakage. *J Biol Chem*, *271*, 26616–26621.

Ruiz-Argüello, M. B., Veiga, M. P., Arrondo, J. L. R., Goñi, F. M., & Alonso, A. (2002). Sphingomyelinase cleavage of sphingomyelin in pure and mixed lipid membranes. Influence of the physical state of the sphingolipid. *Chem Phys Lipids*, *114*, 11–20.

Russell, M. R. G., Lerner, T. R., Burden, J. J., Nkwe, D. O., Pelchen-Matthews, A., Domart, M. C., … Collinson, L. M. (2016). 3D correlative light and electron microscopy of cultured cells using serial blockface scanning electron microscopy. *J Cell Sci*. http://dx.doi.org/10.1242/jcs.188433

Ruvolo, P. P., Deng, X., Ito, T., Carr, B. K., & May, W. S. (1999). Ceramide induces Bcl2 dephosphorylation via a mechanism involving mitochondrial PP2A. *J Biol Chem*, *274*, 20296–20300.

Sagiv, Y., Legesse-Miller, A., Porat, A., & Elazar, Z. (2000). GATE-16, a membrane transport modulator, interacts with NSF and the Golgi v-SNARE GOS-28. *EMBO J*, *19*, 1494–504.

Sakakibara, K., Eiyama, A., Suzuki, S. W., Sakoh-Nakatogawa, M., Okumura, N., Tani, M., … Okamoto, K. (2015). Phospholipid methylation controls Atg32-mediated mitophagy and Atg8 recycling. *EMBO J*, *34*, 2703–19.

Salazar, M., Carracedo, A., Salanueva, Í. J., Hernández-Tiedra, S., Lorente, M., Egia, A., … Velasco, G. (2009). Cannabinoid action induces autophagy-mediated cell death through stimulation of ER stress in human glioma cells. *J Clin Invest, 119*,

1359–1372.

Salazar, M., Lorente, M., García-Taboada, E., Hernández-Tiedra, S., Davila, D., Francis, S. E., … Velasco, G. (2013). The pseudokinase tribbles homologue-3 plays a crucial role in cannabinoid anticancer action. *Biochim Biophys Acta*, *1831*, 1573–1578.

Sambrook, J., & MacCallum, P. (2001). *Molecular Cloning: A Laboratory Manual.* 3rd edition. Cold Spring Harb Lab Press.

Sandoval, H., Thiagarajan, P., Dasgupta, S. K., Schumacher, A., Prchal, J. T., Chen, M., & Wang, J. (2008). Essential role for Nix in autophagic maturation of erythroid cells. *Nature*, *454*, 232–235.

Santel, A., & Fuller, M. T. (2001). Control of mitochondrial morphology by a human mitofusin. *J Cell Sci*, *114*, 867–874.

Schaaf, M. B. E., Keulers, T. G., Vooijs, M. A., & Rouschop, K. M. A. (2016). LC3/GABARAP family proteins: autophagy-(un)related functions. *FASEB J. http://dx.doi.org/10.1096/fj.201600698R*

Schenck, M., Carpinteiro, A., Grassmé, H., Lang, F., & Gulbins, E. (2007). Ceramide: Physiological and pathophysiological aspects. *Arch Biochem Biophys, 462,* 171–5.

Scherz-Shouval, R., & Elazar, Z. (2007). ROS, mitochondria and the regulation of autophagy. *Trends Cell Biol*, *17*, 422–427.

Schlame, M. (2008). Thematic Review Series: Glycerolipids. Cardiolipin synthesis for the assembly of bacterial and mitochondrial membranes. *J Lipid Res*, *49*, 1607–1620.

Schlame, M. (2013). Cardiolipin remodeling and the function of tafazzin. *Biochim Biophys Acta, 1831,* 582–8.

Schlame, M., Acehan, D., Berno, B., Xu, Y., Valvo, S., Ren, M., … Epand, R. M. (2012). The physical state of lipid substrates provides transacylation specificity for tafazzin. *Nat Chem Biol*, *8*, 862–9.

Schlame, M., Ren, M., Xu, Y., Greenberg, M. L., & Haller, I. (2005). Molecular symmetry in mitochondrial cardiolipins. *Chem Phys Lipids*, *138*, 38–49.

Schlattner, U., Tokarska-Schlattner, M., Ramirez, S., Tyurina, Y. Y., Amoscato, A. A., Mohammadyani, D., … Kagan, V. E. (2013). Dual function of mitochondrial Nm23-H4 protein in phosphotransfer and intermembrane lipid transfer: A cardiolipin-dependent switch. *J Biol Chem*, *288*, 111–121.

Schreiber, A., & Peter, M. (2014). Substrate recognition in selective autophagy and the ubiquitin-proteasome system. *Biochim Biophys Acta, 1843*, 163–81.

Schwarten, M., Stoldt, M., Mohrlüder, J., & Willbold, D. (2010). Solution structure of Atg8 reveals conformational polymorphism of the N-terminal domain. *Biochem*

Biophys Res Commun, *395*, 426–431.

Schweers, R. L., Zhang, J., Randall, M. S., Loyd, M. R., Li, W., Dorsey, F. C., … Ney, P. A. (2007). NIX is required for programmed mitochondrial clearance during reticulocyte maturation. *Proc Natl Acad Sci U S A*, *104*, 19500–19505.

Sengupta, A., Molkentin, J. D., & Yutzey, K. E. (2009). FoxO transcription factors promote autophagy in cardiomyocytes. *J Biol Chem*, *284*, 28319–28331.

Sentelle, R. D., Senkal, C. E., Jiang, W., Ponnusamy, S., Gencer, S., Panneer Selvam, S., … Ogretmen, B. (2012). Ceramide targets autophagosomes to mitochondria and induces lethal mitophagy. *Nat Chem Biol*, *8*, 831–8.

Serrano-Puebla, A., & Boya, P. (2015). Lysosomal membrane permeabilization in cell death: new evidence and implications for health and disease. *Ann N Y Acad Sci, 1371,* 30–44.

Shaid, S., Brandts, C. H., Serve, H., & Dikic, I. (2013). Ubiquitination and selective autophagy. *Cell Death Differ*, *20*, 21–30.

Shaikh, S. B., & Nicholson, L. F. (2009). Effects of chronic low dose rotenone treatment on human microglial cells. *Mol Neurodegener*, *4*, 55.

Shaikh, S. R., & Edidin, M. A. (2006). Membranes are not just rafts. *Chem Phys Lipids*, 144, 1–3.

Shaner, N. C., Campbell, R. E., Steinbach, P. A., Giepmans, B. N. G., Palmer, A. E., & Tsien, R. Y. (2004). Improved monomeric red, orange and yellow fluorescent proteins derived from Discosoma sp. red fluorescent protein. *Nat Biotechnol*, *22*, 1567–72.

Shatz, O., Holland, P., Elazar, Z., & Simonsen, A. (2016). Complex relations between phospholipids, autophagy, and neutral lipids. *Trends Biochem Sci, 41,* 907–923.

Shen, H. M., & Codogno, P. (2011). Autophagic cell death: Loch Ness monster or endangered species? *Autophagy*, *7*, 457–65.

Shen, H. M., & Mizushima, N. (2014). At the end of the autophagic road: An emerging understanding of lysosomal functions in autophagy. *Trends Biochem Sci, 39,* 61–71.

Shen, S., Kepp, O., & Kroemer, G. (2012). The end of autophagic cell death? *Autophagy*. 8, 1–3.

Shen, S., Kepp, O., Michaud, M., Martins, I., Minoux, H., Métivier, D., … Kroemer, G. (2011). Association and dissociation of autophagy, apoptosis and necrosis by systematic chemical study. *Oncogene*, *30*, 4544–4556.

Shi, Y., Kirwan, P., Smith, J., Robinson, H. P. C., & Livesey, F. J. (2012). Human cerebral cortex development from pluripotent stem cells to functional excitatory synapses. *Nat Neurosci*, *15*, 477–86.

Shiba-Fukushima, K., Imai, Y., Yoshida, S., Ishihama, Y., Kanao, T., Sato, S., & Hattori, N. (2012). PINK1-mediated phosphorylation of the Parkin ubiquitin-like domain primes mitochondrial translocation of Parkin and regulates mitophagy. *Sci Rep*, *2*, 1002.

Shibutani, S. T., & Yoshimori, T. (2014). A current perspective of autophagosome biogenesis. *Cell Res*, *24*, 58–68.

Shimizu, S., Kanaseki, T., Mizushima, N., Mizuta, T., Arakawa-Kobayashi, S., Thompson, C. B., & Tsujimoto, Y. (2004). Role of Bcl-2 family proteins in a non-apoptotic programmed cell death dependent on autophagy genes. *Nat Cell Biol*, *6*, 1221–1228.

Shpilka, T., Weidberg, H., Pietrokovski, S., & Elazar, Z. (2011). Atg8: an autophagy-related ubiquitin-like protein family. *Genome Biol*, *12*, 226.

Shu, X., Lev-Ram, V., Deerinck, T. J., Qi, Y., Ramko, E. B., Davidson, M. W., … Tsien, R. Y. (2011). A genetically encoded tag for correlated light and electron microscopy of intact cells, tissues, and organisms. *PLoS Biol*, *9*, e1001041.

Shvets, E., Abada, A., Weidberg, H., & Elazar, Z. (2011). Dissecting the involvement of LC3B and GATE-16 in p62 recruitment into autophagosomes. *Autophagy*, *7*, 683–688.

Shvets, E., Fass, E., Scherz-Shouval, R., & Elazar, Z. (2008). The N-terminus and Phe52 residue of LC3 recruit p62/SQSTM1 into autophagosomes. *J Cell Sci*, *121*, 2685–2695.

Sica, V., Galluzzi, L., Bravo-San Pedro, J. M., Izzo, V., Maiuri, M. C., & Kroemer, G. (2015). Organelle-specific initiation of autophagy. *Mol Cell*, *59*, 522–39.

Simons, K., & Ikonen, E. (1997). Functional rafts in cell membranes. *Nature*, *387*, 569–72.

Singer, S. J., & Nicolson, G. L. (1972). The fluid mosaic model of the structure of cell membranes. *Science*, *175*, 720–31.

Singh, S. B., Ornatowski, W., Vergne, I., Naylor, J., Delgado, M., Roberts, E., … Deretic, V. (2010). Human IRGM regulates autophagy and cell-autonomous immunity functions through mitochondria. *Nat Cell Biol*, *12*, 1154–1165.

Smirnova, E., Griparic, L., Shurland, D.-L., & Bliek, A. M. van der. (2001). Dynamin-related protein Drp1 is required for mitochondrial division in mammalian cells. *Mol Biol Cell*, *12*, 2245–2256.

Soloaga, A., Ramírez, J. M., & Goñi, F. M. (1998). Reversible denaturation, self-aggregation, and membrane activity of Escherichia coli α-hemolysin, a protein stable in 6 M urea. *Biochemistry*, *37*, 6387–6393.

Son, J. H., Hee Shim, J., Kim, K.-H., Ha, J.-Y., & Young Han, J. (2012). Neuronal

autophagy and neurodegenerative diseases. *Exp Mol Med*, *44*, 89–98.

Sorice, M., Circella, A., Cristea, I., Garofalo, T., Di Renzo, L., Alessandri, C., … Esposti, M. D. (2004). Cardiolipin and its metabolites move from mitochondria to other cellular membranes during death receptor-mediated apoptosis. *Cell Death Differ*, *11*, 1133–1145.

Spiegel, S., & Milstien, S. (2003). Exogenous and intracellularly generated sphingosine 1-phosphate can regulate cellular processes by divergent pathways. *Biochem Soc Trans*, *31*, 1216–1219.

Spiegelhalter, C., Laporte, J. F., & Schwab, Y. (2014). Correlative light and electron microscopy: From live cell dynamic to 3D ultrastructure. *Methods Mol Biol*, *1117*, 485–501.

Spina, S., Van Laar, A. D., Murrell, J. R., Hamilton, R. L., Kofler, J. K., Epperson, F., … Ghetti, B. (2013). Phenotypic variability in three families with valosin-containing protein mutation. *J Neurol*, *20*, 251–258.

Stadel, D., Millarte, V., Tillmann, K. D., Huber, J., Tamin-Yecheskel, B. C., Akutsu, M., … Behrends, C. (2015). TECPR2 cooperates with LC3C to regulate COPII-dependent ER export. *Mol Cell*, *60*, 89–104.

Stancevic, B., & Kolesnick, R. (2010). Ceramide-rich platforms in transmembrane signaling. *FEBS Lett, 584*,1728–40.

Stangler, T., Mayr, L. M., & Willbold, D. (2002). Solution structure of human GABA(A) receptor-associated protein GABARAP: implications for biolgoical funcrion and its regulation. *J Biol Chem*, *277*, 13363–13366.

Stanley, R. E., Ragusa, M. J., & Hurley, J. H. (2014). The beginning of the end: how scaffolds nucleate autophagosome biogenesis. *Trends Cell Biol*, *24*, 73–81.

Stenmark, H., Aasland, R., Toh, B. H., & D'Arrigo, A. (1996). Endosomal localization of the autoantigen EEA1 is mediated by a zinc-binding FYVE finger. *J Biol Chem*, *271*, 24048–24054.

Stolz, A., Ernst, A., & Dikic, I. (2014). Cargo recognition and trafficking in selective autophagy. *Nat Cell Biol*, *16*, 495–501.

Studer, D., Humbel, B. M., & Chiquet, M. (2008). Electron microscopy of high pressure frozen samples: Bridging the gap between cellular ultrastructure and atomic resolution. *Histochem Cell Biol*, *130*, 877–89.

Subirade, M., Salesse, C., Marion, D., & Pézolet, M. (1995). Interaction of a nonspecific wheat lipid transfer protein with phospholipid monolayers imaged by fluorescence microscopy and studied by infrared spectroscopy. *Biophys J*, *69*, 974–988.

Sugawara, K., Suzuki, N. N., Fujioka, Y., Mizushima, N., Ohsumi, Y., & Inagaki, F. (2004). The crystal structure of microtubule-associated protein light chain 3, a

mammalian homologue of Saccharomyces cerevisiae Atg8. *Genes Cells*, *9*, 611–618.

Sugawara, K., Suzuki, N. N., Fujioka, Y., Mizushima, N., Ohsumi, Y., & Inagaki, F. (2005). Structural basis for the specificity and catalysis of human Atg4B responsible for mammalian autophagy. *J Biol Chem*, *280*, 40058–40065.

Sugiura, T., Kondo, S., Sukagawa, A., Nakane, S., Shinoda, A., Itoh, K., … Waku, K. (1995). 2-Arachidonoylglycerol: a possible endogenous cannabinoid receptor ligand in brain. *Biochem Biophys Res Commun*, *215*, 89–97.

Suzuki, K., Kirisako, T., Kamada, Y., Mizushima, N., Noda, T., & Ohsumi, Y. (2001). The pre-autophagosomal structure organized by concerted functions of APG genes is essential for autophagosome formation. *EMBO J*, *20*, 5971–5981.

Suzuki, K., Kondo, C., Morimoto, M., & Ohsumi, Y. (2010). Selective transport of alpha-mannosidase by autophagic pathways: Identification of a novel receptor, Atg34p. *J Biol Chem*, *285*, 30019–30025.

Svenning, S., & Johansen, T. (2013). Selective autophagy. *Essays Biochem, 55*, 79–92.

Swamy, M. J., & Sankhala, R. S. (2013). Probing the thermodynamics of protein-lipid interactions by isothermal titration calorimetry. *Methods Mol Biol*, *974*, 37–53.

Szoka, F., & Papahadjopoulos, D. (1980). Comparative properties and methods of preparation of lipid vesicles (liposomes). *Annu Rev Biophys, 9*, 467–508.

Taanman, J.-W. (1999). The mitochondrial genome: structure, transcription, translation and replication. *Biochim Biophys Acta, 1410*, 103–123.

Takeshige, K., Baba, M., Tsuboi, S., Noda, T., & Ohsumi, Y. (1992). Autophagy in yeast demonstrated with proteinase-deficient mutants and conditions for its induction. *J Cell Biol*, *119*, 301–311.

Tal, R., Winter, G., Ecker, N., Klionsky, D. J., & Abeliovich, H. (2007). Aup1p, a yeast mitochondrial protein phosphatase homolog, is required for efficient stationary phase mitophagy and cell survival. *J Biol Chem*, *282*, 5617–5624.

Tamura, Y., Harada, Y., Nishikawa, S. I., Yamano, K., Kamiya, M., Shiota, T., … Endo, T. (2013). Tam41 is a CDP-diacylglycerol synthase required for cardiolipin biosynthesis in mitochondria. *Cell Metab*, *17*, 709–718.

Tanaka, A., Cleland, M. M., Xu, S., Narendra, D. P., Suen, D. F., Karbowski, M., & Youle, R. J. (2010). Proteasome and p97 mediate mitophagy and degradation of mitofusins induced by Parkin. *J Cell Biol*, *191*, 1367–1380.

Tang, F., Watkins, J. W., Bermudez, M., Gray, R., Gaban, A., Portie, K., … Craciun, G. (2008). A life-span extending form of autophagy employs the vacuole-vacuole fusion machinery. *Autophagy*, *4*, 874–886.

Tanida, I., Komatsu, M., Ueno, T., & Kominami, E. (2003). GATE-16 and GABARAP are authentic modifiers mediated by Apg7 and Apg3. *Biochem Biophys Res Commun, 300*, 637–644.

Tanida, I., Sou, Y. S., Minematsu-Ikeguchi, N., Ueno, T., & Kominami, E. (2006). Atg8L/Apg8L is the fourth mammalian modifier of mammalian Atg8 conjugation mediated by human Atg4B, Atg7 and Atg3. *FEBS J*, *273*, 2553–2562.

Tanida, I., Tanida-Miyake, E., Komatsu, M., Ueno, T., & Kominami, E. (2002). Human Apg3p/Aut1p homologue is an authentic E2 enzyme for multiple substrates, GATE-16, GABARAP, and MAP-LC3, and facilitates the conjugation of hApg12p to hApg5p. *J Biol Chem*, *277*, 13739–13744.

Tanida, I., Ueno, T., & Kominami, E. (2004a). Human light chain 3/MAP1LC3B Is cleaved at its carboxyl-terminal Met 121 to expose Gly120 for lipidation and targeting to autophagosomal membranes. *J Biol Chem*, *279*, 47704–47710.

Tanida, I., Ueno, T., & Kominami, E. (2004b). LC3 conjugation system in mammalian autophagy. *International J Biochem Cell Biol*, *36*, 2503–2518.

Tanida, I., Wakabayashi, M., Kanematsu, T., Minematsu-Ikeguchi, N., Sou, Y. S., Hirata, M., … Kominami, E. (2006). Lysosomal turnover of GABARAP-phospholipid conjugate is activated during differentiation of C2C12 cells to myotubes without inactivation of the mTor kinase-signaling pathway. *Autophagy*, *2*, 264–271.

Tasset, I., & Cuervo, A. M. (2016). Role of chaperone-mediated autophagy in metabolism. *FEBS J*, *283*, 2403–13.

Tatsuta, T., & Langer, T. (2008). Quality control of mitochondria: protection against neurodegeneration and ageing. *EMBO J*, *27*, 306–14.

Thurston, T. L. M., Ryzhakov, G., Bloor, S., von Muhlinen, N., & Randow, F. (2009). The TBK1 adaptor and autophagy receptor NDP52 restricts the proliferation of ubiquitin-coated bacteria. *Nat Immunol*, *10*, 1215–1221.

Tian, H. F., Feng, J. M., & Wen, J. F. (2012). The evolution of cardiolipin biosynthesis and maturation pathways and its implications for the evolution of eukaryotes. *BMC Evol Biol*, *12*, 32.

Tolkovsky, A. M. (2009). Mitophagy. *Biochim Biophys Acta*, *1793*, 1508–1515.

Tomishige, M., Sako, Y., & Kusumi, A. (1998). Regulation mechanism of the lateral diffusion of band 3 in erythrocyte membranes by the membrane skeleton. *J Cell Biol*, *142*, 989–1000.

Tomiuk, S., Zumbansen, M., & Stoffel, W. (2000). Characterization and subcellular localization of murine and human magnesium-dependent neutral sphingomyelinase. *J Biol Chem*, *275*, 5710–5717.

Tondera, D., Grandemange, S., Jourdain, A., Karbowski, M., Mattenberger, Y., Herzig, S., … Martinou, J.-C. (2009). SLP-2 is required for stress-induced mitochondrial hyperfusion. *EMBO J*, *28*, 1589–1600.

Tooze, S. A. (2010). The role of membrane proteins in mammalian autophagy. *Semin Cell Dev Biol*, *21*, 677–682.

Tooze, S. A., & Yoshimori, T. (2010). The origin of the autophagosomal membrane. *Nat Cell Biol*, *12*, 831–835.

Trempe, J. F., & Fon, E. A. (2013). Structure and function of Parkin, PINK1, and DJ-1, the three musketeers of neuroprotection. *Front Neurol*, *4,* 38.

Twig, G., Elorza, A., Molina, A. J. A., Mohamed, H., Wikstrom, J. D., Walzer, G., … Shirihai, O. S. (2008). Fission and selective fusion govern mitochondrial segregation and elimination by autophagy. *EMBO J*, *27*, 433–446.

Uehara, T., Nakamura, T., Yao, D., Shi, Z.-Q., Gu, Z., Ma, Y., … Lipton, S. A. (2006). S-nitrosylated protein-disulphide isomerase links protein misfolding to neurodegeneration. *Nature*, *441*, 513–517.

Valente, E. M., Abou-Sleiman, P. M., Caputo, V., Muqit, M. M., Harvey, K., Gispert, S., … Wood, N. W. (2004). Hereditary early-onset Parkinson's disease caused by mutations in PINK1. *Science*, *304*, 1158–1160.

Van, Q., Liu, J., Lu, B., Feingold, K. R., Shi, Y., Lee, R. M., & Hatch, G. M. (2007). Phospholipid scramblase-3 regulates cardiolipin de novo biosynthesis and its resynthesis in growing HeLa cells. *Biochem J*, *401*, 103–109.

van Meer, G. (2005). Cellular lipidomics. *EMBO J*, *24*, 3159–65.

van Meer, G., Voelker, D. R., & Feigenson, G. W. (2008). Membrane lipids: where they are and how they behave. *Nat Rev Mol Cell Biol*, *9*, 112–124.

van Rijnsoever, C., Oorschot, V., & Klumperman, J. (2008). Correlative light-electron microscopy (CLEM) combining live-cell imaging and immunolabeling of ultrathin cryosections. *Nat Methods*, *5*, 973–80.

van Weering, J. R. T., Brown, E., Sharp, T. H., Mantell, J., Cullen, P. J., & Verkade, P. (2010). *Intracellular membrane traffic at high resolution*. *Methods Cell Biol*, 96, 619–48.

van Zutphen, T., Baerends, R. J. S., Susanna, K. A., de Jong, A., Kuipers, O. P., Veenhuis, M., & van der Klei, I. J. (2010). Adaptation of Hansenula polymorpha to methanol: a transcriptome analysis. *BMC Genomics*, *11*, 1.

Veatch, S. L., & Keller, S. L. (2005). Miscibility phase diagrams of giant vesicles containing sphingomyelin. *Phys Rev Lett*, *94*, 148101.

Velasco, G., Sánchez, C., & Guzmán, M. (2012). Towards the use of cannabinoids as antitumour agents. *Nat Rev Cancer*, *12*, 436–444.

Venable, M. E., Bielawska, A., & Obeid, L. M. (1996). Ceramide inhibits phospholipase D in a cell-free system. *J Biol Chem*, *271*, 24800–24805.

Verkade, P. (2008). Moving EM: The Rapid Transfer System as a new tool for correlative light and electron microscopy and high throughput for high-pressure freezing. *J Microsc*, *230*, 317–328.

Vidal, R. L., Matus, S., Bargsted, L., & Hetz, C. (2014). Targeting autophagy in neurodegenerative diseases. *Trends Pharmacol Sci*, *35*, 583–591.

Vieira, C. R., Munoz-Olaya, J. M., Sot, J., Jiménez-Baranda, S., Izquierdo-Useros, N., Abad, J. L., … Goñi, F. M. (2010). Dihydrosphingomyelin impairs HIV-1 infection by rigidifying liquid-ordered membrane domains. *Chem Biol*, *17*, 766–775.

Vives-Bauza, C., Zhou, C., Huang, Y., Cui, M., de Vries, R. L. A., Kim, J., … Przedborski, S. (2010). PINK1-dependent recruitment of Parkin to mitochondria in mitophagy. *Proc Natl Acad Sci U S A*, *107*, 378–383.

von Muhlinen, N., Akutsu, M., Ravenhill, B. J., Foeglein, Á., Bloor, S., Rutherford, T. J., … Randow, F. (2012). LC3C, bound selectively by a noncanonical LIR motif in NDP52, is required for antibacterial autophagy. *Mol Cell*, *48*, 329–342.

Walczak, M., & Martens, S. (2013). Dissecting the role of the Atg12-Atg5-Atg16 complex during autophagosome formation. *Autophagy*, *9*, 424–425.

Wang, H., Bedford, F. K., Brandon, N. J., Moss, S. J., & Olsen, R. W. (1999). GABA(A)-receptor-associated protein links GABA(A) receptors and the cytoskeleton. *Nature*, *397*, 69–72.

Wang, L., Chen, M., Yang, J., & Zhang, Z. (2013). LC3 fluorescent puncta in autophagosomes or in protein aggregates can be distinguished by FRAP analysis in living cells. *Autophagy*, *9*, 756–769.

Wang, X., Winter, D., Ashrafi, G., Schlehe, J., Wong, Y. L., Selkoe, D., … Schwarz, T. L. (2011). PINK1 and Parkin target miro for phosphorylation and degradation to arrest mitochondrial motility. *Cell*, *147*, 893–906.

Wang, Y., Nartiss, Y., Steipe, B., McQuibban, G. A., & Kim, P. K. (2012). ROS-induced mitochondrial depolarization initiates PARK2/PARKIN-dependent mitochondrial degradation by autophagy. *Autophagy*, *8*, 1462–1476.

Watts, G. D. J., Wymer, J., Kovach, M. J., Mehta, S. G., Mumm, S., Darvish, D., … Kimonis, V. E. (2004). Inclusion body myopathy associated with Paget disease of bone and frontotemporal dementia is caused by mutant valosin-containing protein. *Nat Genet*, *36*, 377–381.

Wauer, T., & Komander, D. (2013). Structure of the human Parkin ligase domain in an autoinhibited state. *EMBO J*, *32*, 2099–2112.

Webber, J. L., Young, A. R. J., & Tooze, S. A. (2007). Atg9 trafficking in Mammalian

cells. *Autophagy*, *3*, 54–6.

Weidberg, H., Shpilka, T., Shvets, E., Abada, A., Shimron, F., & Elazar, Z. (2011). LC3 and GATE-16 N termini mediate membrane fusion processes required for autophagosome biogenesis. *Dev Cell*, *20*, 444–454.

Weidberg, H., Shvets, E., Shpilka, T., Shimron, F., Shinder, V., & Elazar, Z. (2010). LC3 and GATE-16/GABARAP subfamilies are both essential yet act differently in autophagosome biogenesis. *EMBO J, 29*, 1792–1802.

Weiergräber, O. H., Mohrlüder, J., & Willbold, D. (2013). Atg8 Family Proteins — Autophagy and Beyond. *Autophagy - A Double-Edged Sword - Cell Survival or Death?*, *2*, 13–45.

Wild, P., Farhan, H., McEwan, D. G., Wagner, S., Rogov, V. V, Brady, N. R., … Dikic, I. (2011). Phosphorylation of the autophagy receptor optineurin restricts Salmonella growth. *Science*, *333*, 228–33.

Wild, P., McEwan, D. G., & Dikic, I. (2014). The LC3 interactome at a glance. *Journal of Cell Science*, *127*(Pt 1), 3–9. https://doi.org/10.1242/jcs.140426

Wilhelmy, L. (1863). Ueber die Abhängigkeit der Capillaritäts-Constanten des Alkohols von Substanz und Gestalt des benetzten festen Körpers. *Ann Physik*, *195*, 177–217.

Winklhofer, K. F. (2014). Parkin and mitochondrial quality control: Toward assembling the puzzle. *Trends Cell Biol, 24,* 332–41.

Wirawan, E., Vanden Berghe, T., Lippens, S., Agostinis, P., & Vandenabeele, P. (2012). Autophagy: for better or for worse. *Cell Res*, *22*, 43–61.

Wong, Y. C., & Holzbaur, E. L. F. (2014). Optineurin is an autophagy receptor for damaged mitochondria in parkin-mediated mitophagy that is disrupted by an ALS-linked mutation. *Proc Natl Acad Sci U S A*, *111*, 4439-48.

Xia, C., Meng, Q., Liu, L. Z., Rojanasakul, Y., Wang, X. R., & Jiang, B. H. (2007). Reactive oxygen species regulate angiogenesis and tumor growth through vascular endothelial growth factor. *Cancer Res*, *67*, 10823–10830.

Xie, Z., Nair, U., & Klionsky, D. J. (2008). Atg8 controls phagophore expansion during autophagosome formation. *Mol Biol Cell*, *19*, 3290–8.

Xin, Y., Yu, L., Chen, Z., Zheng, L., Fu, Q., Jiang, J., … Zhao, S. (2001). Cloning, expression patterns, and chromosome localization of three human and two mouse homologues of GABA(A) receptor-associated protein. *Genomics*, *74*, 408–13.

Xu, C., Bailly-Maitre, B., & Reed, J. C. (2005). Endoplasmic reticulum stress: cell life and death decisions. *J Clin Invest*, *115*, 2656–64.

Xu, Y., Condell, M., Plesken, H., Edelman-Novemsky, I., Ma, J., Ren, M., & Schlame, M. (2006). A Drosophila model of Barth syndrome. *Proc Natl Acad Sci U S A*, *103*,

11584–8.

Xu, Y., Hortsman, H., Seet, L., Wong, S. H., & Hong, W. (2001). SNX3 regulates endosomal function through its PX-domain-mediated interaction with PtdIns(3)P. *Nat Cell Biol*, *3*, 658–666.

Yakes, F. M., & Van Houten, B. (1997). Mitochondrial DNA damage is more extensive and persists longer than nuclear DNA damage in human cells following oxidative stress. *Proc Natl Acad Sci U S A*, *94*, 514–519.

Yang, J. Y., & Yang, W. Y. (2013). Bit-by-bit autophagic removal of parkin-labelled mitochondria. *Nat Commun*, *4*, 2428.

Yang, S., Wang, X., Contino, G., Liesa, M., Sahin, E., Ying, H., … Kimmelman, A. C. (2011). Pancreatic cancers require autophagy for tumor growth. *Genes Dev*, *25*, 717–729.

Yang, Y. P., Hu, L. F., Zheng, H. F., Mao, C. J., Hu, W. D., Xiong, K. P., … Liu, C. F. (2013). Application and interpretation of current autophagy inhibitors and activators. *Acta Pharmacol Sin*, *345*, 625–635.

Yang, Z., & Klionsky, D. J. (2010). Mammalian autophagy: Core molecular machinery and signaling regulation. *Curr Opin Cell Biol, 22,* 124–31.

Yethon, J. A., Epand, R. F., Leber, B., Epand, R. M., & Andrews, D. W. (2003). Interaction with a membrane surface triggers a reversible conformational change in Bax normally associated with induction of apoptosis. *J Biol Chem*, *278*, 48935–48941.

Yingchoncharoen, P., Kalinowski, D. S., & Richardson, D. R. (2016). Lipid-based drug delivery systems in cancer therapy: What is available and what is yet to come. *Pharmacol Rev*, *68*, 701–87.

Ylä-Anttila, P., Vihinen, H., Jokitalo, E., & Eskelinen, E. L. (2009). 3D tomography reveals connections between the phagophore and endoplasmic reticulum. *Autophagy*, *5*, 1180–1185.

Yoshii, S. R., & Mizushima, N. (2015). Autophagy machinery in the context of mammalian mitophagy. *Biochim Biophys Acta* , *1853*, 2797–801.

Youle, R. J., & Narendra, D. P. (2011). Mechanisms of mitophagy. *Nat Rev Mol Cell Biol*, *12*, 9–14.

Youle, R. J., & van der Bliek, A. M. (2012). Mitochondrial fission, fusion, and stress. *Science*, *337*, 1062–5.

Yu, L., Alva, A., Su, H., Dutt, P., Freundt, E., Welsh, S., … Lenardo, M. J. (2004). Regulation of an ATG7-beclin 1 program of autophagic cell death by caspase-8. *Science*, *304*, 1500–2.

Yue, Z., Jin, S., Yang, C., Levine, A. J., & Heintz, N. (2003). Beclin 1, an autophagy

gene essential for early embryonic development, is a haploinsufficient tumor suppressor. *Proc Natl Acad Sci U S A*, *100*, 15077–15082.

Zhang, Y., Li, X., Becker, K. A., & Gulbins, E. (2009). Ceramide-enriched membrane domains - Structure and function. *Biochim Biophys Acta, 1788*, 178–83.

Zhang, Y., Yao, B., Delikat, S., Bayoumy, S., Lin, X. H., Basu, S., … Kolesnick, R. (1997). Kinase suppressor of Ras is ceramide-activated protein kinase. *Cell*, *89*, 63–72.

Zhao, H., & Kinnunen, P. K. J. (2002). Binding of the antimicrobial peptide temporin L to liposomes assessed by Trp fluorescence. *J Biol Chem*, *277*, 25170–25177.

Zhao, H., & Lappalainen, P. (2012). A simple guide to biochemical approaches for analyzing protein-lipid interactions. *Mol Biol Cell*, *23*, 2823–30.

Zhao, J., Brault, J. J., Schild, A., Cao, P., Sandri, M., Schiaffino, S., … Goldberg, A. L. (2007). FoxO3 Coordinately Activates Protein Degradation by the Autophagic/Lysosomal and Proteasomal Pathways in Atrophying Muscle Cells. *Cell Metab*, *6*, 472–483.

Zheng, Y. T., Shahnazari, S., Brech, A., Lamark, T., Johansen, T., & Brumell, J. H. (2009). The adaptor protein p62/SQSTM1 targets invading bacteria to the autophagy pathway. *J Immunol*, *183*, 5909–5916.

Zhou, P., Qian, L., D'Aurelio, M., Cho, S., Wang, G., Manfredi, G., … Iadecola, C. (2012). Prohibitin reduces mitochondrial free radical production and protects brain cells from different injury modalities. *J Neurosci*, *32*, 583–92.

Zhu, C., Vourc'h, P., Fernagut, P. O., Fleming, S. M., Lacan, S., Dicarlo, C. D., … Chesselet, M. F. (2004). Variable effects of chronic subcutaneous administration of rotenone on striatal histology. *J Comp Neurol*, *478*, 418–426.

Zinser, E., & Daum, G. (1995). Isolation and biochemical characterization of organelles from the yeast, Saccharomyces cerevisiae. *Yeast*, *11*, 493–536.

Ziviani, E., Tao, R. N., & Whitworth, A. J. (2010). Drosophila parkin requires PINK1 for mitochondrial translocation and ubiquitinates mitofusin. *Proc Natl Acad Sci U S A*, *107*, 5018–23.

Zois, C. E., Giatromanolaki, A., Kainulainen, H., Botaitis, S., Torvinen, S., Simopoulos, C., … Koukourakis, M. I. (2011). Lung autophagic response following exposure of mice to whole body irradiation, with and without amifostine. *Biochem Biophys Res Commun*, *404*, 552–558.

Zufferey, R., Dull, T., Mandel, R. J., Bukovsky, A., Quiroz, D., Naldini, L., & Trono, D. (1998). Self-inactivating lentivirus vector for safe and efficient in vivo gene delivery. *J Virol*, *72*, 9873–80.

Publications

Publications

Antón, Z.*, Landajuela, A.*, Hervás, J. H., Montes, L. R., Hernández-Tiedra, S., Velasco, G., Goñi, F.M. & Alonso, A. (2016). Human Atg8-cardiolipin interactions in mitophagy: Specific properties of LC3B, GABARAPL2 and GABARAP. *Autophagy, 12,* 2386–2403. (*Co-first authors).

Hernández-Tiedra, S., Fabriàs, G., Dávila, D., Salanueva, I. J., Casas, J., Montes, L. R., **Antón, Z.**, … & Velasco, G. (2016). Dihydroceramide accumulation mediates cytotoxic autophagy of cancer cells via autolysosome destabilization. *Autophagy*, *12*, 2213–2229.

Landajuela, A.*, Hervás, J. H.*, **Antón, Z.**, Montes, L. R., Gil, D., Valle, M., Rodriguez, J.F., Goñi, F.M. & Alonso, A. (2016). Lipid geometry and bilayer curvature modulate LC3/GABARAP-mediated model autophagosomal elongation. *Biophys J, 110*, 411–422. (*Co-first authors).

In preparation

Antón, Z., Stathakos, P., Anderson, M., Baines, K., Nistor, P. A., Alonso, A. & Lane, J. D. (2017). *Rotenone-dependent regulation of LC3B, GABARAPL1 and ATG5 mitochondrial recruitment during mitophagy in RPE1 cells and iPSC-derived cortical neurons.*

Antón, Z.*, Hervás, J.H.* & Alonso, A. (2017). Biophysical studies of LC3 family proteins. In *Autophagy Methods*. Berlin, Germany: Springer. (*Co-first authors).

Hervás, J. H., Landajuela, A., **Antón, Z.**, Shnyrova, A. V., Goñi, F.M. & Alonso, A. (2017). *Human ATG3 binding to lipid bilayers: role of lipid geometry, electric charge and bilayer curvature.*

Acknowledgements

Acknowledgements

The present thesis was performed at Instituto Biofisika (CSIC, UPV/EHU) under the supervision of Professor Alicia Alonso. The work was supported by FEDER/Spanish Ministry of Economy (BFU 2011-28566, BFU 2015-66306-P), and the Basque Government (IT838-13, IT849-13). The author was a recipient of a predoctoral fellowship from the University of the Basque Country.

The author is grateful to Dr. Guillermo Velasco and colleagues (Madrid) for their collaboration in the project, and to Dr. Jon Lane (Bristol) for his training in cell biology techniques and useful discussions. She is also indebted to Professor F.M. Goñi, Dr. Ane Landajuela and Dr. Javier Hervás for their help throughout the thesis, and to Ms Araceli Marcos for her skillful technical assistance.